COMPUTATIONAL SIMULATION AND REALIZATION OF THREE-DIMENSIONAL METAMATERIALS WITH VARIOUS EXOTIC PROPERTIES

A THESIS SUBMITTED TO
THE GRADUATE SCHOOL OF NATURAL AND APPLIED SCIENCES
OF
MIDDLE EAST TECHNICAL UNIVERSITY

BY

HANDE İBİLİ

IN PARTIAL FULFILLMENT OF THE REQUIREMENTS
FOR
THE DEGREE OF MASTER OF SCIENCE
IN
ELECTRICAL AND ELECTRONICS ENGINEERING

SEPTEMBER 2019

Approval of the thesis:

COMPUTATIONAL SIMULATION AND REALIZATION OF THREE-DIMENSIONAL METAMATERIALS WITH VARIOUS EXOTIC PROPERTIES

submitted by **HANDE İBİLİ** in partial fulfillment of the requirements for the degree of **Master of Science in Electrical and Electronics Engineering Department, Middle East Technical University** by,

Prof. Dr. Halil Kalıpçılar
Dean, Graduate School of **Natural and Applied Sciences** ________________

Prof. Dr. İlkay Ulusoy
Head of Department, **Electrical and Electronics Engineering** ________________

Assoc. Prof. Dr. Özgür Ergül
Supervisor, **Electrical and Electronics Engineering, METU** ________________

Examining Committee Members:

Prof. Dr. Sencer Koç
Electrical and Electronics Engineering, METU ________________

Assoc. Prof. Dr. Özgür Ergül
Electrical and Electronics Engineering, METU ________________

Prof. Dr. Özlem Aydın Çivi
Electrical and Electronics Engineering, METU ________________

Assoc. Prof. Dr. Lale Alatan
Electrical and Electronics Engineering, METU ________________

Prof. Dr. Vakur Behçet Ertürk
Electrical and Electronics Engineering, Bilkent University ________________

Date:

I hereby declare that all information in this document has been obtained and presented in accordance with academic rules and ethical conduct. I also declare that, as required by these rules and conduct, I have fully cited and referenced all material and results that are not original to this work.

Name, Surname: Hande İbili

Signature :

ABSTRACT

COMPUTATIONAL SIMULATION AND REALIZATION OF THREE-DIMENSIONAL METAMATERIALS WITH VARIOUS EXOTIC PROPERTIES

İbili, Hande
M.S., Department of Electrical and Electronics Engineering
Supervisor: Assoc. Prof. Dr. Özgür Ergül

September 2019, 136 pages

In this study, computational analysis and realization of three-dimensional metamaterial structures that induce negative and zero permittivity and/or permeability values in their host environment, as well as plasmonic nanoparticles that are used to design metamaterials at optical frequencies are presented. All these electromagnetic problems are challenging since effective material properties become negative/zero, while numerical solvers are commonly developed for ordinary positive parameters. In real life, three-dimensional metamaterial structures, involving split-ring resonators (SRR), thin wires, and similar subwavelength elements, are designed to exhibit single negativity (imaginary refractive index) and double negativity (negative refractive index) behaviors. However, metamaterial elements have small details with respect to wavelength and they operate when they resonate. Then, their numerical models lead to large matrix equations that are also ill-conditioned, making their solutions extremely difficult, if not impossible. If performed accurately, homogenization simplifies the analysis of metamaterials, while new challenges arise due to extreme parameters. For example, a combination of zero-index (ZI) and near-zero-index (NZI) materials with ordinary media (metals, free space, etc.) results in a high-contrast problem, and numerical instabilities occur particularly due to huge values of wavelength. Similar difficulties arise when considering the plasmonic effects of metals at optical frequencies since they must be modeled as penetrable bodies with negative real permittivity, leading to imaginary index values. Different surface-integral-equation (SIE) formulations and broadband multilevel fast multipole algorithm (MLFMA) implementations are extensively tested for accurate and efficient numerical solutions of ZI, NZI, imaginary-index, and negative-index materials. In addition to their computational simulations, metamaterial designs are fabricated with a low-cost inkjet-printing setup, which is based on using conventional printers that are modified and loaded with silver-based inks. Measurements demonstrate the feasibility of fabricating very low-cost three-dimensional metamaterials using simple inkjet printing.

Keywords: Metamaterials, Zero-Index Materials, Split-Ring Resonators, Multiband Filters, Electromagnetic Homogenization, Genetic Algorithms, Nanoparticles, Inkjet Printing, Multilevel Fast Multipole Algorithm

ÖZ

ÇEŞİTLİ SIRADIŞI ÖZELLİKLERE SAHİP ÜÇ BOYUTLU METAMALZEMELERİN HESAPLAMALI BENZETİMLERİ VE GERÇEKLENMELERİ

İbili, Hande
Yüksek Lisans, Elektrik ve Elektronik Mühendisliği Bölümü
Tez Yöneticisi: Doç. Dr. Özgür Ergül

Eylül 2019, 136 sayfa

Bu çalışmada, bulundukları ortamda negatif ve sıfır elektrik ve/veya manyetik geçirgenlik değerleri indükleyen üç boyutlu metamalzemelerin ve ayrıca optik frekanslarda metamalzemelerin tasarımında kullanılan plazmonik nanoparçacıkların hesaplamalı benzetimleri ve gerçeklenmeleri sunulmuştur. Sayısal çözücüler çoğunlukla normal pozitif parametreler için geliştirildiğinden, negatif/sıfır materyal özelliklerini içeren bu elektromanyetik problemlerin çözümleri son derece zordur. Gerçek hayatta, ayrık-halka rezonatörleri, ince tel yapılar, ve benzeri şekilde dalga boyundan küçük elemanlar içeren üç boyutlu metamalzemeler, tek negatiflik (sanal kırınım indisi) ve çift negatiflik (negatif kırınım indisi) özellikleri sergilemeleri için tasarlanmıştır. Bununla birlikte metamalzeme elemanları dalga boyuna göre küçük detaylara sahiptir ve bu elemanlar genellikle rezonansa girdiklerinde çalışmaktadırlar. Bu yüzden, sayısal modellemelerde kötü koşullu ve büyük matris denklemleri elde edilmektedir. Doğru şekilde uygulandığında, homojenleştirme metamalzeme analizlerini basitleştirmek için kullanılabilir. Ancak, sıradışı parametrelerden dolayı yeni zorluklar ortaya çıkmaktadır. Örneğin, sıfır indisli veya sıfıra yakın indisli materyallerin normal ortamlarla (metaller, boş uzay, v.b.) beraber incelenmesinde yüksek kontrastlı problemler elde edilir, ve özellikle çok büyük dalga boyu değerleri için sayısal kararsızlıklar oluşur. Sanal indis değerlerine yol açan negatif elektriksel geçirgenliğe sahip cisimler olarak modellenmeleri gerektiğinden, metallerin optik frekanslardaki plazmonik davranışları da benzer biçimde sayısal zorluklar ortaya çıkarmaktadır. Bu doğrultuda, sıfır indisli, sıfıra yakın indisli, sanal indisli, ve negatif indisli materyallerin hassas ve verimli sayısal çözümleri için farklı yüzey integral denklemi formülasyonları ve geniş bantlı çok seviyeli hızlı çokkutup yöntemi uygulamaları kapsamlı olarak incelenmiştir. Hesaplamalı benzetimlerin yanında, gümüş katkılı mürekkeplerle yüklü sıradan yazıcıların kullanılmasına dayanan bir düşük maliyetli inkjet basım ortamında metamateryal tasarımları üretilmiştir. Elde edilen ölçüm sonuçları, geliştirilen inkjet baskı tekniğinin kullanılmasıyla, çok düşük maliyetli üç boyutlu metamalzemelerin üretilmesinin mümkün olduğunu göstermektedir.

Anahtar Kelimeler: Metamalzemeler, Sıfır-İndisli Materyaller, Ayrık-Halka Rezonatörleri, Çok-Bantlı Filtreler, Elektromanyetik Homojenleştirme, Genetik Algoritmalar, Nanoparçacıklar, İnkjet Basım, Çok Seviyeli Hızlı Çokkutup Yöntemi

to my beloved mother and father...

ACKNOWLEDGMENTS

First and foremost, I would like to express my sincere gratitude to my advisor, Assoc. Prof. Dr. Özgür Ergül, for his constant support, invaluable guidance, generous assistance, and powerful inspiration. I could not have imagined having a better advisor and mentor for my Master's study.

I would like to thank Prof. Dr. Sencer Koç, Prof. Dr. Özlem Aydın Çivi, and Assoc. Prof. Dr. Lale Alatan, for all the knowledge they provided to me, throughout both in my undergraduate and graduate education, and for their participation in the jury and valuable comments.

I would also like to thank Prof. Dr. Vakur Behçet Ertürk for his participation in the jury and valuable comments.

I would like to thank Barışcan Karaosmanoğlu, Feza Mutlu, Sadri Güler, Özgür Eriş, Yeşim Koyaz and Selen Keleş for their great cooperation and participation in my studies, Zeina El-Ahdab, Gökhan Karaova, Göktuğ Işıklar, Şirin Yazar, Meriç Gür, and Ali Farshkaran for their valuable discussions, and all group members of CEMMETU for their support.

I would also like to thank Özlem Gümüşkanat, Sena Alkış, Berna Barutcu, Aşkın Altınoklu, Hilal Kübra Dumanlı Aydın, Eren Aydın, Furkan Gökçe, Alperen Çalıkoğlu, Damla Alptekin, Başak Güleçyüz, Selin Akbaş, Eda Korkmaz, Ezgi Uysal, Eray Ercan, Muammer Kozan, Yusuf Deniz, and Serkut Ayvaşık for their constant support and invaluable friendship.

I would like to thank my mother and father. There are no words to express my heartfelt gratitude for their unconditional trust, endless encouragement, everlasting support, and eternal love.

I would like to thank TÜBİTAK for 2210-A scholarship program as the financial support during my Master's study.

TABLE OF CONTENTS

ABSTRACT v

ÖZ vii

ACKNOWLEDGMENTS x

TABLE OF CONTENTS xi

LIST OF FIGURES xiv

LIST OF ABBREVIATIONS xxvii

CHAPTERS

1 INTRODUCTION 1

2 SIMULATIONS OF ZERO-INDEX MATERIALS 7

- 2.1 Simulation Method 7
  - 2.1.1 Surface Integral Equations 7
  - 2.1.2 Surface Formulations 11
  - 2.1.3 Method of Moments 16
  - 2.1.4 Discretization 17
  - 2.1.5 Multilevel Fast Multipole Algorithm 19
  - 2.1.6 Approximate Diagonalization 20
- 2.2 Numerical Results 22
  - 2.2.1 Formulation Tests 23

2.2.2 Analysis of Exotic Lens Structures 37

2.2.3 Analysis of Waveguide Structures with Sharp Corners 55

2.3 Concluding Remarks 61

3 SIMULATION AND REALIZATION OF INKJET-PRINTED METAMATERIALS FOR MICROWAVE FREQUENCIES 63

3.1 Simulation Method 63

3.1.1 Surface Formulation to Solve Three-Dimensional Metamaterial Structures 63

3.1.2 Genetic Algorithms Supported by Full-Wave Solutions for the Homogenization of Metamaterial Structures 64

3.2 Numerical Results 67

3.2.1 Analysis of Single-Band Metamaterials Involving SRRs 68

3.2.2 Analysis of Multiband Metamaterials Involving SRRs 74

3.2.3 Analysis of Composite Metamaterials 93

3.2.4 Homogenization of SRR Structure 93

3.3 Fabrications via Inkjet Printing 99

3.3.1 Very Low-Cost Inkjet Fabrication 99

3.3.2 Inkjet Printing Challenges 100

3.3.3 Sensitivity Analysis 101

3.4 Measurement Results 108

3.4.1 Single-Band SRR Results 108

3.4.2 Multiband SRR Results 108

3.4.3 Composite Metamaterial Results 109

3.5 Concluding Remarks 109

4 SIMULATIONS OF METALLIC NANOPARTICLES AT TERAHERTZ FREQUENCIES 111

4.1 Nanoscale Metals at Terahertz Frequencies 111

4.2 Simulation Method 112

4.3 Numerical Results 113

4.4 Concluding Remarks 121

5 CONCLUSION 123

REFERENCES 127

LIST OF FIGURES

FIGURES

Figure 2.1 Boundary between two penetrable regions. 10

Figure 2.2 Illustration of an RWG function. 17

Figure 2.3 The real part of the electric field intensity (dBV/m) inside and outside the spheres with NZI materials having a set of relative permittivity and/or permeability values close to zero. 22

Figure 2.4 The real part of the magnetic field intensity (dBA/m) inside and outside the spheres with NZI materials having a set of relative permittivity and/or permeability values close to zero. 23

Figure 2.5 The map of the plots in Figures 2.6 and 2.7. 24

Figure 2.6 Relative errors in the far-zone electric field intensity values obtained by using different formulations for scattering problems of NZI spheres with a set of permittivity and/or permeability values close to zero. In the plots, the maximum error is set to 10%. 25

Figure 2.7 Numbers of GMRES iterations obtained by using different formulations for scattering problems of NZI spheres with a set of permittivity and/or permeability values close to zero. In the plots, the maximum number of iterations is set to 2000. 26

Figure 2.8 Far-zone electric field intensity distribution (left) and GMRES iterative convergence (right) plots obtained by using different formulations for the scattering problem of a λ-diameter NZI sphere with $\epsilon_z = 10^{-6}$ and $\mu_z = 10^{-6}$. 28

Figure 2.9 Far-zone electric field intensity distribution (left) and GMRES iterative convergence (right) plots obtained by using different formulations for the scattering problem of a λ-diameter NZI sphere with $\epsilon_z = 10^{-12}$ and $\mu_z = 1.0$. 28

Figure 2.10 Far-zone electric field intensity distribution (left) and GMRES iterative convergence (right) plots obtained by using different formulations for the scattering problem of a λ-diameter NZI sphere with $\epsilon_z = 1.0$ and $\mu_z = 10^{-12}$. 29

Figure 2.11 Far-zone electric field intensity distribution (left) and GMRES iterative convergence (right) plots obtained by using different formulations for the scattering problem of a λ-diameter NZI sphere with $\epsilon_z = 10^{-12}$ and $\mu_z = 10^{-12}$. 29

Figure 2.12 Relative errors in the far-zone electric field intensity values with respect to Mie-series solutions for the scattering problems involving NZI spheres formulated with JMCFIE. 30

Figure 2.13 Numbers of GMRES iterations for the scattering problems involving NZI spheres formulated with JMCFIE. 31

Figure 2.14 Relative errors in the far-zone electric field intensity values with respect to Mie-series solutions for the scattering problems involving NZI spheres formulated with the new mixed formulation. 32

Figure 2.15 Numbers of GMRES iterations for the scattering problems involving NZI spheres formulated with the new mixed formulation. 33

Figure 2.16 Bistatic far-zone electric field intensity distributions obtained for the scattering problems involving NZI spheres with $\epsilon_z = 0.1$ and $\mu_z = 0.1$. 34

Figure 2.17 Bistatic far-zone electric field intensity distributions obtained for the scattering problems involving NZI spheres with $\epsilon_z = 0.01$ and $\mu_z = 0.01$. 35

Figure 2.18 Bistatic far-zone electric field intensity distributions obtained for the scattering problems involving NZI spheres with $\epsilon_z = 0.001$ and $\mu_z = 0.001$. 36

Figure 2.19 Bistatic far-zone electric field intensity distributions obtained for the scattering problems involving NZI spheres with $\epsilon_z = 0.0001$ and $\mu_z = 0.0001$. 37

Figure 2.20 Illustration of a lens geometry (cylindrical extraction from a $2\lambda \times \lambda \times 2\lambda$ block) and its cross section. 38

Figure 2.21 Near-zone electric field intensity (dBV/m) and magnetic field intensity (dBA/m) distributions for the NZI lens structure shown in Figure 2.20 with $\epsilon_z = 0.1$ and $\mu_z = 0.1$, obtained by the new mixed formulation. 39

Figure 2.22 Near-zone electric field intensity (dBV/m) and magnetic field intensity (dBA/m) distributions for the NZI lens structure shown in Figure 2.20 with $\epsilon_z = 0.1$ and $\mu_z = 0.1$, obtained by the JMCFIE formulation. . 39

Figure 2.23 Near-zone electric field intensity (dBV/m) and magnetic field intensity (dBA/m) distributions for the NZI lens structure shown in Figure 2.20 with $\epsilon_z = 0.01$ and $\mu_z = 0.01$, obtained by the new mixed formulation. 40

Figure 2.24 Near-zone electric field intensity (dBV/m) and magnetic field intensity (dBA/m) distributions for the NZI lens structure shown in Figure 2.20 with $\epsilon_z = 0.01$ and $\mu_z = 0.01$, obtained by the JMCFIE formulation. 40

Figure 2.25 Near-zone electric field intensity (dBV/m) and magnetic field intensity (dBA/m) distributions for the NZI lens structure shown in Figure 2.20 with $\epsilon_z = 1$ and $\mu_z = 0.1$, obtained by the new mixed formulation. 41

Figure 2.26 Near-zone electric field intensity (dBV/m) and magnetic field intensity (dBA/m) distributions for the NZI lens structure shown in Figure 2.20 with $\epsilon_z = 1$ and $\mu_z = 0.1$, obtained by the JMCFIE formulation. . . 41

Figure 2.27 Near-zone electric field intensity (dBV/m) and magnetic field intensity (dBA/m) distributions for the NZI lens structure shown in Figure 2.20 with $\epsilon_z = 1$ and $\mu_z = 0.01$, obtained by the new mixed formulation. 42

Figure 2.28 Near-zone electric field intensity (dBV/m) and magnetic field intensity (dBA/m) distributions for the NZI lens structure shown in Figure 2.20 with $\epsilon_z = 1$ and $\mu_z = 0.01$, obtained by the JMCFIE formulation. . 42

Figure 2.29 Near-zone electric field intensity (dBV/m) and magnetic field intensity (dBA/m) distributions for the NZI lens structure shown in Figure 2.20 with $\epsilon_z = 0.1$ and $\mu_z = 1$, obtained by the new mixed formulation. 43

Figure 2.30 Near-zone electric field intensity (dBV/m) and magnetic field intensity (dBA/m) distributions for the NZI lens structure shown in Figure 2.20 with $\epsilon_z = 0.1$ and $\mu_z = 1$, obtained by the JMCFIE formulation. . . 43

Figure 2.31 Near-zone electric field intensity (dBV/m) and magnetic field intensity (dBA/m) distributions for the NZI lens structure shown in Figure 2.20 with $\epsilon_z = 0.01$ and $\mu_z = 1$, obtained by the new mixed formulation. 44

Figure 2.32 Near-zone electric field intensity (dBV/m) and magnetic field intensity (dBA/m) distributions for the NZI lens structure shown in Figure 2.20 with $\epsilon_z = 0.01$ and $\mu_z = 1$, obtained by the JMCFIE formulation. . 44

Figure 2.33 Illustration of a lens geometry (spherical extraction from a $2\lambda \times \lambda \times 2\lambda$ block) and its cross section. 45

Figure 2.34 Near-zone power density (dBW/m^2) distributions for the NZI lens structures shown in Figures 2.20 and 2.33, obtained by using the new mixed and JMCFIE formulations. 46

Figure 2.35 Near-zone power density (dBW/m^2) distributions for different NZI lens structures using the new mixed and JMCFIE formulations. . . 47

Figure 2.36 Large-scale NZI lens structures. 48

Figure 2.37 Near-zone field intensity distributions for the $8\lambda \times 8\lambda \times 8\lambda$ lens structure shown in Figure 2.36 (left) with $\epsilon_z = 0.1$ and $\mu_z = 0.1$, obtained by JMCFIE and the new mixed formulations. 49

Figure 2.38 Near-zone field intensity distributions for the $8\lambda \times 8\lambda \times 8\lambda$ lens structure shown in Figure 2.36 (middle) with $\epsilon_z = 0.1$ and $\mu_z = 0.1$, obtained by JMCFIE and the new mixed formulations. 49

Figure 2.39 Near-zone field intensity distributions for the $8\lambda \times 8\lambda \times 8\lambda$ lens structure shown in Figure 2.36 (right) with $\epsilon_z = 0.1$ and $\mu_z = 0.1$, obtained by JMCFIE and the new mixed formulations. 50

Figure 2.40 Near-zone power density distributions for the $8\lambda \times 8\lambda \times 8\lambda$ lens structures in Figure 2.36 with $\epsilon_z = 0.1$ and $\mu_z = 0.1$, obtained by JMCFIE and the new mixed formulations. 51

Figure 2.41 Iterative solutions of the $8\lambda \times 8\lambda \times 8\lambda$ lens structures in Figure 2.36 with $\epsilon_z = 0.1$ and $\mu_z = 0.1$, when using JMCFIE and the new mixed formulations. 51

Figure 2.42 Near-zone field intensity distributions for the $16\lambda \times 16\lambda \times 16\lambda$ lens structure in Figure 2.36 (left) with $\epsilon_z = 0.1$ and $\mu_z = 0.1$, obtained by JMCFIE and the new mixed formulations. 52

Figure 2.43 Near-zone field intensity distributions for the $16\lambda \times 16\lambda \times 16\lambda$ lens structure in Figure 2.36 (middle) with $\epsilon_z = 0.1$ and $\mu_z = 0.1$, obtained by JMCFIE and the new mixed formulations. 52

Figure 2.44 Near-zone power density distributions for the $16\lambda \times 16\lambda \times 16\lambda$ lens structures in Figure 2.36 with $\epsilon_z = 0.1$ and $\mu_z = 0.1$, obtained by JMCFIE and the new mixed formulations. 53

Figure 2.45 Iterative solutions for the $16\lambda \times 16\lambda \times 16\lambda$ lens structures in Figure 2.36 with $\epsilon_z = 0.1$ and $\mu_z = 0.1$, when using JMCFIE and the new mixed formulations. 54

Figure 2.46 Dimensions of a composite structure involving a WR90-sized waveguide with a sharp corner and an NZI region at the corner of the waveguide. 54

Figure 2.47 Near-zone field intensity distributions for the composite structure in Figure 2.46 involving a WR90-sized waveguide having a sharp corner. One side of the waveguide is open. An EMNZ block is placed at the corner of the waveguide. 55

Figure 2.48 Near-zone field intensity distributions for the composite structure in Figure 2.46 involving a WR90-sized waveguide having a sharp corner. One side of the waveguide is open. An ENZ block is placed at the corner of the waveguide. 56

Figure 2.49 Near-zone field intensity distributions for the composite structure in Figure 2.46 involving a WR90-sized waveguide having a sharp corner. One side of the waveguide is open. An MNZ block is placed at the corner of the waveguide. 57

Figure 2.50 Near-zone electric field intensity distributions for the composite structure in Figure 2.46 without a block and with ENZ, MNZ, and EMNZ blocks at the corner. 58

Figure 2.51 Near-zone magnetic field intensity distributions for the composite structure in Figure 2.46 without a block and with ENZ, MNZ, and EMNZ blocks at the corner. 58

Figure 2.52 Near-zone power density distributions for the composite structure in Figure 2.46 without a block and with ENZ, MNZ, and EMNZ blocks at the corner. 59

Figure 2.53 Dimensions of a composite structure involving a WR90-sized waveguide with three sharp corners and an NZI region. 59

Figure 2.54 Near-zone field intensity distributions for the composite structure in Figure 2.53 involving a WR90-sized waveguide with three sharp corners. An MNZ block is placed inside the waveguide to improve the transmission. 60

Figure 3.1 Representation of the mechanism based on genetic algorithms. . 65

Figure 3.2 Representation of the reproduction procedure. 66

Figure 3.3 Details and dimensions (in mm) of the SRR structure that is designed to resonate at around 7.25 GHz when fabricated with inkjet printing. 67

Figure 3.4 Near-zone field intensity and power density distributions for the SRR structure in Figure 3.3 on the x-y ($z = 0$) plane at 6 GHz and 8.5 GHz. 68

Figure 3.5 Near-zone electric field intensity (dBV/m) distributions for the SRR structure in Figure 3.3 on the x-y ($z = 0$) plane from 6 GHz to 10 GHz at 100 MHz intervals. 69

Figure 3.6 Near-zone magnetic field intensity (dBA/m) distributions for the SRR structure in Figure 3.3 on the x-y ($z = 0$) plane from 6 GHz to 10 GHz at 100 MHz intervals. 69

Figure 3.7 Near-zone power density (dBW/sm) distributions for the SRR structure in Figure 3.3 on the x-y ($z = 0$) plane from 6 GHz to 10 GHz at 100 MHz intervals. 70

Figure 3.8 Details and dimensions (in mm) of the SRR structure that is designed to resonate at around 6 GHz when fabricated with inkjet printing. 71

Figure 3.9 Near-zone electric field intensity (dBV/m) distributions for the SRR structure in Figure 3.8 on the x-y ($z = 0$) and y-z ($x = -6$ cm) planes from 6 GHz to 10 GHz at 100 MHz intervals. 71

Figure 3.10 Near-zone magnetic field intensity (dBA/m) distributions for the SRR structure in Figure 3.8 on the x-y ($z = 0$) and y-z ($x = -6$ cm) planes from 6 GHz to 10 GHz at 100 MHz intervals. 72

Figure 3.11 Near-zone power density (dBW/sm) distributions for the SRR structure in Figure 3.8 on the x-y ($z = 0$) and y-z ($x = -6$ cm) planes from 6 GHz to 10 GHz at 100 MHz intervals. 72

Figure 3.12 Details and dimensions (in mm) of non-scaled and scaled SRR structures that are used to design multiband metamaterials. 73

Figure 3.13 Near-zone power density (dBW/sm) distributions for the non-scaled and scaled SRR arrays (see Figure 3.12) on the x-y ($z = 0$) plane from 4 GHz to 10 GHz at 100 MHz intervals. 74

Figure 3.14 Power transmission coefficient with respect to frequency for the arrays involving SRRs with different scales (see Figure 3.12). 75

Figure 3.15 Arrangements and design parameters to build multiband SRR blocks from the two-dimensional arrays. 75

Figure 3.16 Six successful layouts for dual-band metamaterial designs with AP = 10.5 mm. 77

Figure 3.17 Power density distributions for the dual-band design involving non-scaled and 6/7-scaled SRRs [with the layout given in Figure 3.16 (first from left-hand side)] from 4 GHz to 10 GHz. LP = 15.4 mm (left) and LP = 18.0 mm (right) are used. 78

Figure 3.18 Power density distributions for the dual-band design involving non-scaled and 3/4-scaled SRRs [with the layout given in Figure 3.16 (second from left-hand side)] from 4 GHz to 10 GHz. LP = 13.5 mm (left) and LP = 18.0 mm (right) are used. 78

Figure 3.19 Power density distributions for the dual-band design involving non-scaled and 2/3-scaled SRRs [with the layout given in Figure 3.16 (third from left-hand side)] from 4 GHz to 10 GHz. LP = 12.0 mm (left) and LP = 18.0 mm (right) are used. 79

Figure 3.20 Power density distributions for the dual-band design involving 6/7-scaled and 3/4-scaled SRRs [with the layout given in Figure 3.16 (third from right-hand side)] from 4 GHz to 10 GHz. LP = 13.5 mm (left) and LP = 15.4 mm (right) are used. 79

Figure 3.21 Power density distributions for the dual-band design involving 6/7-scaled and 2/3-scaled SRRs [with the layout given in Figure 3.16 (second from right-hand side)] from 4 GHz to 10 GHz. LP = 12.0 mm (left) and LP = 15.4 mm (right) are used. 80

Figure 3.22 Power density distributions for the dual-band design involving 3/4-scaled and 2/3-scaled SRRs [with the layout given in Figure 3.16 (first from right-hand side)] from 4 GHz to 10 GHz. LP = 12.0 mm (left) and LP = 13.5 mm (right) are used. 80

Figure 3.23 Power transmission coefficients for the dual-band metamaterials with the layouts given in Figure 3.16 (the first three layouts from left-hand side) and with selected layer periodicities. 81

Figure 3.24 Power transmission coefficients for the dual-band metamaterials with the layouts given in Figure 3.16 (the last three layouts from left-hand side) and with selected layer periodicities. 82

Figure 3.25 Six successful layouts for triple-band metamaterial designs with AP = 10.5 mm. 83

Figure 3.26 Power density distributions for the triple-band design involving original, 3/4-scaled, and 2/3-scaled SRRs with LP = 12.0 mm from 4 GHz to 10 GHz at 100 MHz intervals. 84

Figure 3.27 Power density distributions for the triple-band design involving original, 3/4-scaled, and 2/3-scaled SRRs with LP = 13.5 mm from 4 GHz to 10 GHz at 100 MHz intervals. 85

Figure 3.28 Power density distributions for the triple-band design involving original, 3/4-scaled, and 2/3-scaled SRRs with LP = 18.0 mm from 4 GHz to 10 GHz at 100 MHz intervals. 85

Figure 3.29 Power transmission coefficients for the triple-band metamaterials with the layouts given in Figure 3.25 (three layouts at the top) and with selected layer periodicities. 86

Figure 3.30 Power transmission coefficients for the triple-band metamaterials with the layouts given in Figure 3.25 (three layouts at the bottom) and with selected layer periodicities. 87

Figure 3.31 Triple-band metamaterials with a standard layout (right) and with duplicated arrays (left) involving non-scaled, 3/4-scaled, and 2/3-scaled SRRs. 88

Figure 3.32 Power density distributions for the triple-band metamaterial with duplicated arrays depicted in Figure 3.31 from 4 GHz to 10 GHz at 100 MHz intervals. 88

Figure 3.33 Power transmission coefficients for the triple-band metamaterials with the layouts given in Figure 3.31 when LP = 18.0 mm. 89

Figure 3.34 Quad-band metamaterials with a standard layout (right) and with duplicated and rearranged arrays (left) involving non-scaled, 2/3-scaled, 6/7-scaled, and 3/4-scaled SRR arrays. 89

Figure 3.35 Power density distributions for the quad-band matematerial with duplicated arrays depicted in Figure 3.34 from 4 GHz to 10 GHz at 100 MHz intervals. 90

Figure 3.36 Power transmission coefficients for the quad-band metamaterials with the layouts given in Figure 3.34. For the layout with duplicated and rearranged arrays, different LP values are used. 90

Figure 3.37 Details and dimensions (in mm) of the composite metamaterial that involves SRRs and thin wires. 92

Figure 3.38 Power density distributions for the composite metamaterial design from 5.0 GHz to 16.0 GHz at 100 MHz intervals. 92

Figure 3.39 Representation of the mechanism used for the homogenization of SRR arrays. 94

Figure 3.40 Illustration of the optimization problem involving a non-dielectric slab and a sample line for the near-zone power density values. 94

Figure 3.41 Cost function and relative permeability for the optimization problems of slabs with known permeability values. 95

Figure 3.42 Optimized relative permeability and relative difference in the permeability values with respect to frequency for the optimization problem involving an SRR array. 96

Figure 3.43 Transmitted power density through the real and homogenized models of the SRR array with respect to frequency. 97

Figure 3.44 Power density distributions on the central line obtained for the real and homogenized models with respect to frequency. 97

Figure 3.45 Steps to fabricate three-dimensional metamaterial structures and validation of simulation/measurement results. 98

Figure 3.46 SRR samples with different outer ring sizes (R: outer radius) fabricated via low-cost inkjet printing. 100

Figure 3.47 Simulation results for near-zone power density distributions on x-y and y-z planes for the SRR array in Figure 3.8 with different fabrication errors. The frequency is set to 7.8 GHz, while the structures are located in vacuum. 102

Figure 3.48 Photograph of a fabricated SRR array. The design is shown in Figure 3.8. 103

Figure 3.49 Simulation and measurement results for the power transmission values of the SRR array in Figure 3.48. 103

Figure 3.50 Photographs of a fabricated SRR array. The design is shown in Figure 3.3. 104

Figure 3.51 Simulation and measurement results for the power transmission values of the SRR array in Figure 3.50. 104

Figure 3.52 Photographs of a fabricated triple-band metamaterial. The design is shown in Figure 3.31. 105

Figure 3.53 Simulation and measurement results for the power transmission values of the triple-band metamaterial in Figure 3.52. 105

Figure 3.54 Photographs of a fabricated quad-band metamaterial. The design is shown in Figure 3.34. 106

Figure 3.55 Simulation and measurement results for the power transmission values of the quad-band metamaterial in Figure 3.54. 106

Figure 3.56 Photographs of a fabricated composite metamaterial. The design is shown in Figure 3.37. 107

Figure 3.57 Simulation and measurement results for the power transmission values of the composite metamaterial in Figure 3.56. 107

Figure 4.1 Relative complex permittivity of silver (Ag) with respect to frequency. 112

Figure 4.2 Near-zone field intensity and power density distributions for the scattering problems involving PEC and Ag spheres of diameter 1 µm at 1 THz obtained with different mesh sizes. 113

Figure 4.3 Near-zone electric field intensity distributions for scattering problems involving PEC and Ag spheres of diameter 1 µm at different frequencies. 114

Figure 4.4 Near-zone magnetic field intensity distributions for scattering problems involving PEC and Ag spheres of diameter 1 µm at different frequencies. 114

Figure 4.5 Near-zone power density distributions for scattering problems involving PEC and Ag spheres of diameter 1 µm at different frequencies. 115

Figure 4.6 Far-zone electric field intensity with respect to bistatic angle for scattering problems involving PEC and Ag spheres of diameter 1 µm at different frequencies. 115

Figure 4.7 Near-zone electric field intensity distributions for scattering problems involving PEC and Ag spheres of different sizes at 50 THz. 116

Figure 4.8 Near-zone magnetic field intensity distributions for scattering problems involving PEC and Ag spheres of different sizes at 50 THz. . . 116

Figure 4.9 Near-zone power density distributions for scattering problems involving PEC and Ag spheres of different sizes at 50 THz. 117

Figure 4.10 Far-zone electric field intensity with respect to bistatic angle on the E-plane for scattering problems involving PEC and Ag spheres of different sizes at 50 THz. 118

Figure 4.11 Iterative solutions of scattering problems involving PEC and Ag spheres of different sizes at 50 THz. 119

Figure 4.12 Near-zone magnetic field intensity distributions for scattering problems involving PEC and Ag thin slabs (with 1 µm × 1 µm base size) of 50 nm and 25 nm thicknesses at different frequencies. 120

LIST OF ABBREVIATIONS

AD	Approximate diagonalization
CTF	Combined T formulation
EFIE	Electric-field integral equation
EMNZ	ϵ-μ-near-zero
ENZ	ϵ-near-zero
FMM	Fast multipole method
GMRES	Generalized minimal residual
JMCFIE	Electric-magnetic current combined-field integral equation
MCTF	Modified combined T formulation
MFIE	Magnetic-field integral equation
MLFMA	Multilevel fast multipole algorithm
MNMF	Modified N Müller formulation
MNZ	μ-near-zero
MOM	Method of moments
NMF	N Müller formulation
NZI	Near-zero-index
PEC	Perfect electric conductor
PMCHWT	Poggio-Miller-Chang-Harrington-Wu-Tsai
RWG	Rao-Wilton-Glisson
SIE	Surface integral equation
SRR	Split-ring resonator
ZI	Zero-index

CHAPTER 1

INTRODUCTION

Three-dimensional metamaterial structures exhibit exotic properties, such as imaginary index, negative index, zero index (ZI), and near-zero index (NZI), that are useful in diverse applications. Similar to others, artificially created ZI and NZI materials have recently attracted the interest of many researchers due to their potential abilities for a variety of applications in electronics and optics [1–7]. Very small refractive indices, i.e., very small permittivity and/or permeability values, indicate very large wavelengths, even at radio, microwave, and optical frequencies, which can be used for practical purposes. For example, such an object with zero refractive index may act as a perfect coupler for bending and tunneling electromagnetic waves (e.g., through waveguides [2, 3, 6]), since it theoretically corresponds to a single point, where entering energy immediately leaves. The same concept can be used to design directive antennas, optical diodes, and nano-optical imaging components [1, 4, 5]. In practice, similar to negative permittivity and permeability, zero electromagnetic parameters are generally obtained in macroscopic scales by periodically arranging meta-atoms [4,5].

Thanks to their great flexibility, surface-integral-equation (SIE) formulations that are developed for ordinary materials can easily be extended or directly applied to exotic materials [1, 8–10], e.g., those with negative, near-zero, and zero permittivity/permeability values. Nevertheless, such direct applications often result in inaccuracy, inefficiency, and/or instability issues, which may become intolerable particularly when structures under interest become electrically large such that iterative solutions are inevitable. In the case of ZI or NZI materials, for which permittivity/permeability are zero or close to zero, there are two underlying problems that make many analysis remarkably challenging. First, inner domains simply correspond to dense-discretization (low-frequency) problems, whose solutions are well-known to be difficult in the literature. We note that outer problems mainly put constraints on the discretization (e.g., triangle sizes), considering the smaller wavelength values associated with them. As the second issue, inner low-frequency problems are superposed with outer high-frequency problems that are related to the host media (e.g., vacuum). In such a superposition of two very different regimes, combination itself (enforcing boundary conditions) can be numerically challenging when dealing with operators of different scales.

In the first part of this study, we aim to develop accurate, stable, and efficient SIE solvers for rigorous analysis of three-dimensional electromagnetic problems involving NZI materials. In this class of objects, permittivity (ENZ: ϵ-near-zero), permeability (MNZ: μ-near-zero), or both can possess extraordinarily small values. Considering this generalization, none of the available surface formulations are truly stable as the permittivity/permeability go to zero. Therefore, new formulations, such as a mixed formulation, which can provide both accurate and efficient iterative solutions for arbitrarily small refractive index values, are developed. In addition, for fast analysis of electrically large structures (with respect to wavelength values in host media), a broadband version of the multilevel fast multipole algorithm (MLFMA) using an approximate diagonalization scheme (AD-MLFMA) [11] is further used. Numerical examples, some of which are presented in this thesis, demonstrate the effectiveness of the implementation based on AD-MLFMA and the new mixed formulation.

There is also a well-established literature on metamaterials with negative and imaginary indices, as they have become fundamental components of microwave devices in the last several decades [12–21]. Many different designs of metamaterials can be found in a plethora of studies, where they are employed as filters, shields, absorbers, radiation enhancers, and lenses at microwave frequencies. Most of the designs involve fundamental geometries, such as split-ring resonators (SRRs) [12] and straight wires [13], while these unit cells are modified in accordance with application purposes. Depending on target accuracy and desired preciseness, common design processes involve a variety of approaches from circuit theory to unit-cell modeling. When the structures under interest become complicated, however, full-wave methods become inevitable [22], [23], especially when considering three-dimensional arrangements of unit cells. Nonidentical elements and lack of periodicity further necessitate full-wave solutions to investigate strong interactions between unit cells and overall responses of metamaterials to excitations.

In the second part of this study, we consider accurate designs of single-band metamaterials demonstrating single-negativity and double-negativity behaviors, as well as multiband metamaterials at microwave frequencies. Three-dimensional single-band metamaterials involving full arrangements of identical SRRs and their combinations with thin wires are demonstrated. As particular examples for multiband metamaterials, three-dimensional arrangements of SRRs are considered such that the designed metamaterial blocks exhibit band-stop characteristics at multiple frequencies. For a given resonance frequency, designing the dimensions of a single SRR is already well-known in the literature. Besides, frequency shifts when identical SRRs are used together have been studied. However, interactions between nonidentical SRRs, particularly when they are arranged in three-dimensional volumes, are not well-known. As opposed to their nested arrangements [19, 20], arranging different-sized SRRs in free form provides more flexibility in designing resonance frequencies [18]. On the other hand, array parameters, i.e., arrangements of SRRs, must be tuned carefully in order to obtain satisfactory electromagnetic responses. For example, SRRs with similar dimensions tend to have stronger interactions that must be considered when ordering multiple one-dimensional arrays. Some of the designed metamaterials are further fabricated via low-cost inkjet printing and tested in a measurement setup to demonstrate the favorable properties of the designs.

Recently, there is a growing interest in manufacturing wireless components, especially antennas, radio-frequency tags, and sensors [24–34], via the inkjet-printing technology due to the favorable properties of the fabricated devices, including flexibility, being environmentally friendly, and being low cost. Fabrications of metamaterials, frequency-selective surfaces, and similar microwave devices using inkjet printers have also been considered by various researchers [35–37]. On the other hand, a majority of these studies use special material printers that enable easier fabrication procedures and highly flexible products at the expense of increased cost. Considering particularly metamaterials, only a few recent studies demonstrate the feasibility of very low-cost fabrications using standard printers [38], while the produced structures are only two dimensional. In this study, we demonstrate three-dimensional metamaterials that are produced by using silver-based inks in standard commercial printers. The produced metamaterials are quite inexpensive, while they provide the required electromagnetic properties similar to their high-frequency counterparts. In fact, such low-cost setups maintain the main advantages of inkjet printing, i.e., being inexpensive and easily accessible. On the other side, relatively poor printing quality of the conventional printers becomes a major issue that limits the user. In addition to the favorable properties described above, inkjet printing has the advantages of additive manufacturing. Fabricating detailed surfaces, such as fractal structures, brings no additional challenge in comparison to fabricating coarse surfaces, unless resolution issues arise. In fact, in a low-cost inkjet-printing setup, fabrication of coarse and large areas can be more challenging due to difficulties in maintaining uniformity. Similarly, printing different-sized structures simultaneously on the same paper is a straightforward process in inkjet printing.

As commonly practiced, homogenization of complex metamaterial structures may simplify and facilitate their numerical solutions. However, homogenization should be performed carefully to avoid excessive modeling errors, especially for finite structures. In the context of the second part of this study, we present rigorous homogenization of finite metamaterials while considering them as three-dimensional structures. Numerical examples are presented for SRR arrays that demonstrate band-stop behavior, while the procedure is easily applicable to other types of metamaterials. Our approach is based on parametric optimization using genetic algorithms, supported by three-dimensional full-wave solutions in the frequency domain. We focus on the magnetic characteristics of finite SRR structures and retrieve the effective permeability induced by them in their host medium. The results demonstrate the effectiveness of the proposed approach for finite structures.

In the third part of this study, we focus on electromagnetic properties of small metallic particles at high frequencies. Numerical problems arise when considering plasmonic effects of metals at optical frequencies since they must be modeled as penetrable bodies with negative real permittivity, leading to imaginary index values. Even though the frequency is relatively low, we show that penetrable models are needed for accurately representing electromagnetic characteristics of nanostructures, especially to predict penetrating magnetic fields inside small particles. Due to large permittivity values with negative real parts, stable formulations are needed to obtain equivalent currents and secondary fields. It is shown that a modified combined tangential formulation, which was proposed for plasmonic simulations in wide frequency ranges, provide accurate solutions that are consistent with analytical results for spherical nanoparticles.

The chapters of this thesis are organized in accordance with the conducted studies described above. In Chapter 2, SIE formulations for problems involving perfect electric conductors (PECs) and dielectric materials, discretizations of SIE formulations, as well as the concepts of method of moments (MOM), MLFMA, and approximate diagonalization are explained. We present numerical solutions of various canonical and realistic problems in order to compare the performances of the conventional and proposed implementations to analyze NZI structures. In Chapter 3, three-dimensional computational simulation and realization of metamaterial structures with different exotic properties, e.g., negative refractive index, at microwave frequencies are considered. The low-cost inkjet printing fabrication procedure, the challenges arise during low-cost inkjet printing, and sensitivity analysis to test fabrication errors are presented. In Chapter 4, we discuss numerical simulations of metallic nanoparticles at lower THz frequencies. Comparisons of PEC and penetrable models, as well as the accuracy and efficiency of penetrable formulations, are investigated. Finally, Chapter 5 summarizes the whole study and highlights potential future works.

CHAPTER 2

SIMULATIONS OF ZERO-INDEX MATERIALS

Computational analysis of electromagnetic problems involving ZI and NZI materials are discussed in this chapter. The simulation method for numerical solutions and numerical examples involving canonical and realistic problems are presented.

2.1 Simulation Method

In this section, SIE formulations are derived for problems involving PEC and dielectric materials. The discretization of SIE formulations is described. The concepts of MOM, MLFMA, and approximate diagonalization are explained.

2.1.1 Surface Integral Equations

Maxwell's equations in the frequency domain assuming $\exp(-i\omega t)$ time convention, including the magnetic current density $\boldsymbol{M}$ and the magnetic charge density ρ_m, are given for a simple medium as

$$\nabla \times \boldsymbol{E}(\boldsymbol{r}) = i\omega\mu\boldsymbol{H}(\boldsymbol{r}) - \boldsymbol{M}(\boldsymbol{r}) \tag{2.1}$$

$$\nabla \times \boldsymbol{H}(\boldsymbol{r}) = -i\omega\epsilon\boldsymbol{E}(\boldsymbol{r}) + \boldsymbol{J}(\boldsymbol{r}) \tag{2.2}$$

$$\nabla \cdot \boldsymbol{E}(\boldsymbol{r}) = \frac{1}{\epsilon}\rho_e(\boldsymbol{r}) \tag{2.3}$$

$$\nabla \cdot \boldsymbol{H}(\boldsymbol{r}) = \frac{1}{\mu}\rho_m(\boldsymbol{r}), \tag{2.4}$$

where $\boldsymbol{E}$ and $\boldsymbol{H}$ are electric and magnetic field intensities, $\boldsymbol{J}$ and ρ_e are electric current and electric charge densities, and ϵ and μ are permittivity and permeability values for the medium. The continuity equations relating current and charge densities are expressed as

$$\nabla \cdot \boldsymbol{J}(\boldsymbol{r}) = i\omega\rho_e(\boldsymbol{r}) \tag{2.5}$$

$$\nabla \cdot \boldsymbol{M}(\boldsymbol{r}) = i\omega\rho_m(\boldsymbol{r}). \tag{2.6}$$

The electric and magnetic fields can be written in terms of vector and scalar potentials as

$$\boldsymbol{E}(\boldsymbol{r}) = i\omega\boldsymbol{A}_m(\boldsymbol{r}) - \nabla\phi_e(\boldsymbol{r}) - \frac{1}{\epsilon}\nabla \times \boldsymbol{A}_e(\boldsymbol{r}) \tag{2.7}$$

$$\boldsymbol{H}(\boldsymbol{r}) = i\omega\boldsymbol{A}_e(\boldsymbol{r}) - \nabla\phi_m(\boldsymbol{r}) + \frac{1}{\mu}\nabla \times \boldsymbol{A}_m(\boldsymbol{r}), \tag{2.8}$$

where $\boldsymbol{A}_e$ and $\boldsymbol{A}_m$ are electric vector and magnetic vector potentials, and ϕ_e and ϕ_m are electric scalar and magnetic scalar potentials. Using Equations 2.7 and 2.8, and employing the Lorentz gauge that is given as

$$\nabla \cdot \boldsymbol{A}_m(\boldsymbol{r}) = i\omega\epsilon\mu\phi_e(\boldsymbol{r}) \tag{2.9}$$

$$\nabla \cdot \boldsymbol{A}_e(\boldsymbol{r}) = i\omega\mu\epsilon\phi_m(\boldsymbol{r}), \tag{2.10}$$

Helmholtz equations for potentials are obtained as

$$\nabla^2\phi_e(\boldsymbol{r}) + k^2\phi_e(\boldsymbol{r}) = -\frac{1}{\epsilon}\rho_e(\boldsymbol{r}) \tag{2.11}$$

$$\nabla^2\phi_m(\boldsymbol{r}) + k^2\phi_m(\boldsymbol{r}) = -\frac{1}{\mu}\rho_m(\boldsymbol{r}) \tag{2.12}$$

$$\nabla^2\boldsymbol{A}_e(\boldsymbol{r}) + k^2\boldsymbol{A}_e(\boldsymbol{r}) = -\epsilon\boldsymbol{M}(\boldsymbol{r}) \tag{2.13}$$

$$\nabla^2\boldsymbol{A}_m(\boldsymbol{r}) + k^2\boldsymbol{A}_m(\boldsymbol{r}) = -\mu\boldsymbol{J}(\boldsymbol{r}), \tag{2.14}$$

where $k = \omega\sqrt{\epsilon\mu} = 2\pi/\lambda$ is the wavenumber and λ is the wavelength. The homogeneous-space Green's function for a point source is given as

$$g(\boldsymbol{r}, \boldsymbol{r}') = \frac{\exp(ik|\boldsymbol{r} - \boldsymbol{r}'|)}{4\pi|\boldsymbol{r} - \boldsymbol{r}'|}, \tag{2.15}$$

where $\boldsymbol{r}$ is the observation point and $\boldsymbol{r}'$ is the source point. For arbitrary current and charge distributions, Helmholtz equations in Equations 2.11–2.14 can be solved by using the homogeneous-space Green's function in Equation 2.15 as the kernel. Then, the vector and scalar potentials are obtained as

$$\phi_e(\boldsymbol{r}) = \frac{1}{\epsilon}\int d\boldsymbol{r}' g(\boldsymbol{r},\boldsymbol{r}')\rho_e(\boldsymbol{r}') \tag{2.16}$$

$$\phi_m(\boldsymbol{r}) = \frac{1}{\mu}\int d\boldsymbol{r}' g(\boldsymbol{r},\boldsymbol{r}')\rho_m(\boldsymbol{r}') \tag{2.17}$$

$$\boldsymbol{A}_e(\boldsymbol{r}) = \epsilon\int d\boldsymbol{r}' g(\boldsymbol{r},\boldsymbol{r}')\boldsymbol{M}(\boldsymbol{r}') \tag{2.18}$$

$$\boldsymbol{A}_m(\boldsymbol{r}) = \mu\int d\boldsymbol{r}' g(\boldsymbol{r},\boldsymbol{r}')\boldsymbol{J}(\boldsymbol{r}'). \tag{2.19}$$

Electric and magnetic fields in terms of current and charge densities can be derived by inserting Equations 2.16–2.19 into Equations 2.7 and 2.8 as

$$\begin{aligned}\boldsymbol{E}(\boldsymbol{r}) = {} & ik\eta\int d\boldsymbol{r}'\left[\boldsymbol{J}(\boldsymbol{r}') + \frac{1}{k^2}\nabla'\cdot\boldsymbol{J}(\boldsymbol{r}')\nabla\right]g(\boldsymbol{r},\boldsymbol{r}') \\ & - \int d\boldsymbol{r}'\nabla g(\boldsymbol{r},\boldsymbol{r}')\times\boldsymbol{M}(\boldsymbol{r}')\end{aligned} \tag{2.20}$$

$$\begin{aligned}\boldsymbol{H}(\boldsymbol{r}) = {} & ik\eta^{-1}\int d\boldsymbol{r}'\left[\boldsymbol{M}(\boldsymbol{r}') + \frac{1}{k^2}\nabla'\cdot\boldsymbol{M}(\boldsymbol{r}')\nabla\right]g(\boldsymbol{r},\boldsymbol{r}') \\ & + \int d\boldsymbol{r}'\nabla g(\boldsymbol{r},\boldsymbol{r}')\times\boldsymbol{J}(\boldsymbol{r}'),\end{aligned} \tag{2.21}$$

where $\eta = \sqrt{\mu/\epsilon}$ is the intrinsic impedance. Integro-differential operators can be defined as

$$\boldsymbol{\mathcal{T}}\{\boldsymbol{X}\}(\boldsymbol{r}) = ik\int d\boldsymbol{r}'\left[\boldsymbol{X}(\boldsymbol{r}') + \frac{1}{k^2}\nabla'\cdot\boldsymbol{X}(\boldsymbol{r}')\nabla\right]g(\boldsymbol{r},\boldsymbol{r}') \tag{2.22}$$

$$\boldsymbol{\mathcal{K}}\{\boldsymbol{X}\}(\boldsymbol{r}) = \int d\boldsymbol{r}'\boldsymbol{X}(\boldsymbol{r}')\times\nabla' g(\boldsymbol{r},\boldsymbol{r}'). \tag{2.23}$$

Then, Equations 2.20 and 2.21 can be simplified by employing integro-differential operators given in Equations 2.22 and 2.23 as

$$\boldsymbol{E}(\boldsymbol{r}) = \eta\boldsymbol{\mathcal{T}}\{\boldsymbol{J}\}(\boldsymbol{r}) - \boldsymbol{\mathcal{K}}\{\boldsymbol{M}\}(\boldsymbol{r}) \tag{2.24}$$

$$\boldsymbol{H}(\boldsymbol{r}) = \eta^{-1}\boldsymbol{\mathcal{T}}\{\boldsymbol{M}\}(\boldsymbol{r}) + \boldsymbol{\mathcal{K}}\{\boldsymbol{J}\}(\boldsymbol{r}). \tag{2.25}$$

In order to derive SIEs for problems including perfectly conducting and/or penetrable objects, equivalence principle and boundary conditions are used to reduce the original problems into equivalent problems and to obtain equivalent currents on bounding surfaces. Considering the boundary between a homogeneous penetrable region D_u enclosed by a surface S_u and a homogeneous penetrable region D_v enclosed by a surface S_v as depicted in Figure 2.1 [39], equivalent electric and magnetic currents

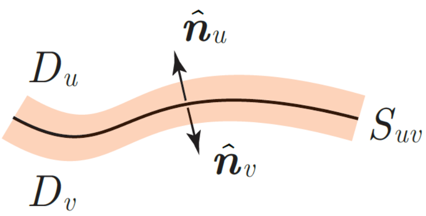

Figure 2.1: Boundary between two penetrable regions.

on the surfaces due to the continuity of tangential electric and magnetic fields can be written as

$$\boldsymbol{J}_u(\boldsymbol{r}) = -\boldsymbol{J}_v(\boldsymbol{r}) = \boldsymbol{J}(\boldsymbol{r}) = \hat{\boldsymbol{n}} \times \boldsymbol{H}(\boldsymbol{r}) \tag{2.26}$$

$$\boldsymbol{M}_u(\boldsymbol{r}) = -\boldsymbol{M}_v(\boldsymbol{r}) = \boldsymbol{M}(\boldsymbol{r}) = -\hat{\boldsymbol{n}} \times \boldsymbol{E}(\boldsymbol{r}), \tag{2.27}$$

where $\hat{\boldsymbol{n}} = \hat{\boldsymbol{n}}_u$ represents the inward normal unit vector of surface S_u, $\boldsymbol{E}(\boldsymbol{r})$ and $\boldsymbol{H}(\boldsymbol{r})$ are total electric and magnetic fields, $\boldsymbol{J}_u(\boldsymbol{r})$ and $\boldsymbol{M}_u(\boldsymbol{r})$ are equivalent electric and magnetic currents induced on surface S_u, and $\boldsymbol{J}_v(\boldsymbol{r})$ and $\boldsymbol{M}_v(\boldsymbol{r})$ are equivalent electric and magnetic currents induced on surface S_v. Starting from Equations 2.26 and 2.27, integral equations can be derived as (when $\boldsymbol{r} \in S_u$)

$$\begin{aligned}
\boldsymbol{J}_u(\boldsymbol{r}) &= \hat{\boldsymbol{n}}_u \times \boldsymbol{H}(\boldsymbol{r}) = \hat{\boldsymbol{n}}_u \times \boldsymbol{H}_u^{inc}(\boldsymbol{r}) + \hat{\boldsymbol{n}}_u \times \boldsymbol{H}_u^{sec}(\boldsymbol{r}) && (2.28)\\
&= \hat{\boldsymbol{n}}_u \times \boldsymbol{H}_u^{inc}(\boldsymbol{r}) + \eta_u^{-1}\hat{\boldsymbol{n}}_u \times \boldsymbol{\mathcal{T}}_u\{\boldsymbol{M}_u\}(\boldsymbol{r}) + \hat{\boldsymbol{n}}_u \times \boldsymbol{\mathcal{K}}_u\{\boldsymbol{J}_u\}(\boldsymbol{r}) && (2.29)\\
-\boldsymbol{M}_u(\boldsymbol{r}) &= \hat{\boldsymbol{n}}_u \times \boldsymbol{E}(\boldsymbol{r}) = \hat{\boldsymbol{n}}_u \times \boldsymbol{E}_u^{inc}(\boldsymbol{r}) + \hat{\boldsymbol{n}}_u \times \boldsymbol{E}_u^{sec}(\boldsymbol{r}) && (2.30)\\
&= \hat{\boldsymbol{n}}_u \times \boldsymbol{E}_u^{inc}(\boldsymbol{r}) + \eta_u\hat{\boldsymbol{n}}_u \times \boldsymbol{\mathcal{T}}_u\{\boldsymbol{J}_u\}(\boldsymbol{r}) - \hat{\boldsymbol{n}}_u \times \boldsymbol{\mathcal{K}}_u\{\boldsymbol{M}_u\}(\boldsymbol{r}), && (2.31)
\end{aligned}$$

where $\boldsymbol{E}_u^{inc}(\boldsymbol{r})$ and $\boldsymbol{H}_u^{inc}(\boldsymbol{r})$ are incident electric and magnetic fields, and $\boldsymbol{E}_u^{sec}(\boldsymbol{r})$ and $\boldsymbol{H}_u^{sec}(\boldsymbol{r})$ are secondary electric and magnetic fields in D_u. Operator $\boldsymbol{\mathcal{K}}_u$ is commonly separated into limit and principal parts as

$$\boldsymbol{\mathcal{K}}_u\{\boldsymbol{X}\}(\boldsymbol{r}) = \boldsymbol{\mathcal{K}}_u^{PV}\{\boldsymbol{X}\}(\boldsymbol{r}) - \frac{4\pi - \Omega_u}{4\pi}\hat{\boldsymbol{n}}_u \times \boldsymbol{X}(\boldsymbol{r}), \tag{2.32}$$

where $\boldsymbol{\mathcal{K}}_u^{PV}\{\boldsymbol{X}\}(\boldsymbol{r})$ is the principal value of $\boldsymbol{\mathcal{K}}_u\{\boldsymbol{X}\}(\boldsymbol{r})$ and $0 \leq \Omega_u \leq 4\pi$ is the internal solid angle at the observation point. Inserting Equation 2.32 into Equations 2.29 and 2.31, and rearranging the terms, we obtain N-MFIE (MFIE: magnetic-field integral equation) and N-EFIE (EFIE: electric-field integral equation) as

$$\begin{aligned}
&\eta_u^{-1}\hat{\boldsymbol{n}}_u \times \boldsymbol{\mathcal{T}}_u\{\boldsymbol{M}_u\}(\boldsymbol{r}) + \hat{\boldsymbol{n}}_u \times \boldsymbol{\mathcal{K}}_u^{PV}\{\boldsymbol{J}_u\}(\boldsymbol{r}) \\
&\qquad\qquad - \frac{\Omega_u}{4\pi}\boldsymbol{J}_u(\boldsymbol{r}) = -\hat{\boldsymbol{n}}_u \times \boldsymbol{H}_u^{inc}(\boldsymbol{r}) \qquad (2.33)\\
&\eta_u\hat{\boldsymbol{n}}_u \times \boldsymbol{\mathcal{T}}_u\{\boldsymbol{J}_u\}(\boldsymbol{r}) - \hat{\boldsymbol{n}}_u \times \boldsymbol{\mathcal{K}}_u^{PV}\{\boldsymbol{M}_u\}(\boldsymbol{r}) \\
&\qquad\qquad + \frac{\Omega_u}{4\pi}\boldsymbol{M}_u(\boldsymbol{r}) = -\hat{\boldsymbol{n}}_u \times \boldsymbol{E}_u^{inc}(\boldsymbol{r}). \qquad (2.34)
\end{aligned}$$

By simply multiplying both sides with $-\hat{\boldsymbol{n}}_u$ in Equations 2.33 and 2.34, T-MFIE and T-EFIE can be written as

$$\begin{aligned}
&-\eta_u^{-1}\hat{\boldsymbol{n}}_u \times \hat{\boldsymbol{n}}_u \times \boldsymbol{\mathcal{T}}_u\{\boldsymbol{M}_u\}(\boldsymbol{r}) - \hat{\boldsymbol{n}}_u \times \hat{\boldsymbol{n}}_u \times \boldsymbol{\mathcal{K}}_u^{PV}\{\boldsymbol{J}_u\}(\boldsymbol{r}) \\
&\qquad\qquad + \frac{\Omega_u}{4\pi}\hat{\boldsymbol{n}}_u \times \boldsymbol{J}_u(\boldsymbol{r}) = \hat{\boldsymbol{n}}_u \times \hat{\boldsymbol{n}}_u \times \boldsymbol{H}_u^{inc}(\boldsymbol{r}) \qquad (2.35)\\
&-\eta_u\hat{\boldsymbol{n}}_u \times \hat{\boldsymbol{n}}_u \times \boldsymbol{\mathcal{T}}_u\{\boldsymbol{J}_u\}(\boldsymbol{r}) + \hat{\boldsymbol{n}}_u \times \hat{\boldsymbol{n}}_u \times \boldsymbol{\mathcal{K}}_u^{PV}\{\boldsymbol{M}_u\}(\boldsymbol{r}) \\
&\qquad\qquad - \frac{\Omega_u}{4\pi}\hat{\boldsymbol{n}}_u \times \boldsymbol{M}_u(\boldsymbol{r}) = \hat{\boldsymbol{n}}_u \times \hat{\boldsymbol{n}}_u \times \boldsymbol{E}_u^{inc}(\boldsymbol{r}). \qquad (2.36)
\end{aligned}$$

N-MFIE, N-EFIE, T-MFIE, and T-EFIE are building blocks of surface formulations.

2.1.2 Surface Formulations

Considering a problem including a homogeneous penetrable object (region D_i) inside a homogeneous penetrable medium (region D_o), similar to the general case given in Figure 2.1, integral equations for inner and outer problems can be written as (assuming that excitations only exist in D_o)

$$\begin{aligned}
&\textbf{N-MFIE-I}: \eta_i^{-1}\hat{\boldsymbol{n}} \times \boldsymbol{\mathcal{T}}_i\{\boldsymbol{M}\}(\boldsymbol{r}) + \hat{\boldsymbol{n}} \times \boldsymbol{\mathcal{K}}_i^{PV}\{\boldsymbol{J}\}(\boldsymbol{r}) \\
&\qquad\qquad + \frac{\Omega_i}{4\pi}\boldsymbol{J}(\boldsymbol{r}) = 0 \qquad (2.37)\\
&\textbf{N-EFIE-I}: \eta_i\hat{\boldsymbol{n}} \times \boldsymbol{\mathcal{T}}_i\{\boldsymbol{J}\}(\boldsymbol{r}) - \hat{\boldsymbol{n}} \times \boldsymbol{\mathcal{K}}_i^{PV}\{\boldsymbol{M}\}(\boldsymbol{r}) \\
&\qquad\qquad - \frac{\Omega_i}{4\pi}\boldsymbol{M}(\boldsymbol{r}) = 0 \qquad (2.38)\\
&\textbf{T-MFIE-I}: -\eta_i^{-1}\hat{\boldsymbol{n}} \times \hat{\boldsymbol{n}} \times \boldsymbol{\mathcal{T}}_i\{\boldsymbol{M}\}(\boldsymbol{r}) - \hat{\boldsymbol{n}} \times \hat{\boldsymbol{n}} \times \boldsymbol{\mathcal{K}}_i^{PV}\{\boldsymbol{J}\}(\boldsymbol{r}) \\
&\qquad\qquad - \frac{\Omega_i}{4\pi}\hat{\boldsymbol{n}} \times \boldsymbol{J}(\boldsymbol{r}) = 0 \qquad (2.39)\\
&\textbf{T-EFIE-I}: -\eta_i\hat{\boldsymbol{n}} \times \hat{\boldsymbol{n}} \times \boldsymbol{\mathcal{T}}_i\{\boldsymbol{J}\}(\boldsymbol{r}) + \hat{\boldsymbol{n}} \times \hat{\boldsymbol{n}} \times \boldsymbol{\mathcal{K}}_i^{PV}\{\boldsymbol{M}\}(\boldsymbol{r}) \\
&\qquad\qquad + \frac{\Omega_i}{4\pi}\hat{\boldsymbol{n}} \times \boldsymbol{M}(\boldsymbol{r}) = 0 \qquad (2.40)
\end{aligned}$$

$$\begin{aligned}
\textbf{N-MFIE-O}: \eta_o^{-1}\hat{\boldsymbol{n}} \times \boldsymbol{\mathcal{T}}_o\{\boldsymbol{M}\}(\boldsymbol{r}) + \hat{\boldsymbol{n}} \times \boldsymbol{\mathcal{K}}_o^{PV}\{\boldsymbol{J}\}(\boldsymbol{r}) \\
- \frac{\Omega_o}{4\pi}\boldsymbol{J}(\boldsymbol{r}) = -\hat{\boldsymbol{n}} \times \boldsymbol{H}^{inc}(\boldsymbol{r}) \qquad (2.41)
\end{aligned}$$

$$\begin{aligned}
\textbf{N-EFIE-O}: \eta_o\hat{\boldsymbol{n}} \times \boldsymbol{\mathcal{T}}_o\{\boldsymbol{J}\}(\boldsymbol{r}) - \hat{\boldsymbol{n}} \times \boldsymbol{\mathcal{K}}_o^{PV}\{\boldsymbol{M}\}(\boldsymbol{r}) \\
+ \frac{\Omega_o}{4\pi}\boldsymbol{M}(\boldsymbol{r}) = -\hat{\boldsymbol{n}} \times \boldsymbol{E}^{inc}(\boldsymbol{r}) \qquad (2.42)
\end{aligned}$$

$$\begin{aligned}
\textbf{T-MFIE-O}: -\eta_o^{-1}\hat{\boldsymbol{n}} \times \hat{\boldsymbol{n}} \times \boldsymbol{\mathcal{T}}_o\{\boldsymbol{M}\}(\boldsymbol{r}) - \hat{\boldsymbol{n}} \times \hat{\boldsymbol{n}} \times \boldsymbol{\mathcal{K}}_o^{PV}\{\boldsymbol{J}\}(\boldsymbol{r}) \\
+ \frac{\Omega_o}{4\pi}\hat{\boldsymbol{n}} \times \boldsymbol{J}(\boldsymbol{r}) = \hat{\boldsymbol{n}} \times \hat{\boldsymbol{n}} \times \boldsymbol{H}^{inc}(\boldsymbol{r}) \qquad (2.43)
\end{aligned}$$

$$\begin{aligned}
\textbf{T-EFIE-O}: -\eta_o\hat{\boldsymbol{n}} \times \hat{\boldsymbol{n}} \times \boldsymbol{\mathcal{T}}_o\{\boldsymbol{J}\}(\boldsymbol{r}) + \hat{\boldsymbol{n}} \times \hat{\boldsymbol{n}} \times \boldsymbol{\mathcal{K}}_o^{PV}\{\boldsymbol{M}\}(\boldsymbol{r}) \\
- \frac{\Omega_o}{4\pi}\hat{\boldsymbol{n}} \times \boldsymbol{M}(\boldsymbol{r}) = \hat{\boldsymbol{n}} \times \hat{\boldsymbol{n}} \times \boldsymbol{E}^{inc}(\boldsymbol{r}), \qquad (2.44)
\end{aligned}$$

where $\eta_i = \sqrt{\mu_i/\epsilon_i}$ and $\eta_o = \sqrt{\mu_o/\epsilon_o}$ are intrinsic impedances of the inner and outer media, $\hat{\boldsymbol{n}}$ is the outward normal unit vector of the inner medium, and $\Omega_i = 4\pi - \Omega_o$ and Ω_o are internal and external solid angles. Also, we note that $\Omega_o = \Omega_i = 2\pi$ for planar surfaces. The general form of SIE formulations obtained by combining integral equations in Equations 2.37−2.44 can be written as

$$\begin{bmatrix} a\text{T-EFIE-O} + b\text{T-EFIE-I} + e\text{N-MFIE-O} - f\text{N-MFIE-I} \\ c\text{T-MFIE-O} + d\text{T-MFIE-I} - g\text{N-EFIE-O} + h\text{N-EFIE-I} \end{bmatrix}. \tag{2.45}$$

The general form in Equation 2.45 can be expressed in a matrix form as

$$\begin{bmatrix} \boldsymbol{\mathcal{Z}}_{11} & \boldsymbol{\mathcal{Z}}_{12} \\ \boldsymbol{\mathcal{Z}}_{21} & \boldsymbol{\mathcal{Z}}_{22} \end{bmatrix} \cdot \begin{bmatrix} \boldsymbol{J} \\ \boldsymbol{M} \end{bmatrix}(\boldsymbol{r}) = \begin{bmatrix} \boldsymbol{w}_1 \\ \boldsymbol{w}_2 \end{bmatrix}(\boldsymbol{r}), \tag{2.46}$$

where

$$\begin{aligned}
\boldsymbol{\mathcal{Z}}_{11} &= -a\eta_o\hat{\boldsymbol{n}} \times \hat{\boldsymbol{n}} \times \boldsymbol{\mathcal{T}}_o - b\eta_i\hat{\boldsymbol{n}} \times \hat{\boldsymbol{n}} \times \boldsymbol{\mathcal{T}}_i \\
&\quad + e\hat{\boldsymbol{n}} \times \boldsymbol{\mathcal{K}}_o^{PV} - f\hat{\boldsymbol{n}} \times \boldsymbol{\mathcal{K}}_i^{PV} - (e+f)\boldsymbol{\mathcal{I}}/2 && (2.47) \\
\boldsymbol{\mathcal{Z}}_{12} &= a\hat{\boldsymbol{n}} \times \hat{\boldsymbol{n}} \times \boldsymbol{\mathcal{K}}_o^{PV} + b\hat{\boldsymbol{n}} \times \hat{\boldsymbol{n}} \times \boldsymbol{\mathcal{K}}_i^{PV} \\
&\quad - (a-b)\hat{\boldsymbol{n}} \times \boldsymbol{\mathcal{I}}/2 + e\eta_o^{-1}\hat{\boldsymbol{n}} \times \boldsymbol{\mathcal{T}}_o - f\eta_i^{-1}\hat{\boldsymbol{n}} \times \boldsymbol{\mathcal{T}}_i && (2.48) \\
\boldsymbol{\mathcal{Z}}_{21} &= -c\hat{\boldsymbol{n}} \times \hat{\boldsymbol{n}} \times \boldsymbol{\mathcal{K}}_o^{PV} - d\hat{\boldsymbol{n}} \times \hat{\boldsymbol{n}} \times \boldsymbol{\mathcal{K}}_i^{PV} \\
&\quad + (c-d)\hat{\boldsymbol{n}} \times \boldsymbol{\mathcal{I}}/2 - g\eta_o\hat{\boldsymbol{n}} \times \boldsymbol{\mathcal{T}}_o + h\eta_i\hat{\boldsymbol{n}} \times \boldsymbol{\mathcal{T}}_i && (2.49) \\
\boldsymbol{\mathcal{Z}}_{22} &= -c\eta_o^{-1}\hat{\boldsymbol{n}} \times \hat{\boldsymbol{n}} \times \boldsymbol{\mathcal{T}}_o - d\eta_i^{-1}\hat{\boldsymbol{n}} \times \hat{\boldsymbol{n}} \times \boldsymbol{\mathcal{T}}_i \\
&\quad + g\hat{\boldsymbol{n}} \times \boldsymbol{\mathcal{K}}_o^{PV} - h\hat{\boldsymbol{n}} \times \boldsymbol{\mathcal{K}}_i^{PV} - (g+h)\boldsymbol{\mathcal{I}}/2 && (2.50)
\end{aligned}$$

$$\boldsymbol{w}_1 = a\hat{\boldsymbol{n}} \times \hat{\boldsymbol{n}} \times \boldsymbol{E}^{inc}(\boldsymbol{r}) - e\hat{\boldsymbol{n}} \times \boldsymbol{H}^{inc}(\boldsymbol{r}) \tag{2.51}$$

$$\boldsymbol{w}_2 = c\hat{\boldsymbol{n}} \times \hat{\boldsymbol{n}} \times \boldsymbol{H}^{inc}(\boldsymbol{r}) + g\hat{\boldsymbol{n}} \times \boldsymbol{E}^{inc}(\boldsymbol{r}). \tag{2.52}$$

In the above, $\boldsymbol{\mathcal{I}}$ is the identity operator. By using the generalized form given in Equation 2.46 and selecting constants $\{a, b, c, d, e, f, g, h\}$, some of the conventional SIE formulations can be written as follows.

- Poggio-Miller-Chang-Harrington-Wu-Tsai (PMCHWT) formulation [40–42]:
  $a = 1, b = 1, c = 1, d = 1, e = 0, f = 0, g = 0, h = 0$
- Combined T formulation (CTF) [43]:
  $a = \eta_o^{-1}, b = \eta_i^{-1}, c = \eta_o, d = \eta_i, e = 0, f = 0, g = 0, h = 0$
- Modified combined T formulation (MCTF) [10]:
  $a = 1, b = 1, c = \eta_o\eta_i, d = \eta_o\eta_i, e = 0, f = 0, g = 0, h = 0$
- N Müller formulation (NMF) [44]:
  $a = 0, b = 0, c = 0, d = 0, e = \mu_o, f = \mu_i, g = \epsilon_o, h = \epsilon_i$
- Modified N Müller formulation (MNMF) [45]:
  $a = 0, b = 0, c = 0, d = 0, e = \mu_o/(\mu_o+\mu_i), f = \mu_i/(\mu_o+\mu_i), g = \epsilon_o/(\epsilon_o+\epsilon_i),$
  $h = \epsilon_i(\epsilon_o + \epsilon_i)$
- Electric-magnetic current combined-field integral equation (JMCFIE) [46]:
  $a = \eta_o^{-1}, b = \eta_i^{-1}, c = \eta_o, d = \eta_i, e = 1, f = 1, g = 1, h = 1$

Using Galerkin discretizations [47], $\boldsymbol{\mathcal{T}}$ and $\boldsymbol{\mathcal{I}}$ operators are well tested with $\boldsymbol{t}_m$, while $\boldsymbol{\mathcal{K}}$ operator is well tested with $\hat{\boldsymbol{n}} \times \boldsymbol{t}_m$. Discretization of the operators is discussed further in this section.

As well-known in the literature, only the tangential type of the PMCHWT formulation is stable with a Galerkin discretization, despite that both normal and tangential forms of this formulation exist [39]. It is also known that, PMCHWT provides accurate results, but it, unfortunately, suffers from ill-conditioning [48]. CTF is also a tangential formulation, but often with better conditioning in comparison to the PMCHWT formulation since it has identical diagonal partitions [39]. MCTF, another T-type formulation, is mainly proposed for plasmonic structures with its coefficients specifically adjusted to handle very large permittivity values. On the other side, NMF and MNMF are N-type formulations, and MNMF typically provides better-conditioned matrix equations than NMF. Finally, JMCFIE is a mixed-type formulation, involving both T-type and N-type integral equations, and it is particularly well-conditioned for ordinary materials [49].

For ZI and NZI materials, numerical difficulties arise due to huge contrasts between inner and outer problems, leading to unbalanced inner and outer terms. Some of the conventional SIE formulations were applied to very limited ranges of NZI values in the literature, and NMF was presented as a stable formulation [50]. On the other hand, in the next section, the conventional SIE formulations (including NMF) are extensively tested by considering wide ranges of NZI values, and their failure when permittivity and/or permeability values go to zero is clearly demonstrated via numerical results. With careful considerations on the limit cases, i.e., when relative permittivity and/or permeability values are close to zero, novel SIE formulations having balanced integral-equation operators are proposed by selecting constants $\{a, b, c, d, e, f, g, h\}$ as follows.

- New tangential formulation [51–53]:
  $a = \eta_o^{-1}$, $b = \epsilon_i\epsilon_o^{-1}\eta_o^{-1}$, $c = \eta_o$, $d = \mu_i\mu_o^{-1}\eta_o$, $e = 0$, $f = 0$, $g = 0$, $h = 0$
- New mixed formulation [51–53]:
  $a = \eta_o^{-1}$, $b = \epsilon_i\epsilon_o^{-1}\eta_o^{-1}$, $c = \eta_o$, $d = \mu_i\mu_o^{-1}\eta_o$, $e = 1$, $f = \mu_i\mu_o^{-1}$, $g = 1$, $h = \epsilon_i\epsilon_o^{-1}$

In order to understand why these formulations are more stable when analyzing NZI objects, we may consider their forms in limit cases, i.e., for ENZ, MNZ, and EMNZ (ϵ-μ-near-zero) materials. First, for μ_i values close to zero (MNZ case), the matrix elements of the new mixed formulation become

$$\boldsymbol{\mathcal{Z}}_{11} = -\hat{\boldsymbol{n}}\times\hat{\boldsymbol{n}}\times\boldsymbol{\mathcal{T}}_o - k_o^{-1}k_i\hat{\boldsymbol{n}}\times\hat{\boldsymbol{n}}\times\boldsymbol{\mathcal{T}}_i + \hat{\boldsymbol{n}}\times\boldsymbol{\mathcal{K}}_o^{PV} - \frac{1}{2}\boldsymbol{\mathcal{I}} \tag{2.53}$$

$$\begin{aligned}\boldsymbol{\mathcal{Z}}_{12} = {} & \eta_o^{-1}\hat{\boldsymbol{n}}\times\hat{\boldsymbol{n}}\times\boldsymbol{\mathcal{K}}_o^{PV} + \epsilon_i\epsilon_o^{-1}\eta_o^{-1}\hat{\boldsymbol{n}}\times\hat{\boldsymbol{n}}\times\boldsymbol{\mathcal{K}}_i^{PV} - \frac{1}{2}\eta_o^{-1}(1-\epsilon_i\epsilon_o^{-1})\hat{\boldsymbol{n}}\times\boldsymbol{\mathcal{I}} \\ & + \eta_o^{-1}\hat{\boldsymbol{n}}\times\boldsymbol{\mathcal{T}}_o - \omega^{-1}\mu_o^{-1}k_i\hat{\boldsymbol{n}}\times\boldsymbol{\mathcal{T}}_i\end{aligned} \tag{2.54}$$

$$\boldsymbol{\mathcal{Z}}_{21} = -\eta_o \hat{\boldsymbol{n}} \times \hat{\boldsymbol{n}} \times \boldsymbol{\mathcal{K}}_o^{PV} + \frac{1}{2}\eta_o \hat{\boldsymbol{n}} \times \boldsymbol{\mathcal{I}} - \eta_o \hat{\boldsymbol{n}} \times \boldsymbol{\mathcal{T}}_o + \omega^{-1}\epsilon_o^{-1} k_i \eta_i \hat{\boldsymbol{n}} \times \boldsymbol{\mathcal{T}}_i \quad (2.55)$$

$$\boldsymbol{\mathcal{Z}}_{22} = -\hat{\boldsymbol{n}} \times \hat{\boldsymbol{n}} \times \boldsymbol{\mathcal{T}}_o - k_o^{-1} k_i \hat{\boldsymbol{n}} \times \hat{\boldsymbol{n}} \times \boldsymbol{\mathcal{T}}_i + \hat{\boldsymbol{n}} \times \boldsymbol{\mathcal{K}}_o^{PV} - \epsilon_i \epsilon_o^{-1} \hat{\boldsymbol{n}} \times \boldsymbol{\mathcal{K}}_i^{PV} - \frac{1}{2}(1 + \epsilon_i \epsilon_o^{-1})\boldsymbol{\mathcal{I}}. \quad (2.56)$$

In these expressions, all terms are well-balanced with each other, even when both k_i and η_i become zero. It is remarkable that the problematic operator, i.e., the inner T operator, is always multiplied with k_i. Similarly, for ϵ_i values close to zero (ENZ case), the matrix elements of the new mixed formulation become

$$\boldsymbol{\mathcal{Z}}_{11} = -\hat{\boldsymbol{n}} \times \hat{\boldsymbol{n}} \times \boldsymbol{\mathcal{T}}_o - k_o^{-1} k_i \hat{\boldsymbol{n}} \times \hat{\boldsymbol{n}} \times \boldsymbol{\mathcal{T}}_i + \hat{\boldsymbol{n}} \times \boldsymbol{\mathcal{K}}_o^{PV} - \mu_i \mu_o^{-1} \hat{\boldsymbol{n}} \times \boldsymbol{\mathcal{K}}_i^{PV} - \frac{1}{2}(1 + \mu_i \mu_o^{-1})\boldsymbol{\mathcal{I}} \quad (2.57)$$

$$\boldsymbol{\mathcal{Z}}_{12} = \eta_o^{-1} \hat{\boldsymbol{n}} \times \hat{\boldsymbol{n}} \times \boldsymbol{\mathcal{K}}_o^{PV} - \frac{1}{2}\eta_o^{-1} \hat{\boldsymbol{n}} \times \boldsymbol{\mathcal{I}} + \eta_o^{-1} \hat{\boldsymbol{n}} \times \boldsymbol{\mathcal{T}}_o - \omega^{-1}\mu_o^{-1} k_i \hat{\boldsymbol{n}} \times \boldsymbol{\mathcal{T}}_i \quad (2.58)$$

$$\boldsymbol{\mathcal{Z}}_{21} = -\eta_o \hat{\boldsymbol{n}} \times \hat{\boldsymbol{n}} \times \boldsymbol{\mathcal{K}}_o^{PV} - \mu_i \mu_o^{-1} \eta_o \hat{\boldsymbol{n}} \times \hat{\boldsymbol{n}} \times \boldsymbol{\mathcal{K}}_i^{PV} + \frac{1}{2}\eta_o (1 - \mu_i \mu_o^{-1}) \hat{\boldsymbol{n}} \times \boldsymbol{\mathcal{I}} - \eta_o \hat{\boldsymbol{n}} \times \boldsymbol{\mathcal{T}}_o + \omega^{-1}\epsilon_o^{-1} k_i \hat{\boldsymbol{n}} \times \boldsymbol{\mathcal{T}}_i \quad (2.59)$$

$$\boldsymbol{\mathcal{Z}}_{22} = -\hat{\boldsymbol{n}} \times \hat{\boldsymbol{n}} \times \boldsymbol{\mathcal{T}}_o - k_o^{-1} k_i \hat{\boldsymbol{n}} \times \hat{\boldsymbol{n}} \times \boldsymbol{\mathcal{T}}_i + \hat{\boldsymbol{n}} \times \boldsymbol{\mathcal{K}}_o^{PV} - \frac{1}{2}\boldsymbol{\mathcal{I}}, \quad (2.60)$$

which are again stable when k_i converges to zero. Finally, when both ϵ_i and μ_i values close to zero (EMNZ case), the matrix elements of the new mixed formulation can be written as

$$\boldsymbol{\mathcal{Z}}_{11} = -\hat{\boldsymbol{n}} \times \hat{\boldsymbol{n}} \times \boldsymbol{\mathcal{T}}_o - k_o^{-1} k_i \hat{\boldsymbol{n}} \times \hat{\boldsymbol{n}} \times \boldsymbol{\mathcal{T}}_i + \hat{\boldsymbol{n}} \times \boldsymbol{\mathcal{K}}_o^{PV} - \frac{1}{2}\boldsymbol{\mathcal{I}} \quad (2.61)$$

$$\boldsymbol{\mathcal{Z}}_{12} = \eta_o^{-1} \hat{\boldsymbol{n}} \times \hat{\boldsymbol{n}} \times \boldsymbol{\mathcal{K}}_o^{PV} - \frac{1}{2}\eta_o^{-1} \hat{\boldsymbol{n}} \times \boldsymbol{\mathcal{I}} + \eta_o^{-1} \hat{\boldsymbol{n}} \times \boldsymbol{\mathcal{T}}_o - \omega^{-1}\mu_o^{-1} k_i \hat{\boldsymbol{n}} \times \boldsymbol{\mathcal{T}}_i \quad (2.62)$$

$$\boldsymbol{\mathcal{Z}}_{21} = -\eta_o \hat{\boldsymbol{n}} \times \hat{\boldsymbol{n}} \times \boldsymbol{\mathcal{K}}_o^{PV} + \frac{1}{2}\eta_o \hat{\boldsymbol{n}} \times \boldsymbol{\mathcal{I}} - \eta_o \hat{\boldsymbol{n}} \times \boldsymbol{\mathcal{T}}_o + \omega^{-1}\epsilon_o^{-1} k_i \hat{\boldsymbol{n}} \times \boldsymbol{\mathcal{T}}_i \quad (2.63)$$

$$\boldsymbol{\mathcal{Z}}_{22} = -\hat{\boldsymbol{n}} \times \hat{\boldsymbol{n}} \times \boldsymbol{\mathcal{T}}_o - k_o^{-1} k_i \hat{\boldsymbol{n}} \times \hat{\boldsymbol{n}} \times \boldsymbol{\mathcal{T}}_i + \hat{\boldsymbol{n}} \times \boldsymbol{\mathcal{K}}_o^{PV} - \frac{1}{2}\boldsymbol{\mathcal{I}}, \quad (2.64)$$

which also demonstrate stability against small values of k_i. Consequently, in the new mixed formulation, all operators (terms) are well-balanced with each other in ENZ, MNZ, and EMNZ cases. In addition, well-tested identity operators remain in the diagonal blocks in all three limit cases. We note that the new tangential formulation is a part of the new mixed formulation with only T-tested operators. It is also stable for

NZI materials except when either permittivity or permeability is unity.

As shown in the numerical results in the next section, these formulations clearly outperform the conventional formulations in terms of accuracy and/or efficiency.

2.1.3 Method of Moments

In order to solve SIE formulations with MOM [54, 55], these formulations can be considered in general as

$$\boldsymbol{\mathcal{L}}\{\boldsymbol{f}\}(\boldsymbol{r}) = \boldsymbol{g}(\boldsymbol{r}), \tag{2.65}$$

where $\boldsymbol{\mathcal{L}}$ is a linear operator, $\boldsymbol{g}(\boldsymbol{r})$ is the known vector function, and $\boldsymbol{f}(\boldsymbol{r})$ is the unknown vector function. These correspond to a combination of integro-differential ($\boldsymbol{\mathcal{T}}$ and $\boldsymbol{\mathcal{K}}$) operators and the identity ($\boldsymbol{\mathcal{I}}$) operator, the excitation (right-hand-side) vector, and the unknown electric and magnetic current distributions, respectively, in the SIE formulations. The unknown function $\boldsymbol{f}(\boldsymbol{r})$ can be expressed in terms of known basis functions $\boldsymbol{b}_n$ as

$$\boldsymbol{f}(\boldsymbol{r}) \approx \sum_{n=1}^{N} \boldsymbol{a}[n]\boldsymbol{b}_n(\boldsymbol{r}), \tag{2.66}$$

where $\boldsymbol{a}[n]$ is the nth unknown coefficient. Equation 2.66 is substituted into Equation 2.65 and both sides are weighted by testing functions $\boldsymbol{t}_m$ (where $m = 1, 2, ..., N$) as

$$\int d\boldsymbol{r}\boldsymbol{t}_m(\boldsymbol{r}) \cdot \sum_{n=1}^{N} \boldsymbol{a}[n]\boldsymbol{\mathcal{L}}\{\boldsymbol{b}_n\}(\boldsymbol{r}) = \int d\boldsymbol{r}\boldsymbol{t}_m(\boldsymbol{r}) \cdot \boldsymbol{g}(\boldsymbol{r}). \tag{2.67}$$

To write the equation in a matrix form, the order of summation and integration can be changed as

$$\sum_{n=1}^{N} \boldsymbol{a}[n] \int d\boldsymbol{r}\boldsymbol{t}_m(\boldsymbol{r}) \cdot \boldsymbol{\mathcal{L}}\{\boldsymbol{b}_n\}(\boldsymbol{r}) = \int d\boldsymbol{r}\boldsymbol{t}_m(\boldsymbol{r}) \cdot \boldsymbol{g}(\boldsymbol{r}). \tag{2.68}$$

Finally, a matrix equation is obtained as

$$\sum_{n=1}^{N} \boldsymbol{a}[n]\bar{\boldsymbol{Z}}[m,n] = \boldsymbol{w}[m], \tag{2.69}$$

where

$$\bar{\boldsymbol{Z}}[m,n] = \int d\boldsymbol{r}\boldsymbol{t}_m(\boldsymbol{r}) \cdot \boldsymbol{\mathcal{L}}\{\boldsymbol{b}_n\}(\boldsymbol{r}) \tag{2.70}$$

$$\boldsymbol{w}[m] = \int d\boldsymbol{r}\boldsymbol{t}_m(\boldsymbol{r}) \cdot \boldsymbol{g}(\boldsymbol{r}). \tag{2.71}$$

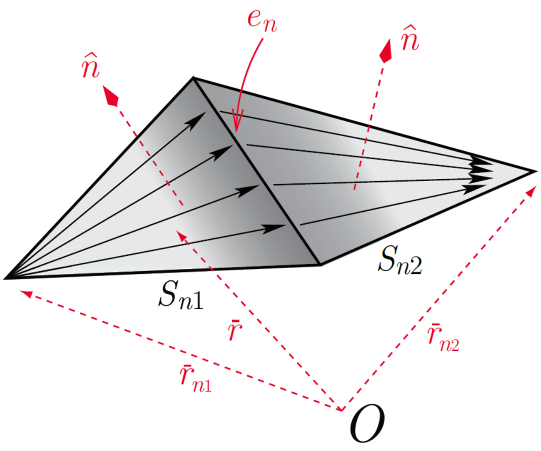

Figure 2.2: Illustration of an RWG function.

Electromagnetic problems can be described by Equation 2.69, where $\bar{\boldsymbol{Z}}$ represents interactions between the discretized elements, $\boldsymbol{a}$ represents coefficients expanding the electric and/or magnetic currents, and $\boldsymbol{w}$ represents the excitation vector.

2.1.4 Discretization

For three-dimensional SIE implementations, triangulation is commonly selected for the discretization of objects. In addition, the Galerkin method [47], which is selecting the same set of functions for both expansion and testing operations, is followed in this study. Accordingly, the Rao-Wilton-Glisson (RWG) functions on planar edges [56] are used for both basis and testing functions. An RWG function is defined on a triangle pair with a common edge, as given in Figure 2.2 [39], and it can be written as

$$\boldsymbol{b}_n^{\text{RWG}}(\boldsymbol{r}) = \begin{cases} \dfrac{l_n}{2A_{n1}}(\boldsymbol{r} - \boldsymbol{r}_{n1}), & \boldsymbol{r} \in S_{n1} \\ \dfrac{l_n}{2A_{n2}}(\boldsymbol{r}_{n2} - \boldsymbol{r}), & \boldsymbol{r} \in S_{n2} \\ 0, & \boldsymbol{r} \notin S_n, \end{cases} \tag{2.72}$$

where l_n is the length of the common edge, and A_{n1} and A_{n2} refer to the areas of the first (S_{n1}) and second (S_{n2}) triangles, respectively ($S_{n1} \bigcup S_{n2} = S_n$). The RWG functions guarantee finite divergence everywhere and charge neutrality since

$$\nabla \cdot \boldsymbol{b}_n^{\text{RWG}}(\boldsymbol{r}) = \begin{cases} \dfrac{l_n}{A_{n1}}, & \boldsymbol{r} \in S_{n1} \\ -\dfrac{l_n}{A_{n2}}, & \boldsymbol{r} \in S_{n2} \\ 0, & \boldsymbol{r} \notin S_n. \end{cases} \tag{2.73}$$

Then, the integro-differential operators $\boldsymbol{\mathcal{T}}$ and $\boldsymbol{\mathcal{K}}$, as well as the identity operator $\boldsymbol{\mathcal{I}}$ can be discretized by employing the RWG functions as

$$\begin{aligned}
\bar{\boldsymbol{T}}_u^T[m,n] &= ik_u \int_{S_m} d\boldsymbol{r} \boldsymbol{t}_m(\boldsymbol{r}) \cdot \int_{S_n} d\boldsymbol{r}' g_u(\boldsymbol{r},\boldsymbol{r}')\boldsymbol{b}_n(\boldsymbol{r}') \\
&\quad + \frac{i}{k_u} \int_{S_m} d\boldsymbol{r} \boldsymbol{t}_m(\boldsymbol{r}) \cdot \int_{S_n} d\boldsymbol{r}' \nabla g_u(\boldsymbol{r},\boldsymbol{r}') \nabla' \cdot \boldsymbol{b}_n(\boldsymbol{r}') && (2.74) \\
\bar{\boldsymbol{T}}_u^N[m,n] &= ik_u \int_{S_m} d\boldsymbol{r} \boldsymbol{t}_m(\boldsymbol{r}) \cdot \hat{\boldsymbol{n}} \times \int_{S_n} d\boldsymbol{r}' g_u(\boldsymbol{r},\boldsymbol{r}')\boldsymbol{b}_n(\boldsymbol{r}') \\
&\quad + \frac{i}{k_u} \int_{S_m} d\boldsymbol{r} \boldsymbol{t}_m(\boldsymbol{r}) \cdot \hat{\boldsymbol{n}} \times \int_{S_n} d\boldsymbol{r}' \nabla g_u(\boldsymbol{r},\boldsymbol{r}') \nabla' \cdot \boldsymbol{b}_n(\boldsymbol{r}') && (2.75) \\
\bar{\boldsymbol{K}}_{PV,u}^T[m,n] &= \int_{S_m} d\boldsymbol{r} \boldsymbol{t}_m(\boldsymbol{r}) \cdot \int_{PV,S_n} d\boldsymbol{r}' \boldsymbol{b}_n(\boldsymbol{r}') \times \nabla' g_u(\boldsymbol{r},\boldsymbol{r}') && (2.76) \\
\bar{\boldsymbol{K}}_{PV,u}^N[m,n] &= \int_{S_m} d\boldsymbol{r} \boldsymbol{t}_m(\boldsymbol{r}) \cdot \hat{\boldsymbol{n}} \times \int_{PV,S_n} d\boldsymbol{r}' \boldsymbol{b}_n(\boldsymbol{r}') \times \nabla' g_u(\boldsymbol{r},\boldsymbol{r}') && (2.77) \\
\bar{\boldsymbol{I}}^T[m,n] &= \int_{S_m} d\boldsymbol{r} \boldsymbol{t}_m(\boldsymbol{r}) \cdot \boldsymbol{b}_n(\boldsymbol{r}) && (2.78) \\
\bar{\boldsymbol{I}}^N[m,n] &= \int_{S_m} d\boldsymbol{r} \boldsymbol{t}_m(\boldsymbol{r}) \cdot \hat{\boldsymbol{n}} \times \boldsymbol{b}_n(\boldsymbol{r}), && (2.79)
\end{aligned}$$

where $u = o, i$. By considering the interaction of two half RWG functions $\boldsymbol{t}_{ma}^{\text{RWG}}$ and $\boldsymbol{b}_{nb}^{\text{RWG}}$, where a and m refer to the ath triangle of the mth edge, and b and n refer to the bth triangle of the nth edge, Equations 2.74–2.79 can be rewritten as

$$\begin{aligned}
\bar{\boldsymbol{T}}_u^T[m,n,a,b] &= ik_u \mathcal{A}_{ma,nb} \int_{S_{ma}} d\boldsymbol{r} (\boldsymbol{r} - \boldsymbol{r}_{ma}) \cdot \int_{S_{nb}} d\boldsymbol{r}' (\boldsymbol{r}' - \boldsymbol{r}_{nb}) g_u(\boldsymbol{r},\boldsymbol{r}') \\
&\quad - \frac{4i}{k_u} \mathcal{A}_{ma,nb} \int_{S_{ma}} d\boldsymbol{r} \int_{S_{nb}} d\boldsymbol{r}' g_u(\boldsymbol{r},\boldsymbol{r}') && (2.80) \\
\bar{\boldsymbol{T}}_u^N[m,n,a,b] &= ik_u \mathcal{A}_{ma,nb} \int_{S_{ma}} d\boldsymbol{r} \left[(\boldsymbol{r} - \boldsymbol{r}_{ma}) \times \hat{\boldsymbol{n}}\right] \cdot \int_{S_{nb}} d\boldsymbol{r}' (\boldsymbol{r}' - \boldsymbol{r}_{nb}) g_u(\boldsymbol{r},\boldsymbol{r}') \\
&\quad - \frac{2i}{k_u} \mathcal{A}_{ma,nb} \int_{S_{ma}} d\boldsymbol{r} \left[(\boldsymbol{r} - \boldsymbol{r}_{ma}) \times \hat{\boldsymbol{n}}\right] \cdot \int_{S_{nb}} d\boldsymbol{r}' \nabla' g_u(\boldsymbol{r},\boldsymbol{r}') && (2.81)
\end{aligned}$$

$$\bar{\boldsymbol{K}}^{T}_{PV,u}[m,n,a,b] = \mathcal{A}_{ma,nb}\int_{S_{ma}} d\boldsymbol{r}(\boldsymbol{r}-\boldsymbol{r}_{ma}) \cdot \left[(\boldsymbol{r}-\boldsymbol{r}_{nb}) \times \int_{PV,S_{nb}} d\boldsymbol{r}'\nabla' g_u(\boldsymbol{r},\boldsymbol{r}')\right] \quad (2.82)$$

$$\bar{\boldsymbol{K}}^{N}_{PV,u}[m,n,a,b] = \mathcal{A}_{ma,nb}\int_{S_{ma}} d\boldsymbol{r}\,[(\boldsymbol{r}-\boldsymbol{r}_{ma}) \times \hat{\boldsymbol{n}}] \cdot \left[(\boldsymbol{r}-\boldsymbol{r}_{nb}) \times \int_{PV,S_{nb}} d\boldsymbol{r}'\nabla' g_u(\boldsymbol{r},\boldsymbol{r}')\right] \quad (2.83)$$

$$\bar{\boldsymbol{I}}^{T}[m,n,a,b] = \mathcal{A}_{ma,nb}\delta_{ma,nb}\int_{S_{ma}} d\boldsymbol{r}(\boldsymbol{r}-\boldsymbol{r}_{ma}) \cdot (\boldsymbol{r}-\boldsymbol{r}_{nb}) \quad (2.84)$$

$$\bar{\boldsymbol{I}}^{N}[m,n,a,b] = \mathcal{A}_{ma,nb}\delta_{ma,nb}\int_{S_{ma}} d\boldsymbol{r}(\boldsymbol{r}-\boldsymbol{r}_{ma}) \cdot \hat{\boldsymbol{n}} \times (\boldsymbol{r}-\boldsymbol{r}_{nb}), \quad (2.85)$$

where

$$\mathcal{A}_{ma,nb} = \frac{l_m l_n}{4A_{ma}A_{nb}}\gamma_{ma}\gamma_{nb} \quad (2.86)$$

and $\gamma_{nb}, \gamma_{ma} = \pm 1$, depending on the direction of the testing and basis functions on triangles. In the above, $\delta_{ma,nb}$ represents the Kronecker delta.

2.1.5 Multilevel Fast Multipole Algorithm

Electromagnetic problems can be solved iteratively and an iterative solver may reduce the complexity of a solution from $\mathcal{O}(N^3)$ to $\mathcal{O}(N^2)$. Nevertheless, an iterative solver alone is not feasible for problems involving electrically large or densely discretized objects due to need for extensive memory usage and very long solution times. Since all interactions of testing and basis functions are stored in memory in MOM, memory and time complexities are $\mathcal{O}(N^2)$, where N represents the number of unknowns. In the literature, fast multipole method (FMM) was introduced to make the solution of large numbers of unknowns possible [57] by reducing the computational complexity from $\mathcal{O}(N^2)$ to $\mathcal{O}(N^{3/2})$. By extending the concept of FMM with a recursive clustering scheme, MLFMA was developed to solve even larger problems [58].

In MLFMA, far-field interactions are calculated on-the-fly (without being stored) in a group-by-group manner through the factorization of the Green's function by employing the Gegenbauer's addition theorem, leading to the reduction of the complexity from $\mathcal{O}(N^{3/2})$ to $\mathcal{O}(N \log N)$ [39]. In order to construct a multilevel tree structure, a recursive clustering scheme is employed by recursively dividing the cubic box (that encloses the object) into sub-boxes until the smallest allowed box size is reached, without considering empty boxes.

Three major stages of MLFMA, i.e., aggregation, translation, and disaggregation, are performed in each matrix-vector multiplication to perform far-field interactions by using the constructed multilevel tree structure. In aggregation, radiated fields are computed from the lowest level to the highest level of the tree structure; shifting is applied from basis functions to the lowest-level box centers and then from lower-level boxes to higher-level boxes. In translation, the conversion of radiated fields into incoming fields occurs. Finally, in disaggregation, incoming fields are computed from the highest level to the lowest level; shifting is applied from higher-level boxes to lower-level boxes and then from the lowest-level box centers to testing functions.

2.1.6 Approximate Diagonalization

For electrically large structures, MLFMA is required to enable and accelerate solutions; however, its conventional mechanism is not a suitable option for NZI or ZI materials. Electromagnetic problems involving NZI or ZI materials are inherently multiscale because of the large variation of the wavelength. As mentioned previously, NZI and ZI materials are special structures with very small refractive index values, resulting in wavelengths locally stretching to infinity. The trianglulation size for an NZI object is decided by the outer problem wavelength, which is very short compared to the wavelength of the inner problem. Consequently, the inner problem turns into a low-frequency problem due to its apparently dense discretization.

The low-frequency breakdown of MLFMA is already well-known in the literature [59]. It is simply the result of the violation of the plane-wave expansion criteria in MLFMA. To overcome the low-frequency breakdown, various techniques, such as factorizing Green's function in terms of multipoles [60], using evanescent waves for the interactions at the lower levels [61], approximate diagonalization [11, 62], etc., have been employed. An approximate diagonalization scheme, leading to AD-MLFMA, is implemented in this study.

In the context of AD-MLFMA, the diagonalized form of Green's function can be written as

$$g(\boldsymbol{r},\boldsymbol{r}') = \frac{\exp(ik|\boldsymbol{r}-\boldsymbol{r}'|)}{4\pi|\boldsymbol{r}-\boldsymbol{r}'|} = \frac{\exp(ik|\boldsymbol{z}+\boldsymbol{v}|)}{4\pi|\boldsymbol{z}+\boldsymbol{v}|}$$

$$= \frac{1}{16\pi^2}\int d^2\hat{\boldsymbol{k}}\beta^s(\boldsymbol{k},\boldsymbol{v})\alpha^s(\boldsymbol{k},\boldsymbol{z}), \tag{2.87}$$

where $|\boldsymbol{r}-\boldsymbol{r}'| = |\boldsymbol{z}+\boldsymbol{v}|$, $z = |\boldsymbol{z}| > v = |\boldsymbol{v}|$, and $\boldsymbol{k} = k\hat{\boldsymbol{k}}$. In the above, $\beta^s(\boldsymbol{k},\boldsymbol{v})$ is the diagonal shift operator and $\alpha^s(\boldsymbol{k},\boldsymbol{z})$ is the diagonal translation operator that can be written as

$$\beta^s(\boldsymbol{k},\boldsymbol{v}) = \sum_{t=0}^{\infty}(2t+1)\mathcal{J}_t^s(kv)P_t(\hat{\boldsymbol{k}}\cdot\hat{\boldsymbol{v}}) \tag{2.88}$$

$$\alpha^s(\boldsymbol{k},\boldsymbol{z}) = \sum_{t=0}^{\infty}(2t+1)\mathcal{H}_t^s(kv)P_t(\hat{\boldsymbol{k}}\cdot\hat{\boldsymbol{z}}) \tag{2.89}$$

$$\mathcal{J}_t^s(kv) = (i/s)^t j_t(kv) \tag{2.90}$$

$$\mathcal{H}_t^s(kv) = (is)^t(ik)h_t^{(1)}(kv), \tag{2.91}$$

where $\mathcal{J}_t^s$ represents the scaled spherical Bessel function of the first kind, $\mathcal{H}_t^s$ represents the scaled spherical Hankel function of the first kind, P_t represents Legendre polynomial, and s is a scaling factor. Note that the standard diagonalization corresponds to $s = 1$ case.

In an implementation, conventional MLFMA is still used for the higher-level interactions. On the other hand, the approximate diagonalization scheme is involved in the lower-level interactions to eliminate the low-frequency breakdown ($k \to 0$). The approximation is related to the scaling factor (s) value. Dealing with small kz values, as in the inner problems of NZI structures, a scaling value $s \approx kz$ leads to numerically stable $\mathcal{H}_t^s$ and translation operators. For efficient computations, the scaled spherical Bessel function of the first kind can be approximated as

$$\mathcal{J}_t^s = i^t j_t(kv)s^{-t} \approx i^t\frac{(kv)^t}{(2l+1)!!}s^{-t} = i^t\frac{(kv/s)^t}{(2l+1)!!} \approx i^t j_t(kv/s), \tag{2.92}$$

assuming $kv \ll 1$ and $kv \ll s$, which requires rigorous considerations to avoid violating $s \approx kz$ condition. Then, the diagonal shift operator can be approximated as

$$\beta^s(\boldsymbol{k},\boldsymbol{v}) \approx \exp(i\boldsymbol{k}\cdot\boldsymbol{v}/s), \tag{2.93}$$

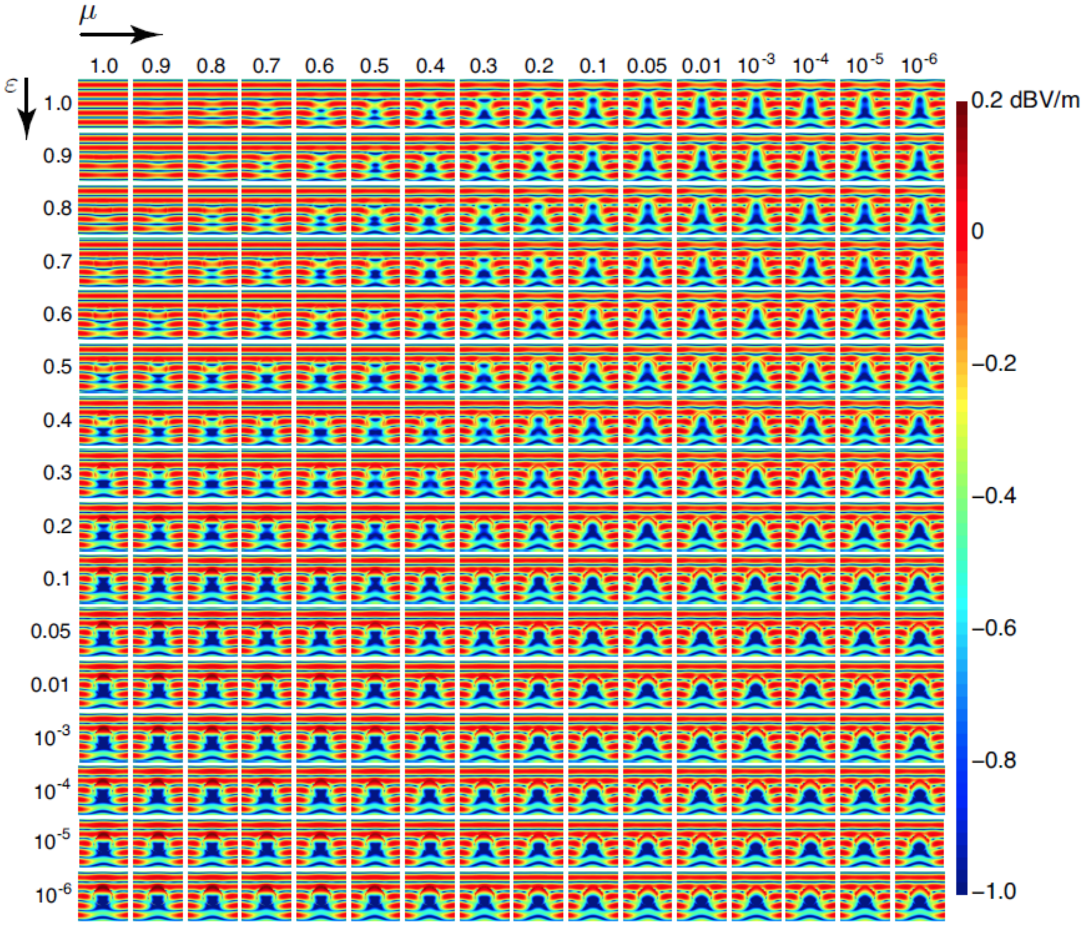

Figure 2.3: The real part of the electric field intensity (dBV/m) inside and outside the spheres with NZI materials having a set of relative permittivity and/or permeability values close to zero.

which is suitable for group-by-group interactions. Finally, we reach the approximate diagonalization of the Green's function as

$$g(\boldsymbol{r}, \boldsymbol{r}') \approx \frac{1}{16\pi^2} \int d^2\hat{\boldsymbol{k}} \exp(i\boldsymbol{k} \cdot \boldsymbol{v}/s) \alpha^s(\boldsymbol{k}, \boldsymbol{z}), \tag{2.94}$$

whose application is very similar to the conventional diagonalization while being stable for arbitrarily short-distance interactions.

2.2 Numerical Results

In this section, we consider numerical solutions of various canonical and realistic problems in order to compare the performances of the conventional and proposed formulations to analyze NZI structures. For iterative solutions, the generalized minimal

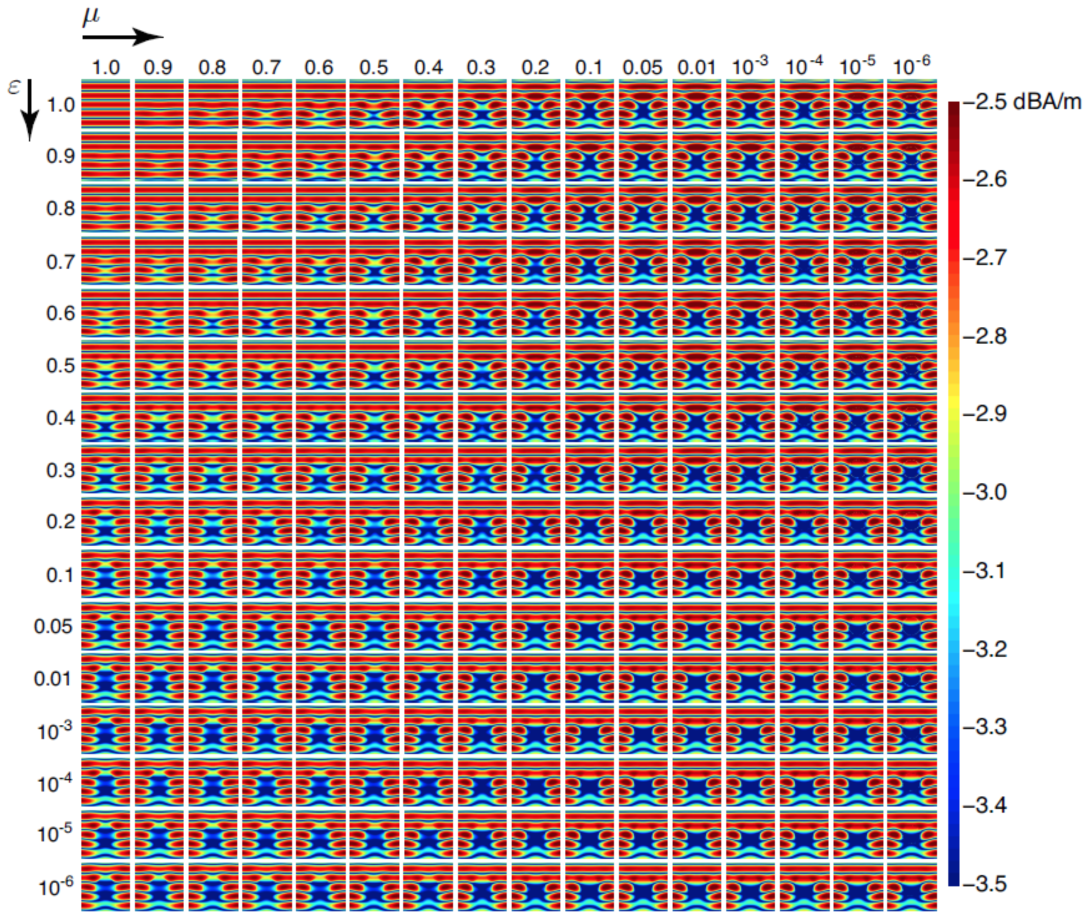

Figure 2.4: The real part of the magnetic field intensity (dBA/m) inside and outside the spheres with NZI materials having a set of relative permittivity and/or permeability values close to zero.

residual (GMRES) algorithm [63] is used without any restart and preconditioning, while the target residual error is set to 10^{-4} in all simulations.

2.2.1 Formulation Tests

In the following examples, the conventional SIE formulations, i.e., PMCHWT, NMF, MNMF, JMCFIE, CTF, and MCTF, as well as the proposed tangential and mixed formulations are investigated, with particular focus on accuracy and efficiency of solutions in the analysis of objects composed of homogeneous NZI and ZI materials with small permittivity and/or permeability values.

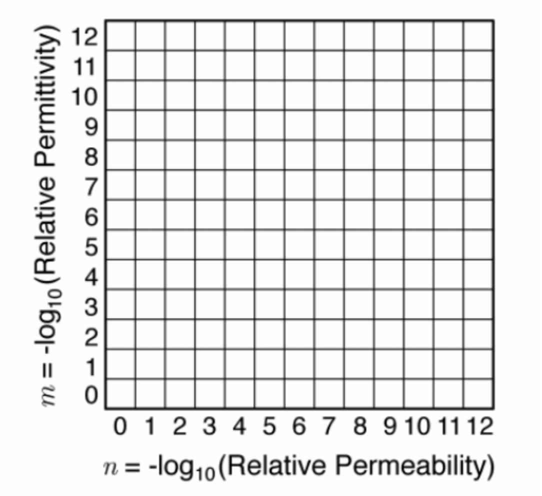
m = -log$_{10}$(Relative Permittivity)
0
1
2
3
4
5
6
7
8
9
10
11
12
0 1 2 3 4 5 6 7 8 9 10 11 12
n = -log$_{10}$(Relative Permeability)

Figure 2.5: The map of the plots in Figures 2.6 and 2.7.

The first set of numerical results is again on the solutions of spheres with diameter λ ($\lambda = 0.6$ m) located in free space, while the mesh size is fixed to $\lambda/10$. Plane-wave excitation is used with 1 V/m, and a set of relative permittivity ($\epsilon_z = 10^{-m}$) and permeability ($\mu_z = 10^{-n}$) values are scanned for $m = 0, 1, ..., 6$ and $n = 0, 1, ..., 6$ to observe electromagnetic responses of NZI objects with different material properties. Direct calculations of matrix interactions and JMCFIE formulation are adopted. Real parts of the electric field intensity (dBV/m) and the magnetic field intensity (dBA/m) inside and outside the spheres in center cross sections are shown in Figures 2.3 and 2.4, respectively. In each plot that covers $2\lambda \times 2\lambda$ area, the sphere is located at the center. When both relative permittivity and permeability values become smaller than 0.1, it can be noticed that electromagnetic responses are similar; hence, in order to have a clear understanding about the effect of relative permittivity and/or permeability values smaller than 0.1, the results should be investigated in more detail. These results agree well with the observations on the performance of the JMCFIE formulation for the first set of problems.

In the second set of numerical results, electromagnetic scattering problems involving spheres with diameter $\lambda = 0.6$ m located in free space are considered with all of the mentioned SIE formulations, i.e., NMF, MNMF, CTF, MCTF, PMCHWT, JMCFIE, as well as the new tangential and mixed formulations. The mesh size is fixed as $\lambda/20$, while the excitation is again plane wave with 1 V/m amplitude. The plane wave

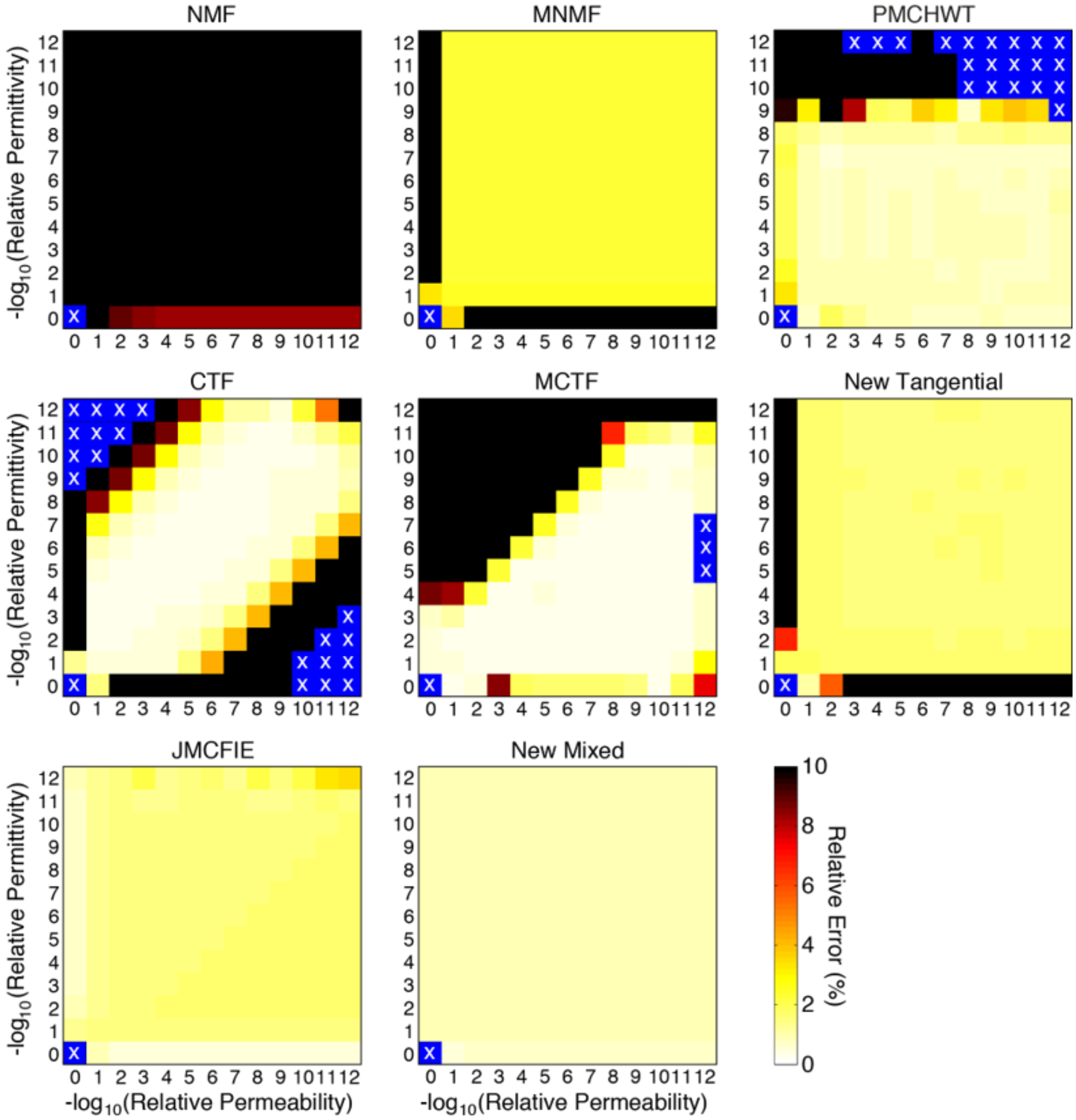

Figure 2.6: Relative errors in the far-zone electric field intensity values obtained by using different formulations for scattering problems of NZI spheres with a set of permittivity and/or permeability values close to zero. In the plots, the maximum error is set to 10%.

is propagating in the x direction, with the electric field polarized in the y direction. In order to compare the SIE formulations, a set of relative permittivity ($\epsilon_z = 10^{-m}$) and relative permeability ($\mu_z = 10^{-n}$) values is scanned for $m = 0, 1, ..., 12$ and $n = 0, 1, ..., 12$, except for the $m = n = 0$ case since it corresponds to free space. All matrix elements are calculated directly. All of the formulations are compared by considering relative errors in the far-zone electric field intensity values with respect to

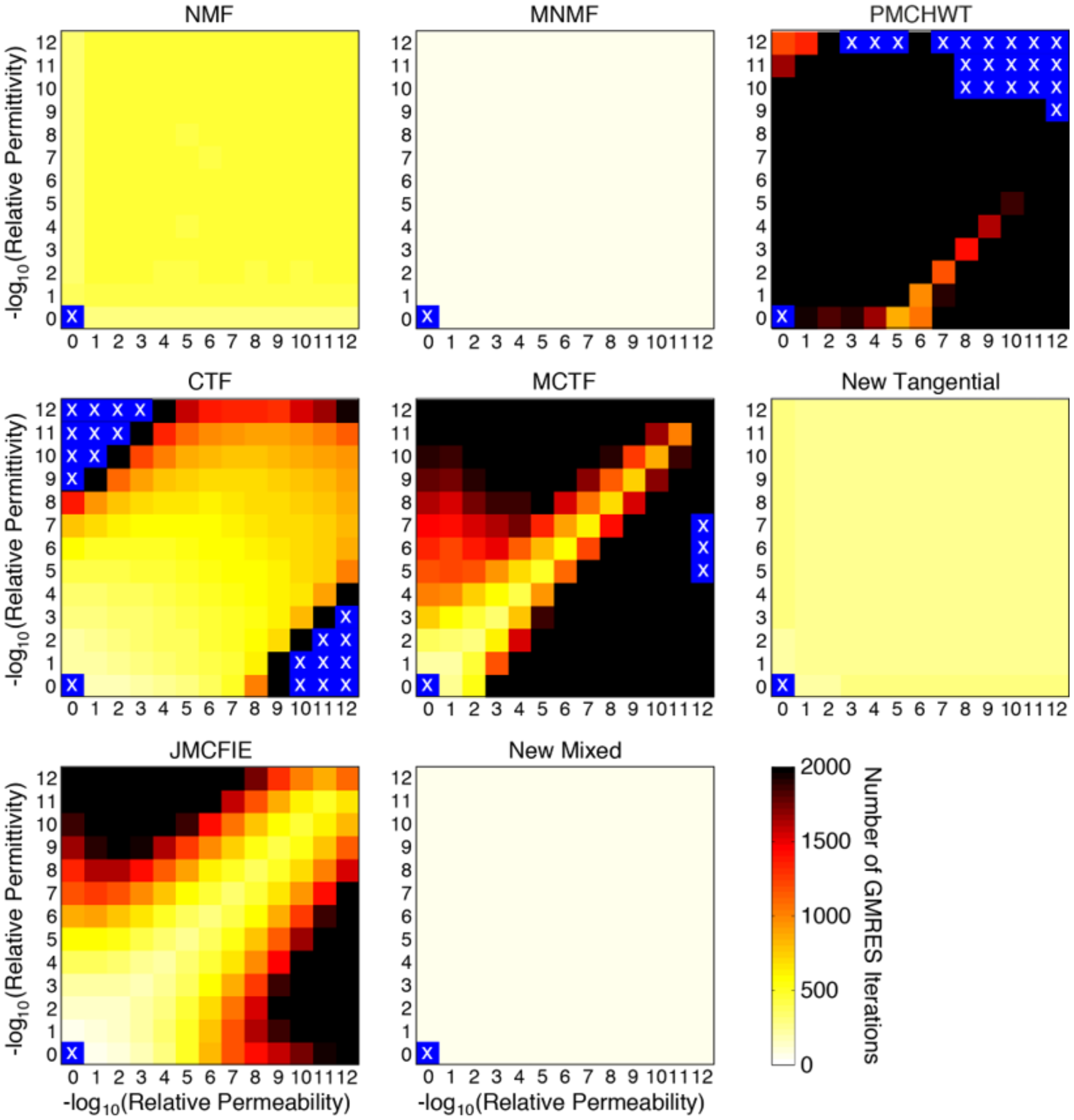

Figure 2.7: Numbers of GMRES iterations obtained by using different formulations for scattering problems of NZI spheres with a set of permittivity and/or permeability values close to zero. In the plots, the maximum number of iterations is set to 2000.

Mie-series solutions as shown in Figure 2.6 and the numbers of GMRES iterations as shown in Figure 2.7. The map of the plots in Figures 2.6 and 2.7 is described in Figure 2.5. The number of iterations is limited to 5000 iterations, and the non-convergent results are marked with cross signs with a blue background color. In each plot, x axis represents relative permeability values (n) and y axis represents relative permittivity values (m) as described in Figure 2.5. In all simulations, the relative error is defined as

$$\text{Relative Error} = \frac{||\boldsymbol{E}_a^\infty - \boldsymbol{E}_c^\infty||_2}{||\boldsymbol{E}_a^\infty||_2}, \tag{2.95}$$

where $\boldsymbol{E}_c^\infty$ and $\boldsymbol{E}_a^\infty$ are vectors containing the computational and analytical values of the far-zone electric field intensity on the E-plane (with 360 sample points), respectively.

The following observations are made by examining the relative errors and numbers of iterations for different formulations in Figures 2.6 and 2.7:

- Between the conventional formulations, i.e., without considering the new formulations, the JMCFIE formulation is in general accurate with relative error values below 1.5%, but exceeding 3% when both ϵ_z and μ_z are very small. Nonetheless, difficulties in iterative convergence occur when either ϵ_z or μ_z becomes smaller.
- CTF becomes ill-conditioned, leading to poor accuracy observed as large relative errors for the outside of the diagonal region. For the diagonal region, where ϵ_z and μ_z are proportional to each other, the accuracy of CTF is comparably good.
- In particular for accuracy, PMCHWT fails in the entire upper region, where ϵ_z has very small values, while it provides fairly good accuracy when μ_z is very small. Also, PMCHWT has convergence issues through the overall span.
- Outside of the upper diagonal region, MCTF has a relatively good performance in terms of accuracy, while it has a clear disadvantage in terms of iterative convergence.
- MNMF is an acceptable formulation since it provides good iterative convergence and relatively good accuracy in all regions other than either $\epsilon_z = 1$ or $\mu_z = 1$, whereas NMF severely fails with relative error values larger than 8% in the overall scan.
- It is remarkable that the new tangential formulation has relative error values below 2% in general, except when ϵ_z or μ_z is equal to unity. This formulation also has a very good and stable iterative convergence.

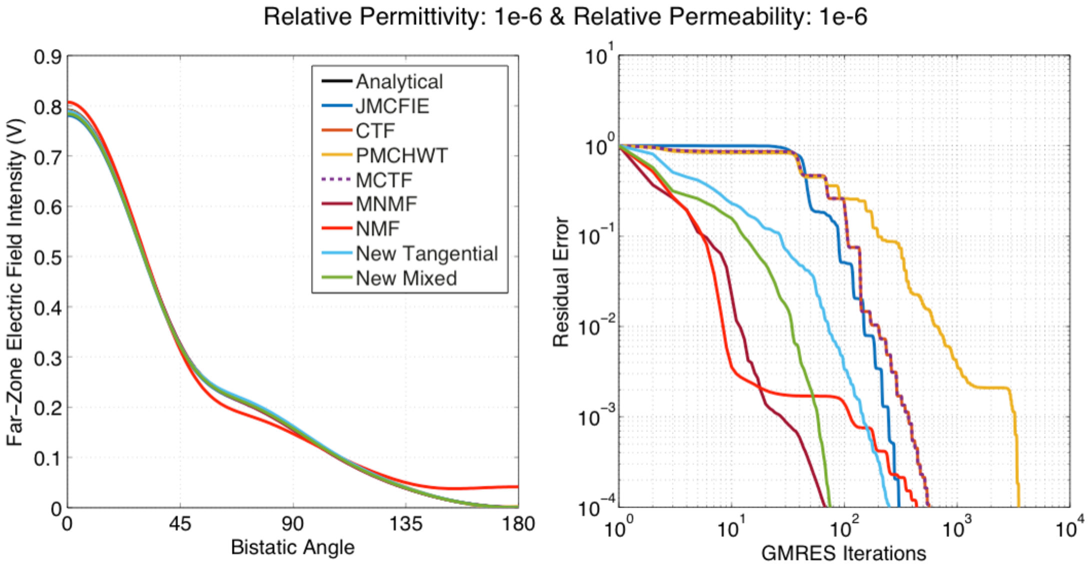

Figure 2.8: Far-zone electric field intensity distribution (left) and GMRES iterative convergence (right) plots obtained by using different formulations for the scattering problem of a λ-diameter NZI sphere with $\epsilon_z = 10^{-6}$ and $\mu_z = 10^{-6}$.

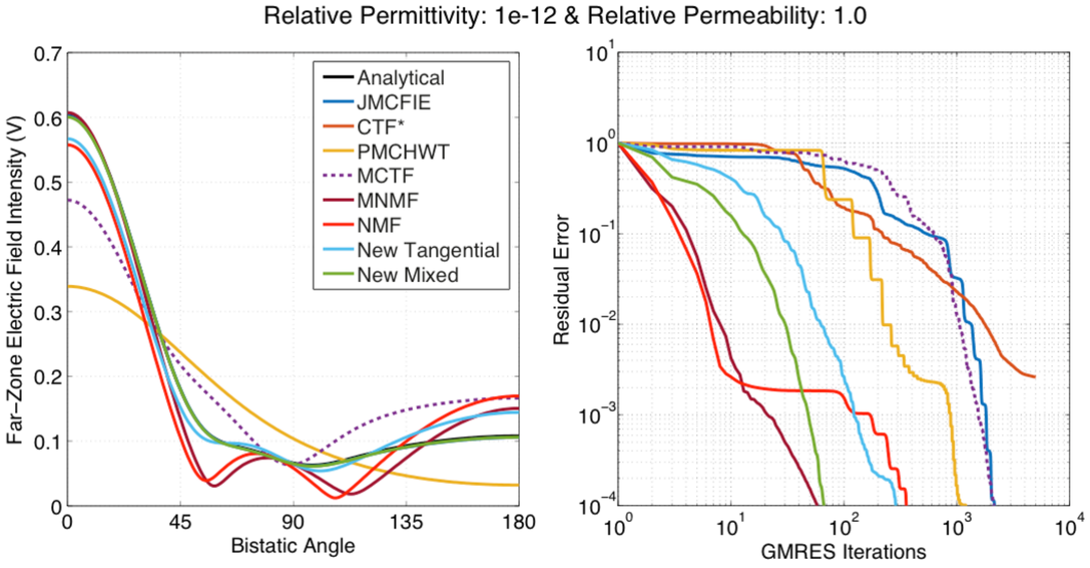

Figure 2.9: Far-zone electric field intensity distribution (left) and GMRES iterative convergence (right) plots obtained by using different formulations for the scattering problem of a λ-diameter NZI sphere with $\epsilon_z = 10^{-12}$ and $\mu_z = 1.0$.

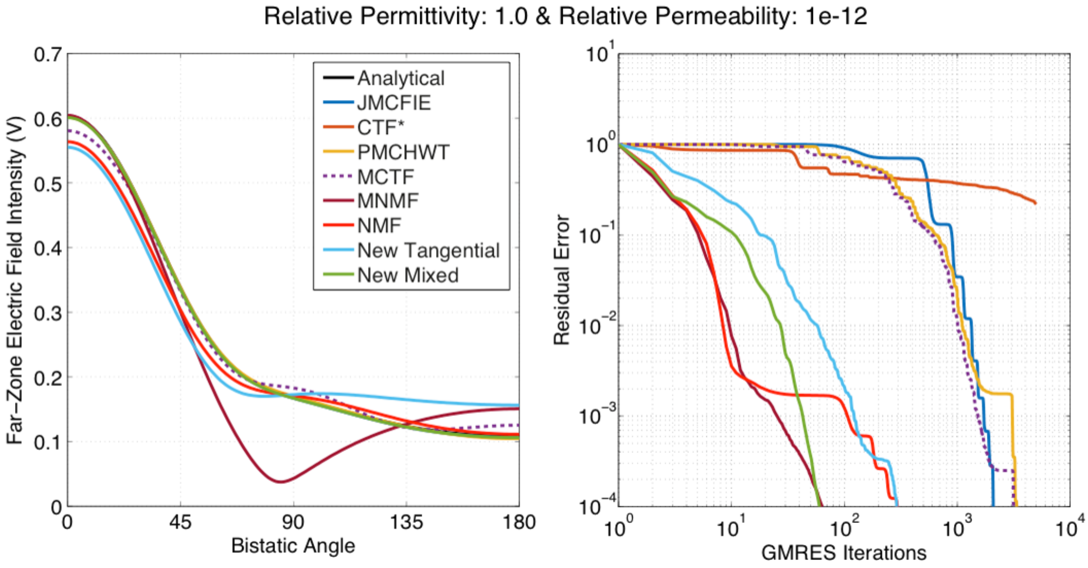

Figure 2.10: Far-zone electric field intensity distribution (left) and GMRES iterative convergence (right) plots obtained by using different formulations for the scattering problem of a λ-diameter NZI sphere with $\epsilon_z = 1.0$ and $\mu_z = 10^{-12}$.

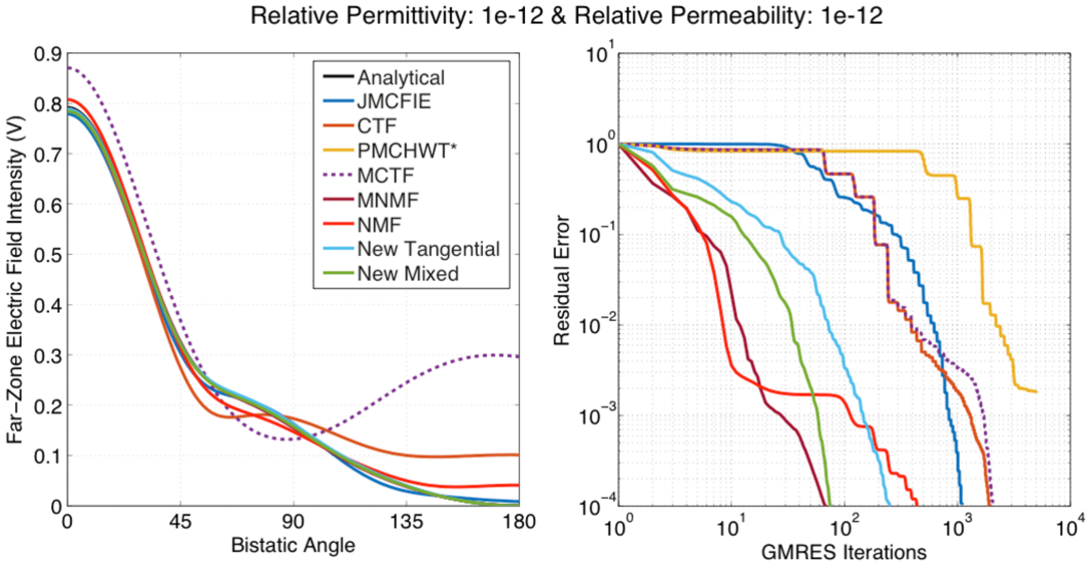

Figure 2.11: Far-zone electric field intensity distribution (left) and GMRES iterative convergence (right) plots obtained by using different formulations for the scattering problem of a λ-diameter NZI sphere with $\epsilon_z = 10^{-12}$ and $\mu_z = 10^{-12}$.

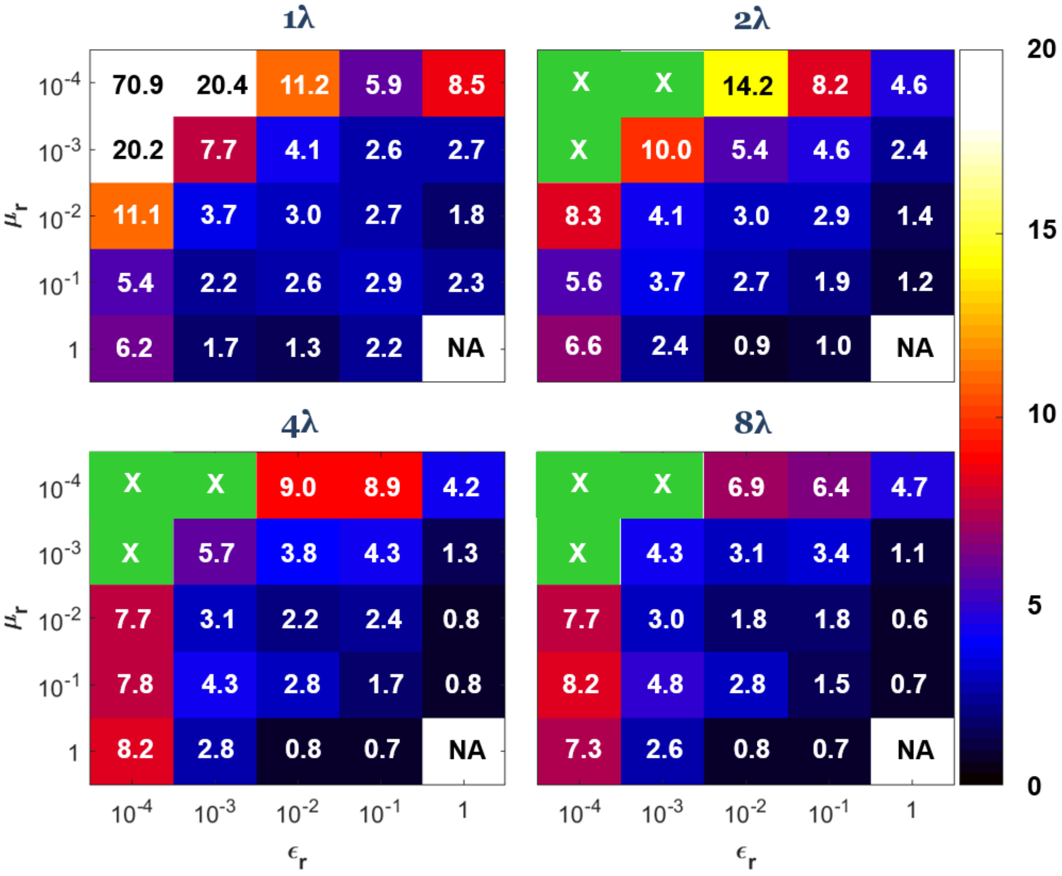

1λ

μ_r \ ϵ_r	10^{-4}	10^{-3}	10^{-2}	10^{-1}	1
10^{-4}	70.9	20.4	11.2	5.9	8.5
10^{-3}	20.2	7.7	4.1	2.6	2.7
10^{-2}	11.1	3.7	3.0	2.7	1.8
10^{-1}	5.4	2.2	2.6	2.9	2.3
1	6.2	1.7	1.3	2.2	NA

2λ

μ_r \ ϵ_r	10^{-4}	10^{-3}	10^{-2}	10^{-1}	1
10^{-4}	X	X	14.2	8.2	4.6
10^{-3}	X	10.0	5.4	4.6	2.4
10^{-2}	8.3	4.1	3.0	2.9	1.4
10^{-1}	5.6	3.7	2.7	1.9	1.2
1	6.6	2.4	0.9	1.0	NA

4λ

μ_r \ ϵ_r	10^{-4}	10^{-3}	10^{-2}	10^{-1}	1
10^{-4}	X	X	9.0	8.9	4.2
10^{-3}	X	5.7	3.8	4.3	1.3
10^{-2}	7.7	3.1	2.2	2.4	0.8
10^{-1}	7.8	4.3	2.8	1.7	0.8
1	8.2	2.8	0.8	0.7	NA

8λ

μ_r \ ϵ_r	10^{-4}	10^{-3}	10^{-2}	10^{-1}	1
10^{-4}	X	X	6.9	6.4	4.7
10^{-3}	X	4.3	3.1	3.4	1.1
10^{-2}	7.7	3.0	1.8	1.8	0.6
10^{-1}	8.2	4.8	2.8	1.5	0.7
1	7.3	2.6	0.8	0.7	NA

Figure 2.12: Relative errors in the far-zone electric field intensity values with respect to Mie-series solutions for the scattering problems involving NZI spheres formulated with JMCFIE.

- The superior performance of the new mixed formulation is clearly identified regarding both iterative convergence and accuracy. It has a maximum relative error of 1% and maximum iterative counts of 100 in the entire span.
- It is also observed that there is not an obvious correlation between inaccuracy and convergence issues since they can be caused by different reasons.

For further comparisons of the formulations for relatively small problems, the far-zone electric field intensity with respect to the bistatic angle on the E-plane and the corresponding GMRES iterative convergence histories are examined for four distinct cases with different relative permittivity and/or permeability values of the sphere with λ diameter (continuing the second set of numerical results). As depicted in Figure 2.8, for the case with $\epsilon_z = 10^{-6}$ and $\mu_z = 10^{-6}$, all formulations other than NMF have

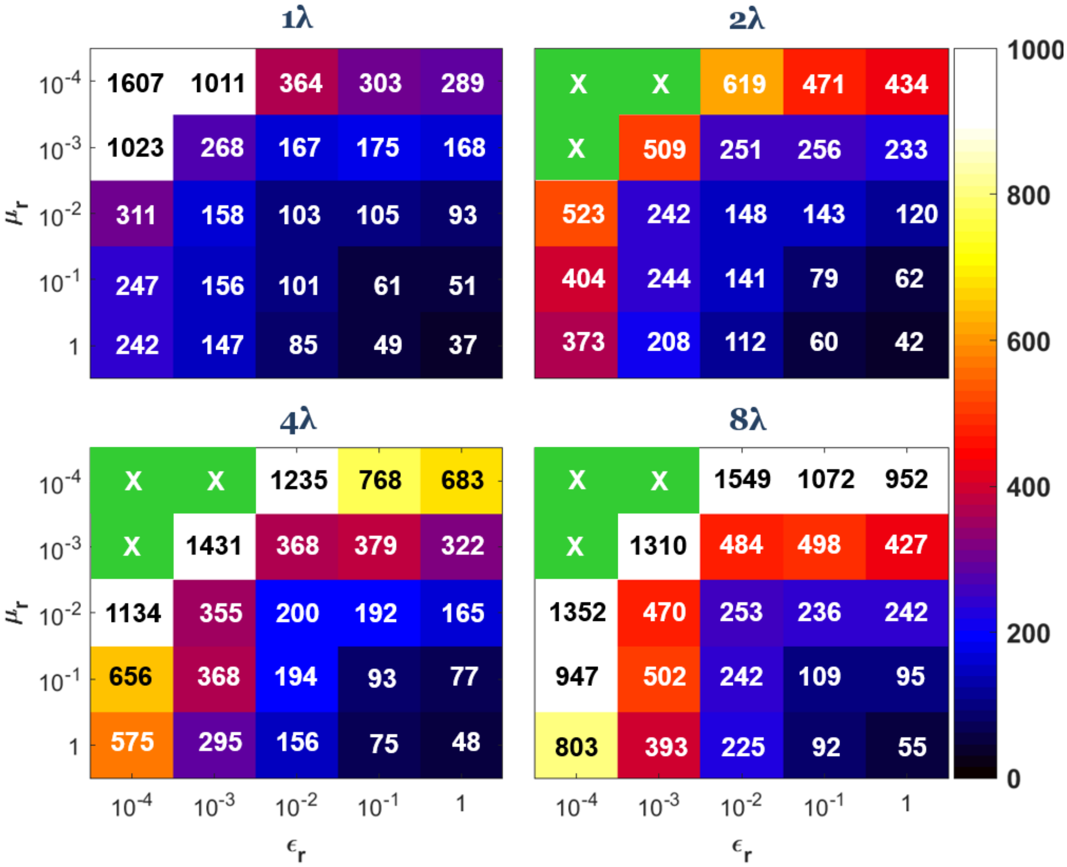

Figure 2.13: Numbers of GMRES iterations for the scattering problems involving NZI spheres formulated with JMCFIE.

relatively good accuracy considering the reference Mie-series solutions. While PMCHWT requires more than 3000 iterations, only MNMF and the new mixed formulation need less than 100 iterations. For the case with $\epsilon_z = 10^{-12}$ and $\mu_z = 1.0$, MCTF, NMF, MNMF, PMCHWT, and even the new tangential formulation provide inaccurate results despite that the convergence is satisfied for each of these formulations, as shown in Figure 2.9. The electric field intensity distribution of CTF is excluded since it does not converge at all. Although JMCFIE provides accurate results, it leads to one of the slowest convergence similar to MCTF. The outstanding performance of the new mixed formulation is clearly visible with its accurate and efficient results. Figure 2.10 presents the case of $\epsilon_z = 1.0$ and $\mu_z = 10^{-12}$, where the non-convergent CTF result is again excluded in the electric-field-intensity results. For this case, NMF, MNMF, MCTF, and the new tangential formulation are inaccurate, whereas PMCHWT and JMCFIE formulations lead to accurate results with iteration numbers more than 3000

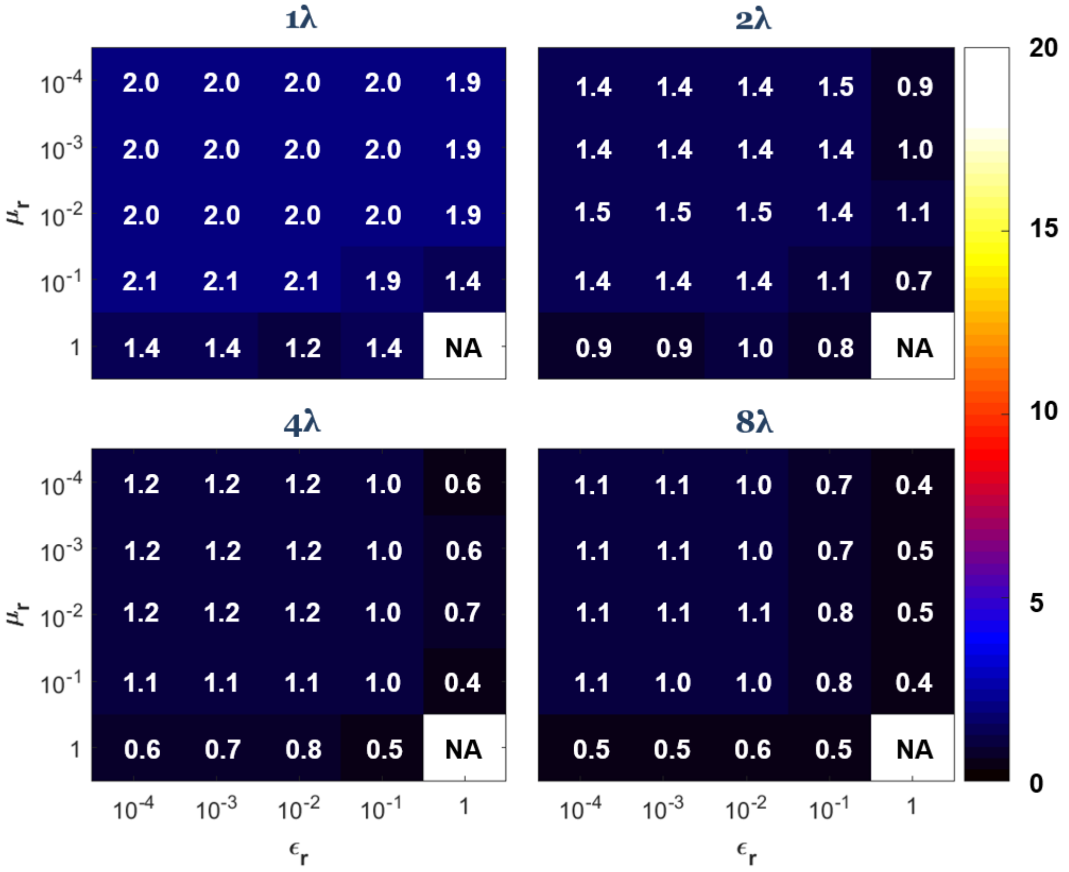

μ_r \ ϵ_r (1λ)	10^{-4}	10^{-3}	10^{-2}	10^{-1}	1
10^{-4}	2.0	2.0	2.0	2.0	1.9
10^{-3}	2.0	2.0	2.0	2.0	1.9
10^{-2}	2.0	2.0	2.0	2.0	1.9
10^{-1}	2.1	2.1	2.1	1.9	1.4
1	1.4	1.4	1.2	1.4	NA

μ_r \ ϵ_r (2λ)	10^{-4}	10^{-3}	10^{-2}	10^{-1}	1
10^{-4}	1.4	1.4	1.4	1.5	0.9
10^{-3}	1.4	1.4	1.4	1.4	1.0
10^{-2}	1.5	1.5	1.5	1.4	1.1
10^{-1}	1.4	1.4	1.4	1.1	0.7
1	0.9	0.9	1.0	0.8	NA

μ_r \ ϵ_r (4λ)	10^{-4}	10^{-3}	10^{-2}	10^{-1}	1
10^{-4}	1.2	1.2	1.2	1.0	0.6
10^{-3}	1.2	1.2	1.2	1.0	0.6
10^{-2}	1.2	1.2	1.2	1.0	0.7
10^{-1}	1.1	1.1	1.1	1.0	0.4
1	0.6	0.7	0.8	0.5	NA

μ_r \ ϵ_r (8λ)	10^{-4}	10^{-3}	10^{-2}	10^{-1}	1
10^{-4}	1.1	1.1	1.0	0.7	0.4
10^{-3}	1.1	1.1	1.0	0.7	0.5
10^{-2}	1.1	1.1	1.1	0.8	0.5
10^{-1}	1.1	1.0	1.0	0.8	0.4
1	0.5	0.5	0.6	0.5	NA

Figure 2.14: Relative errors in the far-zone electric field intensity values with respect to Mie-series solutions for the scattering problems involving NZI spheres formulated with the new mixed formulation.

and 2000, respectively. Once again, the new mixed formulation outshines all of the other formulations with its excellent performance on the accuracy and efficiency. For the last case of $\epsilon_z = 10^{-12}$ and $\mu_z = 10^{-12}$ depicted in Figure 2.11, accurate and efficient results are obtained only with the new mixed formulation and MNMF with relative errors of 0.98% and 2.25%, respectively, while the required numbers of iterations are 76 and 68.

In the last set of numerical results to compare formulations, JMCFIE and the new mixed formulation are considered within the developed AD-MLFMA implementation to investigate their performances on electrically large problems. In the solutions, near-zone interactions are calculated directly with a maximum of 1% error, while AD-MLFMA is used with the smallest box size of $\lambda/4$ for far-zone interac-

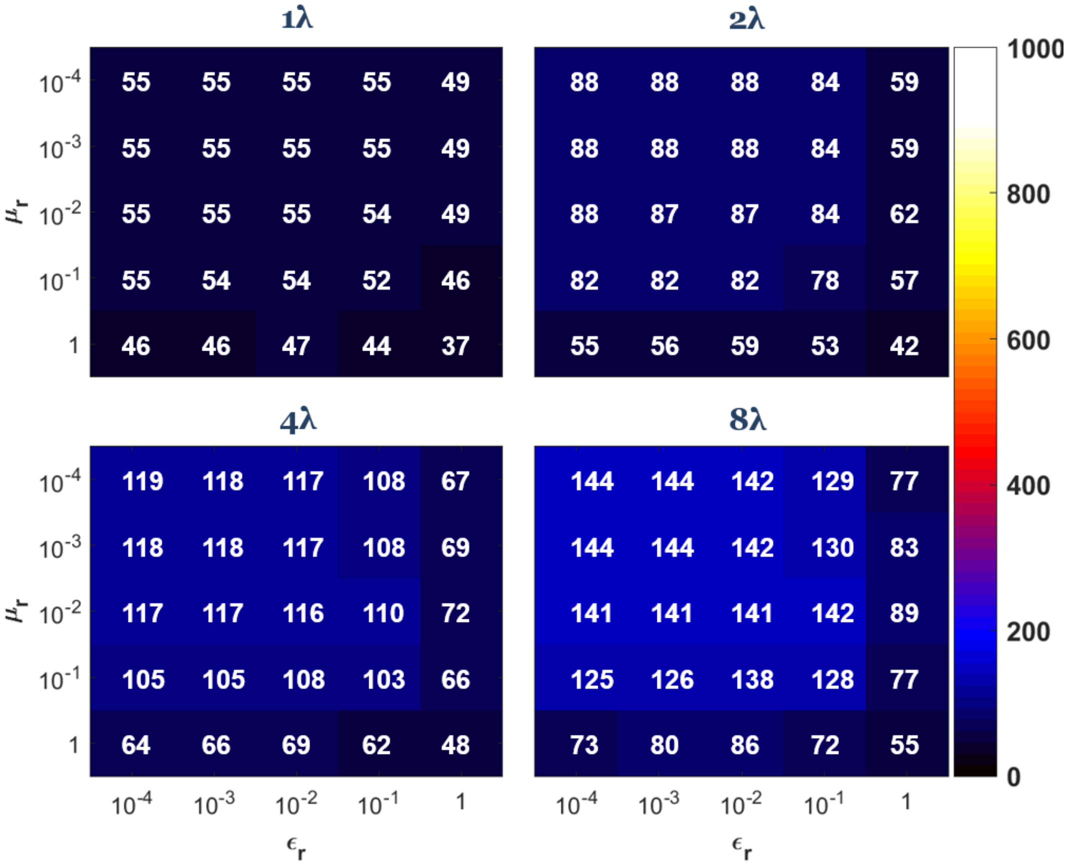

Figure 2.15: Numbers of GMRES iterations for the scattering problems involving NZI spheres formulated with the new mixed formulation.

tions. The maximum number of iterations is set to 5000. In the examples considered here, spheres with $\lambda, 2\lambda, 4\lambda$, and 8λ diameters are discretized with the mesh size of $\lambda/10$, corresponding to matrix equations involving 1974, 8310, 33,768, and 134,718 unknowns, respectively. AD-MLFMA solutions for these diameter values involve tree structures with three, four, five, and six levels, respectively. Similar to the previous problems, plane-wave illumination with 1 V/m amplitude is considered and the host medium is selected as vacuum. To test the formulations rigorously, different relative permittivity ($\epsilon_z = 1.0, 0.1, 0.01, 0.001, 0.0001$) and permeability ($\mu_z = 1.0, 0.1, 0.01, 0.001, 0.0001$) values are selected, excluding the $\epsilon_z = \mu_z = 1.0$ (vacuum sphere) case.

Figures 2.12 and 2.13 display the relative errors and the corresponding numbers of iterations obtained with JMCFIE solutions for the above-mentioned scattering prob-

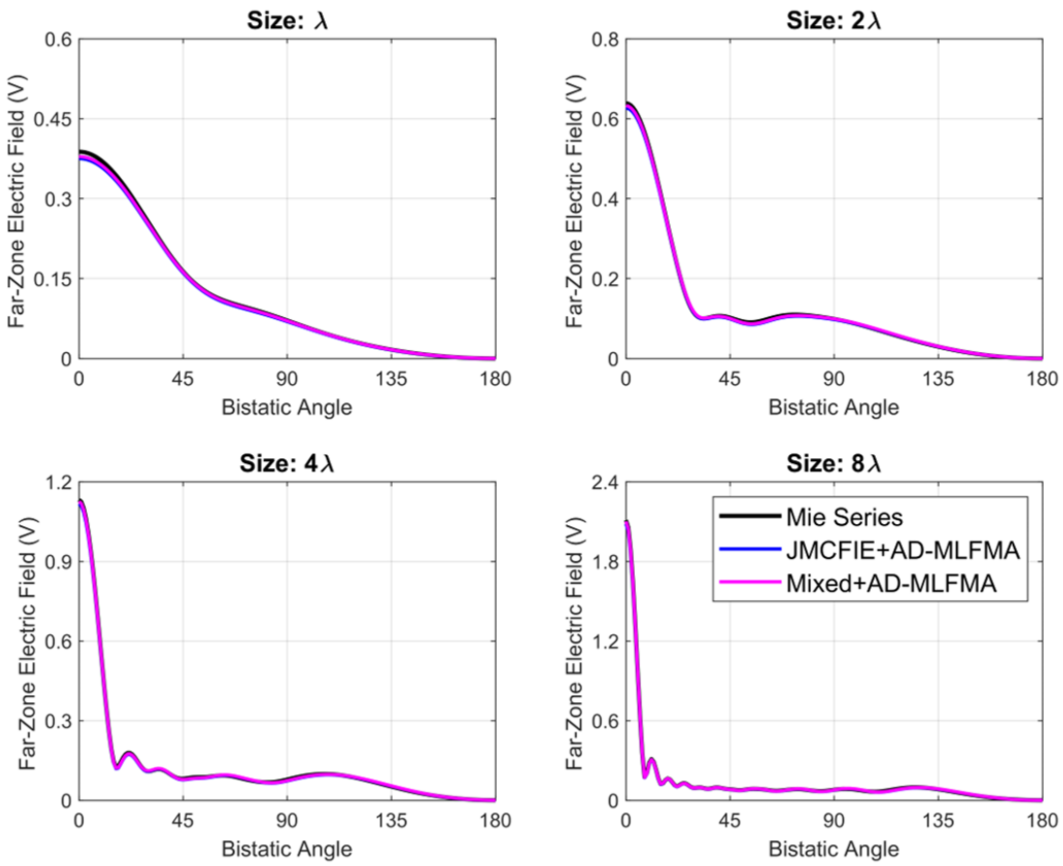

Figure 2.16: Bistatic far-zone electric field intensity distributions obtained for the scattering problems involving NZI spheres with $\epsilon_z = 0.1$ and $\mu_z = 0.1$.

lems. The relative error is calculated by using the far-zone electric field intensity values of the obtained solutions in comparison to Mie-series solutions, similar to the previous results. Note that the results when no-convergence occur are marked with cross signs with green background. It can be observed that convergence is not achieved (with JMCFIE) for relative permeability and permittivity values smaller than 10^{-3} for spheres with $2\lambda, 4\lambda$, and 8λ diameters. While the corresponding solutions seem to converge for the λ-size sphere, the relative errors are greater than 20% due to ill-conditioning issues of JMCFIE, which are more pronounced with the approximate matrix-vector multiplications by AD-MLFMA.

Figures 2.14 and 2.15 display the relative errors and the numbers of iterations obtained with the new mixed formulation for the above-mentioned scattering problems. The mixed formulation outperforms JMCFIE with a maximum relative error of 2%

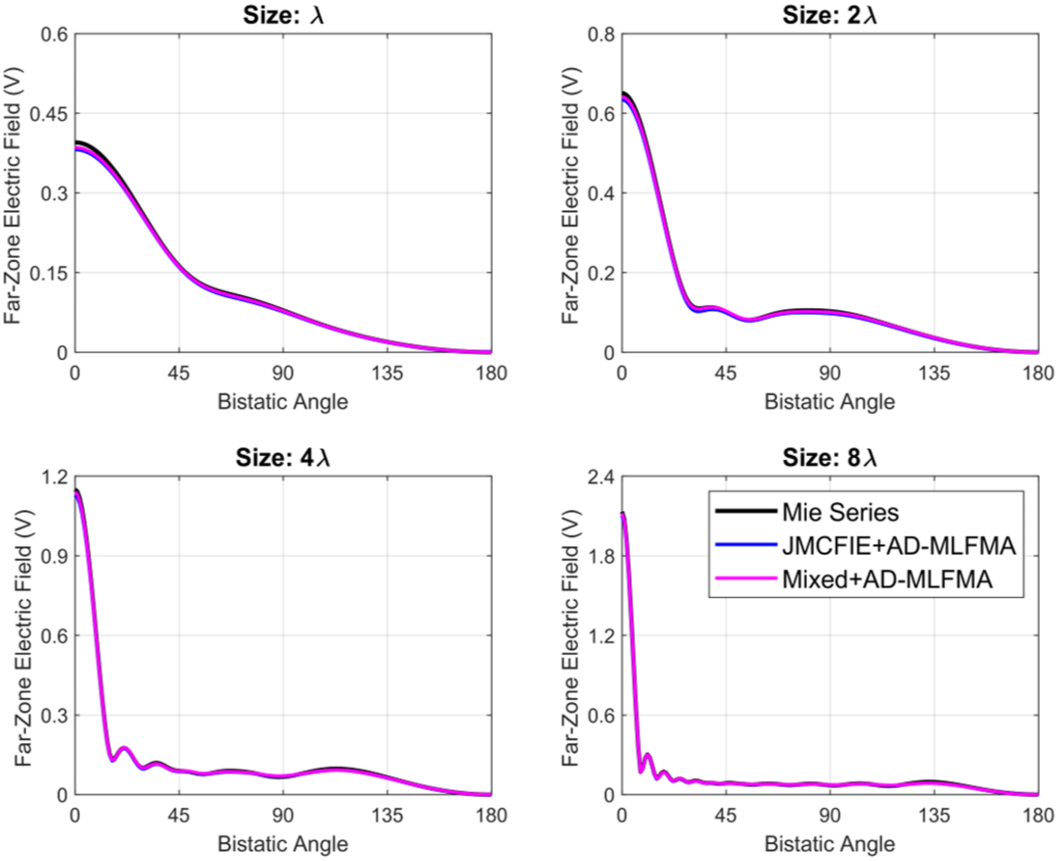

Figure 2.17: Bistatic far-zone electric field intensity distributions obtained for the scattering problems involving NZI spheres with $\epsilon_z = 0.01$ and $\mu_z = 0.01$.

to 1.1% from λ-size sphere to 8λ-size sphere and a maximum number of iterations of 144 (for the 8λ-size sphere when both relative permeability and permittivity are smaller than or equal to 10^{-3}). As the electrical size of the sphere grows and more triangles are used for the discretization, the discretized geometry becomes closer to the ideal sphere geometry that is considered in Mie-series solutions, which explains the better accuracy for larger problems. The numbers of iterations of the solutions with the new mixed formulation in the entire span are remarkably comparable and small for all levels, and very limited increments in the iteration counts through the electrically larger problems demonstrate the stability and reliability of the implementation based on the mixed formulation and AD-MFLMA.

Bistatic far-zone electric field intensity distributions for the increasingly large scattering problems when both relative permittivity and permeability values are equal to

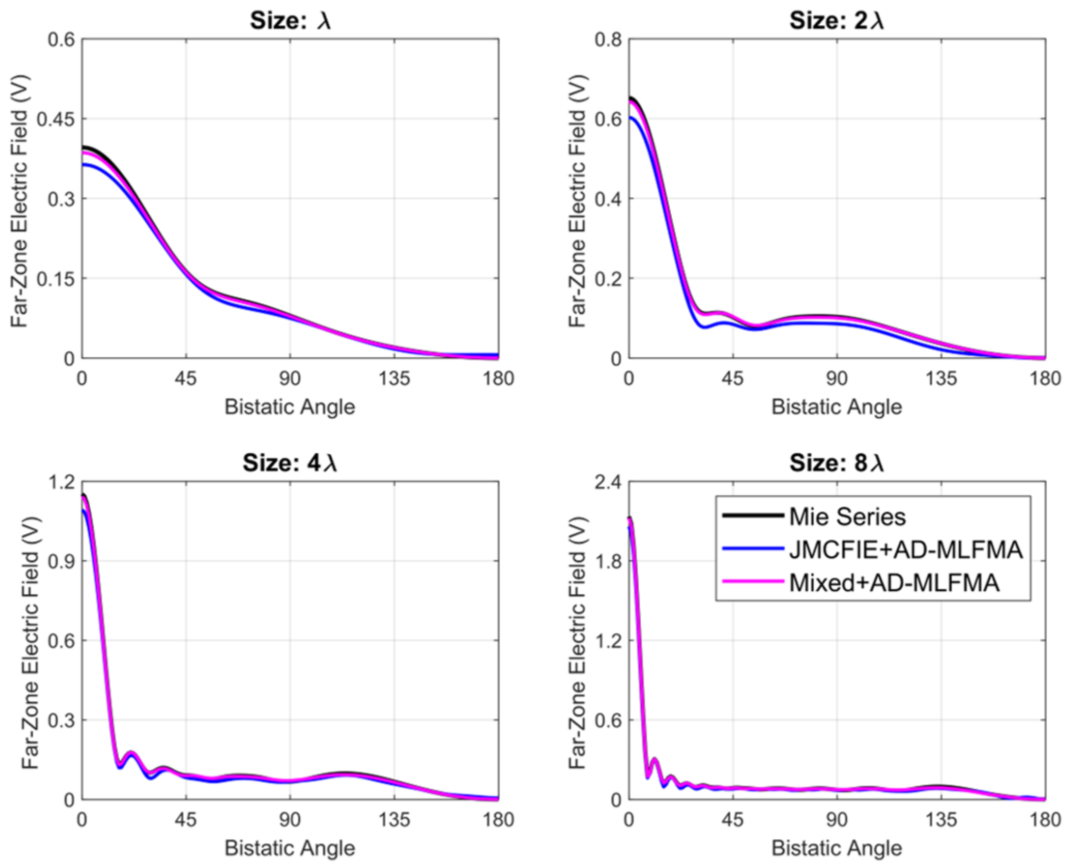

Figure 2.18: Bistatic far-zone electric field intensity distributions obtained for the scattering problems involving NZI spheres with $\epsilon_z = 0.001$ and $\mu_z = 0.001$.

0.1, 0.01, 0.001, and 0.0001 are depicted in Figures 2.16–2.19, respectively. In the plots, the bistatic angle is from 0° (forward-scattering) to 180° (backscattering) on the E-plane. JMCFIE results are omitted in Figure 2.19 since they are iteratively non-convergent. In Figures 2.16 and 2.17, i.e., when the relative permittivity/permeability values are 0.1 and 0.01, respectively, we observe good accuracy of JMCFIE, being consistent with the new mixed formulation and Mie series. But, the inaccuracy issues of JMCFIE become clearly visible in Figure 2.18, i.e., when the relative permittivity and permeability become 0.001. On the other hand, the new mixed formulation is always consistent with the Mie series, even for small values of relative permittivity and permeability, as a clear demonstration of the superiority of this formulation together with the developed AD-MLFMA implementation.

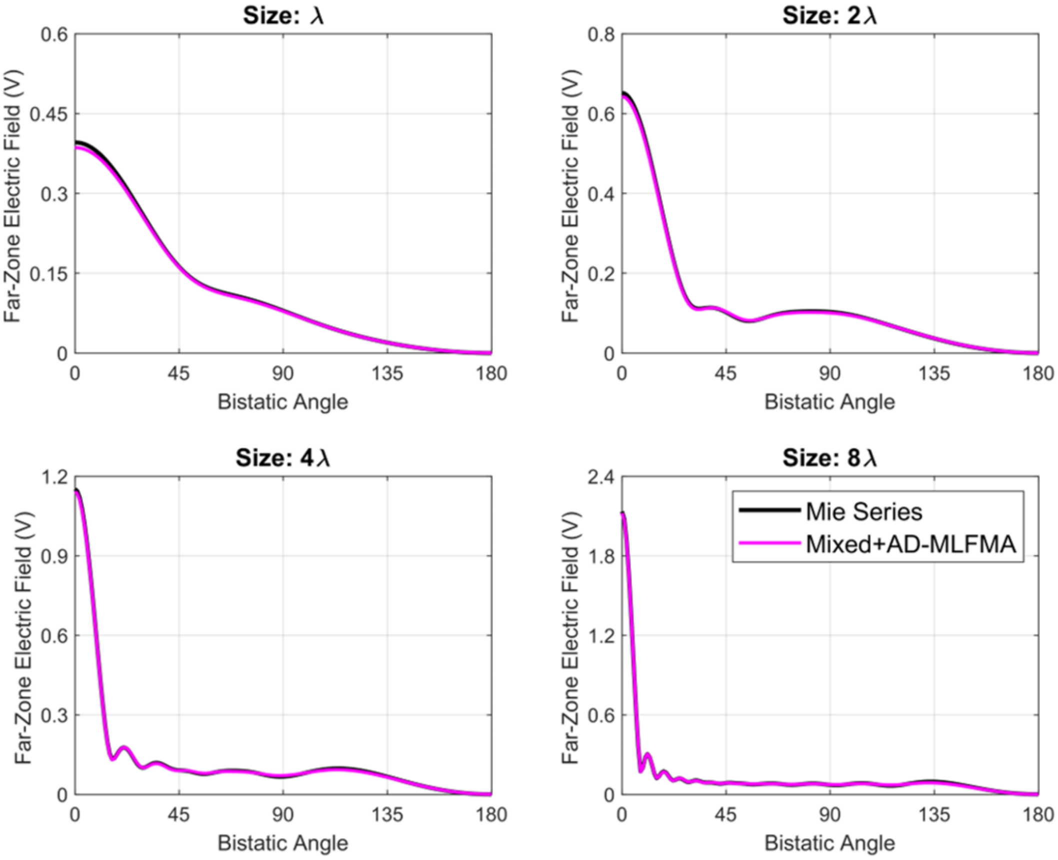

Figure 2.19: Bistatic far-zone electric field intensity distributions obtained for the scattering problems involving NZI spheres with $\epsilon_z = 0.0001$ and $\mu_z = 0.0001$.

2.2.2 Analysis of Exotic Lens Structures

To investigate the performance of the developed implementations further on realistic problems, NZI lens structures having different geometries and different relative permittivity and/or permeability values are analyzed by using JMCFIE and the new mixed formulations together with AD-MLFMA. Plane-wave illumination normally incident on the planar surfaces is considered in all problems, while the host medium is selected as vacuum.

The first lens geometry, which is constructed by a cylindrical extraction (1.25λ radius of curvature) from a $2\lambda \times \lambda \times 2\lambda$ block (λ is the wavelength in vacuum), is depicted in Figure 2.20. The number of unknowns for this lens geometry is 37,794 and four levels are used within AD-MLFMA. Figures 2.21–2.32 present the near-zone electric

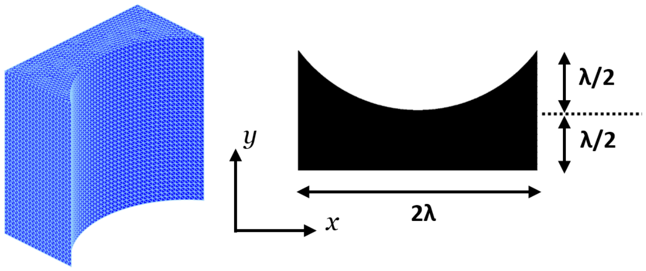

Figure 2.20: Illustration of a lens geometry (cylindrical extraction from a $2\lambda \times \lambda \times 2\lambda$ block) and its cross section.

field intensity (dBV/m) and magnetic field intensity (dBA/m) distributions, considering inner and outer equivalence plots as well as the overall plots, at the center cross section of the lens geometry on the E-plane for different relative permittivity and/or permeability values obtained by using JMCFIE and the new mixed formulations. In the absence of reference analytical solutions, the accuracy can be examined by observing inner and outer equivalence plots, i.e., by confirming small inner fields in the outer problems and small outer fields in the inner problems. For both formulations, good accuracy is verified in Figures 2.21–2.32.

Figures 2.21 and 2.22 show the results for the lens structure in Figure 2.20 when the relative permittivity and permeability values are equal to 0.1, obtained by the new mixed formulation and JMCFIE, respectively. The two formulations have similar results in terms of field distributions and numbers of iterations (120 and 143 iterations, respectively). Figures 2.23 and 2.24 present the results when the relative permittivity and permeability values are equal to 0.01. Although the near-zone distributions seem similar for both formulations, the iteration count for JMCFIE is increased to 336, whereas the iteration count for the new mixed formulation remains only at 138.

Figures 2.25–2.26, and Figures 2.27–2.28 present the results for the MNZ cases when $\mu_z = 0.1$ and $\mu_z = 0.01$, respectively. For $\mu_z = 0.1$, in addition to consistent field distributions, the numbers of iterations required by JMCFIE and the new mixed formulations are 87 and 79, respectively. However, for the $\mu_z = 0.01$ case, inconsistencies are clearly visible between the field distributions provided by the formulations. We note that, since the iterative convergence is achieved within 201 iterations for JM-

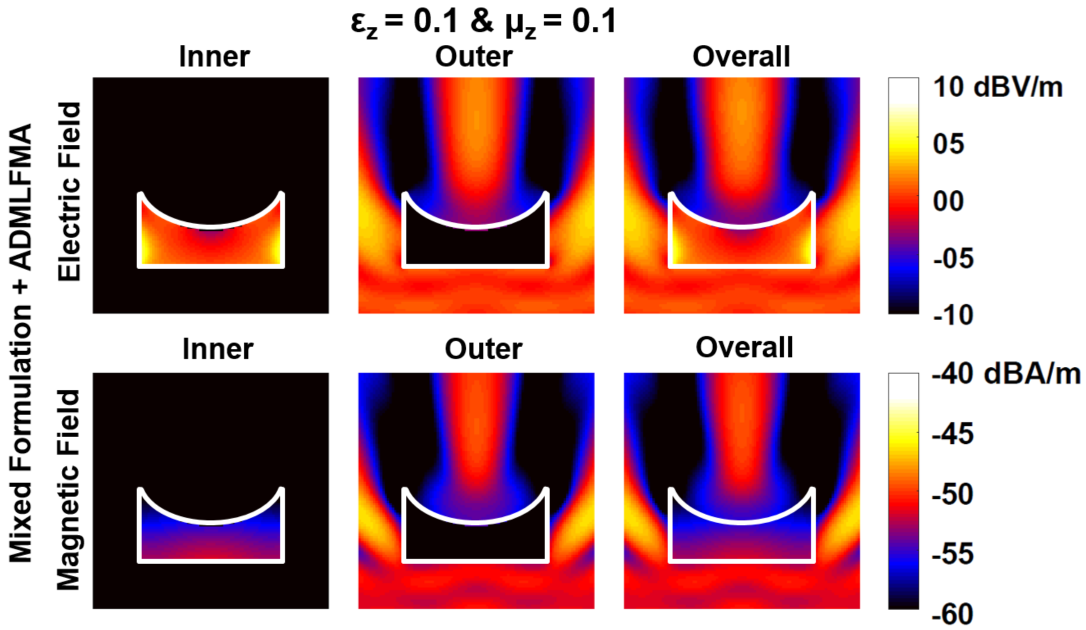

Figure 2.21: Near-zone electric field intensity (dBV/m) and magnetic field intensity (dBA/m) distributions for the NZI lens structure shown in Figure 2.20 with $\epsilon_z = 0.1$ and $\mu_z = 0.1$, obtained by the new mixed formulation.

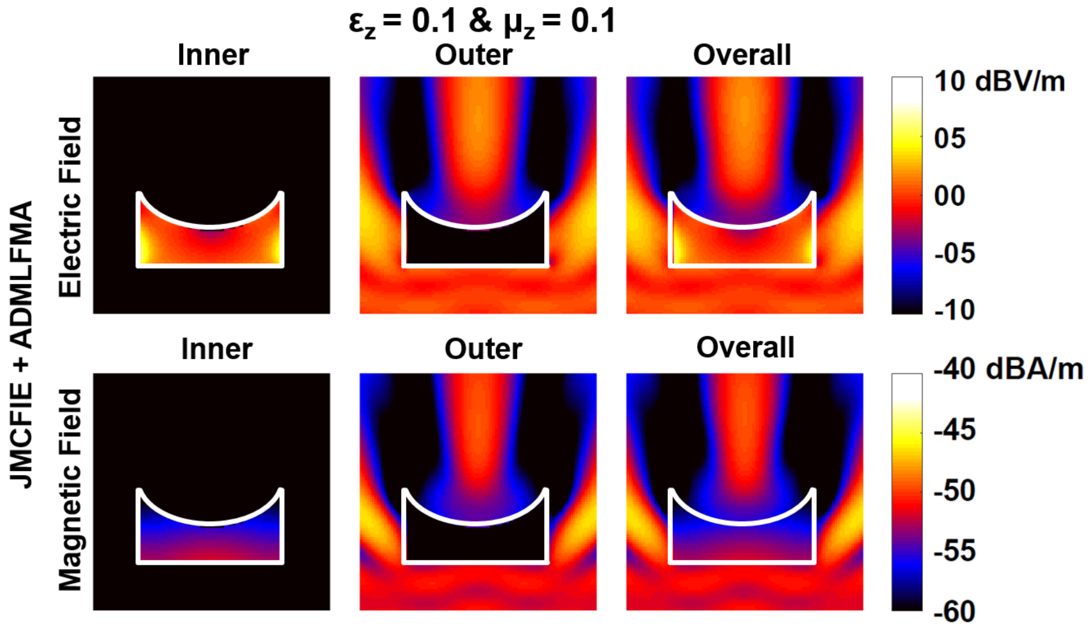

Figure 2.22: Near-zone electric field intensity (dBV/m) and magnetic field intensity (dBA/m) distributions for the NZI lens structure shown in Figure 2.20 with $\epsilon_z = 0.1$ and $\mu_z = 0.1$, obtained by the JMCFIE formulation.

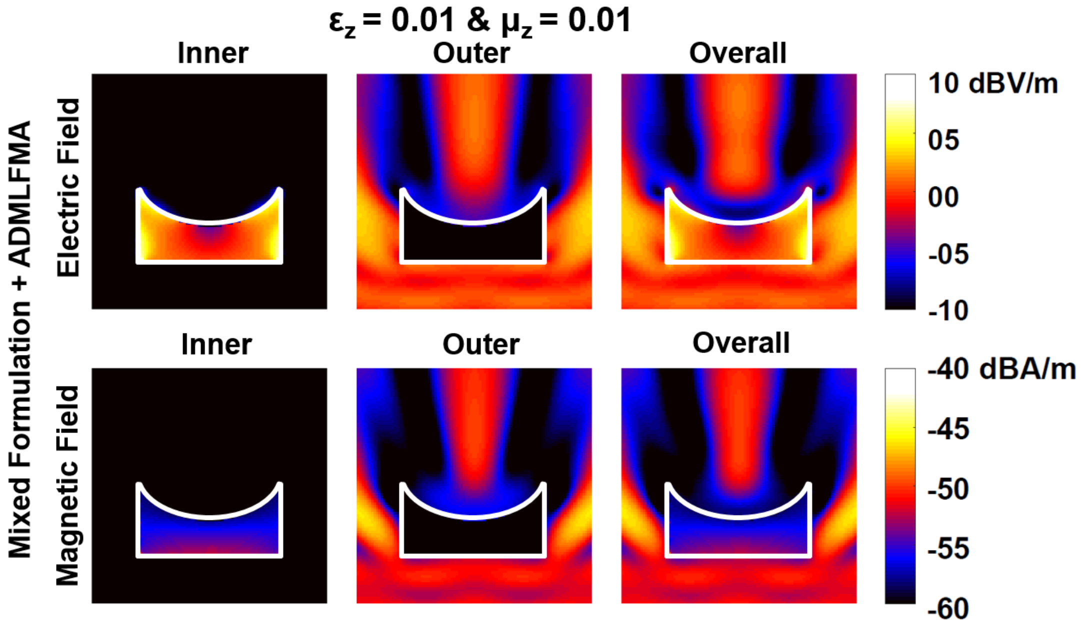

Figure 2.23: Near-zone electric field intensity (dBV/m) and magnetic field intensity (dBA/m) distributions for the NZI lens structure shown in Figure 2.20 with $\epsilon_z = 0.01$ and $\mu_z = 0.01$, obtained by the new mixed formulation.

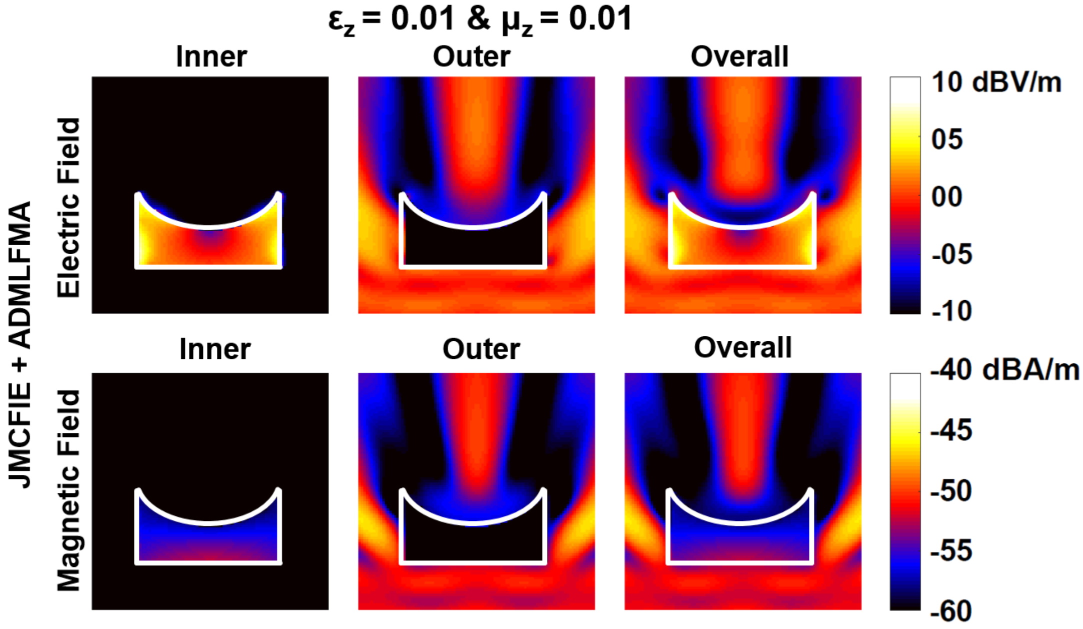

Figure 2.24: Near-zone electric field intensity (dBV/m) and magnetic field intensity (dBA/m) distributions for the NZI lens structure shown in Figure 2.20 with $\epsilon_z = 0.01$ and $\mu_z = 0.01$, obtained by the JMCFIE formulation.

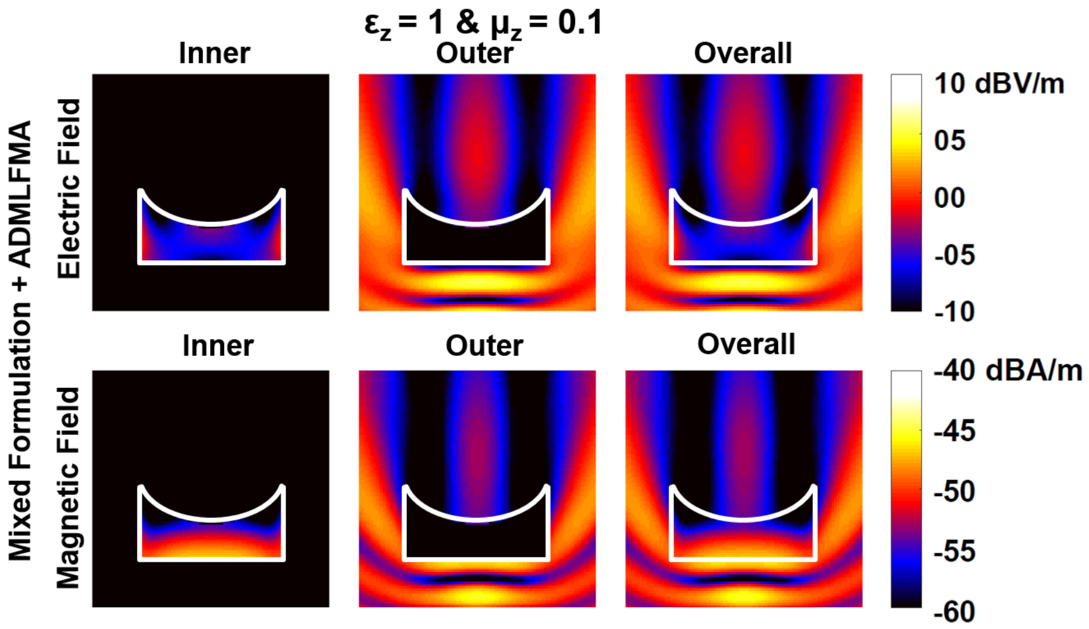

Figure 2.25: Near-zone electric field intensity (dBV/m) and magnetic field intensity (dBA/m) distributions for the NZI lens structure shown in Figure 2.20 with $\epsilon_z = 1$ and $\mu_z = 0.1$, obtained by the new mixed formulation.

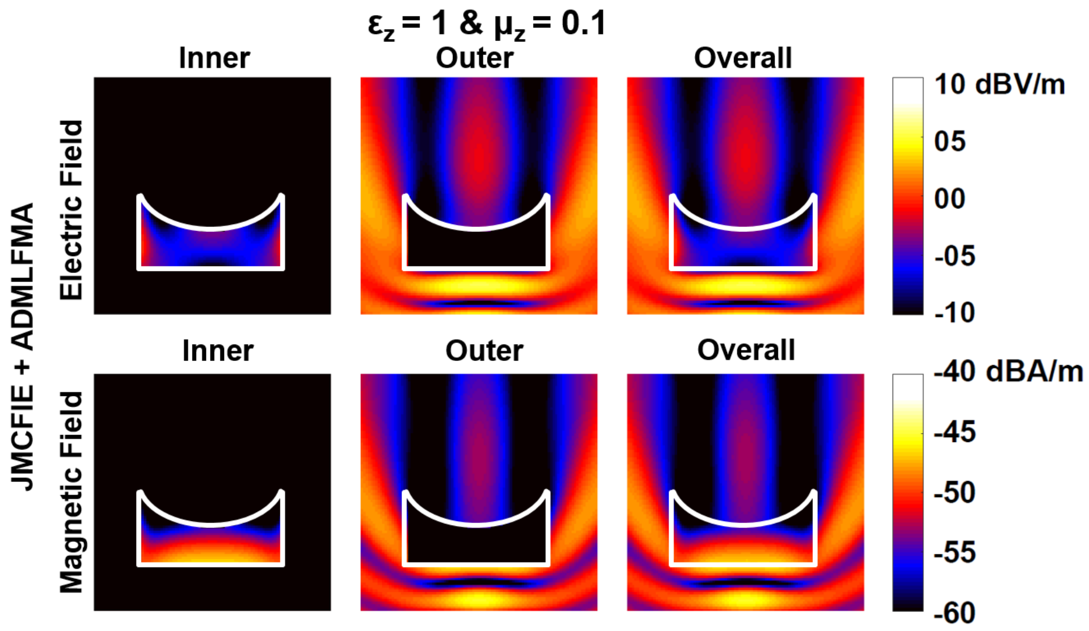

Figure 2.26: Near-zone electric field intensity (dBV/m) and magnetic field intensity (dBA/m) distributions for the NZI lens structure shown in Figure 2.20 with $\epsilon_z = 1$ and $\mu_z = 0.1$, obtained by the JMCFIE formulation.

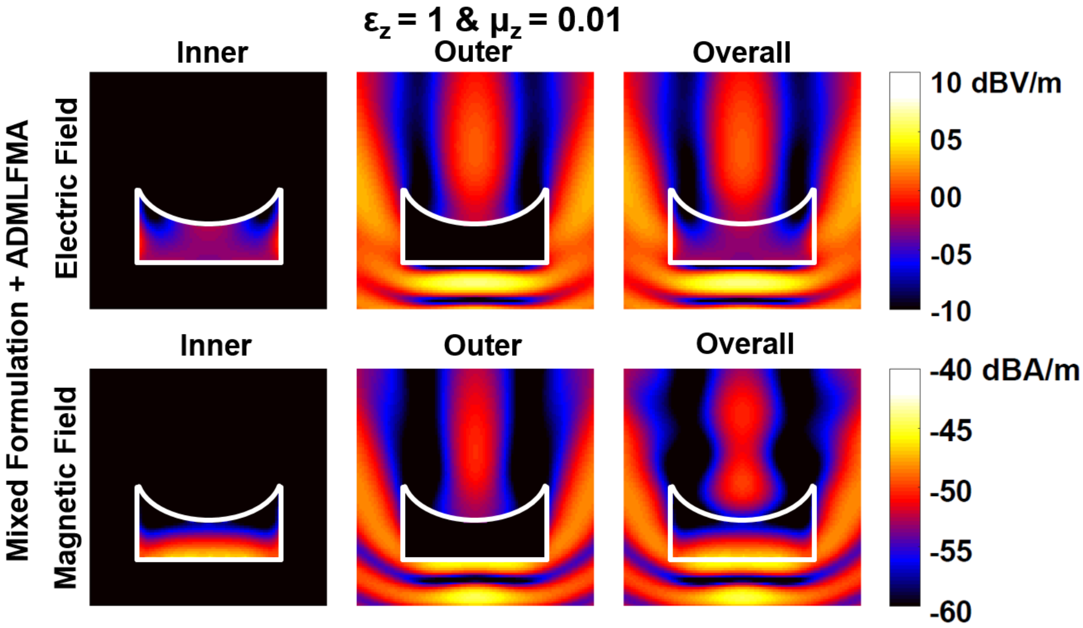

Figure 2.27: Near-zone electric field intensity (dBV/m) and magnetic field intensity (dBA/m) distributions for the NZI lens structure shown in Figure 2.20 with $\epsilon_z = 1$ and $\mu_z = 0.01$, obtained by the new mixed formulation.

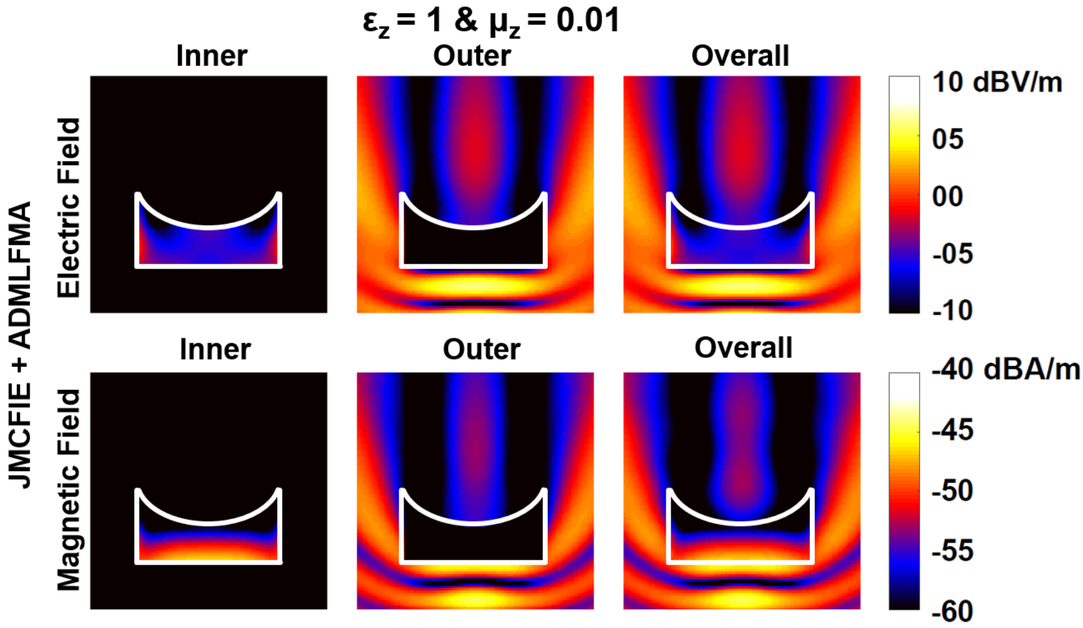

Figure 2.28: Near-zone electric field intensity (dBV/m) and magnetic field intensity (dBA/m) distributions for the NZI lens structure shown in Figure 2.20 with $\epsilon_z = 1$ and $\mu_z = 0.01$, obtained by the JMCFIE formulation.

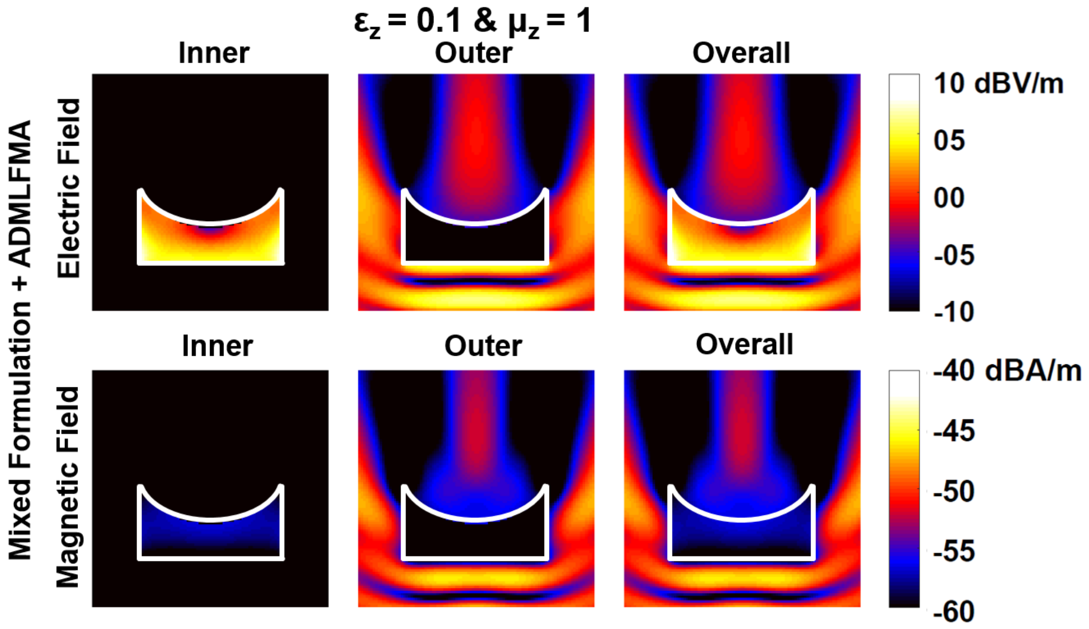

Figure 2.29: Near-zone electric field intensity (dBV/m) and magnetic field intensity (dBA/m) distributions for the NZI lens structure shown in Figure 2.20 with $\epsilon_z = 0.1$ and $\mu_z = 1$, obtained by the new mixed formulation.

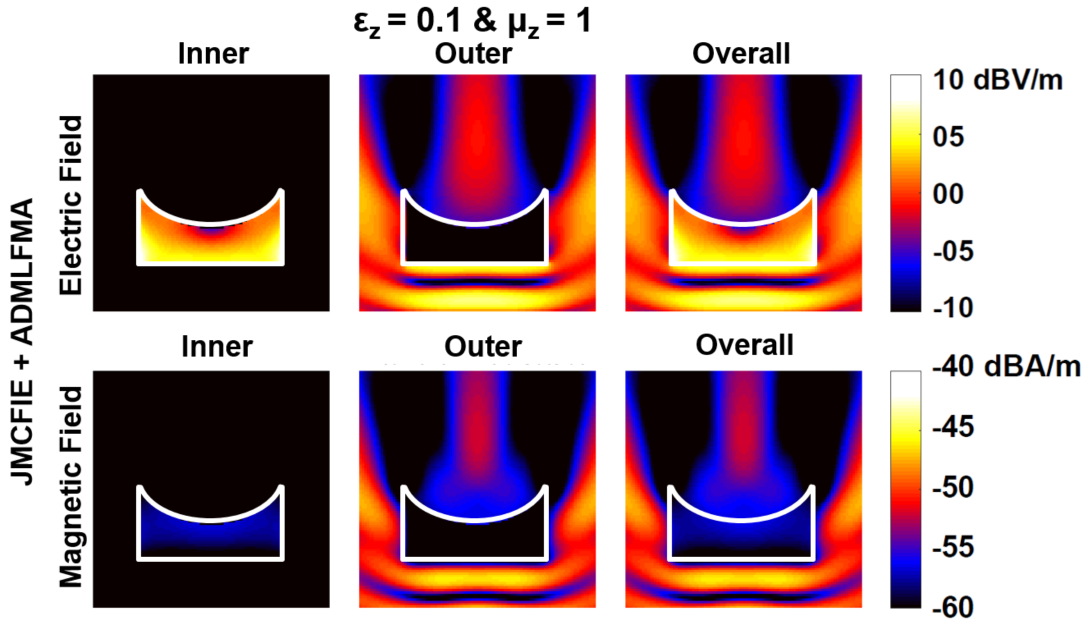

Figure 2.30: Near-zone electric field intensity (dBV/m) and magnetic field intensity (dBA/m) distributions for the NZI lens structure shown in Figure 2.20 with $\epsilon_z = 0.1$ and $\mu_z = 1$, obtained by the JMCFIE formulation.

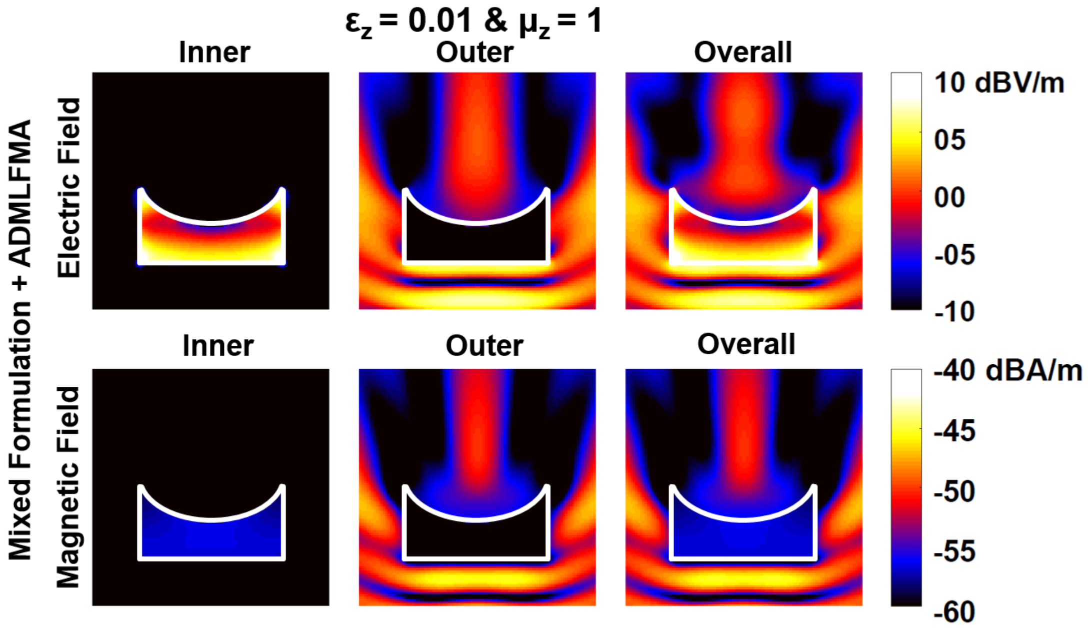

Figure 2.31: Near-zone electric field intensity (dBV/m) and magnetic field intensity (dBA/m) distributions for the NZI lens structure shown in Figure 2.20 with $\epsilon_z = 0.01$ and $\mu_z = 1$, obtained by the new mixed formulation.

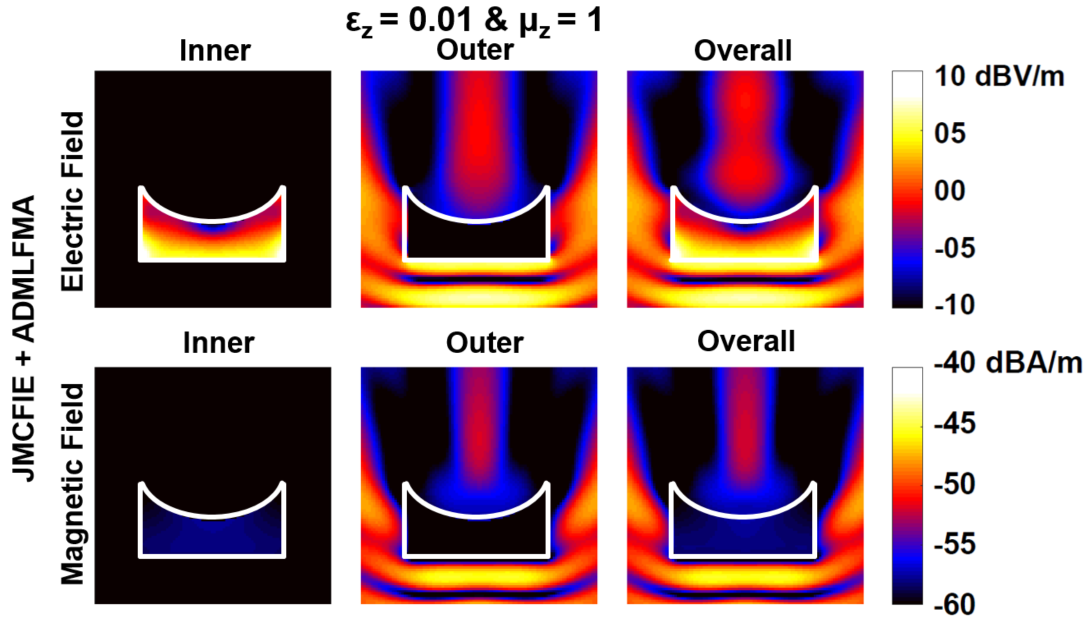

Figure 2.32: Near-zone electric field intensity (dBV/m) and magnetic field intensity (dBA/m) distributions for the NZI lens structure shown in Figure 2.20 with $\epsilon_z = 0.01$ and $\mu_z = 1$, obtained by the JMCFIE formulation.

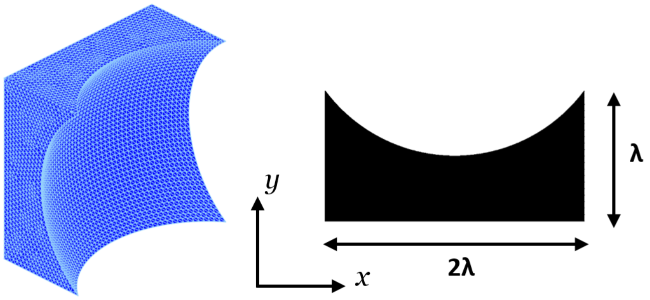

Figure 2.33: Illustration of a lens geometry (spherical extraction from a $2\lambda \times \lambda \times 2\lambda$ block) and its cross section.

CFIE, while the new mixed formulation converges in 123 iterations, JMCFIE is likely to be less accurate than the mixed one. Nevertheless, in both solutions, it is observed that outer magnetic fields in inner problems distort magnetic fields in overall plots, as seen in Figures 2.27 and 2.28.

Figures 2.29–2.30, and Figures 2.31–2.32 depict the results for the ENZ problems with $\epsilon_z = 0.1$ and $\epsilon_z = 0.01$, respectively. As in the MNZ results, consistent solutions are obtained for the $\epsilon_z = 0.1$ case, while inconsistent solutions are encountered for the $\epsilon_z = 0.01$ case using JMCFIE and the new mixed formulations. It is remarkable that, for $\epsilon_z = 0.01$ case, the iteration count for the new mixed formulation (128) is again almost half of that of JMCFIE (214). At the same time, for this case, it is observed that outer electric fields in inner problems distort electric fields in overall plots, as seen in Figures 2.31 and 2.32.

Figure 2.33 shows another lens geometry, which is constructed by a spherical extraction (2.5625λ radius of curvature) from a $2\lambda \times \lambda \times 2\lambda$ block. The number of unknowns for this structure is 37,794 and four levels are used within AD-MLFMA. The power density (dBW/m^2) distributions for the lens structures in Figures 2.20 and 2.33 with different relative permittivity and/or permeability values are depicted in Figure 2.34. For both geometries, the focusing ability of the lenses improves with decreasing relative permittivity and permeability values. In addition, due to reflections, the ENZ and MNZ lens structures demonstrate reduced focusing ability, whereas no reflection is observed for the cases with relative permittivity and permeability values

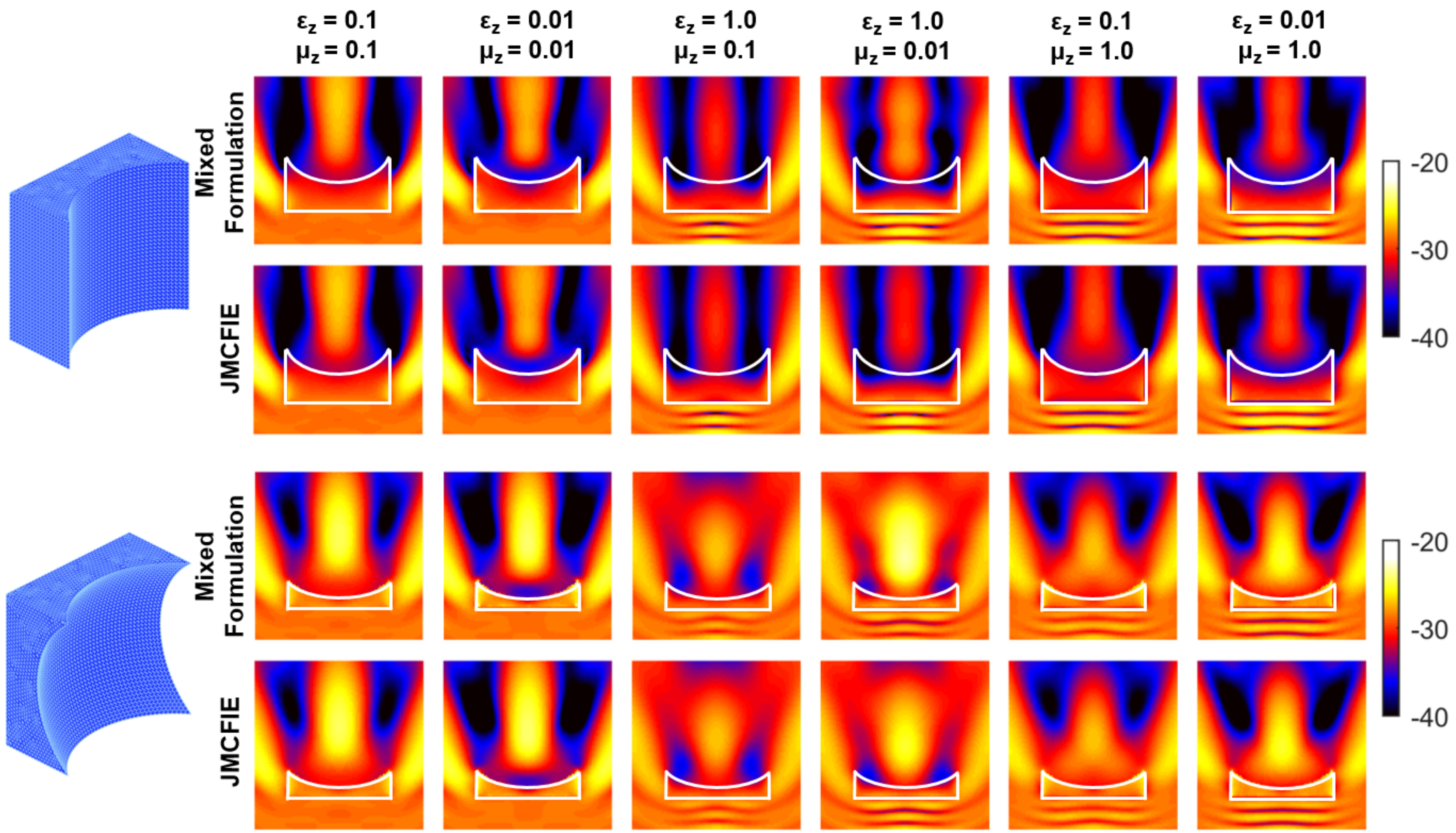

Figure 2.34: Near-zone power density (dBW/m^2) distributions for the NZI lens structures shown in Figures 2.20 and 2.33, obtained by using the new mixed and JMCFIE formulations.

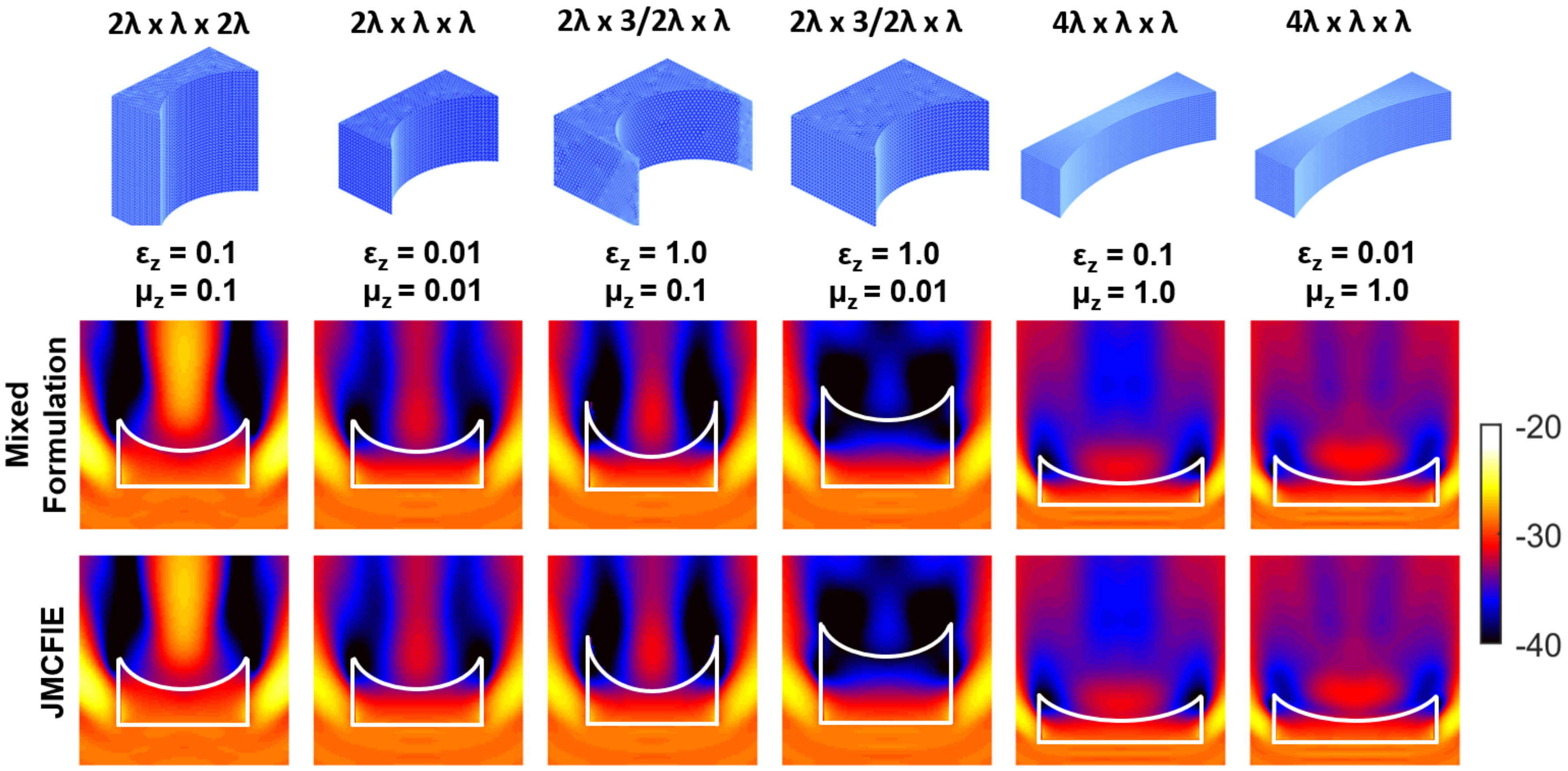

Figure 2.35: Near-zone power density (dBW/m^2) distributions for different NZI lens structures using the new mixed and JMCFIE formulations.

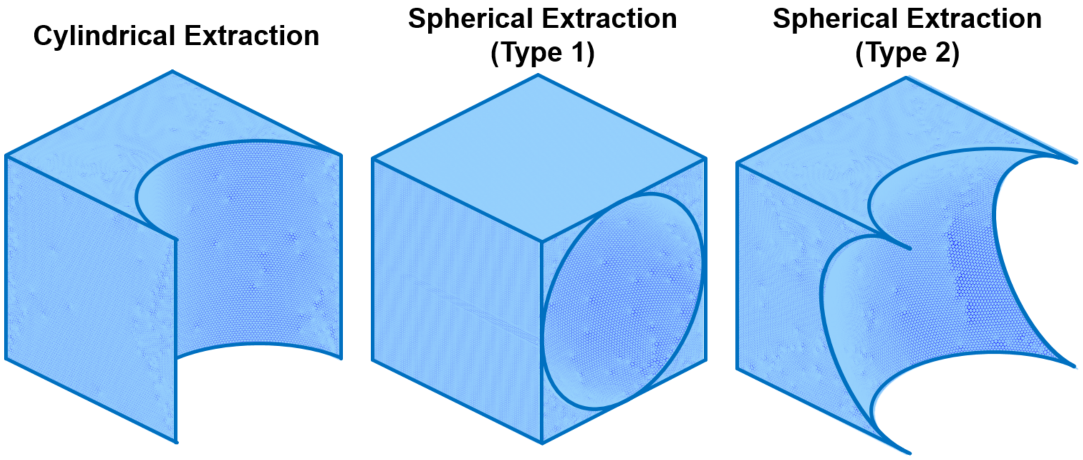

Figure 2.36: Large-scale NZI lens structures.

equally near-zero. For only the MNZ case with $\mu_z = 0.01$, discrepancies between JMCFIE and the new mixed formulations can be observed for both lens structures. For the second lens structure with this particular material properties, the new mixed formulation and JMCFIE converge in 133 and 250 iterations, respectively, supporting the accuracy of the mixed formulation.

For comparisons of different lens structures, Figure 2.35 presents the power density (dBW/m^2) distributions for five different designs with different permittivity and/or permeability values. From left-hand side to right-hand side in Figure 2.35, the first one is the lens structure shown in Figure 2.20, the second one is constructed by a cylindrical extraction (1.25λ radius of curvature) from a $2\lambda \times \lambda \times \lambda$ block, the third one is constructed by a cylindrical extraction (1λ radius of curvature) from a $2\lambda \times 1.5\lambda \times \lambda$ block, the fourth one is constructed by a cylindrical extraction (1.25λ radius of curvature) from a $2\lambda \times 1.5\lambda \times \lambda$ block, and the fifth one is constructed by a cylindrical extraction (4.25λ radius of curvature) from a $4\lambda \times \lambda \times \lambda$ block. The fourth lens structure has the weakest focusing ability, leading to a deep shadow in the transmission region. Among others, the first structure creates the strongest power density values, while the short distance focus of the fifth structure is also remarkable.

Next, large-scale NZI lens structures are considered in order to test the performances of the implementations based on AD-MLFMA. Figure 2.36 depicts three large-scale

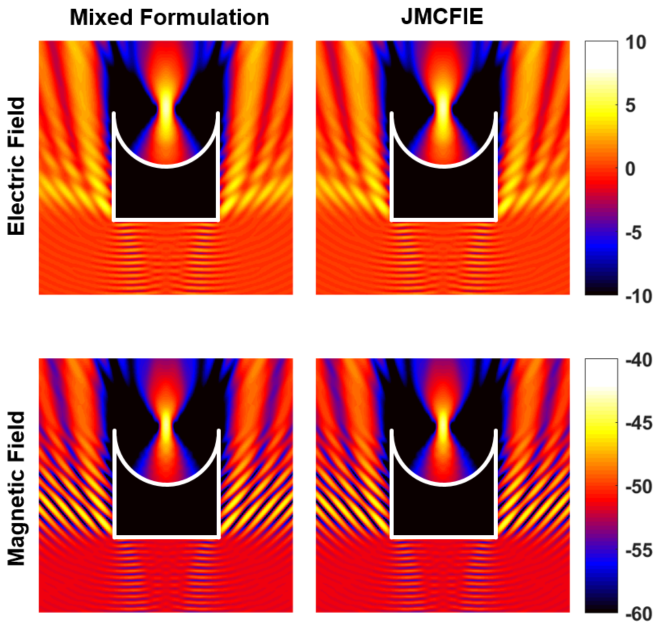

Figure 2.37: Near-zone field intensity distributions for the $8\lambda \times 8\lambda \times 8\lambda$ lens structure shown in Figure 2.36 (left) with $\epsilon_z = 0.1$ and $\mu_z = 0.1$, obtained by JMCFIE and the new mixed formulations.

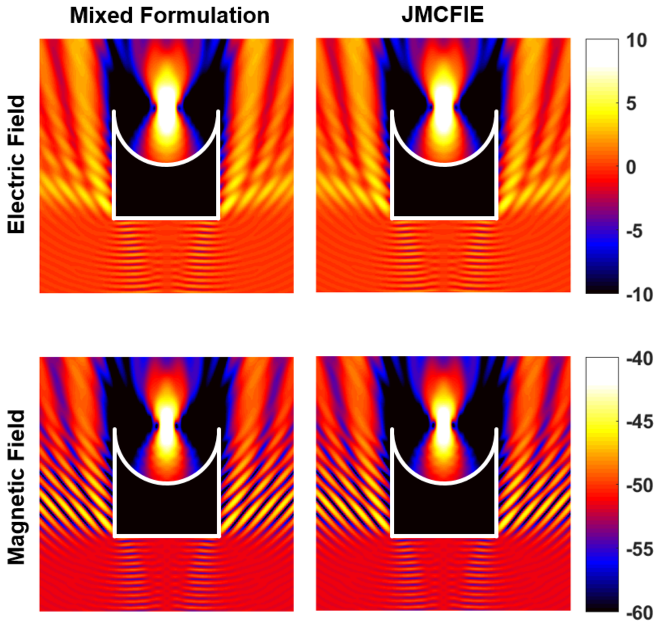

Figure 2.38: Near-zone field intensity distributions for the $8\lambda \times 8\lambda \times 8\lambda$ lens structure shown in Figure 2.36 (middle) with $\epsilon_z = 0.1$ and $\mu_z = 0.1$, obtained by JMCFIE and the new mixed formulations.

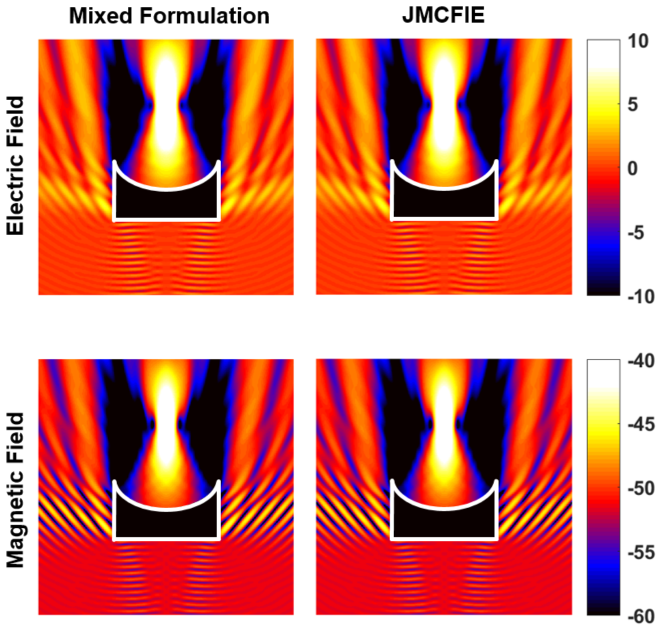

Figure 2.39: Near-zone field intensity distributions for the $8\lambda \times 8\lambda \times 8\lambda$ lens structure shown in Figure 2.36 (right) with $\epsilon_z = 0.1$ and $\mu_z = 0.1$, obtained by JMCFIE and the new mixed formulations.

NZI lens structures. All three lens structures are obtained by extractions from $8\lambda \times 8\lambda \times 8\lambda$ blocks. From left-hand side to right-hand side in Figure 2.36, the first one is constructed by a cylindrical extraction (4λ radius of curvature), the second one is constructed by a spherical extraction (4λ radius of curvature), and the third one is constructed by a spherical extraction ($4\sqrt{2}\lambda$ radius of curvature). From left to right in Figure 2.36, the structures are discretized with 255,882, 341,706, and 209,460 unknowns, respectively, while six levels are used within AD-MLFMA. Figures 2.37–2.39 present the outer near-zone electric field intensity and magnetic field intensity distributions when the lens structures have $\epsilon_z = 0.1$ and $\mu_z = 0.1$, where focusing characteristics are clearly observed. In Figure 2.40, the near-zone power density distributions for these three lens structures are further depicted. It is observed that the focusing behavior of a lens structure strongly depends on the geometry. Iterative solution histories to obtain the results in Figures 2.37–2.40 are shown in Figure 2.41. For the lens structure with cylindrical extraction, the JMCFIE formulation converges in 262 iterations, while the new mixed formulation converges in 186 iterations. Similarly, for the first type lens structure with spherical extraction, JMCFIE and the new

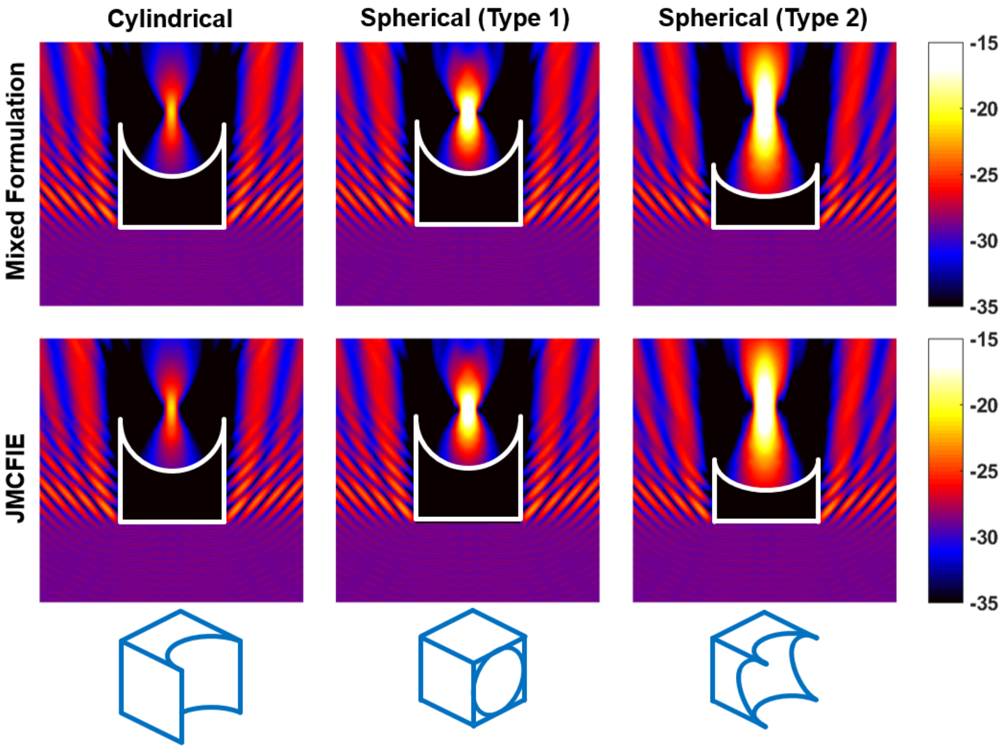

Figure 2.40: Near-zone power density distributions for the $8\lambda\times8\lambda\times8\lambda$ lens structures in Figure 2.36 with $\epsilon_z = 0.1$ and $\mu_z = 0.1$, obtained by JMCFIE and the new mixed formulations.

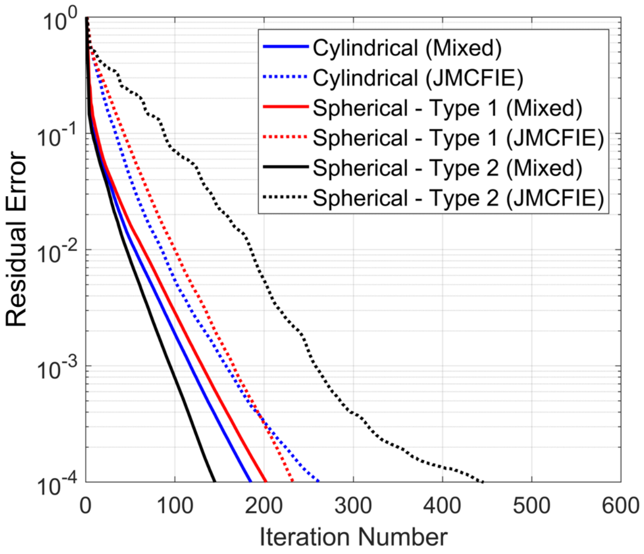

Figure 2.41: Iterative solutions of the $8\lambda \times 8\lambda \times 8\lambda$ lens structures in Figure 2.36 with $\epsilon_z = 0.1$ and $\mu_z = 0.1$, when using JMCFIE and the new mixed formulations.

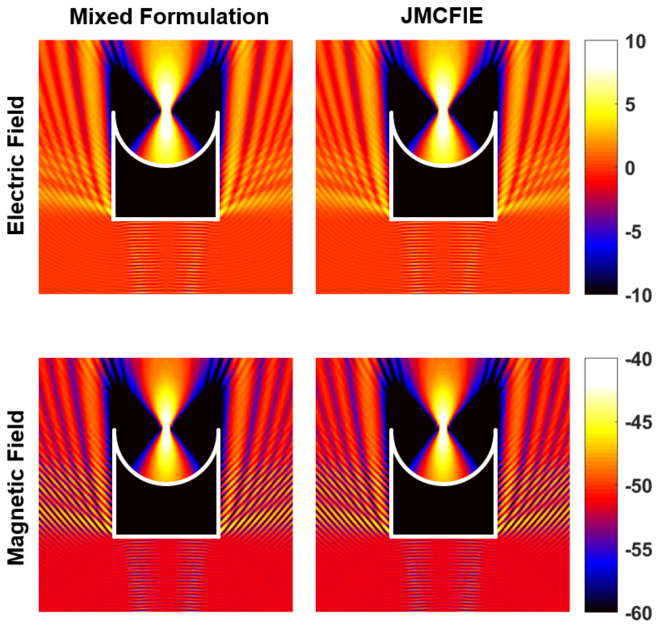

Figure 2.42: Near-zone field intensity distributions for the $16\lambda \times 16\lambda \times 16\lambda$ lens structure in Figure 2.36 (left) with $\epsilon_z = 0.1$ and $\mu_z = 0.1$, obtained by JMCFIE and the new mixed formulations.

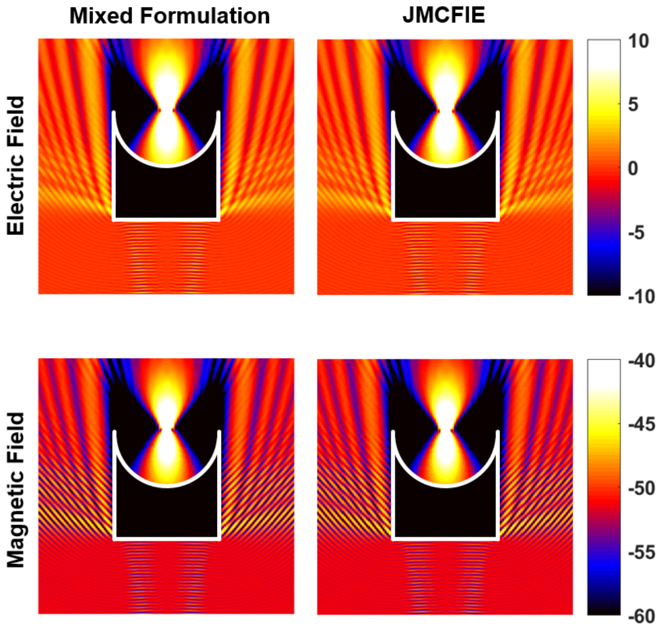

Figure 2.43: Near-zone field intensity distributions for the $16\lambda \times 16\lambda \times 16\lambda$ lens structure in Figure 2.36 (middle) with $\epsilon_z = 0.1$ and $\mu_z = 0.1$, obtained by JMCFIE and the new mixed formulations.

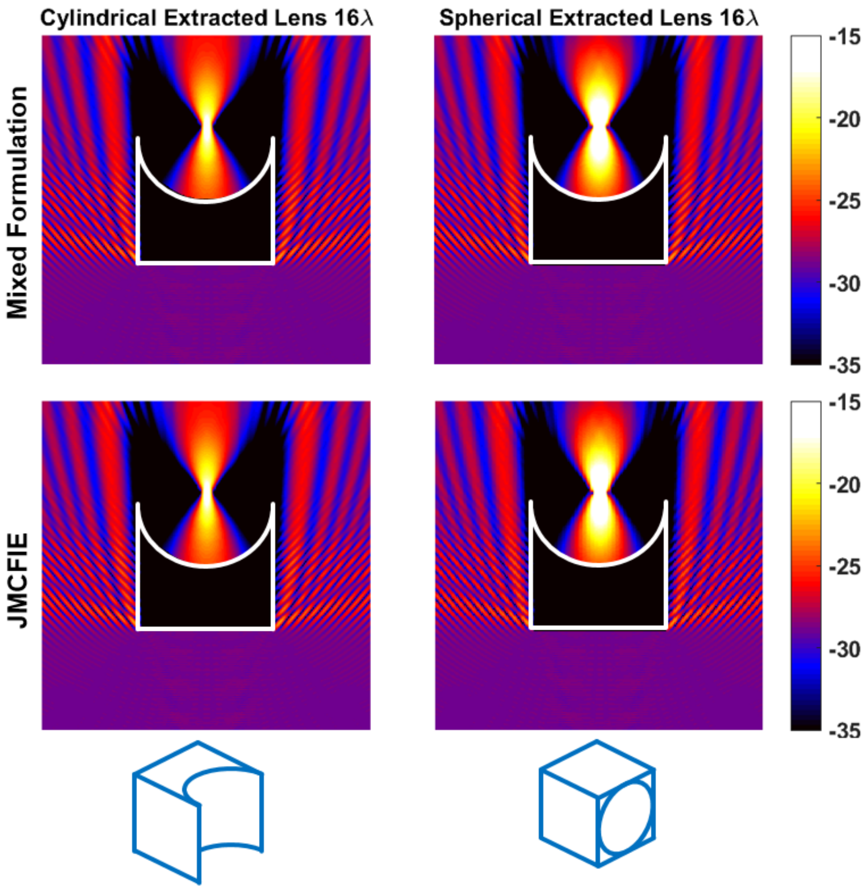

Figure 2.44: Near-zone power density distributions for the $16\lambda \times 16\lambda \times 16\lambda$ lens structures in Figure 2.36 with $\epsilon_z = 0.1$ and $\mu_z = 0.1$, obtained by JMCFIE and the new mixed formulations.

mixed formulations converge in 233 and 203 iterations, respectively. The advantage of the mixed formulation becomes clear for the second type lens structure with spherical extraction, for which the new mixed formulation requires 145 iterations, whereas the JMCFIE formulation requires 446 iterations (more than three times).

Besides the 8λ-sized lens structures, more challenging 16λ-sized lens structures are investigated. The structures with cylindrical extraction (see Figure 2.36, left) and spherical extraction of the first type (see Figure 2.36, middle) are discretized with 1,017,510, and 1,359,546 unknowns, respectively, while seven levels are used within AD-MLFMA. Near-zone outer field intensity distributions obtained for $\epsilon_z = 0.1$ and $\mu_z = 0.1$ demonstrate good focusing characteristics as depicted in Figures 2.42 and 2.43. In Figure 2.44, the near-zone power density distributions approve the strong de-

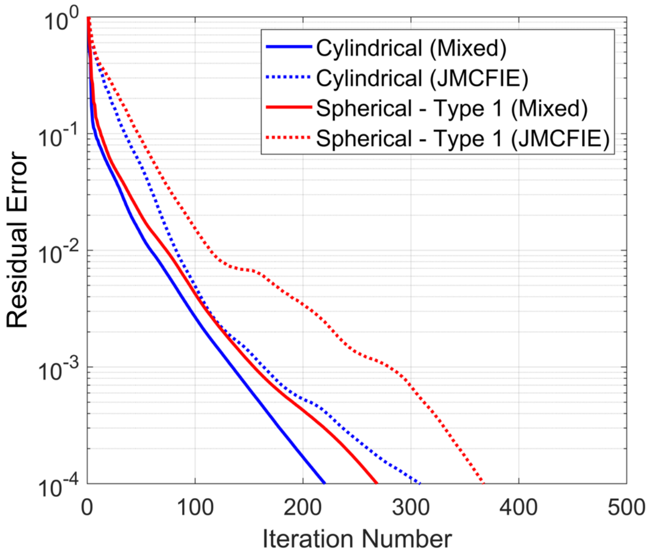

Figure 2.45: Iterative solutions for the $16\lambda \times 16\lambda \times 16\lambda$ lens structures in Figure 2.36 with $\epsilon_z = 0.1$ and $\mu_z = 0.1$, when using JMCFIE and the new mixed formulations.

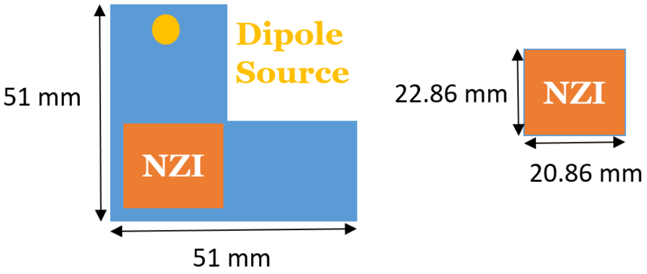

Figure 2.46: Dimensions of a composite structure involving a WR90-sized waveguide with a sharp corner and an NZI region at the corner of the waveguide.

pendence of the focusing ability to geometry. Iterative solutions of the 16λ-sized lens structures are shown in Figure 2.45. For the lens structure with cylindrical extraction, JMCFIE and the new mixed formulations require 309 and 221 iterations (performed in 141 and 103 hours on a single core), respectively, whereas they require 368 and 269 iterations (230 and 166 hours on a single core), respectively, for the lens structure with spherical extraction of the first type.

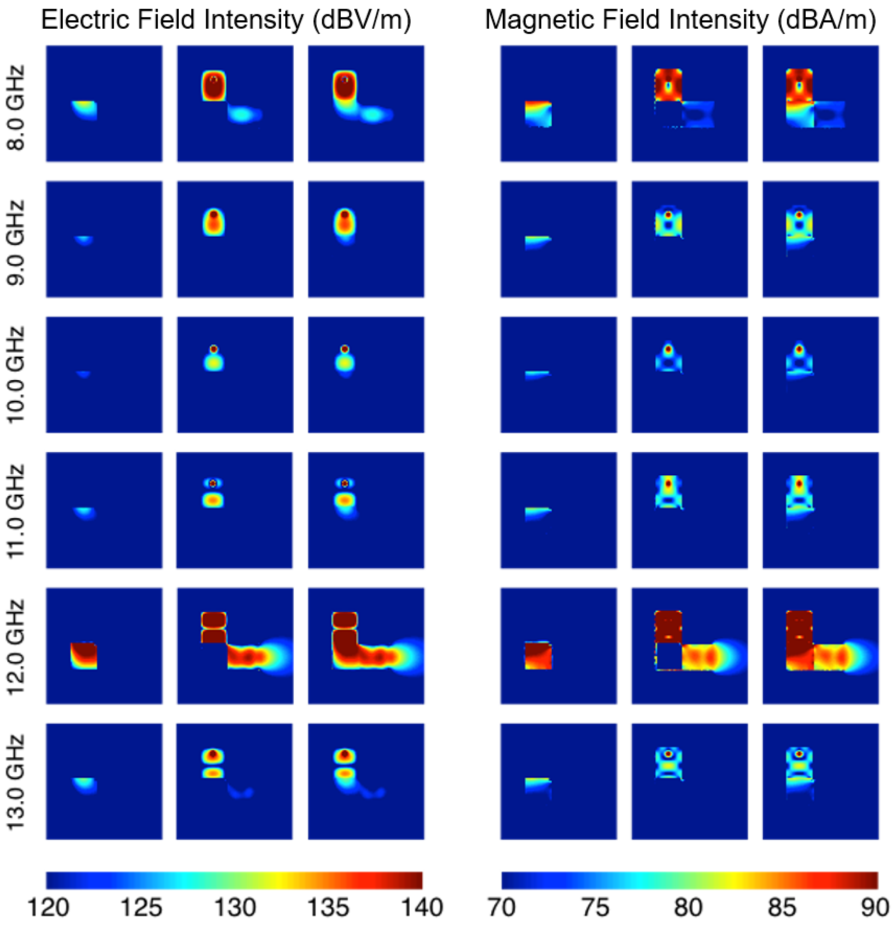

Figure 2.47: Near-zone field intensity distributions for the composite structure in Figure 2.46 involving a WR90-sized waveguide having a sharp corner. One side of the waveguide is open. An EMNZ block is placed at the corner of the waveguide.

2.2.3 Analysis of Waveguide Structures with Sharp Corners

As another class of interesting applications, computational simulations of two composite structures involving WR-90-sized waveguides with sharp corners and NZI materials are presented [64]. The walls of the waveguides are modelled as zero-thickness PEC surfaces. The composite structures are located in free space and Hertzian dipole sources near the closed sides of waveguides are used as excitations, while the other sides are kept open. JMCFIE is used as the formulation. Figure 2.46 depicts the first composite structure involving a waveguide with a sharp corner and an NZI region inside the waveguide at the corner. In Figures 2.47–2.49, the near-zone electric field intensity and magnetic field intensity distributions shown for the NZI blocks (first col-

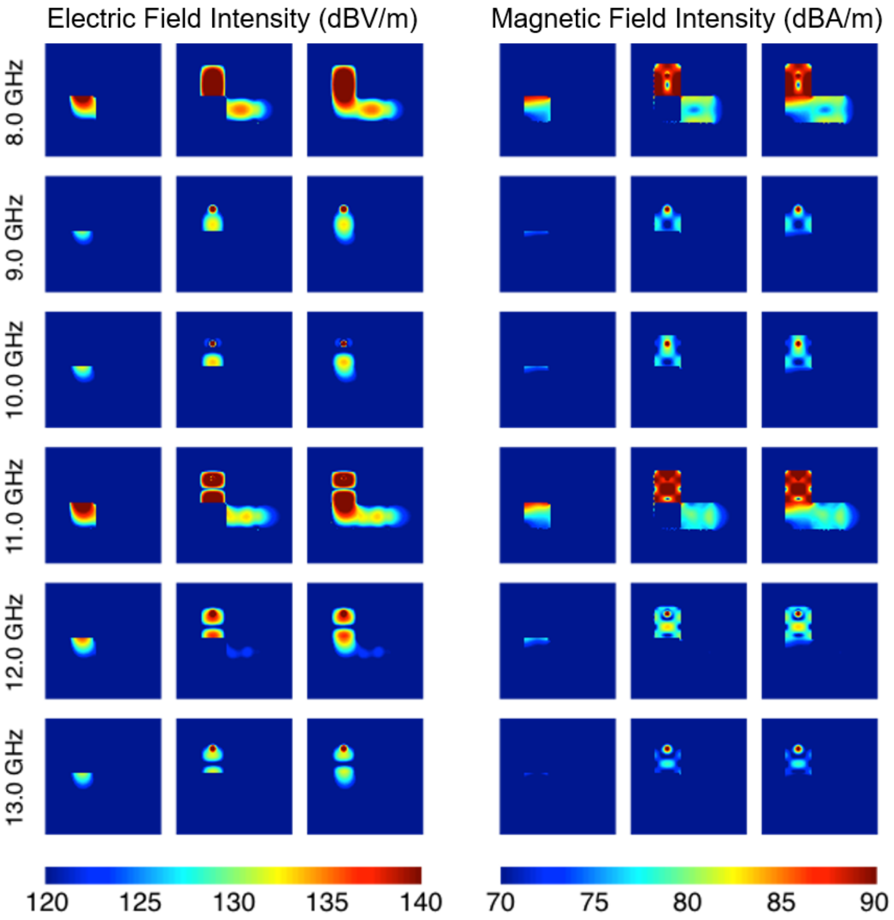

Figure 2.48: Near-zone field intensity distributions for the composite structure in Figure 2.46 involving a WR90-sized waveguide having a sharp corner. One side of the waveguide is open. An ENZ block is placed at the corner of the waveguide.

umn), waveguides (second column), as well as overall problems (third column) when using EMNZ (0.1 relative permittivity and permeability), ENZ (0.1 relative permittivity), and MNZ (0.1 relative permeability) blocks demonstrate the accuracy of the solutions at different frequencies. We note that the NZI blocks are used to enhance the transmission through the waveguide with sharp corner. Figures 2.50–2.52 present the near-zone field intensity and power density distributions for the structure without a block and with ENZ, MNZ, and EMNZ blocks that are placed at the corner at different frequencies. In general, the transmission is improved by using ENZ, MNZ, and EMNZ blocks, depending on the frequency. It is also remarkable that the transmission is more stable in the entire frequency range when using the MNZ block.

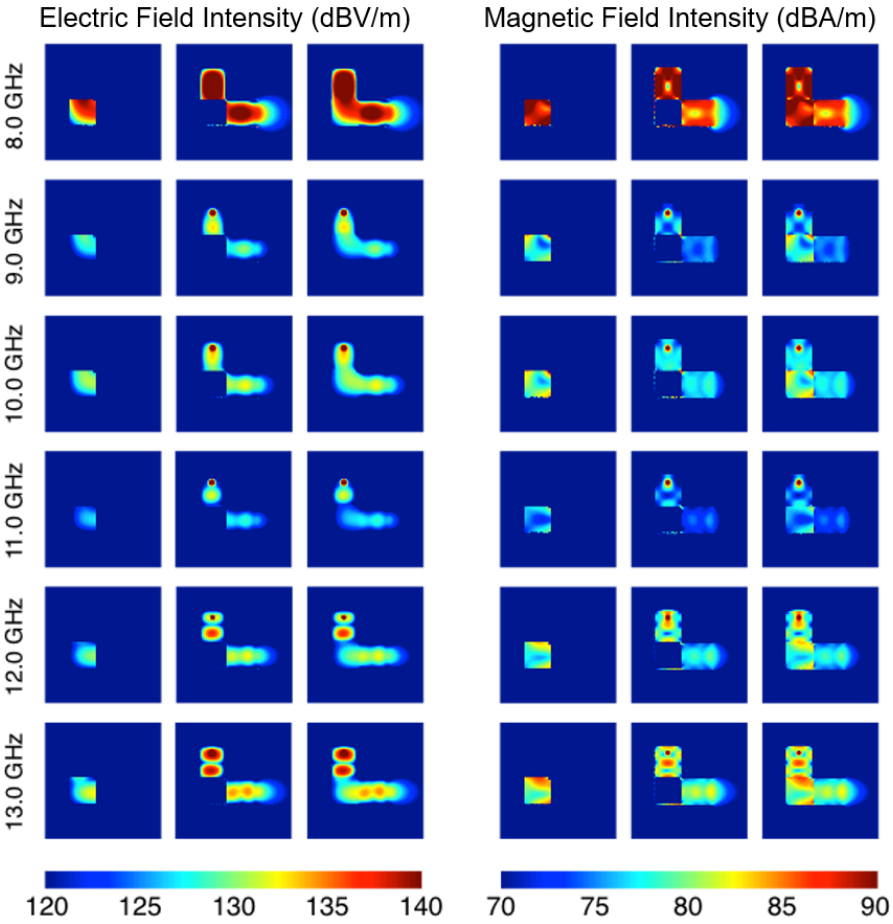

Figure 2.49: Near-zone field intensity distributions for the composite structure in Figure 2.46 involving a WR90-sized waveguide having a sharp corner. One side of the waveguide is open. An MNZ block is placed at the corner of the waveguide.

The second composite structure involves a WR90-sized waveguide with three sharp corners and an NZI region at the middle as depicted in Figure 2.53. Figure 2.54 presents the near-zone electric field intensity and magnetic field intensity distributions with and without an MNZ block. We note that the MNZ material covers 3/5 of the overall waveguide structure. It is observed that the transmission is clearly improved at 9.5 GHz, 11.5 GHz, 12.0 GHz, 12.5 GHz, and 13.0 GHz by using the MNZ block.

Numerical experiments presented above clearly demonstrate the need for computational techniques in order to design effective NZI fillings to improve transmission through bent waveguides. The electromagnetic responses of the structures depend on

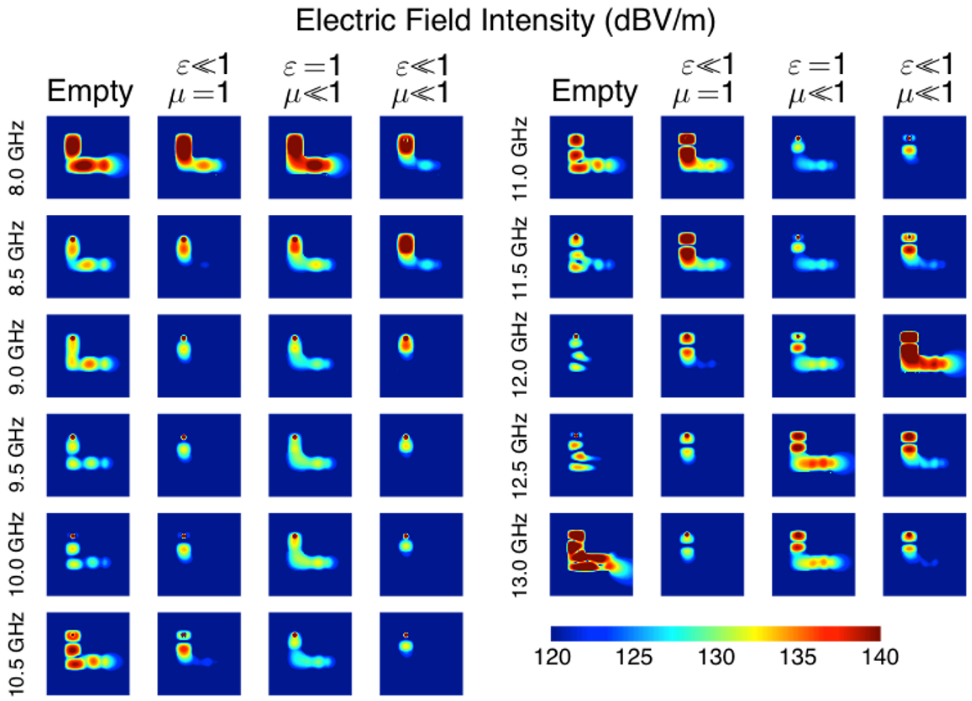

Figure 2.50: Near-zone electric field intensity distributions for the composite structure in Figure 2.46 without a block and with ENZ, MNZ, and EMNZ blocks at the corner.

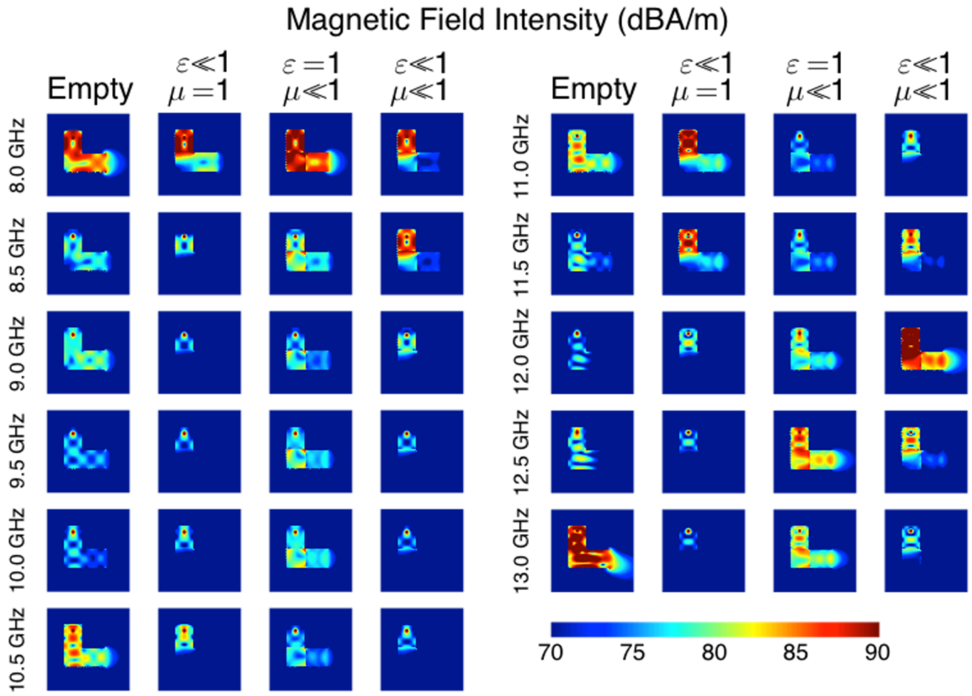

Figure 2.51: Near-zone magnetic field intensity distributions for the composite structure in Figure 2.46 without a block and with ENZ, MNZ, and EMNZ blocks at the corner.

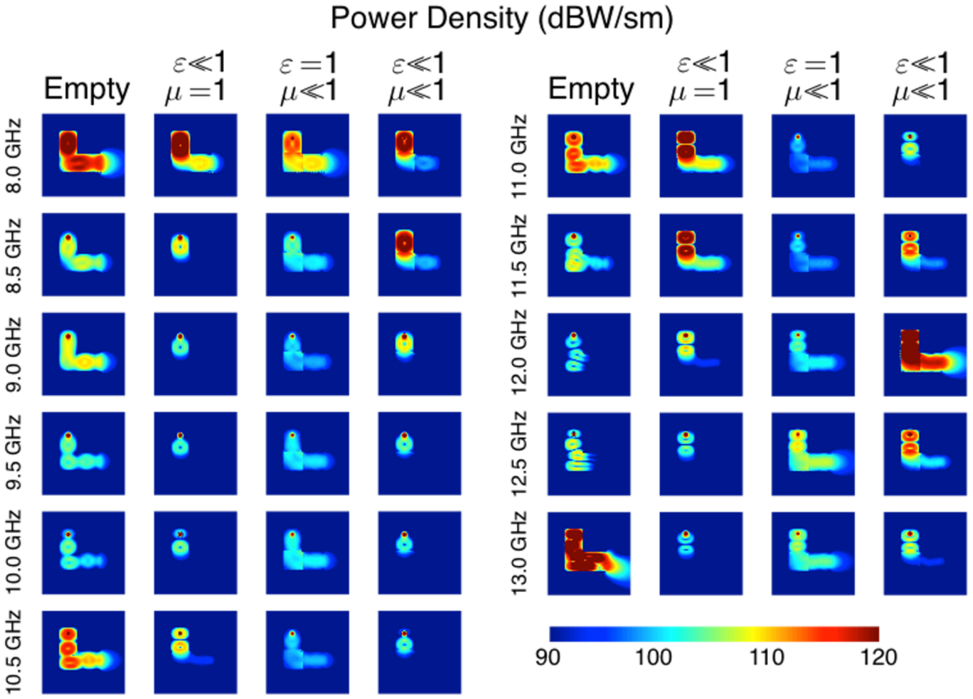

Figure 2.52: Near-zone power density distributions for the composite structure in Figure 2.46 without a block and with ENZ, MNZ, and EMNZ blocks at the corner.

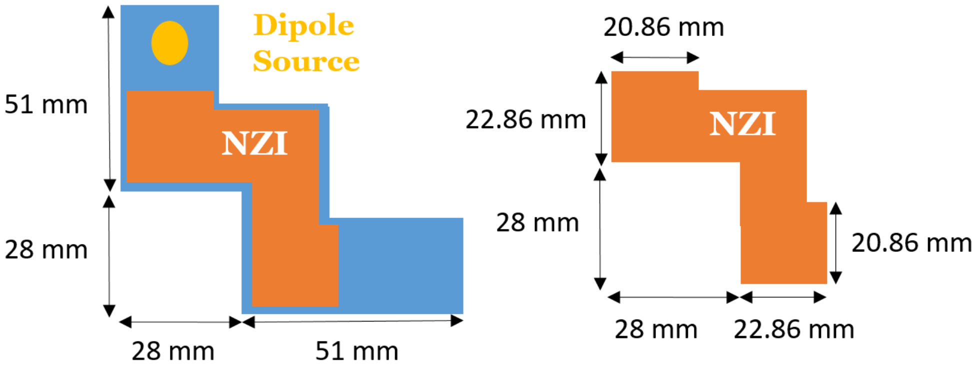
Dipole Source
NZI
51 mm
28 mm
28 mm
51 mm
20.86 mm
22.86 mm
NZI
28 mm
20.86 mm
28 mm
22.86 mm

Figure 2.53: Dimensions of a composite structure involving a WR90-sized waveguide with three sharp corners and an NZI region.

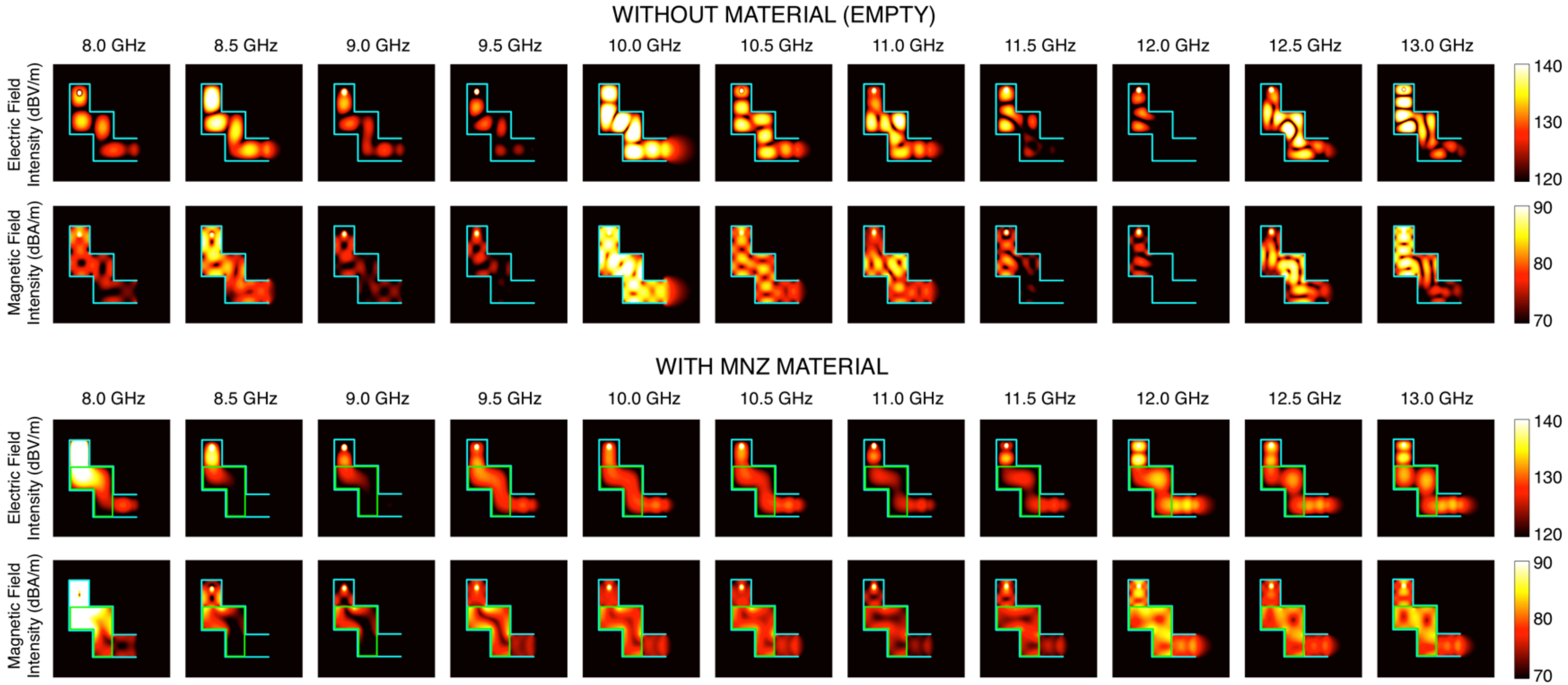

Figure 2.54: Near-zone field intensity distributions for the composite structure in Figure 2.53 involving a WR90-sized waveguide with three sharp corners. An MNZ block is placed inside the waveguide to improve the transmission.

the frequency and dimensions, as well as the material properties, that require extensive analysis to optimize the overall transmission capabilities.

2.3 Concluding Remarks

This chapter is devoted to full-wave simulations of three-dimensional structures involving NZI materials. In this context, accuracy and efficiency of the conventional and two new SIE formulations are particularly investigated. The results on both canonical and lens-like objects show that the numbers of iterations required for the new mixed formulation in wide ranges of near-zero permittivity and permeability values are remarkably small in comparison to all other formulations. Very limited increments in the iteration counts through electrically larger problems demonstrate the stability and reliability of the implementation based on the mixed formulation and AD-MFLMA. As opposed to other formulations, the new mixed formulation is always accurate, even for very small values of permittivity and permeability, as a clear demonstration of the superiority of this formulation together with AD-MLFMA. To investigate the performance of the developed implementations further on more realistic problems, computational simulations of two composite structures involving WR-90-sized waveguides with sharp corners and NZI materials are presented. In general, the transmission is improved by using ENZ, MNZ, and EMNZ blocks, depending on the frequency, while the transmission is more stable in the entire frequency range when using MNZ blocks.

CHAPTER 3

SIMULATION AND REALIZATION OF INKJET-PRINTED METAMATERIALS FOR MICROWAVE FREQUENCIES

Three-dimensional computational simulation and realization of metamaterial structures with different exotic properties, e.g., negative refractive index, at microwave frequencies are considered in this chapter. Following their numerical analysis, very low-cost inkjet printing method is used to fabricate these structures. A sensitivity analysis is also presented to understand the effects of fabrication errors on the performances of the designs.

3.1 Simulation Method

First, we describe the surface formulation used for full-wave simulations of metamaterial structures, as well as genetic algorithms employed in the optimization process to homogenize these structures.

3.1.1 Surface Formulation to Solve Three-Dimensional Metamaterial Structures

At microwave frequencies, three-dimensional metamaterial structures are constructed by using zero-thickness PEC surfaces such that they can be formulated with EFIE derived in Chapter 2. The computational analysis is carried out with MLFMA, which provides efficient full-wave solutions without using any self-similarity or regularity approximations considering that realistic metamaterial structures are finite structures. The matrix representation of EFIE can be written as

$$\bar{\boldsymbol{Z}}^{\text{EFIE}} \cdot \boldsymbol{a_J} = \boldsymbol{w}^{\text{EFIE}}, \tag{3.1}$$

where $\bar{\boldsymbol{Z}}^{\text{EFIE}}$ is the impedance matrix ($N \times N$ matrix), $\boldsymbol{a_J}$ represents coefficients expanding the electric current density ($\boldsymbol{J}$), and $\boldsymbol{w}^{\text{EFIE}}$ is the excitation vector. The elements of the impedance matrix and the excitation vector can be expressed as

$$\begin{aligned}\bar{\boldsymbol{Z}}^{\text{EFIE}}[m,n] = i w \mu \int_{S_m} d\boldsymbol{r} \boldsymbol{t}_m(\boldsymbol{r}) \cdot \int_{S_n} d\boldsymbol{r}' \boldsymbol{b}_n(\boldsymbol{r}') g(\boldsymbol{r},\boldsymbol{r}') \\ + \frac{1}{i w \epsilon} \int_{S_m} d\boldsymbol{r} \nabla \cdot \boldsymbol{t}_m(\boldsymbol{r}) \int_{S_n} d\boldsymbol{r}' g(\boldsymbol{r},\boldsymbol{r}') \nabla' \cdot \boldsymbol{b}_n(\boldsymbol{r}')\end{aligned} \tag{3.2}$$

and

$$\boldsymbol{w}^{\text{EFIE}}[m] = -\int_{S_m} d\boldsymbol{r} \boldsymbol{t}_m(\boldsymbol{r}) \cdot \boldsymbol{E}^{inc}(\boldsymbol{r}), \tag{3.3}$$

respectively. We note that μ and ϵ are the permeability and permittivity values of the host medium, respectively, $g(\boldsymbol{r},\boldsymbol{r}')$ is the homogeneous-space Green's function, $\boldsymbol{E}^{inc}$ is the incident electric field, and $\boldsymbol{b}_n$ and $\boldsymbol{t}_m$ are basis and testing functions (selected as the RWG functions) with $m,n = 1,2,...,N$. In the simulations, the host medium is assumed to be vacuum or be filled with an effective dielectric material that represents substrate.

3.1.2 Genetic Algorithms Supported by Full-Wave Solutions for the Homogenization of Metamaterial Structures

Metamaterials are periodic structures with subwavelength unit-cells; therefore, their homogenization can provide great simplicity and flexibility in their computational analysis. A homogenization is basically estimating the equivalent electromagnetic parameters to represent a metamaterial as a homogeneous structure. On the other hand, a successful homogenization requires rigorous considerations to eliminate disastrous approximation mistakes that can cause deficient and even incorrect characterizations. In the literature, various homogenization implementations to retrieve effective parameters of metamaterials have been proposed, such as Floquet-based methods [65–67], fast full-wave algorithms [68, 69], wave-propagation retrieval methods [70], analytical field-averaging methods [71], dipole approximations [72], and genetic algorithms blended with artificial neural networks [73]. The main simplification in most of these studies is extending the dimensions of the investigated metamaterials to infinity that may lead to distorted and false results.

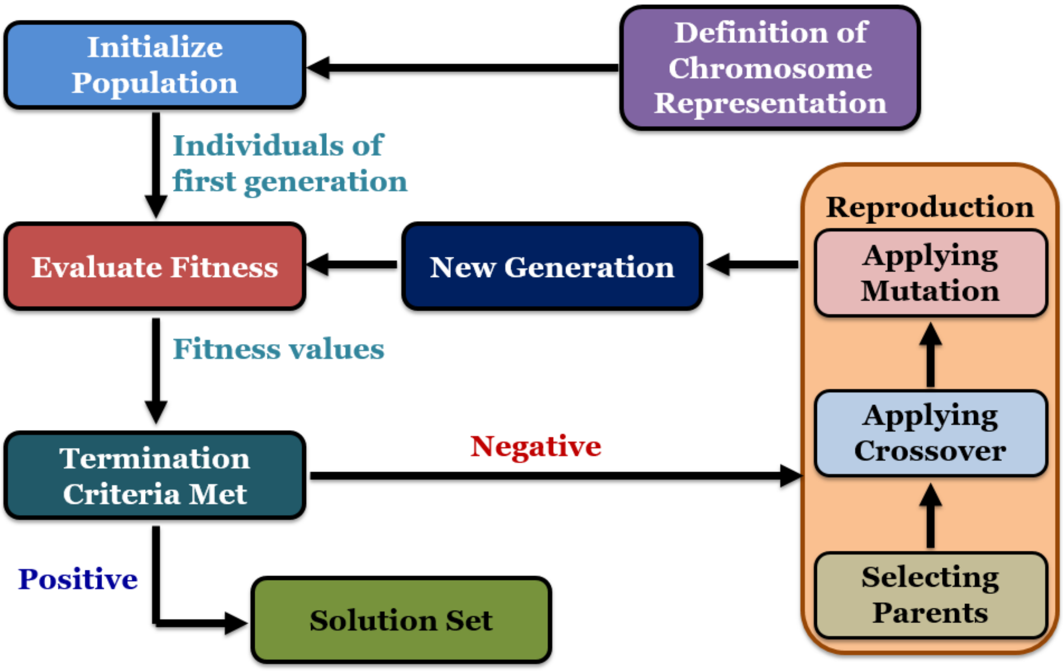
Initialize Population
Definition of Chromosome Representation
Individuals of first generation
Reproduction
Evaluate Fitness
New Generation
Applying Mutation
Fitness values
Applying Crossover
Termination Criteria Met
Negative
Positive
Solution Set
Selecting Parents

Figure 3.1: Representation of the mechanism based on genetic algorithms.

In this study, three-dimensional and finite metamaterial structures are homogenized without the commonly used infinity assumption. The real model, which is constructed by open metallic surfaces, typically involves very small details with respect to wavelength and also demonstrates resonance characteristics, leading to numerically challenging problems. However, the homogenized model is a homogeneous body with a plain geometry. Hence, from the computational point of view, a multiscale problem can be reduced to a single-scale problem via homogenization. This kind of a simplification can be extremely useful, e.g., when the metamaterial itself is a part of a larger system to be analyzed. In the proposed homogenization procedure, a parametric optimization environment based on genetic algorithms and a full-wave solver based on MLFMA is utilized. Genetic algorithms are among the most popular heuristic algorithms and they are in demand for various applications, including but not limited to electromagnetic problems.

The constructed mechanism based on genetic algorithms is shown in Figure 3.1 [74]. First, given input parameters, the chromosome representation is defined. In general, binary bits of a chromosome represent the relative permittivity and/or permeability of

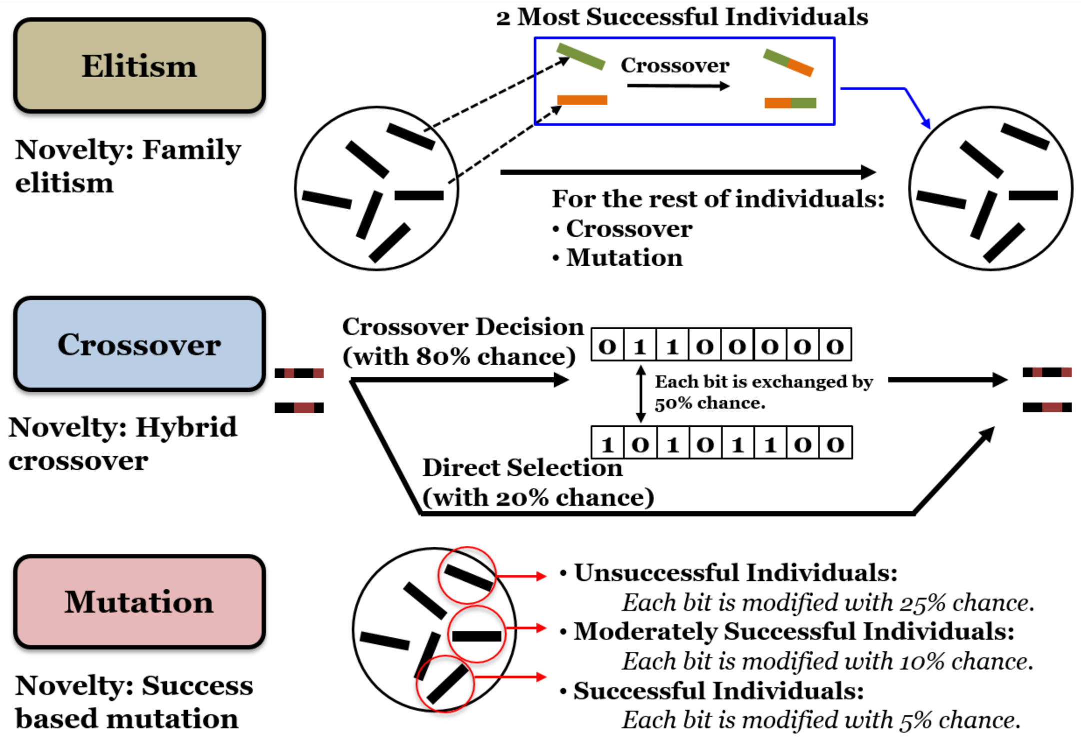
Elitism
Novelty: Family elitism
2 Most Successful Individuals
Crossover
For the rest of individuals:
• Crossover
• Mutation
Crossover
Novelty: Hybrid crossover
Crossover Decision (with 80% chance)
0 1 1 0 0 0 0 0
Each bit is exchanged by 50% chance.
1 0 1 0 1 1 0 0
Direct Selection (with 20% chance)
Mutation
Novelty: Success based mutation
• Unsuccessful Individuals:
Each bit is modified with 25% chance.
• Moderately Successful Individuals:
Each bit is modified with 10% chance.
• Successful Individuals:
Each bit is modified with 5% chance.

Figure 3.2: Representation of the reproduction procedure.

the corresponding homogenized model. Then, a population is initialized by creating the individuals of the first generation, whose fitness values are obtained. The reproduction cycle is applied to produce new generations until the termination criteria are satisfied. Once the termination criteria are met, the required solution set (homogeneous model or models) is obtained.

There are three main stages of the reproduction procedure, i.e., selecting parents, applying crossover, and applying mutation, as depicted in Figure 3.2. Elitism is actually transferring two of the successful individuals and their children (family elitism) across generations to assure the quality of the pool. In crossover operation, bit-by-bit exchanges are made between the chromosomes of selected parents with 50% chance for each bit, while the decision of a crossover is made with 80% chance. Mutations are applied based on the success of the individuals. For unsuccessful, moderately successful, and successful individuals, bits are modified (0 to 1 and 1 to 0) with 25%, 10%, and 5% chances, respectively.

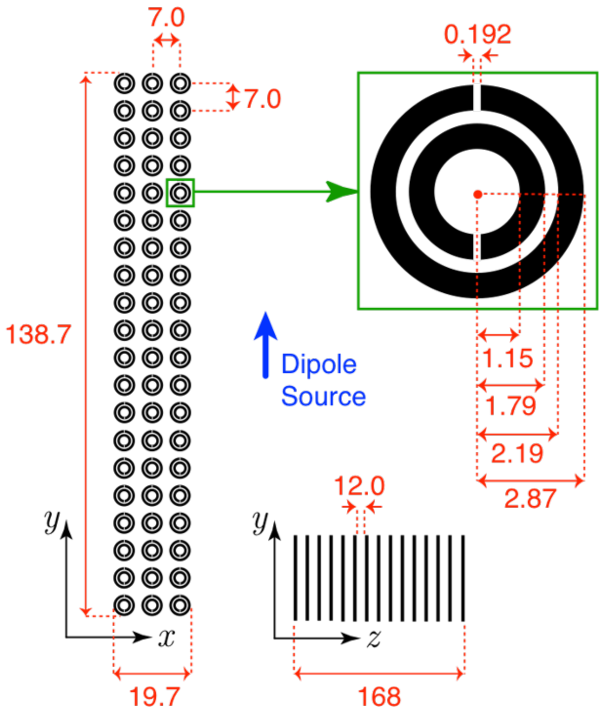

Figure 3.3: Details and dimensions (in mm) of the SRR structure that is designed to resonate at around 7.25 GHz when fabricated with inkjet printing.

3.2 Numerical Results

Since metamaterials involve small details with respect to wavelength and they exhibit strong resonances, their computational analysis requires critical considerations. But if performed accurately, simulations of metamaterials can provide essential information on the behavior of these structures before their actual realizations. As discussed above, full-wave simulations of metamaterials are performed by using EFIE and MLFMA. Apart from such direct numerical solutions of metamaterial designs, the optimization processes described above involve solutions of homogenized models using MLFMA and JMCFIE presented in Chapter 2. In all cases, the GMRES solver is used with a residual error of 10^{-3} for iterative solutions. The near-zone field intensity and power density distributions are calculated from the obtained current coefficients. The power transmission coefficients are found by averaging power density samples in a volume in the transmission region. The calculated average power density values are normalized with the average incident power density values.

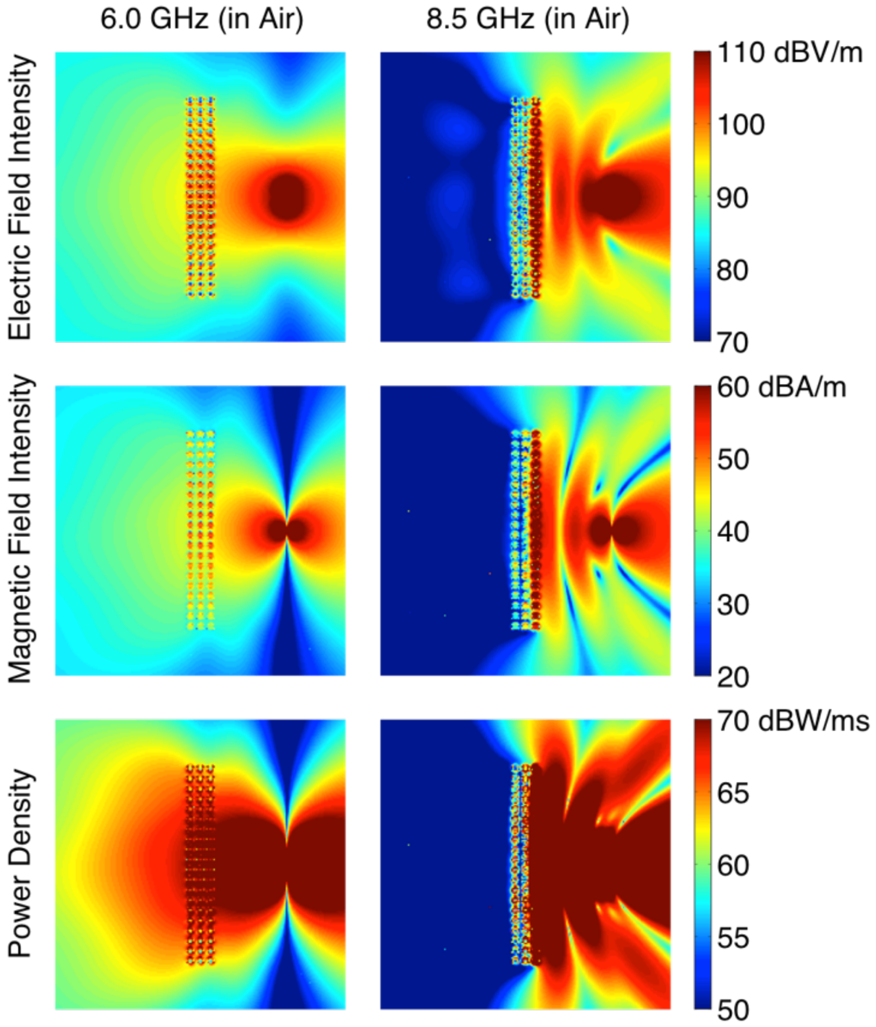

Figure 3.4: Near-zone field intensity and power density distributions for the SRR structure in Figure 3.3 on the x-y ($z = 0$) plane at 6 GHz and 8.5 GHz.

3.2.1 Analysis of Single-Band Metamaterials Involving SRRs

In this study, two different three-dimensional single-band SRR structures are investigated. The first SRR structure is designed to resonate at around 7.25 GHz when fabricated with inkjet printing, while the second one is designed to resonate at around 6 GHz. Details and important dimensions of the first design are depicted in Figure 3.3 [75]. This three-dimensional metamaterial structure ($3 \times 20 \times 15$ SRR array) is excited by a y-directed Hertzian dipole with 6 cm distance from the center of the ar-

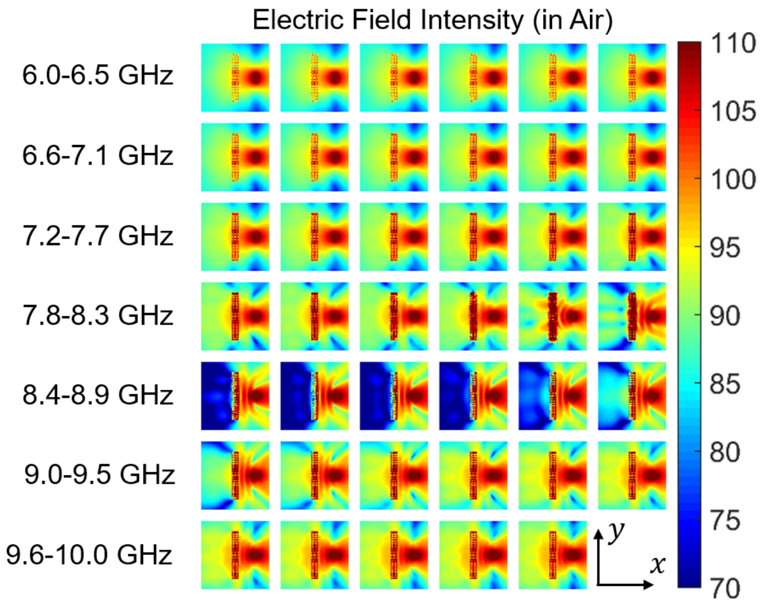

Figure 3.5: Near-zone electric field intensity (dBV/m) distributions for the SRR structure in Figure 3.3 on the x-y ($z = 0$) plane from 6 GHz to 10 GHz at 100 MHz intervals.

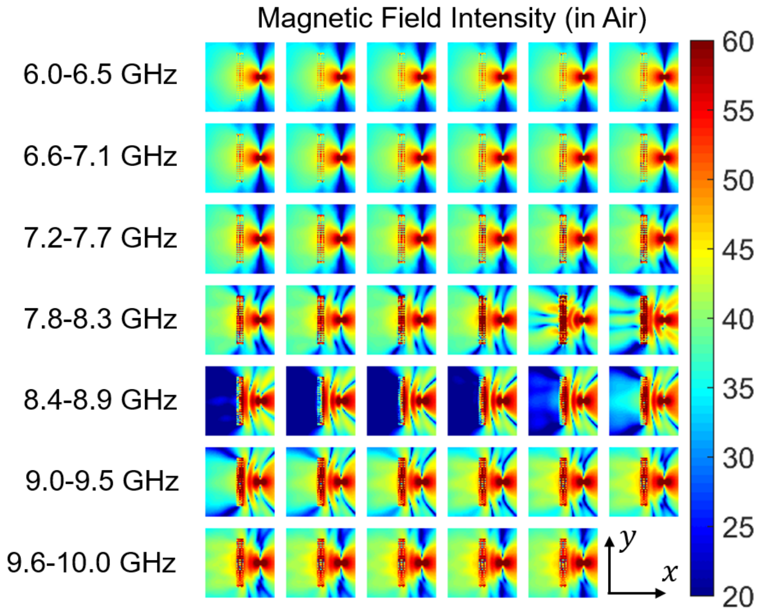

Figure 3.6: Near-zone magnetic field intensity (dBA/m) distributions for the SRR structure in Figure 3.3 on the x-y ($z = 0$) plane from 6 GHz to 10 GHz at 100 MHz intervals.

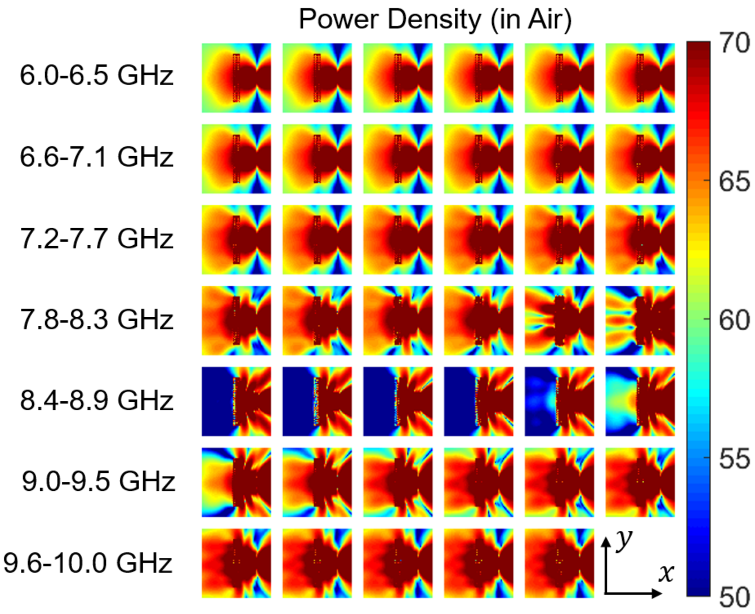

Figure 3.7: Near-zone power density (dBW/sm) distributions for the SRR structure in Figure 3.3 on the x-y ($z = 0$) plane from 6 GHz to 10 GHz at 100 MHz intervals.

ray in the x direction (it is centered along the y and z directions). The periodicity in the x and y directions are 7 mm, while the layer periodicity is 12 mm. We note that increasing the size and the number of SRRs in the transverse plane tends to increase the quality of resonances. At the same time, increasing the number of layers also have positive effects on the quality and band of resonances. Therefore, given a number of SRRs, it is an interesting design problem to decide how to arrange them to satisfy the desired transmission properties. The near-zone electric field intensity (dBV/m), magnetic field intensity (dBA/m), and power density (dBW/sm) distributions on the x-y ($z = 0$) plane at 6 GHz and 8.5 GHz are focused in Figure 3.4. Inhibition of the electromagnetic wave propagation at 8.5 GHz, as well as the good transmission at 6 GHz are clearly observed. We also note that resonances of the SRRs are clearly visible in field and density plots at 8.5 GHz. For a better observation, Figures 3.5, 3.6, and 3.7 present the near-zone electric field intensity (dBV/m), magnetic field intensity (dBA/m), and power density (dBW/sm) distributions on the x-y ($z = 0$) plane from 6 GHz to 10 GHz. Between 8.4 GHz and 8.8 GHz, opaqueness is clearly observed as an expected outcome of the resonance. At other frequencies, good transmission of the incident wave occurs since SRRs are inactive.

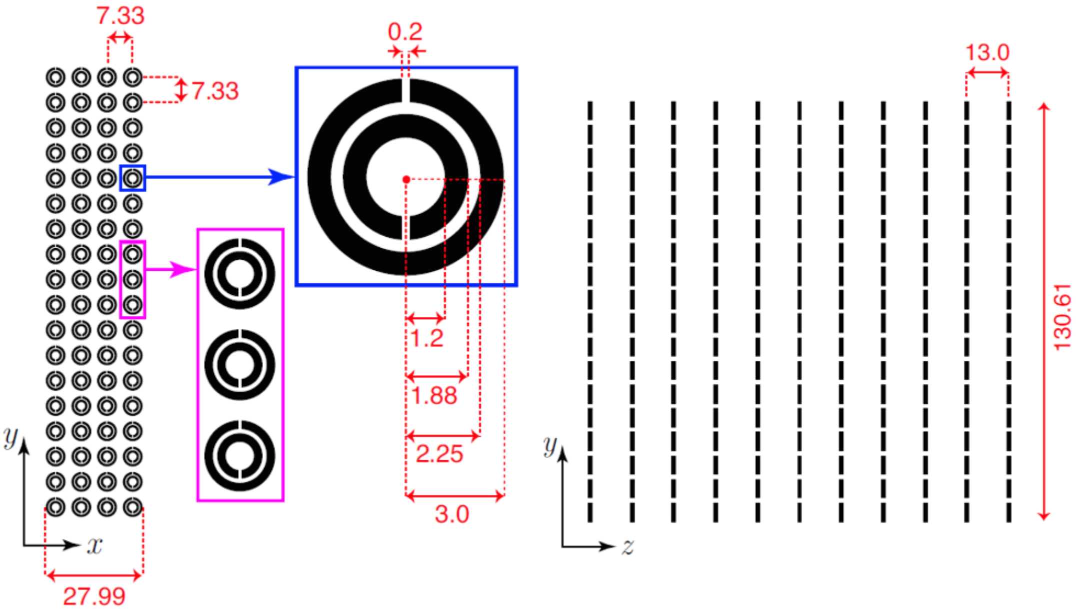

Figure 3.8: Details and dimensions (in mm) of the SRR structure that is designed to resonate at around 6 GHz when fabricated with inkjet printing.

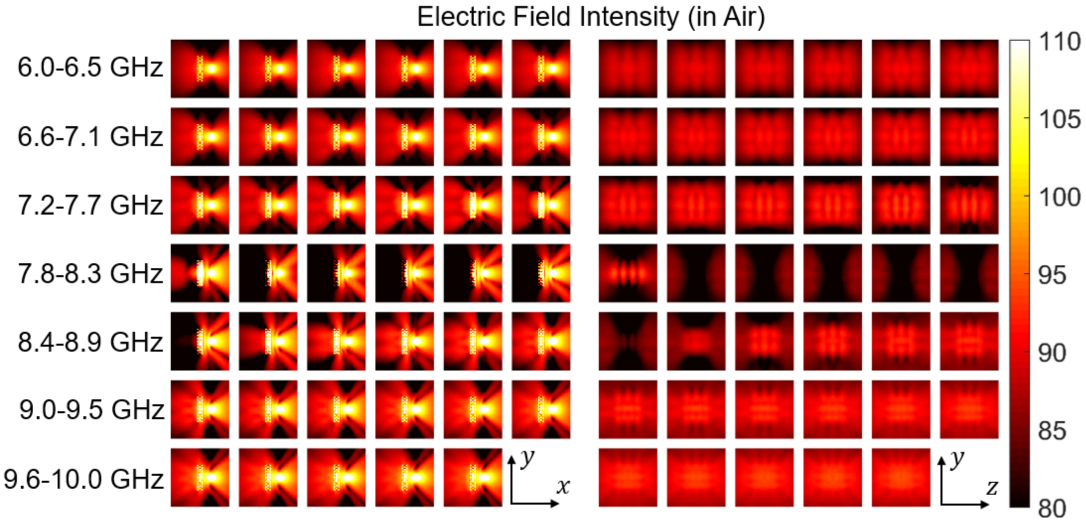

Figure 3.9: Near-zone electric field intensity (dBV/m) distributions for the SRR structure in Figure 3.8 on the x-y ($z = 0$) and y-z ($x = -6$ cm) planes from 6 GHz to 10 GHz at 100 MHz intervals.

The dimensions of the second structure, which is a $4 \times 18 \times 11$ SRR array that consists of 792 identical SRRs, is given in Figure 3.8 [76]. The single SRR involves two

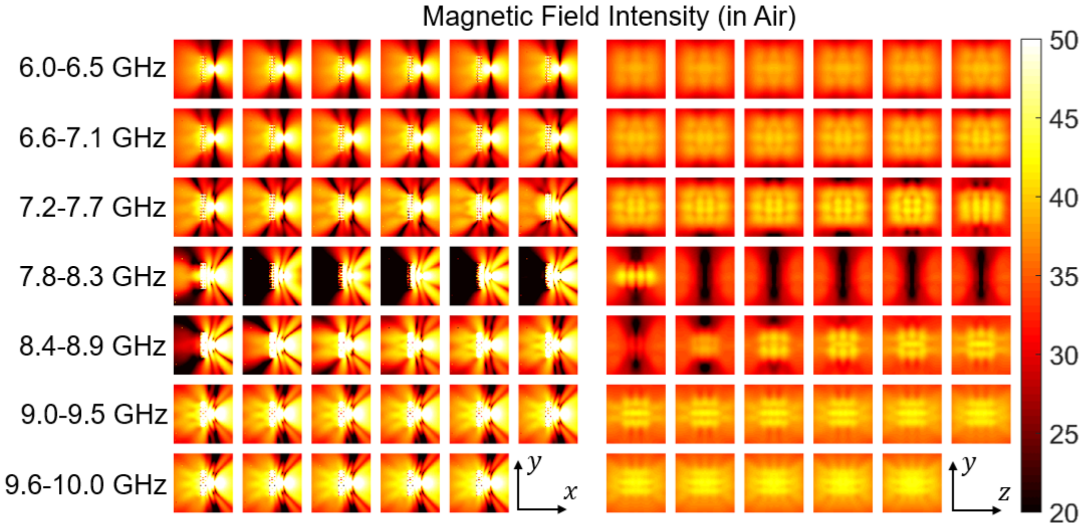

Figure 3.10: Near-zone magnetic field intensity (dBA/m) distributions for the SRR structure in Figure 3.8 on the x-y ($z = 0$) and y-z ($x = -6$ cm) planes from 6 GHz to 10 GHz at 100 MHz intervals.

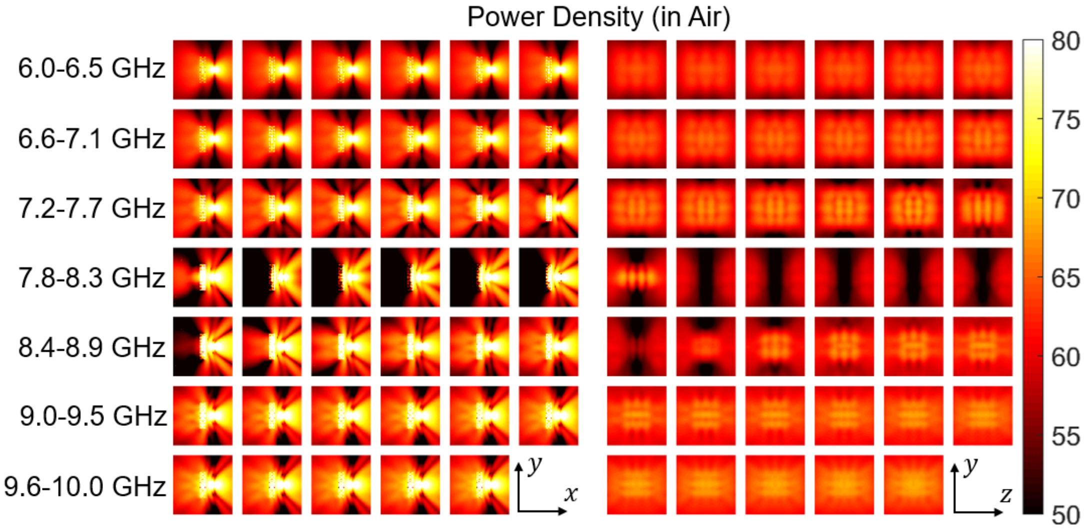

Figure 3.11: Near-zone power density (dBW/sm) distributions for the SRR structure in Figure 3.8 on the x-y ($z = 0$) and y-z ($x = -6$ cm) planes from 6 GHz to 10 GHz at 100 MHz intervals.

concentric rings with splits (with a gap width of 0.2 mm) at the opposite sides of the rings in the y direction. The overall SRR array is formed by layering two-dimensional (4×18) arrays in the z direction with 13 mm distance between the layers. Each two-

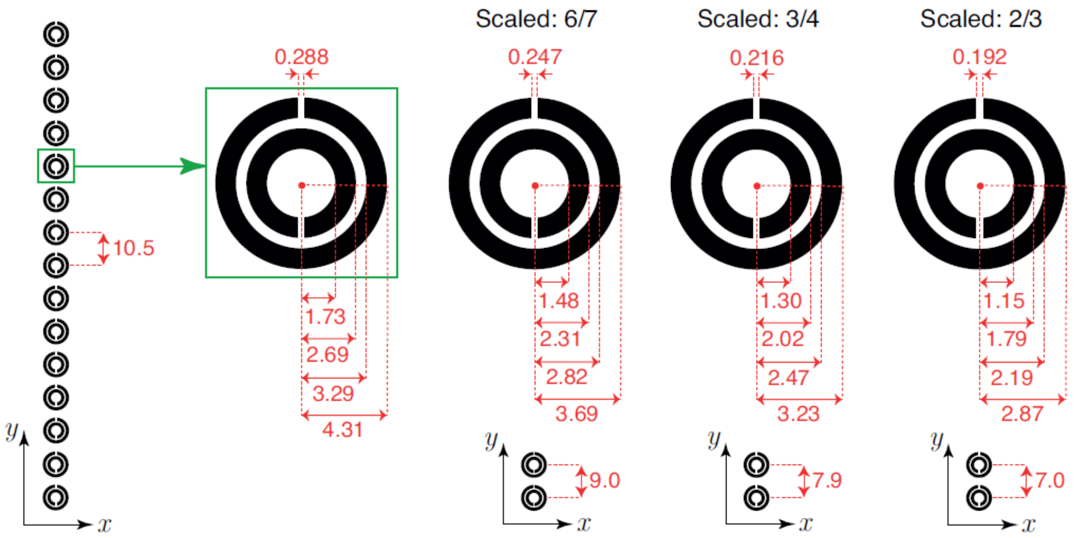

Figure 3.12: Details and dimensions (in mm) of non-scaled and scaled SRR structures that are used to design multiband metamaterials.

dimensional array is an arrangement of 4×18 SRRs with 7.33 mm center-to-center distances in both x and y directions. For the excitation, a y-directed Hertzian dipole placed 6 cm away in only x direction from its center is used.

Since the design of the SRR structure is similar to the one in an earlier study, yet at a different scale, the resonance frequency is predicted to be approximately 8.2 GHz when the structure is located in air [22]. The near-zone electric field intensity (dBV/m), magnetic field intensity (dBA/m), and power density (dBW/sm) distributions on the x-y ($z = 0$) and y-z ($x = -6$ cm) planes for the frequency range between 6 GHz and 10 GHz are presented in Figures 3.9, 3.10, and 3.11, respectively. We note that the origin is at the center of the SRR structure. As expected, the blocking behavior of the SRR structure is observed in the resonance band (7.9–8.4 GHz), whereas, for the rest of the frequencies, transparency is observed. The shadowing effect is due to the resonance characteristics of the SRR structures. Specifically, when SRRs resonate, they induce negative permeability in their surrounding media, leading to intense attenuation of electromagnetic waves. At the same time, as a result of diffractions due to its finite size, the SRR structure does not perfectly shield electromagnetic waves.

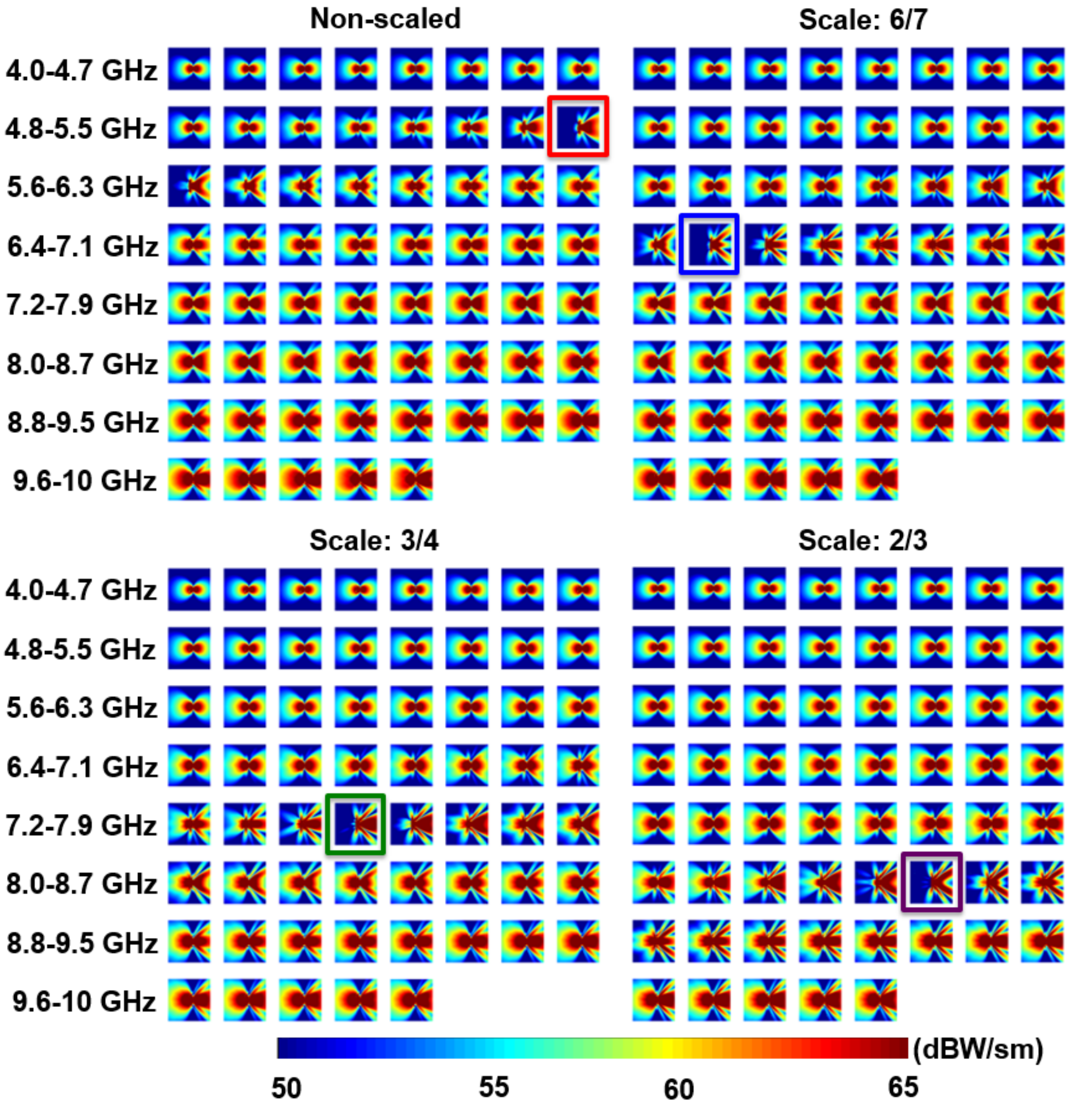

Figure 3.13: Near-zone power density (dBW/sm) distributions for the non-scaled and scaled SRR arrays (see Figure 3.12) on the x-y ($z = 0$) plane from 4 GHz to 10 GHz at 100 MHz intervals.

3.2.2 Analysis of Multiband Metamaterials Involving SRRs

Three-dimensional microwave multiband metamaterial designs by combining SRRs with different scales are investigated in this study [77, 78]. The aim is to obtain successful combinations of SRR arrays to achieve band-stop characteristics at multiple frequencies, while good transmission is ensured at the rest of the frequencies. Since resonances are inherent properties of SRR structures, we particularly focus on the in-

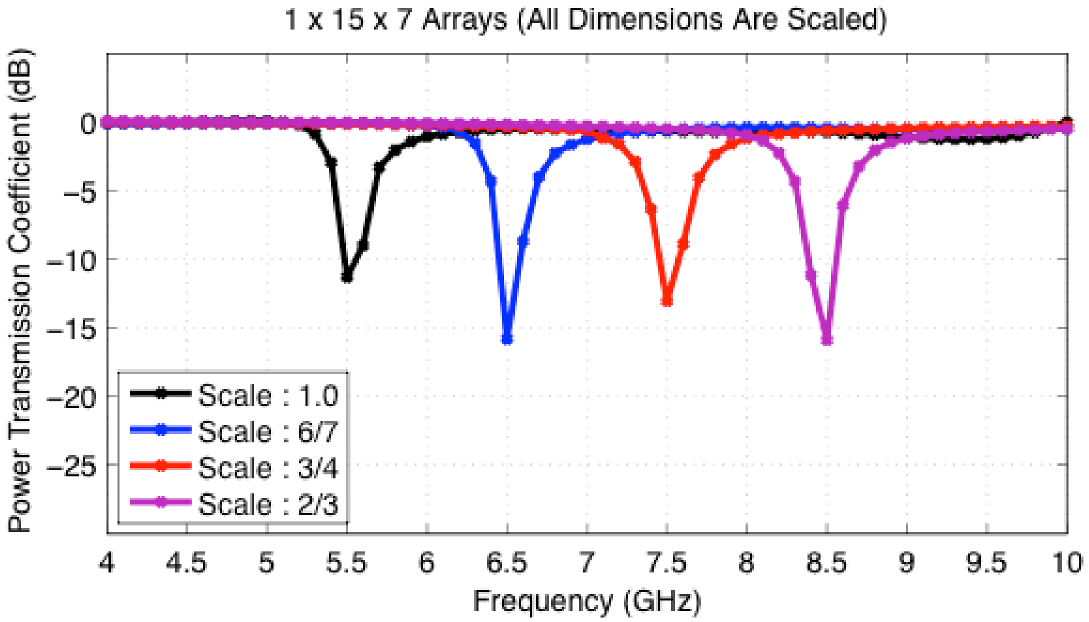

Figure 3.14: Power transmission coefficient with respect to frequency for the arrays involving SRRs with different scales (see Figure 3.12).

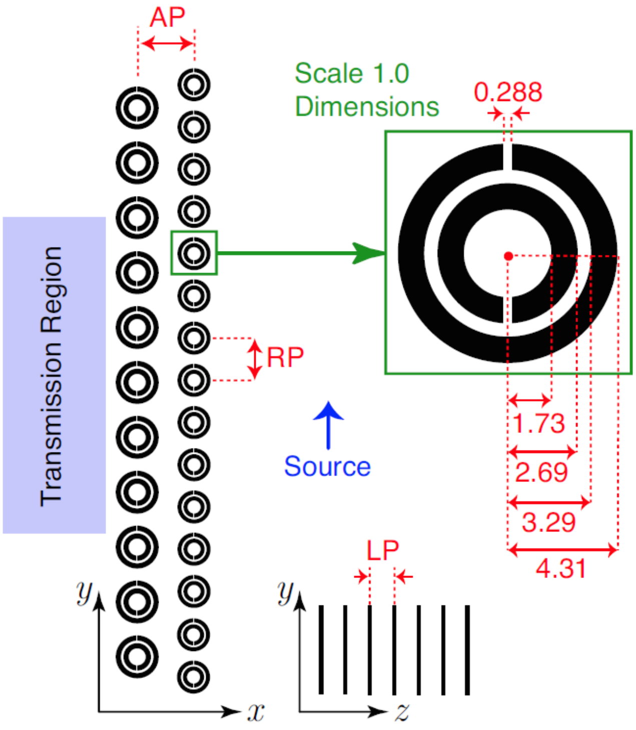
AP
Scale 1.0
Dimensions
0.288
Transmission Region
RP
Source
1.73
2.69
3.29
4.31
LP
y
x
y
z

Figure 3.15: Arrangements and design parameters to build multiband SRR blocks from the two-dimensional arrays.

teractions of identical and non-identical SRRs in three-dimensional arrangements to comprehend their responses in multiband operations. In order to maintain the compactness of the designs, non-identical SRR arrays cannot be separated too much from each other; however, to avoid disastrous effects of strong couplings between them, they should be carefully positioned. In addition, a sufficient number of SRRs must be used with periodic arrangements to obtain efficient multiband characteristics.

The original and scaled versions of the SRRs discussed in the previous subsection are used to construct multiband metamaterial designs. Figure 3.12 depicts the dimensions of the non-scaled SRR and its scaled versions with 6/7, 3/4, and 2/3 ratios. By arranging identical SRRs periodically in the y direction, one-dimensional SRR arrays are created. Layering these one-dimensional arrays in the z direction, two-dimensional arrays are constructed, which are then further combined to obtain three-dimensional arrays for multiband operations. We note that the scale factors are selected according to the desired resonance frequencies when the non-scaled SRR is treated as a kernel. The three-dimensional SRR structures are excited via a Hertzian dipole of 1 Am dipole moment in the y direction, as in the previous simulations. Near-zone power density distributions on the x-y ($z = 0$) plane for the two-dimensional non-scaled, 6/7-scaled, 3/4-scaled, and 2/3-scaled SRR arrays in free space from 4 GHz to 10 GHz are shown in Figure 3.13. The plots show resonances at the desired frequencies that are 5.5 GHz, 6.5 GHz, 7.5 GHz, and 8.5 GHz for the corresponding scales of 1, 6/7, 3/4, 2/3, respectively. The band-stop characteristics of different SRR arrays are further observed in the power transmission coefficient plots given in Figure 3.14.

Figure 3.15 depicts the arrangements and design parameters when combining two-dimensional SRR arrays to construct three-dimensional multiband blocks. The design parameters can be listed as follows.

- The distance between the identical SRRs in the y direction (resonator periodicity: RP)
- The distance between the layers in the z direction (layer periodicity: LP)
- The distance between the two-dimensional SRR arrays in the x direction (array periodicity: AP)

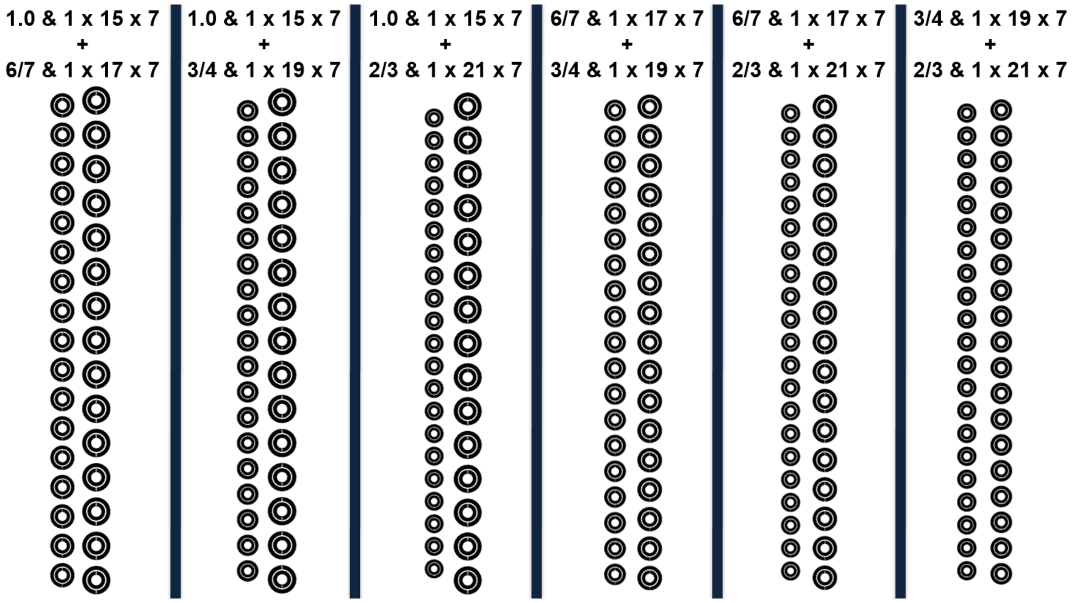

Figure 3.16: Six successful layouts for dual-band metamaterial designs with AP = 10.5 mm.

- The number of two-dimensional SRR arrays
- Selected scales for the two-dimensional SRR arrays
- The number of layers in the z direction
- The number of identical SRRs in the y direction

In the design procedure, some of the parameters given above are fixed depending on various constraints in the fabrications and measurement setups. Since inkjet-printing is used for the fabrication of the designed multiband metamaterial structures, non-identical SRRs in the same layer are simultaneously fabricated without any special procedure. The number of layers in the z direction is selected as seven. The distances between identical SRRs in the y direction are determined as 10.5 mm, 9.0 mm, 7.9 mm, and 7.0 mm, while the numbers of identical SRRs in the y direction are selected as 15, 17, 19, and 21 (to balance the dimensions of the one-dimensional SRR arrays) for the SRR scales of 1.0, 6/7, 3/4, and 2/3, respectively. For the rest of the parameters, various possibilities are immensely considered in terms of resonance qualities, thanks to the flexibility and efficiency of the simulation environment.

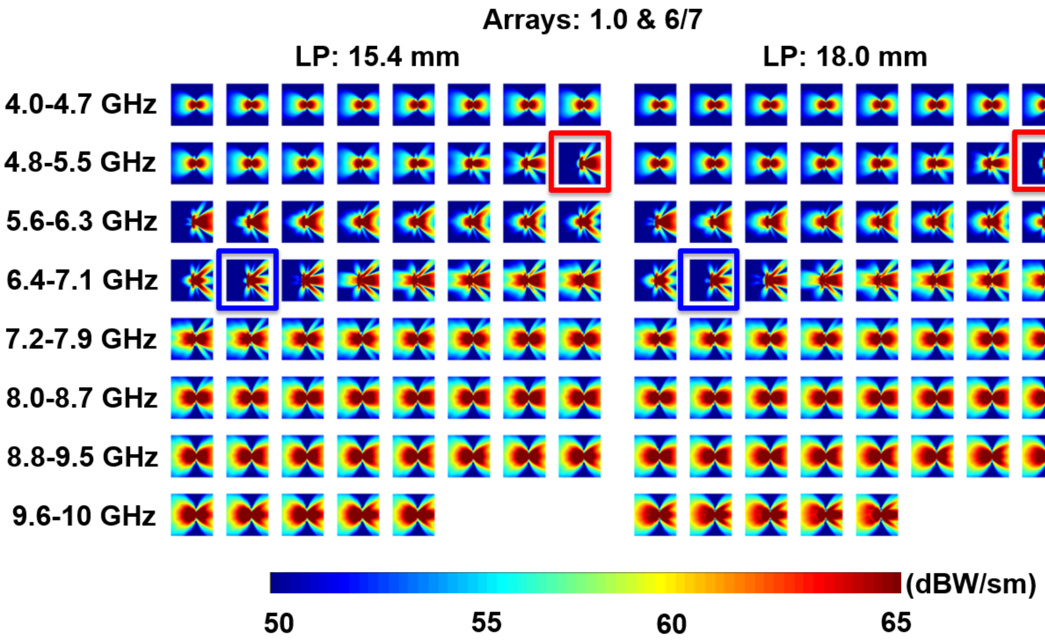

Figure 3.17: Power density distributions for the dual-band design involving non-scaled and 6/7-scaled SRRs [with the layout given in Figure 3.16 (first from left-hand side)] from 4 GHz to 10 GHz. LP = 15.4 mm (left) and LP = 18.0 mm (right) are used.

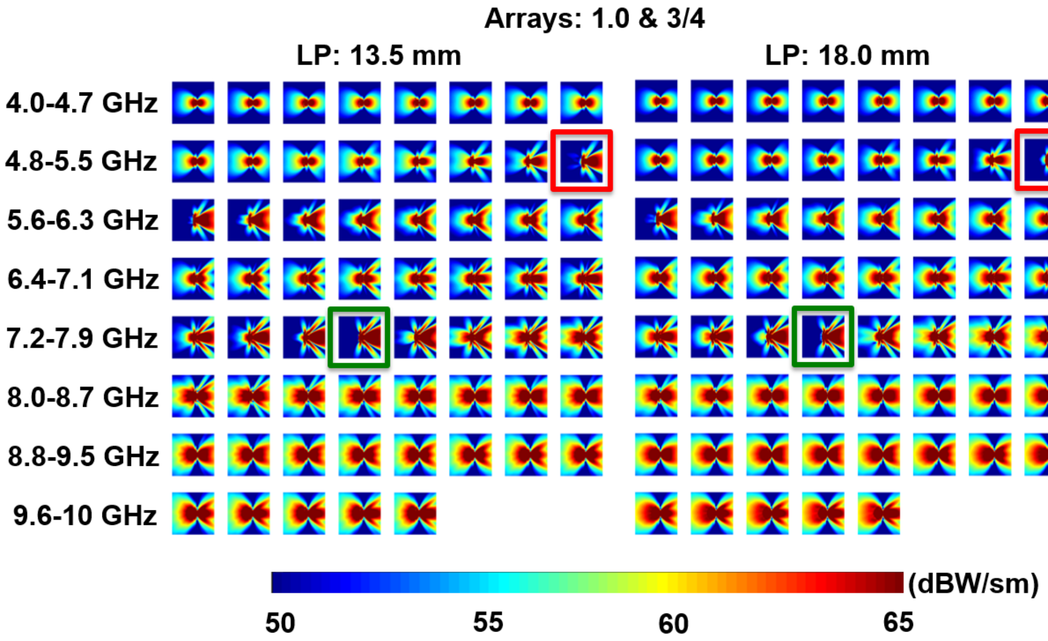

Figure 3.18: Power density distributions for the dual-band design involving non-scaled and 3/4-scaled SRRs [with the layout given in Figure 3.16 (second from left-hand side)] from 4 GHz to 10 GHz. LP = 13.5 mm (left) and LP = 18.0 mm (right) are used.

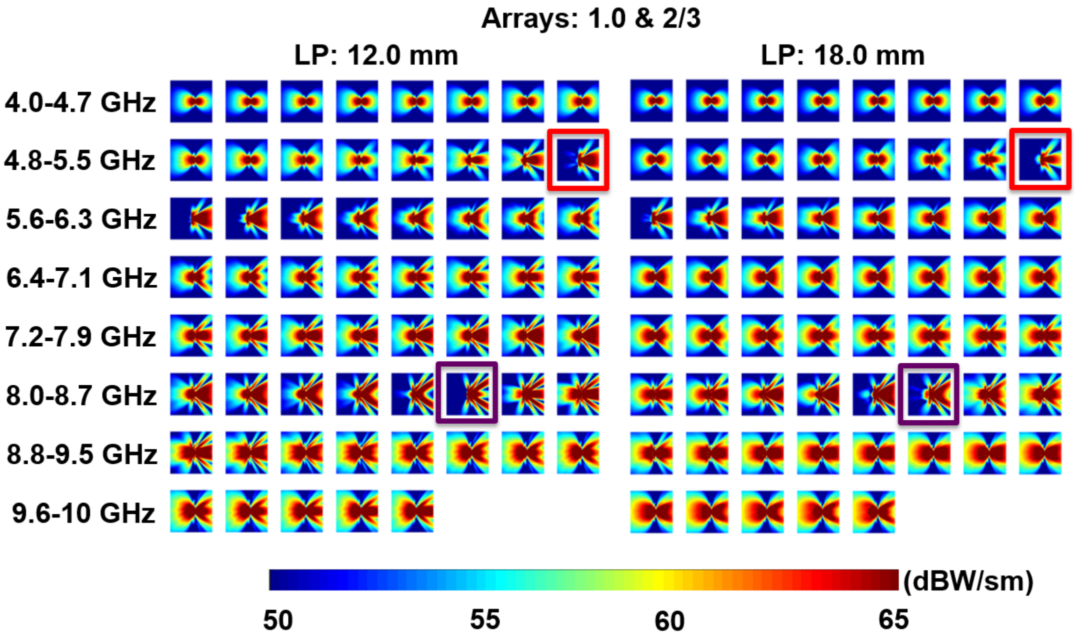

Figure 3.19: Power density distributions for the dual-band design involving non-scaled and 2/3-scaled SRRs [with the layout given in Figure 3.16 (third from left-hand side)] from 4 GHz to 10 GHz. LP = 12.0 mm (left) and LP = 18.0 mm (right) are used.

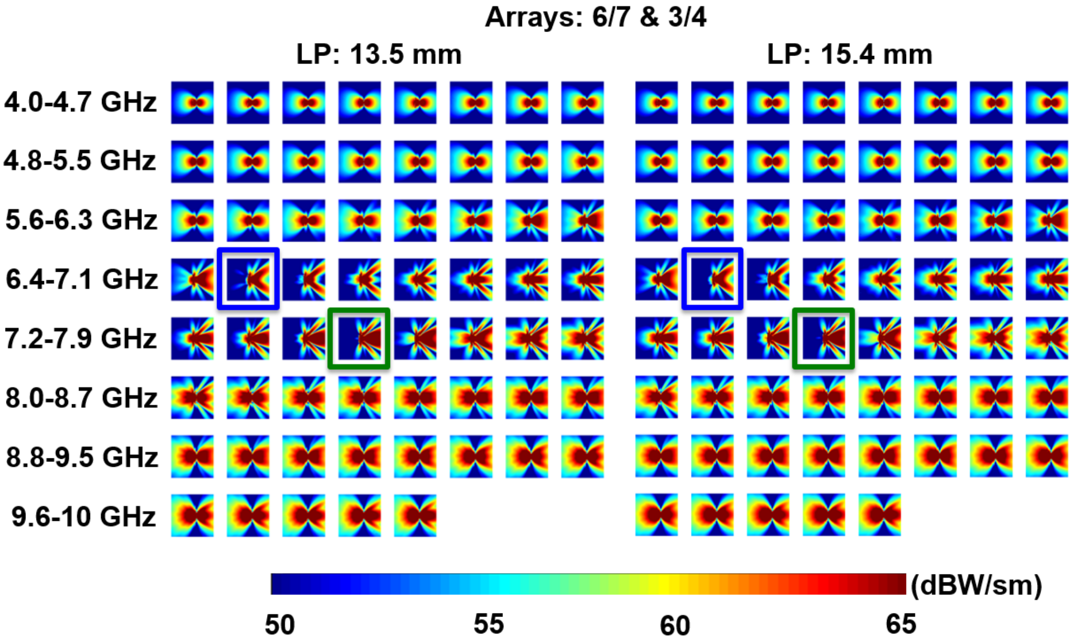

Figure 3.20: Power density distributions for the dual-band design involving 6/7-scaled and 3/4-scaled SRRs [with the layout given in Figure 3.16 (third from right-hand side)] from 4 GHz to 10 GHz. LP = 13.5 mm (left) and LP = 15.4 mm (right) are used.

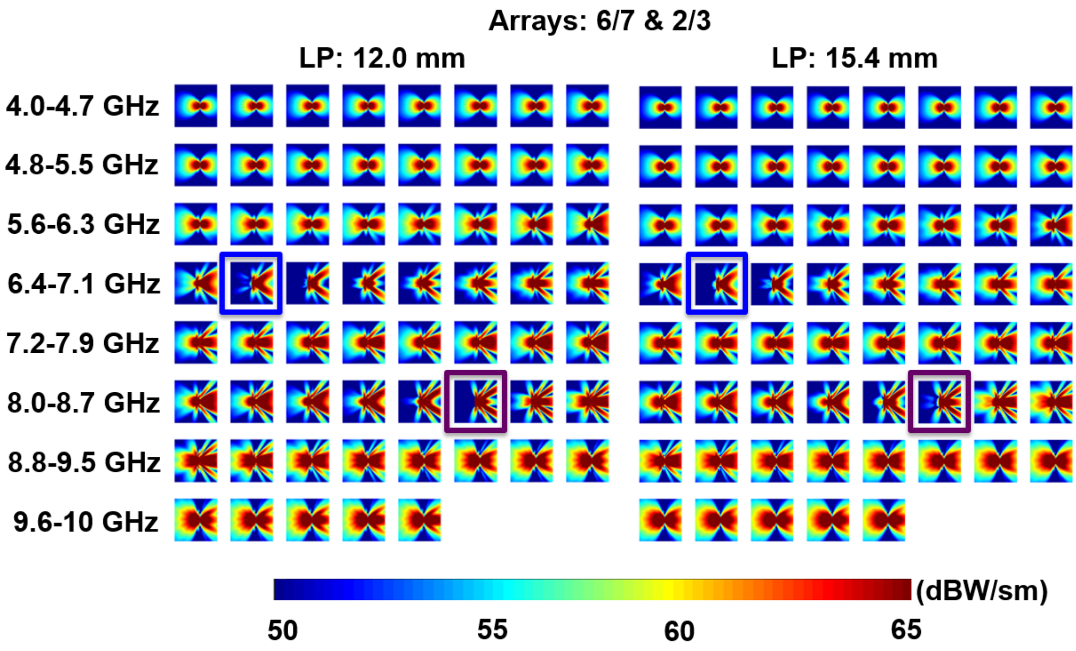

Figure 3.21: Power density distributions for the dual-band design involving 6/7-scaled and 2/3-scaled SRRs [with the layout given in Figure 3.16 (second from right-hand side)] from 4 GHz to 10 GHz. LP = 12.0 mm (left) and LP = 15.4 mm (right) are used.

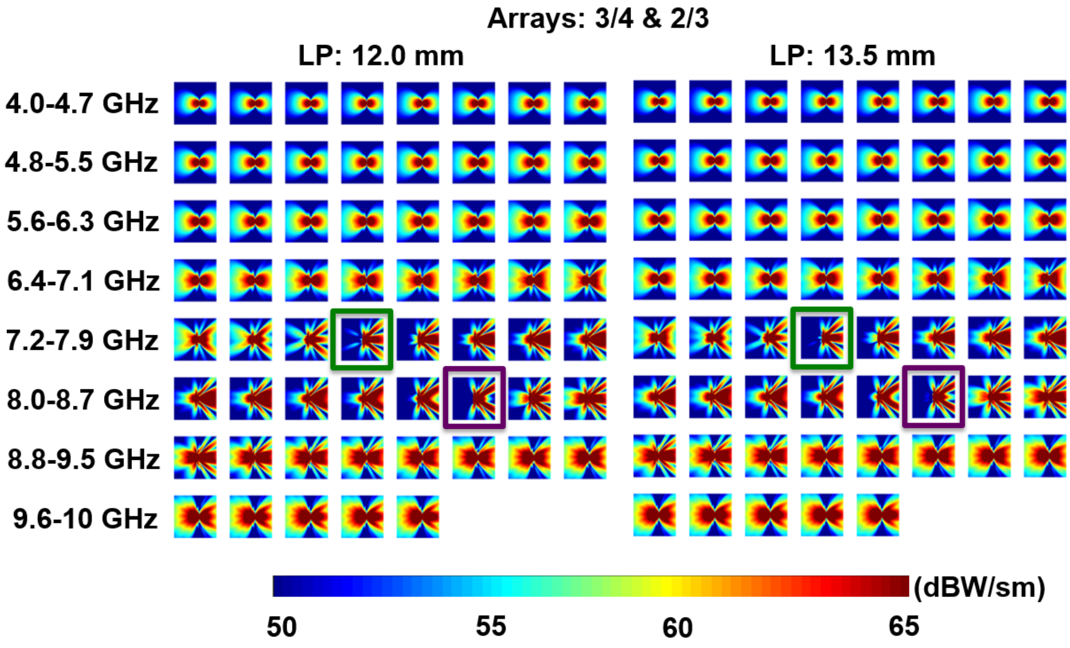

Figure 3.22: Power density distributions for the dual-band design involving 3/4-scaled and 2/3-scaled SRRs [with the layout given in Figure 3.16 (first from right-hand side)] from 4 GHz to 10 GHz. LP = 12.0 mm (left) and LP = 13.5 mm (right) are used.

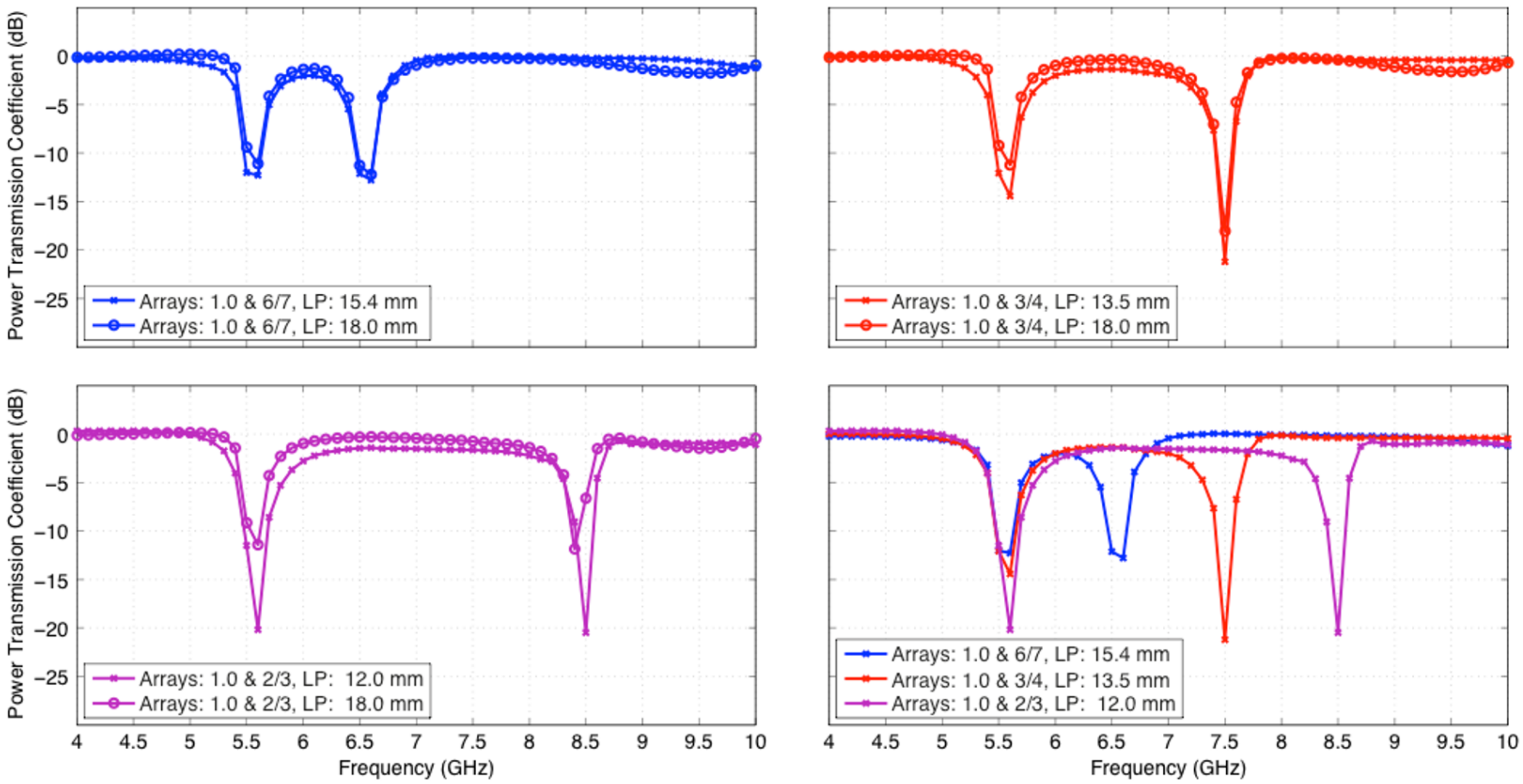

Figure 3.23: Power transmission coefficients for the dual-band metamaterials with the layouts given in Figure 3.16 (the first three layouts from left-hand side) and with selected layer periodicities.

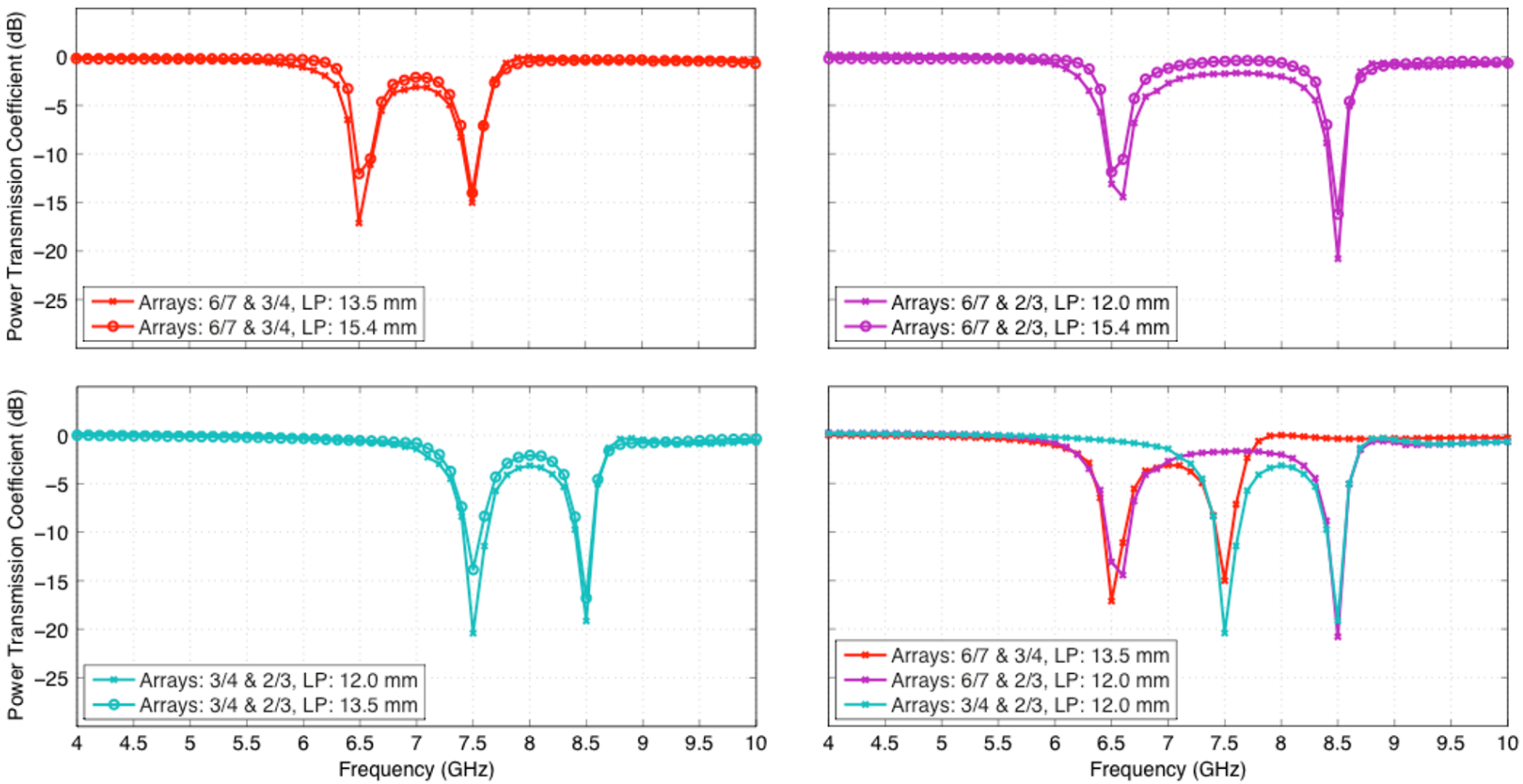

Figure 3.24: Power transmission coefficients for the dual-band metamaterials with the layouts given in Figure 3.16 (the last three layouts from left-hand side) and with selected layer periodicities.

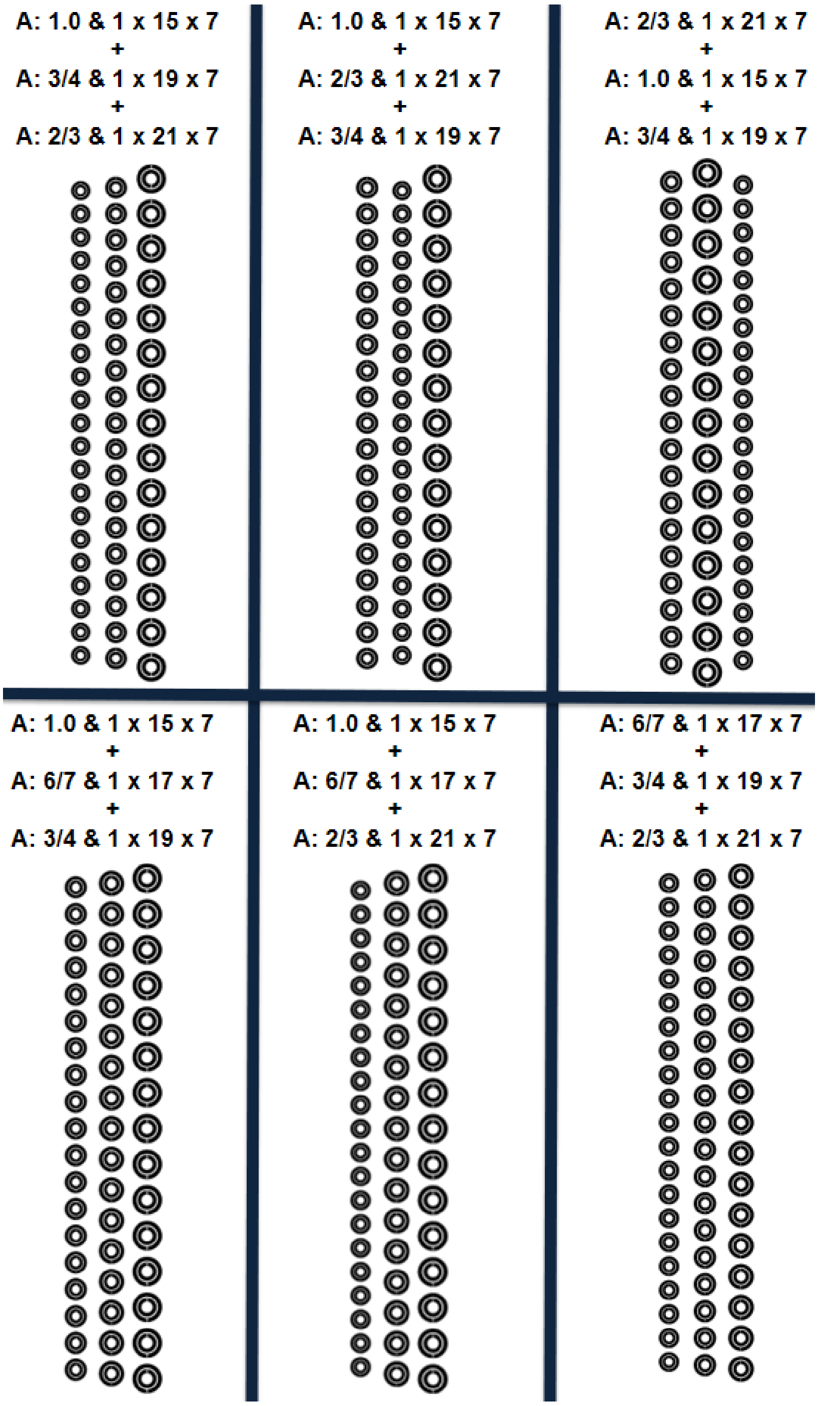
A: 1.0 & 1 x 15 x 7
+
A: 3/4 & 1 x 19 x 7
+
A: 2/3 & 1 x 21 x 7
A: 1.0 & 1 x 15 x 7
+
A: 2/3 & 1 x 21 x 7
+
A: 3/4 & 1 x 19 x 7
A: 2/3 & 1 x 21 x 7
+
A: 1.0 & 1 x 15 x 7
+
A: 3/4 & 1 x 19 x 7
A: 1.0 & 1 x 15 x 7
+
A: 6/7 & 1 x 17 x 7
+
A: 3/4 & 1 x 19 x 7
A: 1.0 & 1 x 15 x 7
+
A: 6/7 & 1 x 17 x 7
+
A: 2/3 & 1 x 21 x 7
A: 6/7 & 1 x 17 x 7
+
A: 3/4 & 1 x 19 x 7
+
A: 2/3 & 1 x 21 x 7

Figure 3.25: Six successful layouts for triple-band metamaterial designs with AP = 10.5 mm.

Figure 3.16 depicts six relatively successful layouts (x-y plane views) for dual-band metamaterial designs. The layouts are constructed by combining different scales with AP = 10.5 mm, which corresponds to the resonator periodicity of the original

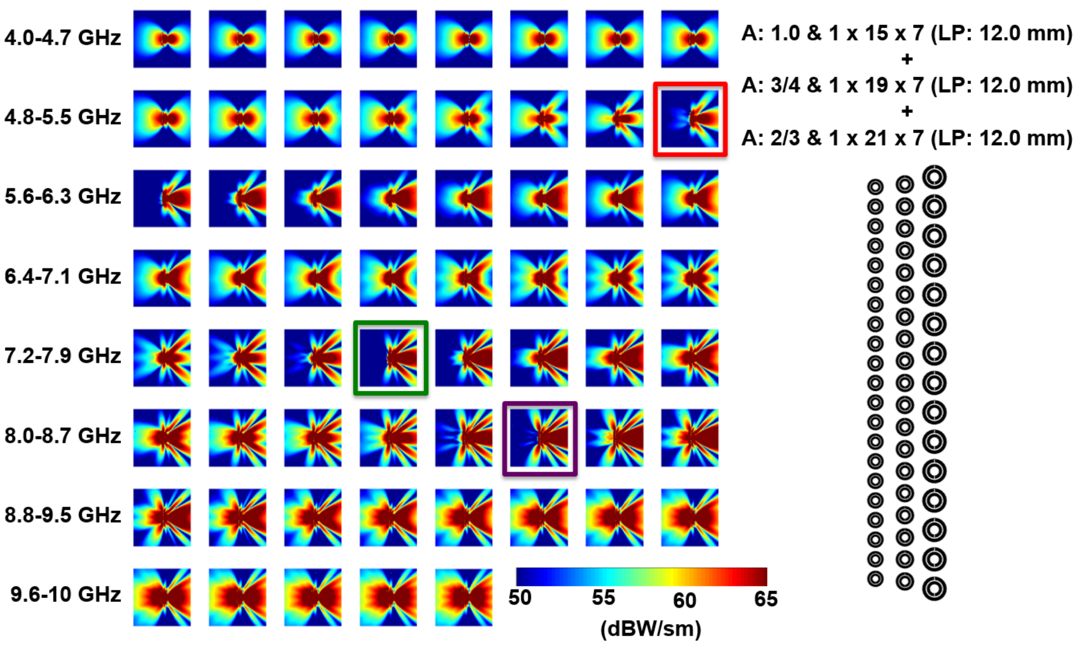

Figure 3.26: Power density distributions for the triple-band design involving original, 3/4-scaled, and 2/3-scaled SRRs with LP = 12.0 mm from 4 GHz to 10 GHz at 100 MHz intervals.

scale. The six layouts from the left-hand side to the right-hand side involve original and 6/7-scaled, original and 3/4-scaled, original and 2/3-scaled, 6/7-scaled and 3/4-scaled, 6/7-scaled and 2/3-scaled, and 3/4-scaled and 2/3-scaled SRRs, respectively. The layer periodicity of each design is carefully selected to obtain high-quality resonances. In the following results, comparisons of successful layer periodicity selections are presented for each layout. In Figures 3.17–3.22, near-zone power density (dBW/sm) distributions on the x-y ($z = 0$) plane from 4 GHz to 10 GHz at 100 MHz intervals are presented. Square frames with different colors are used to emphasize the resonance frequencies corresponding to the SRRs used in the designs, i.e., the red frame represents 5.5 GHz, the blue frame represents 6.5 GHz, the green frame represents 7.5 GHz, and the purple frame represents 8.5 GHz. It is remarkable that shadowing effects are successfully obtained at the resonance frequencies in accordance with the selected SRR scales to construct the structures. Figures 3.23 and 3.24 present the power transmission coefficients for the successful layouts given in Figure 3.16 with the selected layer periodicities. It is also evident in these plots that dual-band operation is achieved with the constructed designs. At the same time, SRRs

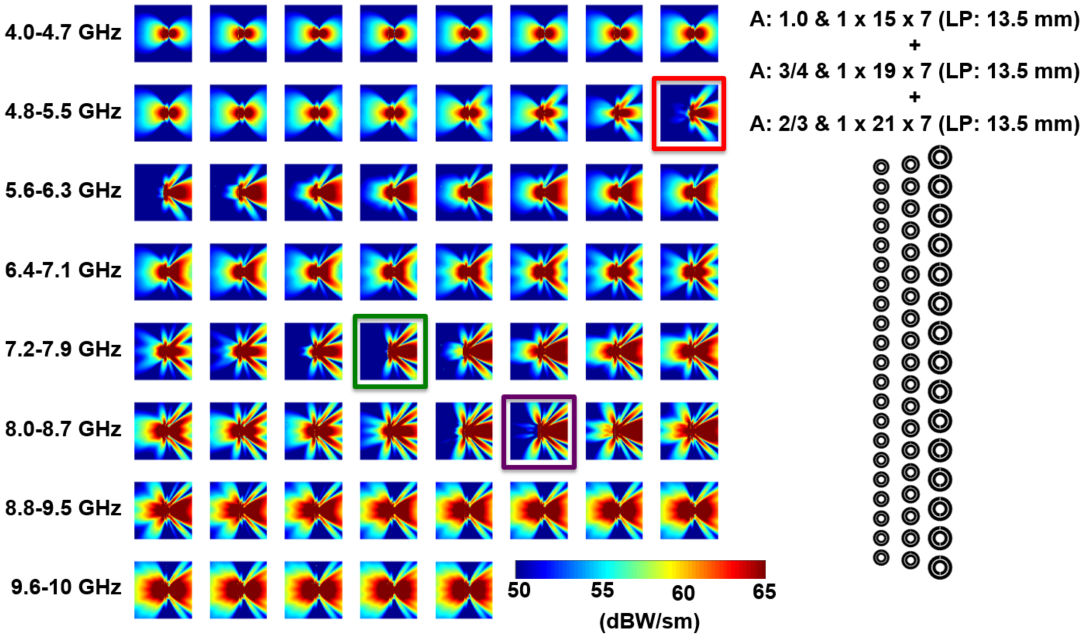

Figure 3.27: Power density distributions for the triple-band design involving original, 3/4-scaled, and 2/3-scaled SRRs with LP = 13.5 mm from 4 GHz to 10 GHz at 100 MHz intervals.

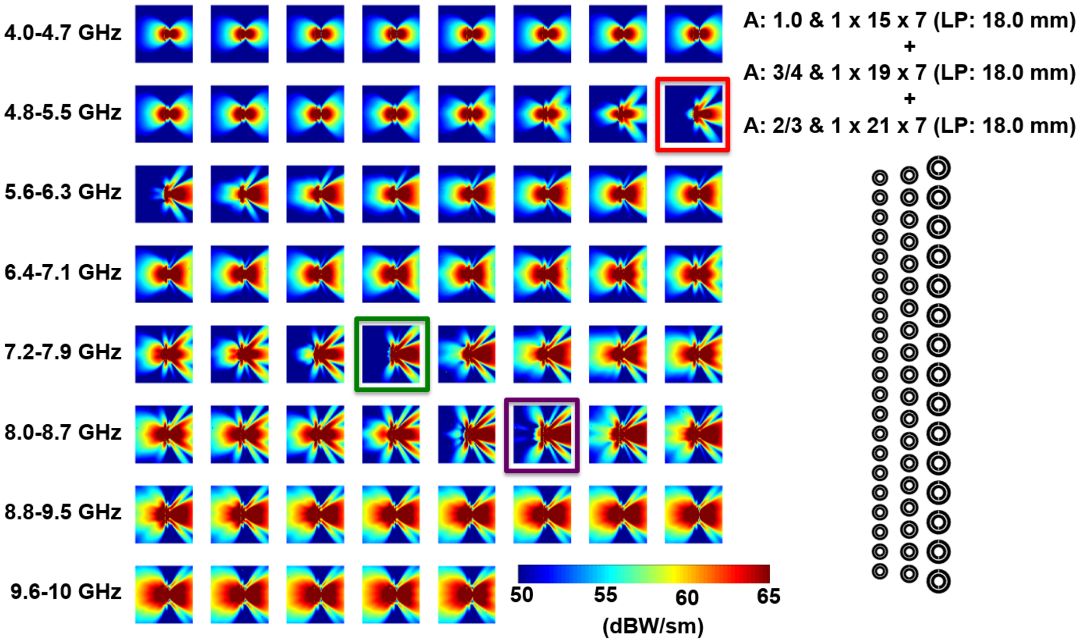

Figure 3.28: Power density distributions for the triple-band design involving original, 3/4-scaled, and 2/3-scaled SRRs with LP = 18.0 mm from 4 GHz to 10 GHz at 100 MHz intervals.

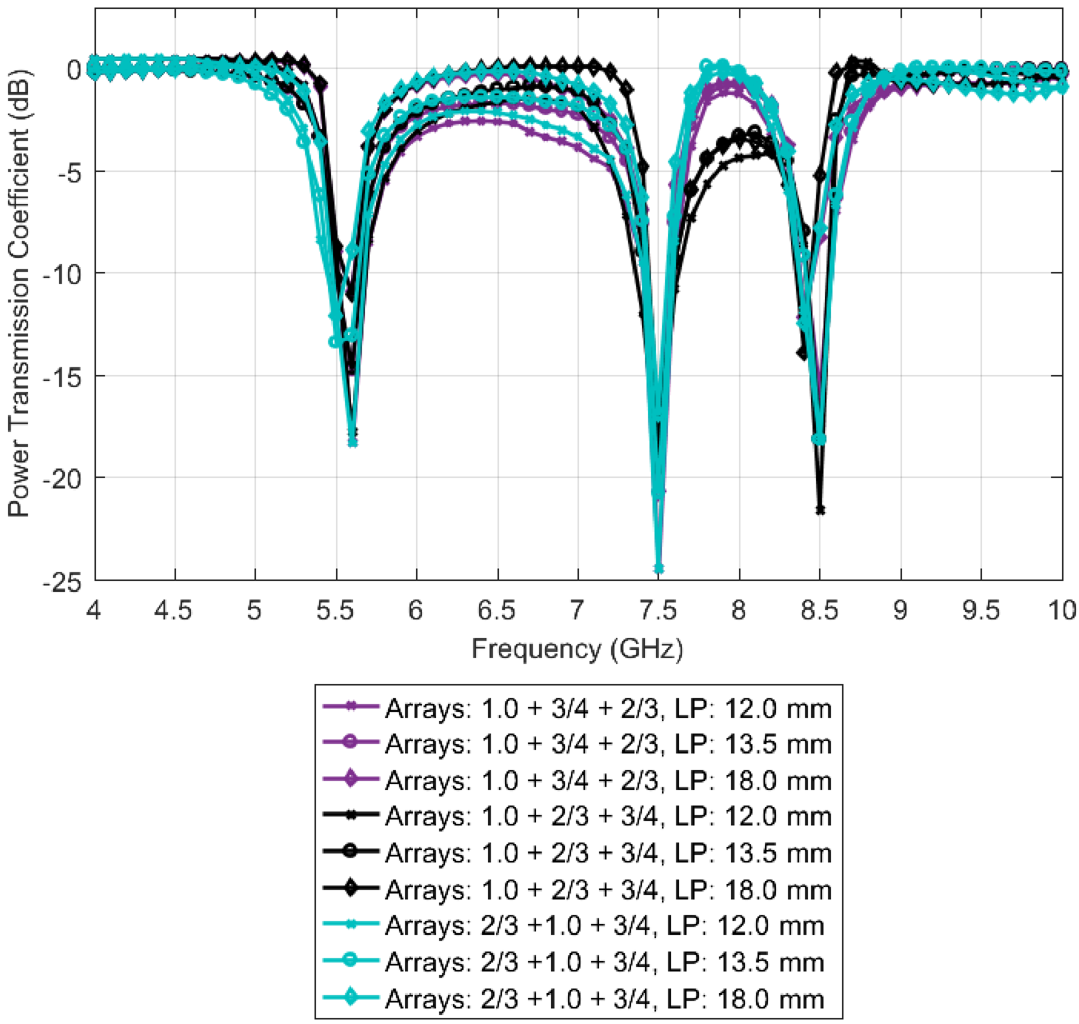

Figure 3.29: Power transmission coefficients for the triple-band metamaterials with the layouts given in Figure 3.25 (three layouts at the top) and with selected layer periodicities.

with similar sizes strongly interact with each other, resulting in reduced transparency at no-resonance frequencies. We further observe that decreasing the layer periodicity improves the dips in the dual-band operation, while inter-resonance transparency is negatively affected.

Similarly, Figure 3.25 presents six relatively successful layouts (x-y plane views) for triple-band metamaterial designs. By combining SRRs with different scales in different placement orders and with AP = 10.5 mm, relatively good performances are obtained in terms of the triple-band operation. The six layouts are composed of the

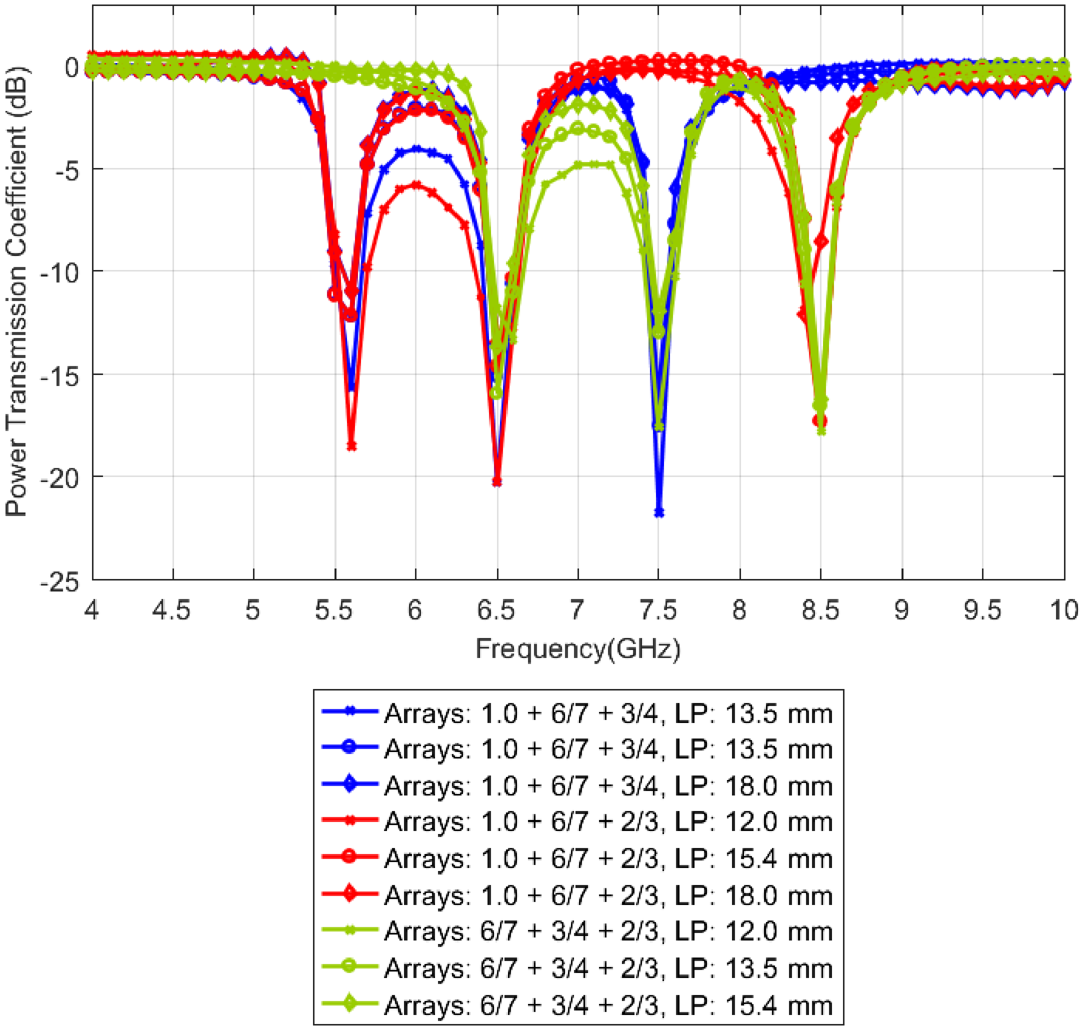

Figure 3.30: Power transmission coefficients for the triple-band metamaterials with the layouts given in Figure 3.25 (three layouts at the bottom) and with selected layer periodicities.

following two-dimensional SRR arrays (with the order of placement from right-hand side to left-hand side): Original, 3/4-scaled, and 2/3-scaled (top-left); original, 2/3-scaled, and 3/4-scaled (top-middle); 2/3-scaled, original, and 3/4-scaled (top-right); original, 6/7-scaled, and 3/4-scaled (bottom-left); original, 6/7-scaled, and 2/3-scaled (bottom-middle), and 6/7-scaled, 3/4-scaled, and 2/3-scaled (bottom-right). Near-zone power density (dBW/sm) distributions for the layout given in Figure 3.25 top-left with successful layer periodicities (LP: 12.0 mm, 13.5 mm, and 18.0 mm) on the x-y ($z = 0$) plane from 4 GHz to 10 GHz at 100 MHz intervals are shown in Figures 3.26–3.28. Opaque behaviors at the desired resonance frequencies are successfully

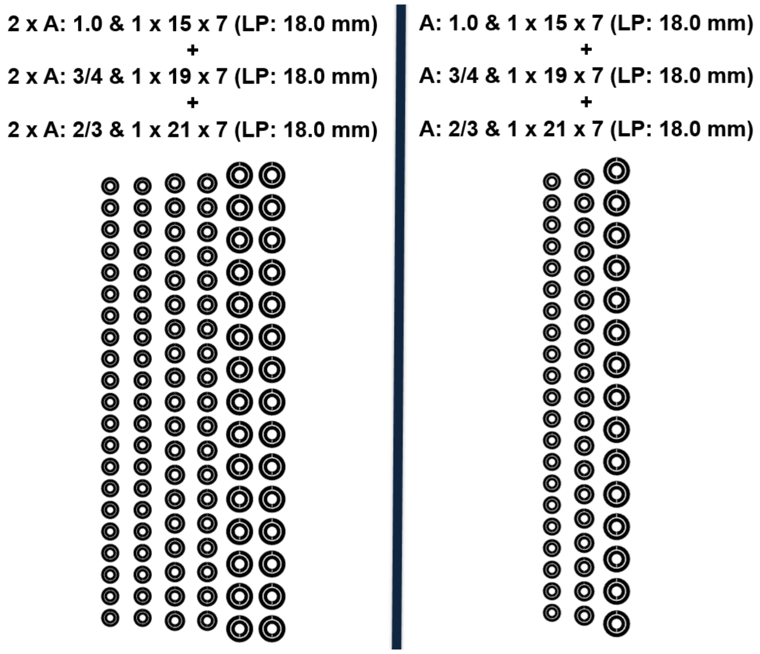
2 x A: 1.0 & 1 x 15 x 7 (LP: 18.0 mm)
+
2 x A: 3/4 & 1 x 19 x 7 (LP: 18.0 mm)
+
2 x A: 2/3 & 1 x 21 x 7 (LP: 18.0 mm)
A: 1.0 & 1 x 15 x 7 (LP: 18.0 mm)
+
A: 3/4 & 1 x 19 x 7 (LP: 18.0 mm)
+
A: 2/3 & 1 x 21 x 7 (LP: 18.0 mm)

Figure 3.31: Triple-band metamaterials with a standard layout (right) and with duplicated arrays (left) involving non-scaled, 3/4-scaled, and 2/3-scaled SRRs.

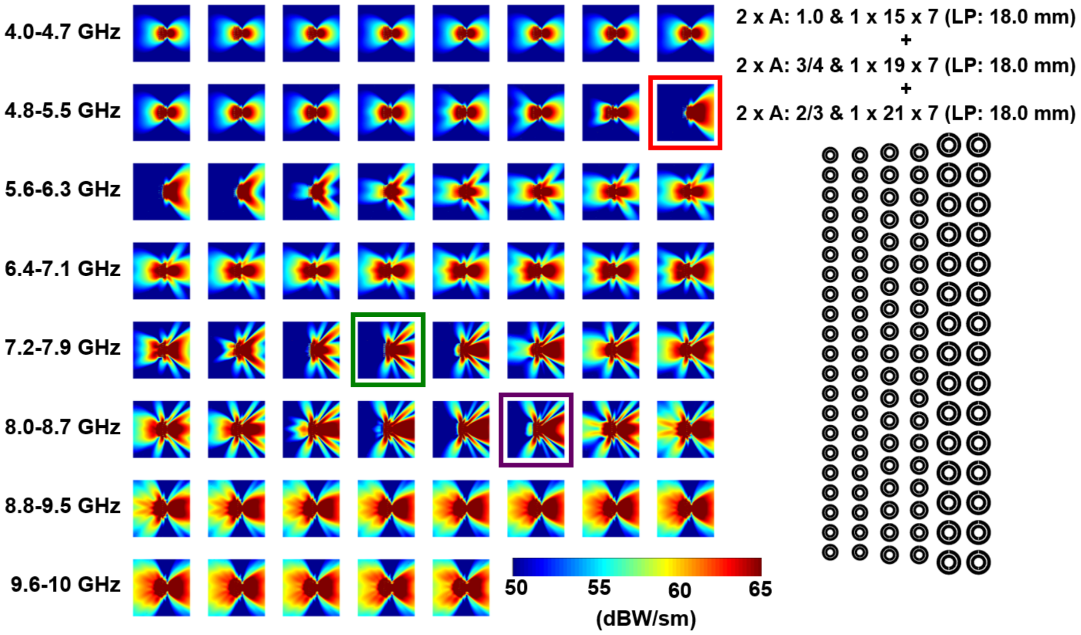

Figure 3.32: Power density distributions for the triple-band metamaterial with duplicated arrays depicted in Figure 3.31 from 4 GHz to 10 GHz at 100 MHz intervals.

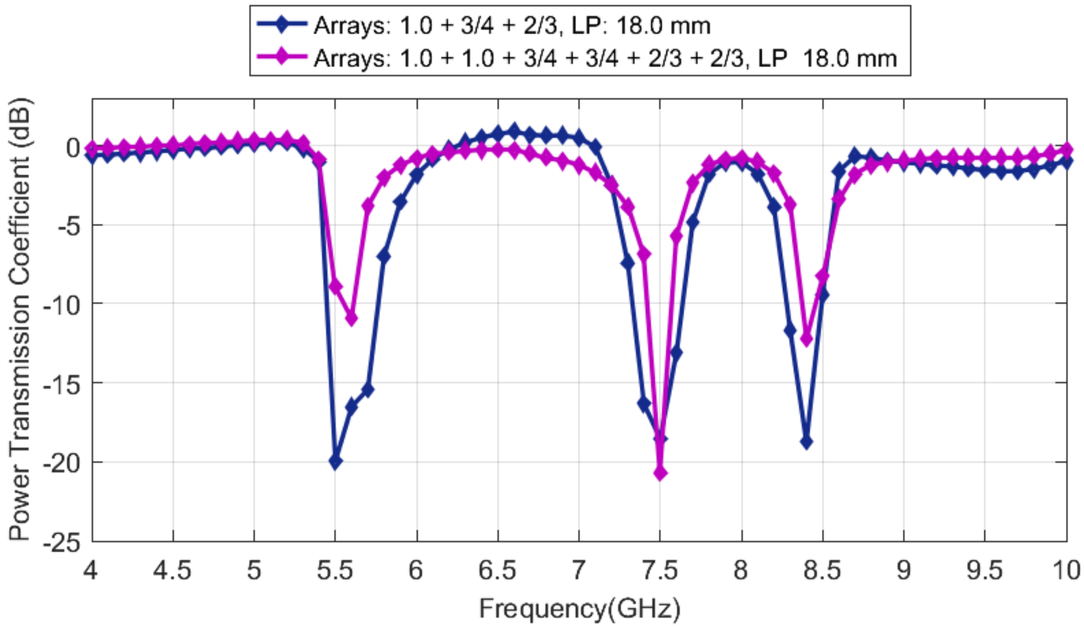

Figure 3.33: Power transmission coefficients for the triple-band metamaterials with the layouts given in Figure 3.31 when LP = 18.0 mm.

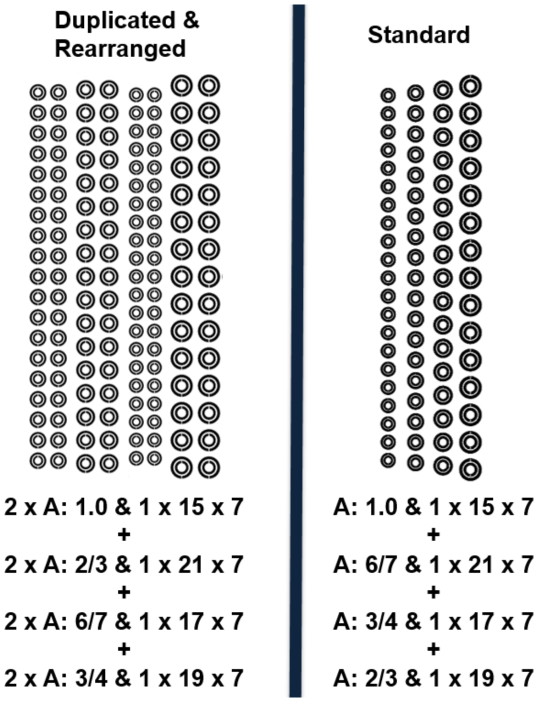
Duplicated & Rearranged
Standard
2 x A: 1.0 & 1 x 15 x 7
+
2 x A: 2/3 & 1 x 21 x 7
+
2 x A: 6/7 & 1 x 17 x 7
+
2 x A: 3/4 & 1 x 19 x 7
A: 1.0 & 1 x 15 x 7
+
A: 6/7 & 1 x 21 x 7
+
A: 3/4 & 1 x 17 x 7
+
A: 2/3 & 1 x 19 x 7

Figure 3.34: Quad-band metamaterials with a standard layout (right) and with duplicated and rearranged arrays (left) involving non-scaled, 2/3-scaled, 6/7-scaled, and 3/4-scaled SRR arrays.

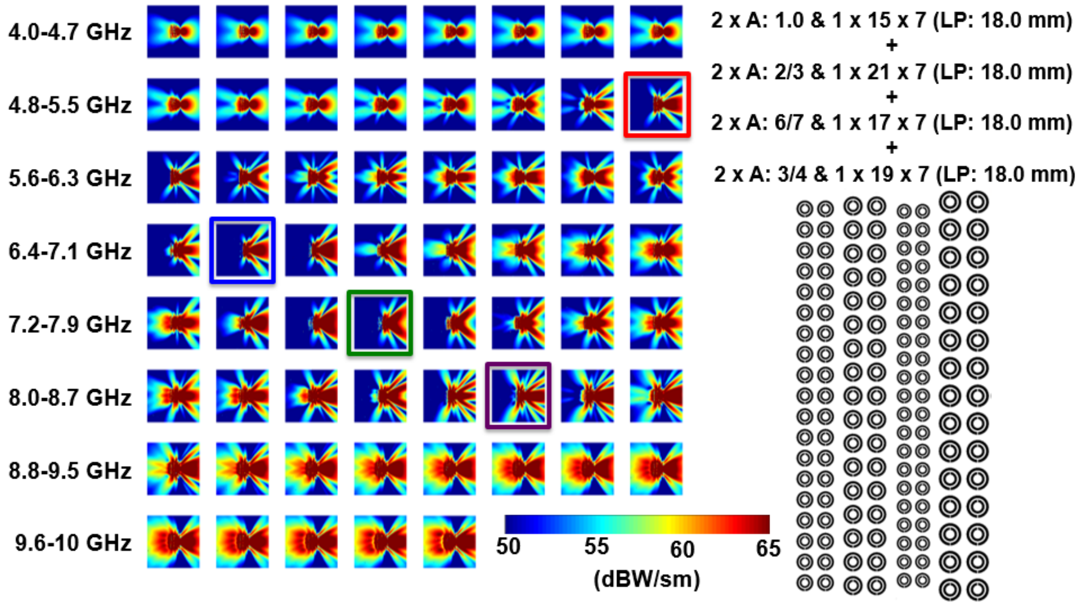
4.0-4.7 GHz
4.8-5.5 GHz
5.6-6.3 GHz
6.4-7.1 GHz
7.2-7.9 GHz
8.0-8.7 GHz
8.8-9.5 GHz
9.6-10 GHz
2 x A: 1.0 & 1 x 15 x 7 (LP: 18.0 mm)
+
2 x A: 2/3 & 1 x 21 x 7 (LP: 18.0 mm)
+
2 x A: 6/7 & 1 x 17 x 7 (LP: 18.0 mm)
+
2 x A: 3/4 & 1 x 19 x 7 (LP: 18.0 mm)
50
55
60
65
(dBW/sm)

Figure 3.35: Power density distributions for the quad-band matematerial with duplicated arrays depicted in Figure 3.34 from 4 GHz to 10 GHz at 100 MHz intervals.

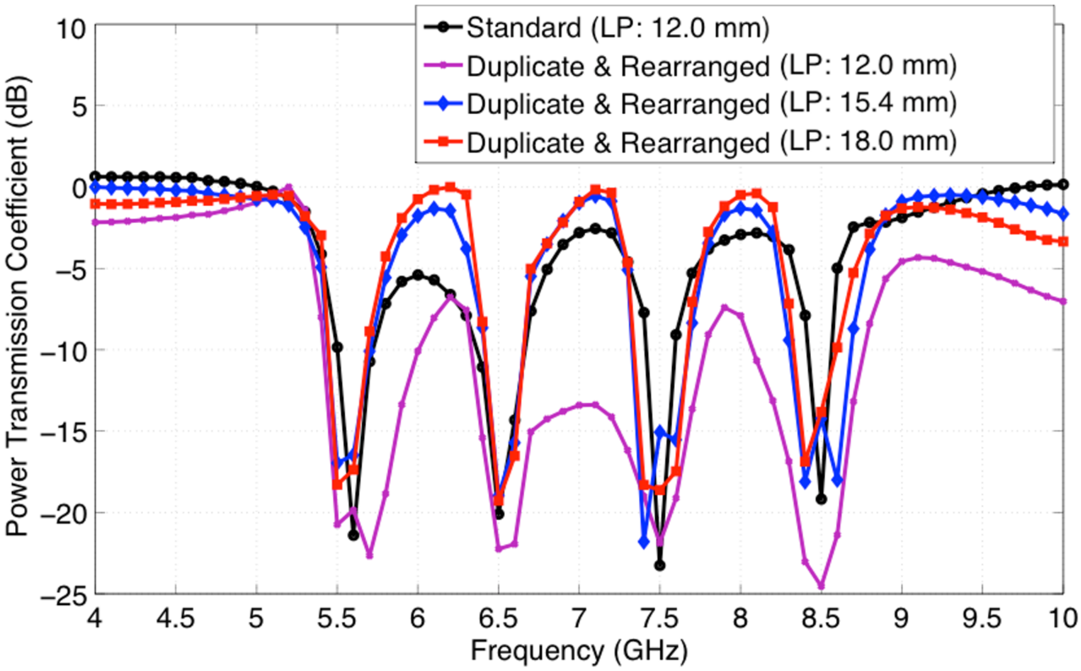

Figure 3.36: Power transmission coefficients for the quad-band metamaterials with the layouts given in Figure 3.34. For the layout with duplicated and rearranged arrays, different LP values are used.

obtained for all designs; however, complex variations in density distributions, especially at around resonance frequencies, require further inspection. For this purpose, power transmission coefficient plots for 18 different metamaterial designs are depicted in Figures 3.29 and 3.30. As also evident in these plots, all of the metamaterial structures demonstrate the desired band-stop characteristics at the resonance frequencies. At the same time, satisfying good transparency at the inter-resonance frequencies seems to be a major challenge. Increasing the layer periodicity and keeping the similar-sized SRRs away from each other improve the transparency at inter-resonance frequencies, while they tend to reduce the quality of resonances.

To further improve the performances of multiband metamaterials, we may use careful arrangements of duplicate arrays at the cost of reduced compactness. As an example, a triple-band metamaterial involving non-scaled, 3/4-scaled, and 2/3-scaled SRRs with duplicate arrays (LP = 18.0 mm and AP = 10.5 mm) is depicted in Figure 3.31. Figure 3.32 presents near-zone power density (dBW/sm) distributions for the layout with duplicated arrays and with LP = 18.0 mm, where improved shadowing effects at resonance frequencies are obtained. The power density comparison in Figure 3.33 reveals that the layout with duplicated arrays results in stronger dips, as well as better transparency at the inter-resonance frequencies. Furthermore, as a well-known result of duplicating arrays, the stopband operations have wider bandwidths.

For quad-band metamaterials, the selection of design parameters becomes more complicated. Figure 3.34 presents two successful quad-band metamaterial designs: a standard layout with LP = 12.0 mm and AP = 10.5 mm (right) and an improved layout (left), in which arrays are duplicated and rearranged to separate similar-sized SRRs. We note that, for the improved layout, nonuniform array periodicities are employed such that AP = 10.5 mm is used between different scaled SRRs, whereas identical SRRs have their own resonator periodicities. In Figure 3.35, near-zone power density (dBW/sm) distributions for the improved layout with LP = 18.0 mm are depicted, where high-quality resonances are observed. Figure 3.36 presents the power transmission coefficient with respect to frequency for four different quad-band metamaterials. It is remarkable that the improved layout with LP = 18.0 mm demonstrates superior performance with stronger dips and improved inter-resonance transparencies.

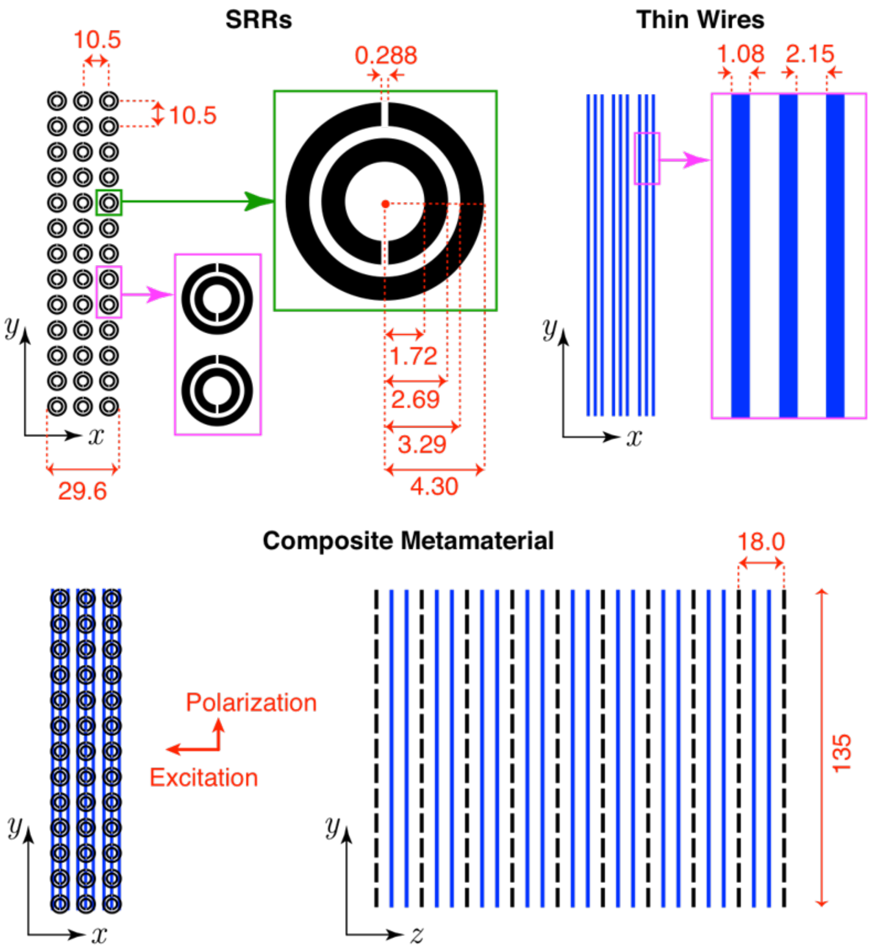
SRRs
10.5
10.5
0.288
1.72
2.69
3.29
4.30
29.6
y
x
Thin Wires
1.08
2.15
y
x
Composite Metamaterial
18.0
Polarization
Excitation
135
y
x
y
z

Figure 3.37: Details and dimensions (in mm) of the composite metamaterial that involves SRRs and thin wires.

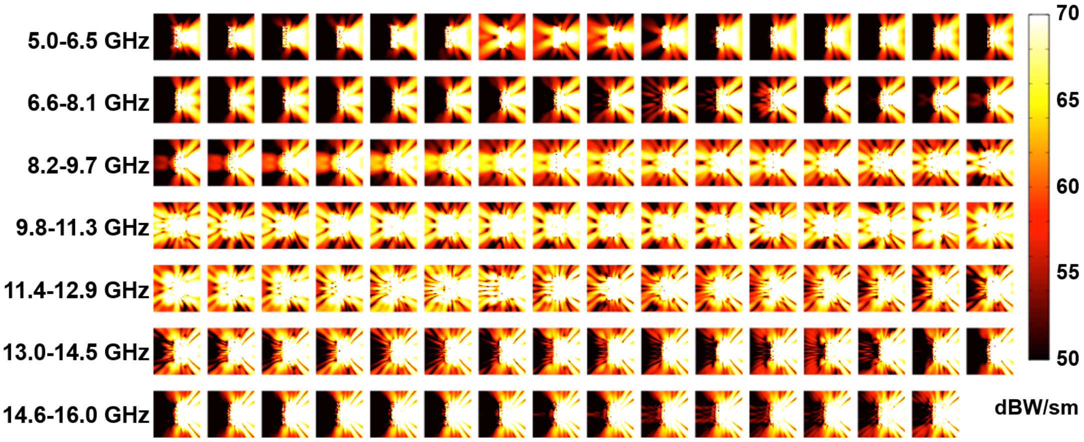

Figure 3.38: Power density distributions for the composite metamaterial design from 5.0 GHz to 16.0 GHz at 100 MHz intervals.

3.2.3 Analysis of Composite Metamaterials

Figure 3.37 presents the design of a composite metamaterial composed of SRRs and thin wires [79]. Between two SRR layers in the z direction, two thin-wire layers are placed. SRRs induce negative permeability values in relatively narrow bands, whereas thin wires induce negative permittivity values in wide bands. Then, the constructed composite metamaterial has a double-negativity characteristics, leading to the transmission of incoming electromagnetic waves with a backward travelling phase velocity at resonances. The SRR structure in Figure 3.37, which has resonances at 5.5 GHz and 11.0 GHz in vacuum, has the SRRs with the original scale considered in the previous subsection. While the resonance at 5.5 GHz is very sharp, the resonance at 11.0 GHz is wider, as expected. The dimensions and the arrangements of the thin wires are carefully designed to match with the SRR structure. The design is basically similar to the proposed geometry in [16], while it is scaled to operate at microwave frequencies. For numerical results, the three-dimensional structure is excited via a Hertzian dipole oriented in the y direction with a dipole moment of 1 Am. The near-zone power density distributions on the x-y ($z = 0$) plane from 5.0 GHz to 16.0 GHz at 100 MHz intervals are shown in Figure 3.38. The composite metamaterial becomes transparent in a narrowband at around 5.5 GHz, while a wideband transmission is observed between 8.2 GHz and 12.5 GHz, as expected. For the rest of the frequencies, the metamaterial exhibits opaque characteristics as desired.

3.2.4 Homogenization of SRR Structure

As discussed in Section 3.1.2, homogenizations of metamaterials can be extremely useful to simplify complex structures and employ simplified models in the analysis of larger systems. At the same time, homogenization itself must be realistic and accurate in order to model the electromagnetic response of the structure. For this purpose, we use genetic algorithms supported via full-wave simulations by MLFMA. Now, we consider numerical examples involving the homogenization of SRR structures. The following numerical results are obtained by using the optimization procedure depicted in Figure 3.39. First, the implementation of genetic algorithms starts by

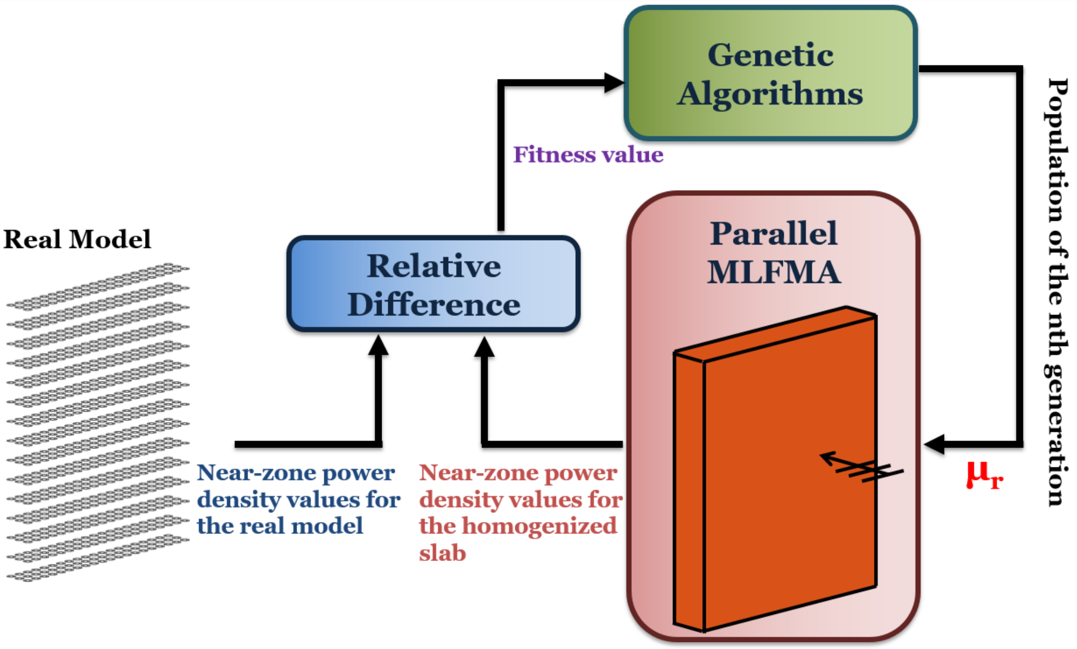
Genetic Algorithms
Fitness value
Population of the nth generation
Real Model
Relative Difference
Parallel MLFMA
Near-zone power density values for the real model
Near-zone power density values for the homogenized slab
μr

Figure 3.39: Representation of the mechanism used for the homogenization of SRR arrays.

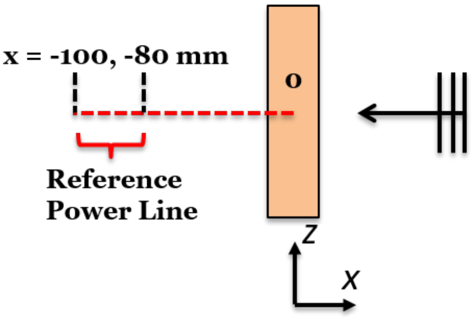
x = -100, -80 mm
o
Reference Power Line
z
x

Figure 3.40: Illustration of the optimization problem involving a non-dielectric slab and a sample line for the near-zone power density values.

initializing the first population. Then, the created permeability values (chromosomes) for the homogenized slab (that encloses the real model) are transferred to the MLFMA solver. The relative difference between the near-zone power density values of real and homogenized models is used in the calculation of the cost function (CF) defined as

$$\mathrm{CF} = ||f(\boldsymbol{r}) - f_{ref}(\boldsymbol{r})||_2/||f_{ref}(\boldsymbol{r})||_2, \tag{3.4}$$

where $f(\boldsymbol{r})$ and $f_{ref}(\boldsymbol{r})$ are updated and reference density values, respectively. We note that the details of genetic algorithms are presented in Section 3.1.2.

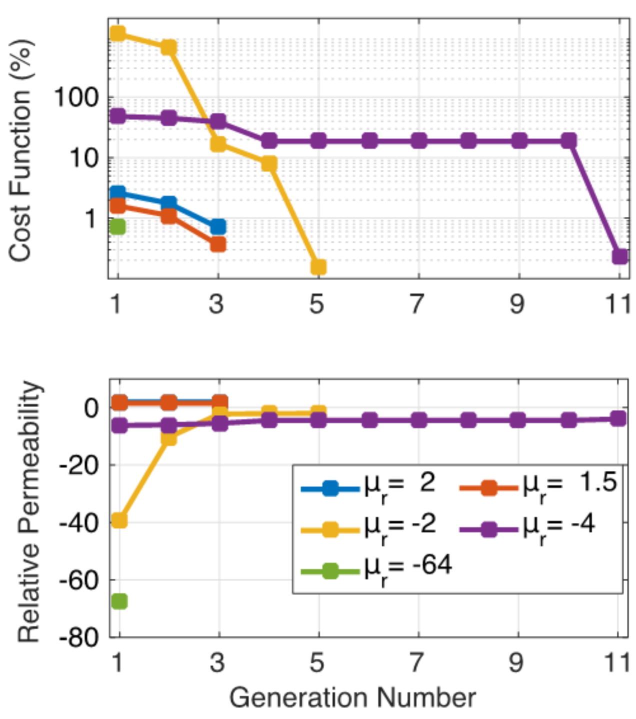

Figure 3.41: Cost function and relative permeability for the optimization problems of slabs with known permeability values.

As numerical examples, two sets of optimization problems are considered [80]. For the first one, non-dielectric slabs with relative permeability values of -64, -4, -2, 1.5 and 2 are solved at 8 GHz as reference solutions for optimization trials. Each slab with a size of $19.7 \times 138.7 \times 168.0$ mm is excited by a plane wave with $-x$ propagation direction and $+y$ polarization, while near-zone power density values are sampled on a line as demonstrated in Figure 3.40. Then, the optimization procedure is employed using the same slab size and relative permeability values in the range from -256 to 4, omitting the region between -1 and $+1$, to reach the given reference solution. Using 14 bits, the range of permeability values is sampled with 0.0159 intervals. If the relative difference of 1% is satisfied, the optimization is terminated. Figure 3.41 presents the cost function and relative permeability plots with respect to generations of the genetic algorithms. For each reference problem, the termination criterion is met after a few generations. It is observed that the optimization immediately converges when the relative permittivity is -64.

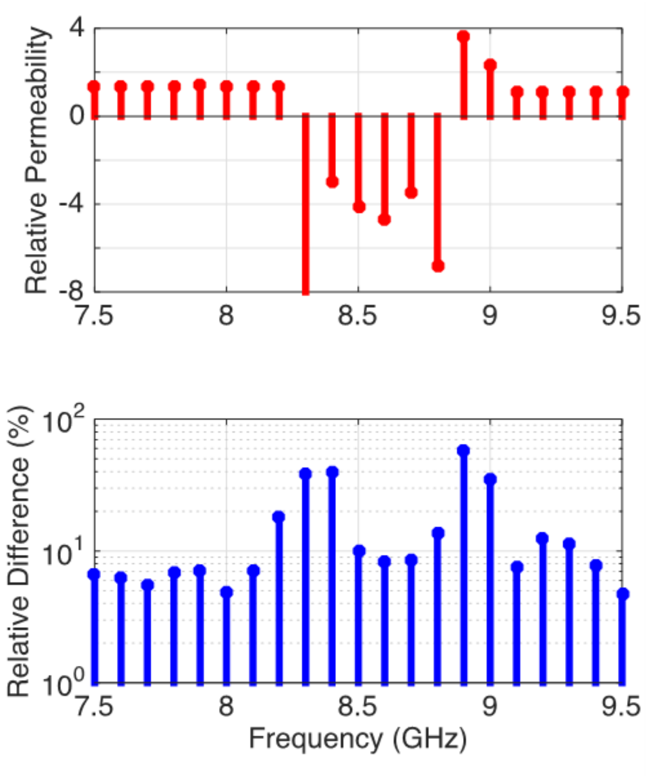

Figure 3.42: Optimized relative permeability and relative difference in the permeability values with respect to frequency for the optimization problem involving an SRR array.

As the second set of problems, the $3 \times 20 \times 15$ SRR array (previously investigated in this chapter) that resonates at around 8.5 GHz in free space (with $19.7 \times 138.7 \times 168.0$ mm size) is homogenized. The SRR array and the slab of the same size are illuminated by plane waves with $-x$ propagation direction and $+y$ polarization, and the sample line used in the first set of problems is considered to compute the power density values. The real and homogenized models are discretized with 57,600 (with 0.75 mm mesh size) and 39,480 (with 3 mm mesh size) unknowns, respectively. Therefore, the simplification of the real model is achieved not only in terms of the complexity of details, but also in terms of the number of unknowns. In the optimization trials, the maximum number of generations is set to 20, while the maximum relative difference is set to 10%. The optimized relative permeability and relative difference plots are shown in Figure 3.42. At 13 frequencies, the termination criterion is met, whereas, at four frequencies, the relative difference is close to the criterion. For the remaining five frequencies, relatively high values are obtained. Figure 3.43 presents the transmitted

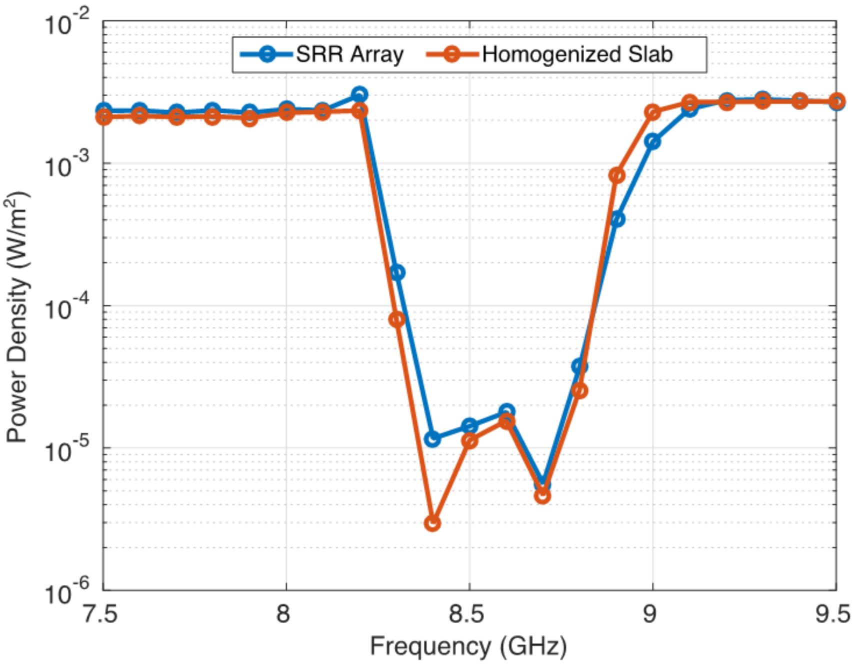

Figure 3.43: Transmitted power density through the real and homogenized models of the SRR array with respect to frequency.

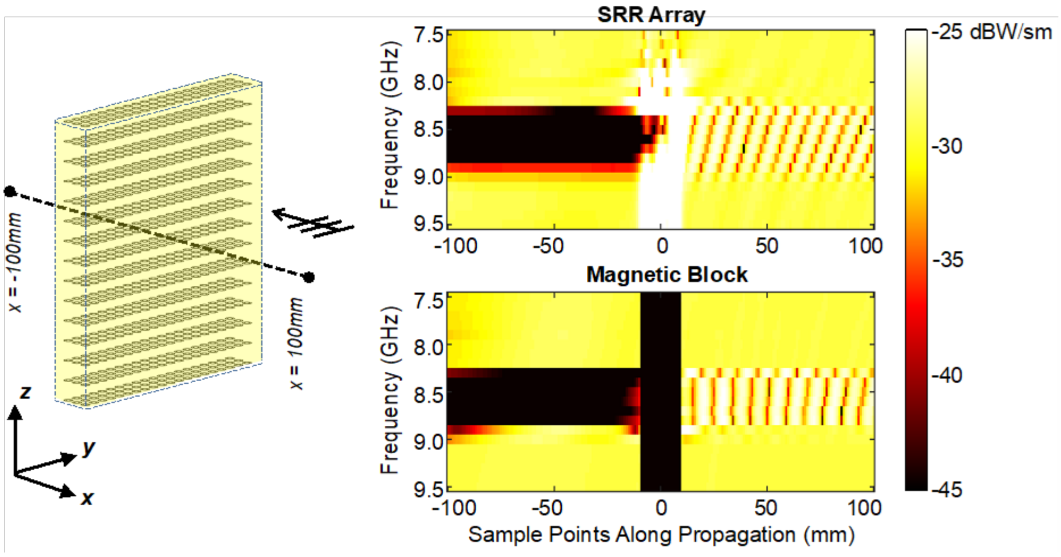

Figure 3.44: Power density distributions on the central line obtained for the real and homogenized models with respect to frequency.

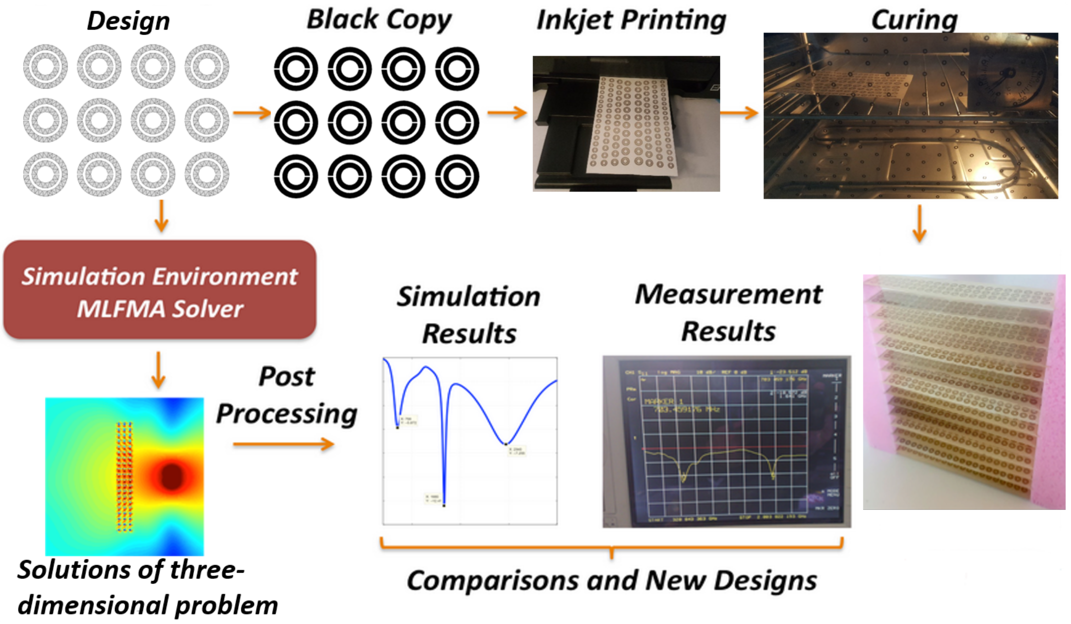
Design
Black Copy
Inkjet Printing
Curing
Simulation Environment MLFMA Solver
Post Processing
Simulation Results
Measurement Results
Solutions of three-dimensional problem
Comparisons and New Designs

Figure 3.45: Steps to fabricate three-dimensional metamaterial structures and validation of simulation/measurement results.

power density through the real and homogenized models with respect to frequency. We observe that the characteristics of the SRR array are presented very well by the homogenization. We further note that small variations between the solutions of the real and homogenized models exist in particular at the stop-band frequencies. Even though there are frequencies at which the termination criterion is not satisfied, it is clear that homogeneous representation is achieved. In fact, the reason for large relative difference values is extremely negative relative permeability values of the SRR structure at around resonance frequencies. Figure 3.44 shows the power density values calculated through the central line with respect to frequency to support our claims on the successful homogenization of the SRR array.

Initial results presented above demonstrate that it is possible to extract equivalent electromagnetic parameters of a metamaterial by using genetic algorithms and full-wave solutions. Application of the developed approach for the homogenization and characterization of metamaterial structures based on their simulations and measurements is the topic of further research.

3.3 Fabrications via Inkjet Printing

Three-dimensional metamaterial structures mentioned in the previous section are fabricated by using a very low-cost inkjet printing method. Standard printers are employed with silver-based inks. The fabrication procedure, the challenges arise during low-cost inkjet printing, and sensitivity analysis to test fabrication errors are presented in this section.

3.3.1 Very Low-Cost Inkjet Fabrication

Figure 3.45 depicts the cycle of the low-cost inkjet-printing procedure, including the validation of measurement and simulation results. After numerical results satisfy the design criteria, the major steps of the low-cost inkjet printing procedure can be listed as follows.

- First, the black copies of the SRR layers are created by using Siemens NX software. It is crucial that the geometries are represented only by black color to have uniform prints.
- The produced copies are printed via Epson Stylus C88+ printer using Novacentrix JS-B25P ink (including 25% silver) on Canon GP-501 Glossy papers by selecting "best-photo option" and "photo-enhance property" for improved resolution. Conductivity issues arise for lower silver concentrations, as well as for higher silver concentrations that lead to reduced absorbance. We note that lower absorbance rates are also obtained for other photograph paper types. Therefore, both ink and paper types are critical in order to produce high-quality inkjet prints.
- Heat curing is applied to improve the conductivity of the printed samples by using standard ovens at 150°–170°C for 90 minutes. Higher temperature values result in cracks in the printed samples, whereas poor conductivity is obtained when using lower temperatures. Therefore, the curing process is optimized in terms of both duration and temperature values. After successful curing, hundreds of kΩ of DC resistance values can be reduced to several ohms for the outer ring of a typical SRR. The dramatical drop in the resistance value is a good demonstration of the improved conductivity.

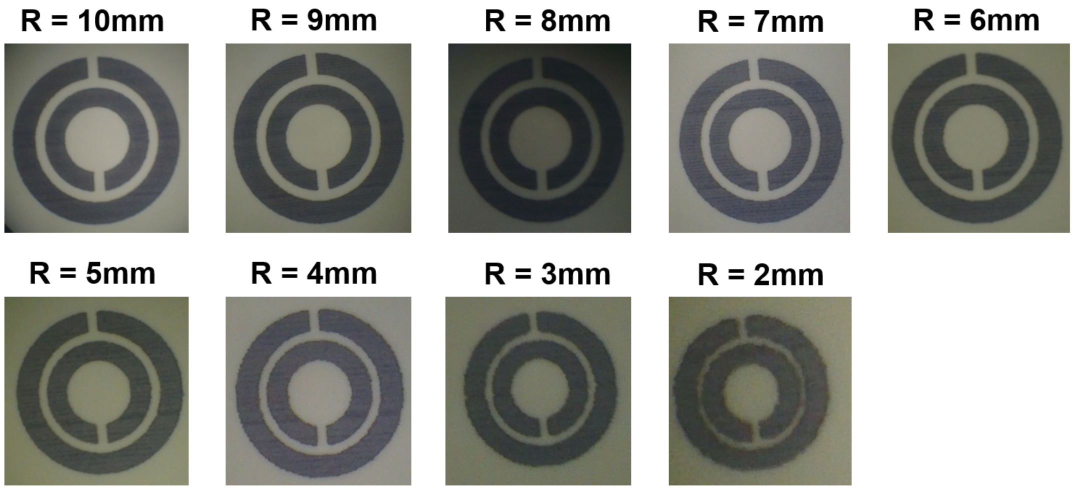

Figure 3.46: SRR samples with different outer ring sizes (R: outer radius) fabricated via low-cost inkjet printing.

- Finally, a three-dimensional structure is constructed by stacking the printed layers with the help of foams.

3.3.2 Inkjet Printing Challenges

Although the low-cost inkjet printing procedure has major advantages, particularly in terms of cost, standard inkjet printers have relatively poor performance in terms of quality compared to the printers that are specifically designed for material printing. Accordingly, the proposed and used low-cost printing method inevitably brings some challenges as follows.

- Curing effect that is optimized for 90 minutes at 150°–170°C cannot be omitted or performed in a different way other than its optimized course. In fact, curing is essential to make silver nanoparticles strongly connect to each other. Hence, it is a crucial part that requires careful attention of the fabrication process.

- Printing inconsistencies between different samples may deteriorate the response of the overall structure. This may occur particularly for SRR arrays, which operate best when the SRRs are perfectly identical.

- In general, printing defects may significantly affect the performance of the printed samples, particularly if the details of the structure becomes comparable to the printing resolution. As an example, some printing defects that become observable when dealing with smaller SRRs are shown in Figure 3.46. The SRR sample with an outer radius of 2 mm reveals visible defects, which even change the geometry itself. We note that minimum resolution that can be obtained with the used printer is 0.1 mm.

- Large and coarse designs are also difficult to produce with inkjet printing since printing uniformity may not be ensured throughout the printing area. However, detailed and complicated designs do not introduce any extra difficulty, unlike large and coarse designs, provided that resolution issues are avoided.
- When printing starts with a new printer, it can be used with the maximum performance for less than a month since clogging blocks the printheads. In order to slow down the clogging problem, a cleaner solution can be used to print many dummy samples until clean samples (without any ink residual) are obtained.

3.3.3 Sensitivity Analysis

As a major drawback of the low-cost inkjet printing besides its challenges, fabrication errors are inevitable. Three different types of fabrication errors, namely, inclined layers, shifted layers, and deformed SRRs are particularly investigated. Random inclinations of layers that typically occur in the process of stacking layers via foams are considered with a maximum of 2° inclination. Similarly, shift of layers with a maximum of ±2 mm deviations from the desired (13 mm) layer periodicity is examined. Considering the resolution issues of the low-cost inkjet printing, deformed SRRs with random geometric deformations are also inspected. Figure 3.47 depicts the near-zone power density distributions for the regular (ideal) SRR array, as well as the cases with three different fabrication errors at 7.8 GHz (significant variations are observed only at 7.8 GHz in the entire frequency range) on x-y and y-z planes when the structures are in vacuum. The effects of shifted layers and deformed SRRs are clearly visible, whereas inclinations of layers almost have no effect on the response of the structure. Since the resonance behavior of the SRRs strongly depends on the shape and geometric parameters, it is indeed expected to observe the distinct impact of fabrication errors via deformed SRRs, while the results show that these effects do not significantly change the basic operation of the constructed structures.

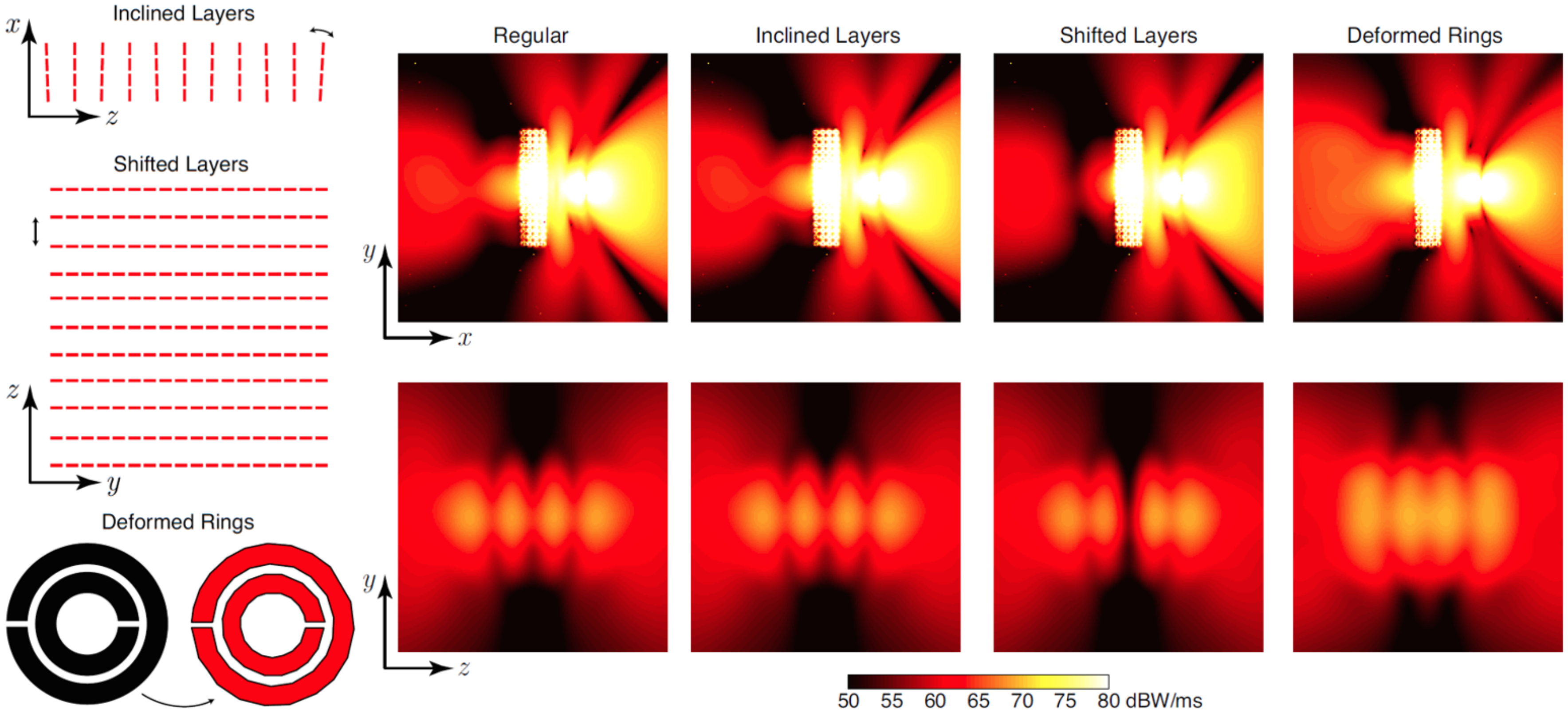

Figure 3.47: Simulation results for near-zone power density distributions on x-y and y-z planes for the SRR array in Figure 3.8 with different fabrication errors. The frequency is set to 7.8 GHz, while the structures are located in vacuum.

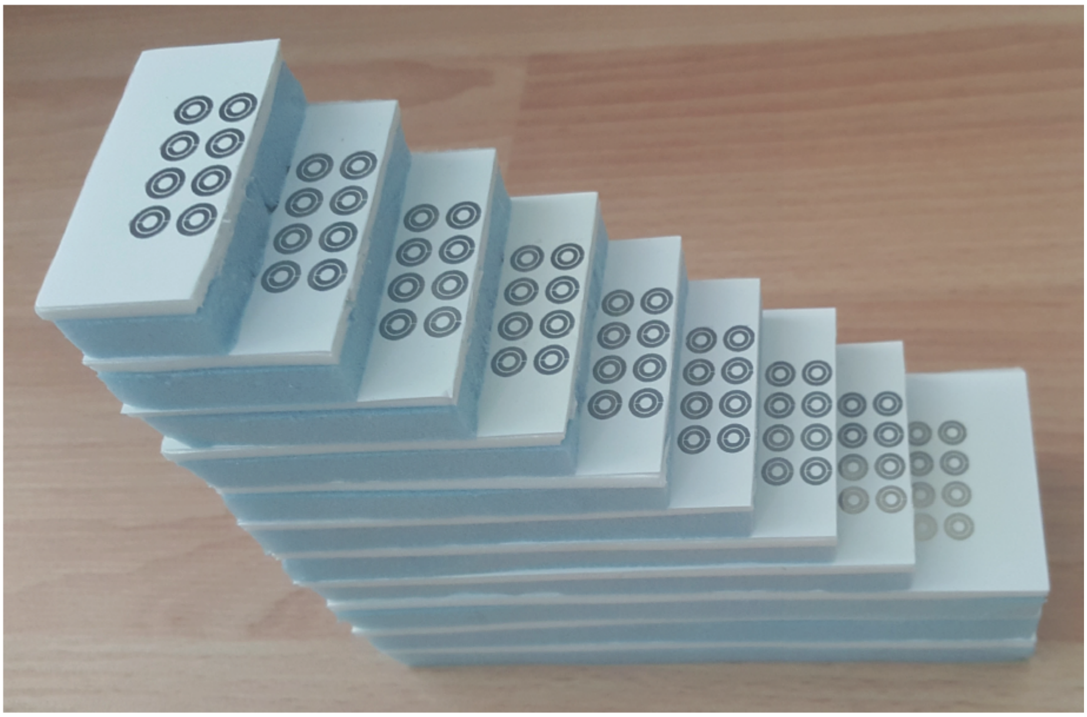

Figure 3.48: Photograph of a fabricated SRR array. The design is shown in Figure 3.8.

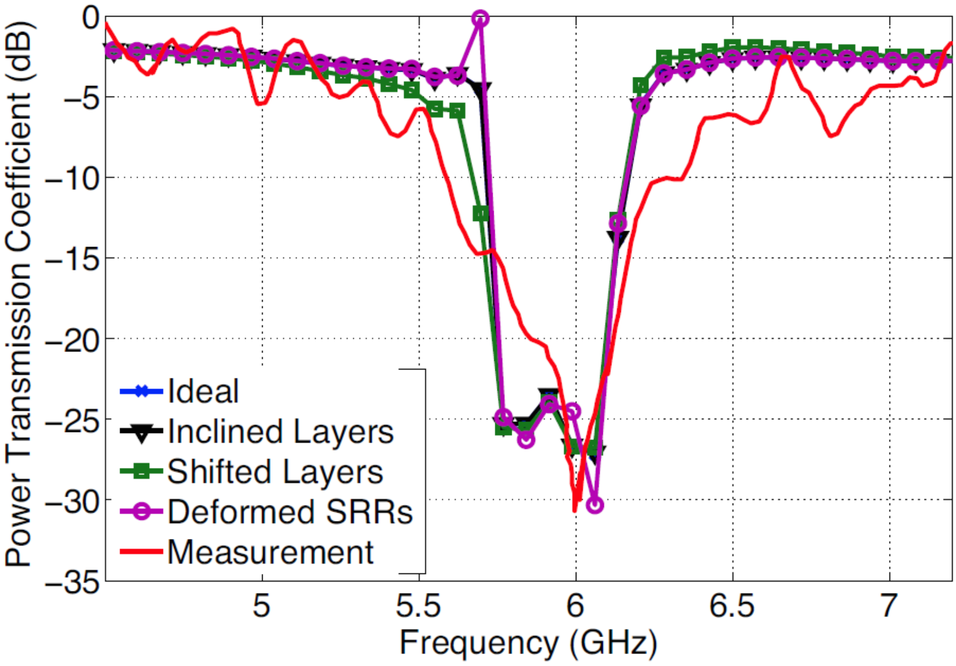

Figure 3.49: Simulation and measurement results for the power transmission values of the SRR array in Figure 3.48.

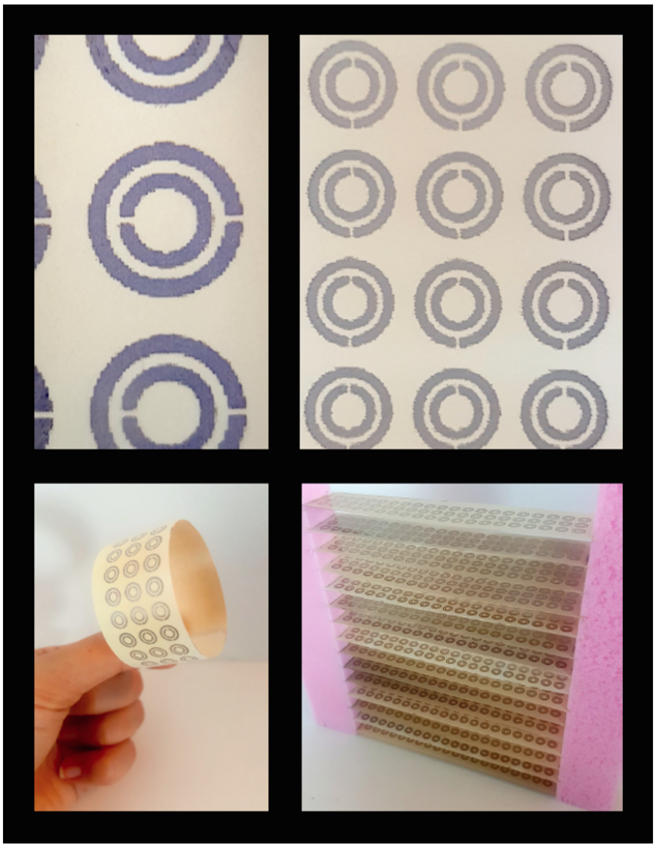

Figure 3.50: Photographs of a fabricated SRR array. The design is shown in Figure 3.3.

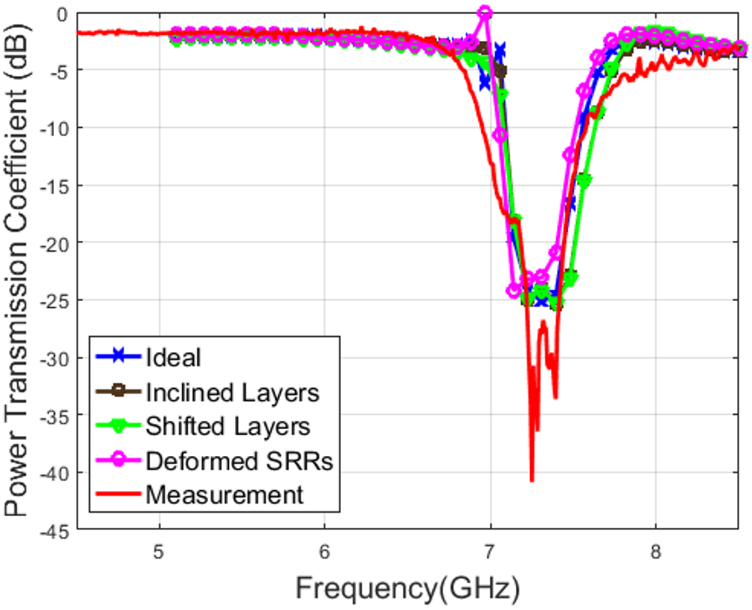

Figure 3.51: Simulation and measurement results for the power transmission values of the SRR array in Figure 3.50.

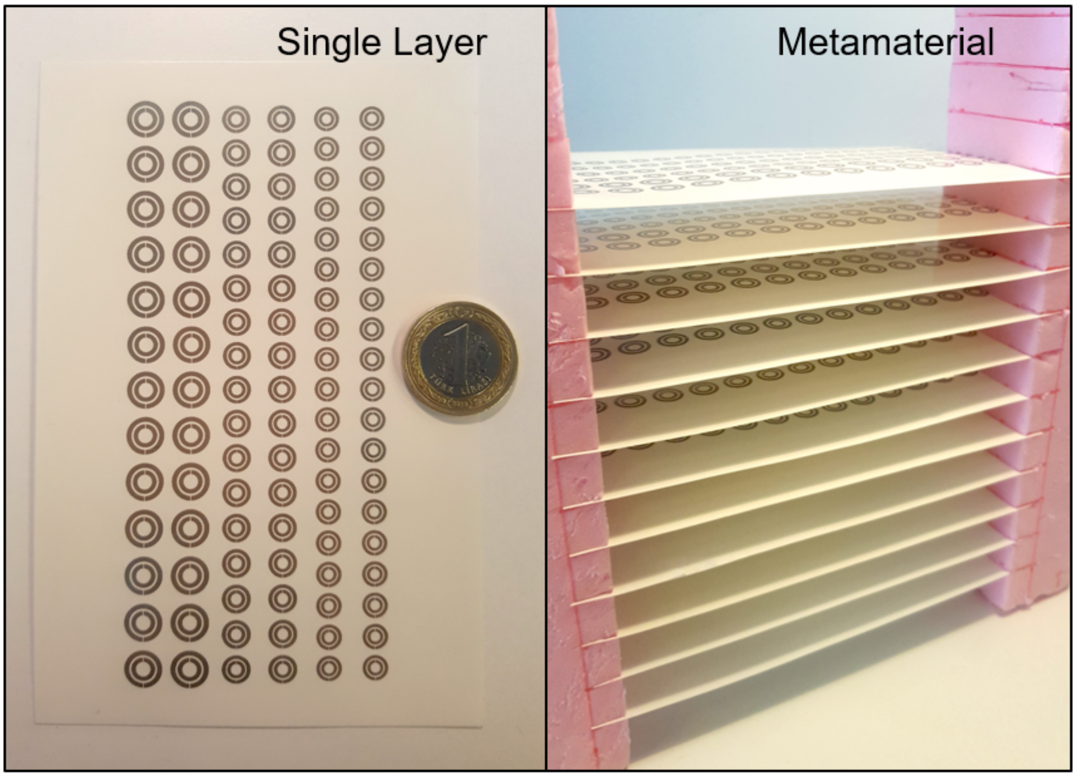
Single Layer
Metamaterial

Figure 3.52: Photographs of a fabricated triple-band metamaterial. The design is shown in Figure 3.31.

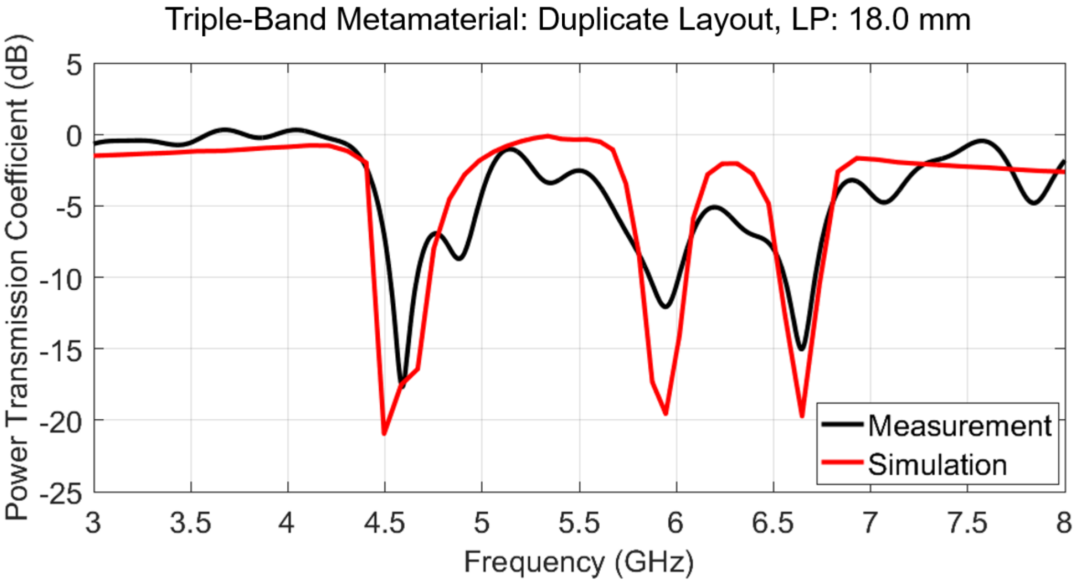

Figure 3.53: Simulation and measurement results for the power transmission values of the triple-band metamaterial in Figure 3.52.

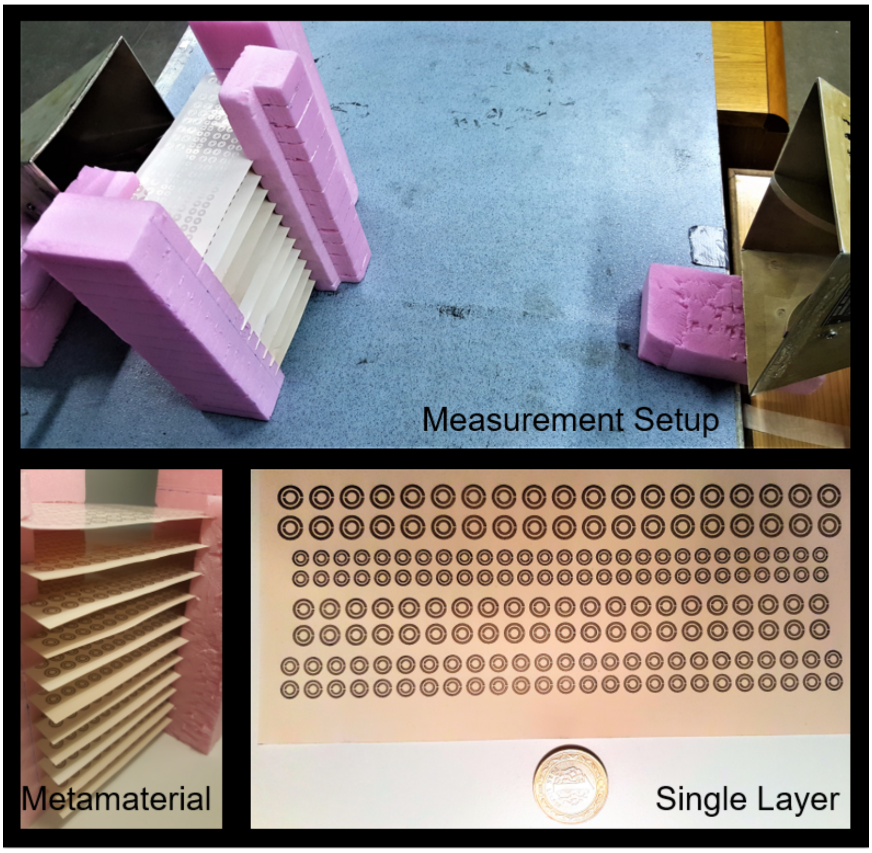
Measurement Setup
Metamaterial
Single Layer

Figure 3.54: Photographs of a fabricated quad-band metamaterial. The design is shown in Figure 3.34.

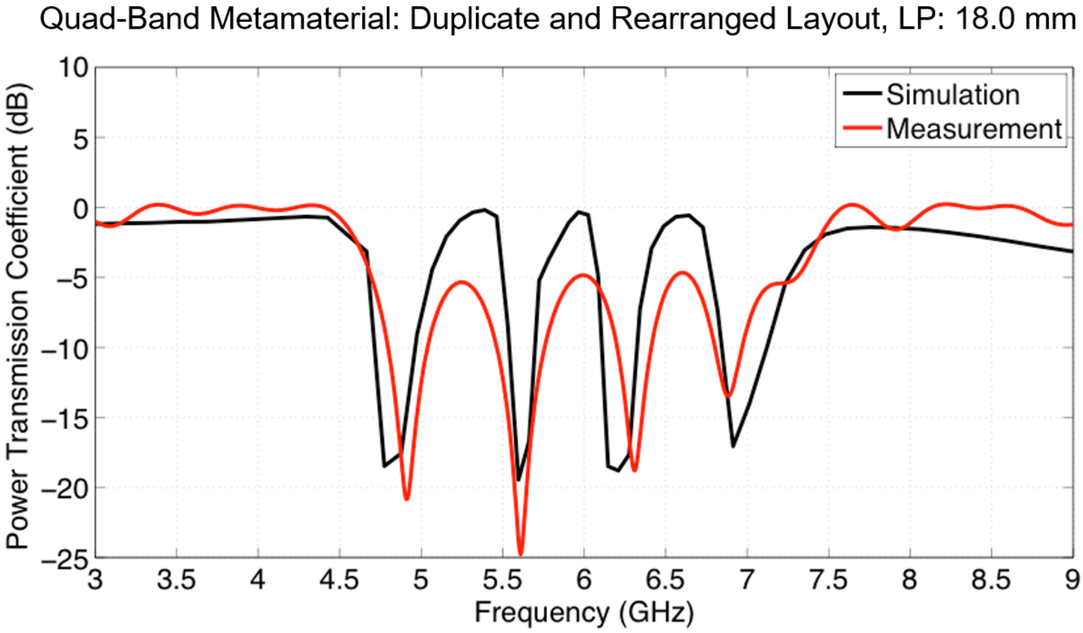

Figure 3.55: Simulation and measurement results for the power transmission values of the quad-band metamaterial in Figure 3.54.

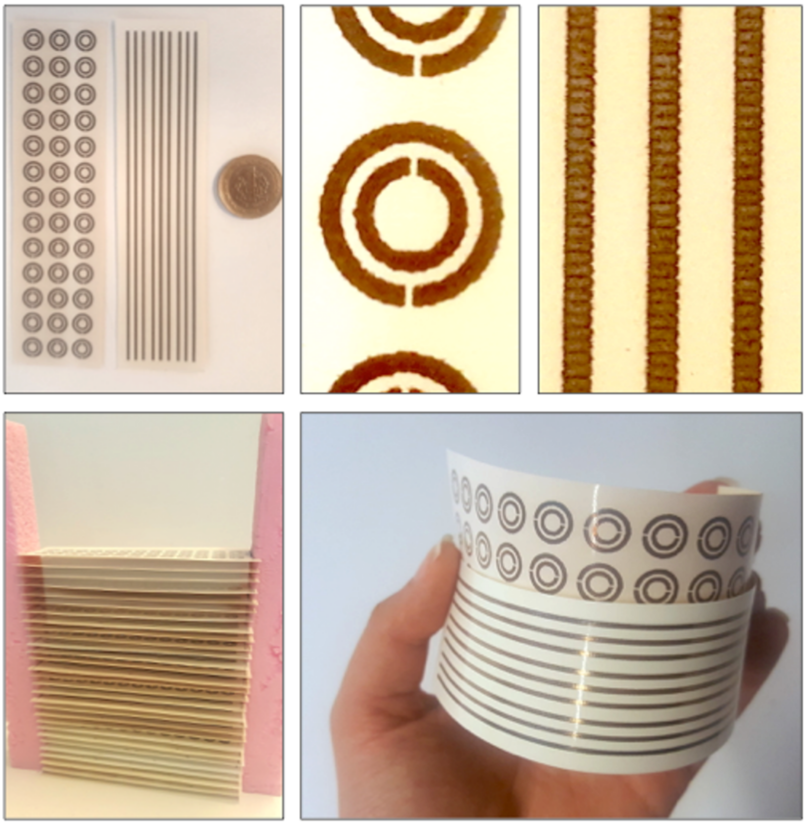

Figure 3.56: Photographs of a fabricated composite metamaterial. The design is shown in Figure 3.37.

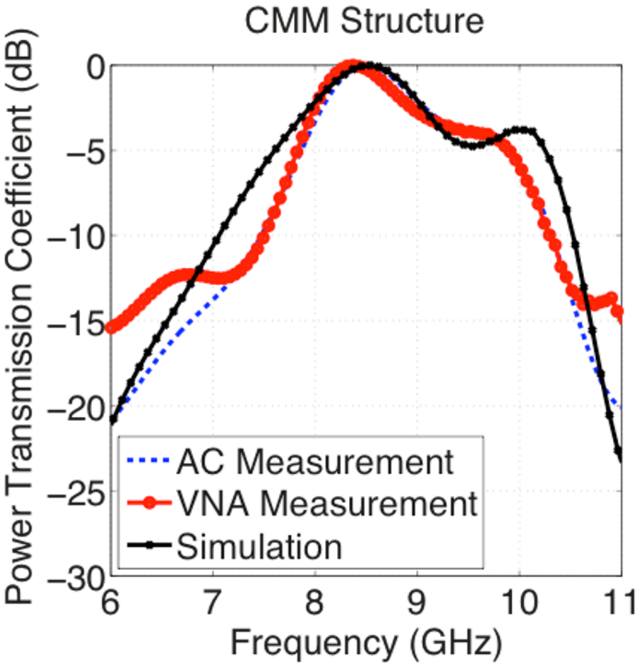

Figure 3.57: Simulation and measurement results for the power transmission values of the composite metamaterial in Figure 3.56.

3.4 Measurement Results

Measurements are carried out either in an anechoic chamber or by using a vector network analyzer and two standard horn antennas. The metamaterials are placed between the horn antennas in both methods and free-space measurements without metamaterials are used for the normalization of transmission. The relative permittivity of the paper in the frequency range is approximately 3.5 and the Maxwell-Garnett approximation is employed with 50% fill rate to include dielectric effects of the paper (effective permittivity of 1.875) in all simulations.

3.4.1 Single-Band SRR Results

Figure 3.49 presents the power transmission values obtained with simulations and anechoic-chamber measurements for the fabricated SRR array shown in Figure 3.48 (see Figure 3.8 for the design). Similarly, Figure 3.51 presents the power transmission values obtained with simulations and anechoic-chamber measurements for the fabricated SRR array shown in Figure 3.50 (see Figure 3.3 for the design). Strong resonances with the transmission values less than -30 dB at 6 GHz and 7.25 GHz are obtained with the fabricated SRR arrays in Figures 3.48 and 3.50, respectively. In addition, a very good agreement between the measured and simulated results is obtained. Figures 3.49 and 3.51 also demonstrate the tolerance of the SRR arrays to fabrication errors. We note that the flexibility of the printed samples is further demonstrated in Figure 3.50.

3.4.2 Multiband SRR Results

Figure 3.53 presents the power transmission values obtained with simulations and vector-network-analyzer measurements for the fabricated triple-band metamaterial shown in Figure 3.52 (see Figure 3.34 for the design). Similarly, Figure 3.55 presents the power transmission values obtained with simulations and vector-network-analyzer measurements for the fabricated quad-band metamaterial shown in Figure 3.54 (see Figure 3.34 for the design). Triple-band and quad-band characteristics are clearly obtained in the measurements, as shown in Figures 3.53 and 3.55, respectively. The discrepencies in the inter-frequency transparency properties seem to be related to excessive metallic losses in the fabricated samples.

3.4.3 Composite Metamaterial Results

Finally, in Figure 3.57, power transmission values obtained via two sets of measurements by using vector network analyzer (VNA) and anechoic chamber (AC) for the fabricated composite structure given in Figure 3.56 (see Figure 3.37 for the design) are shown. Frequency-dependent transparency is achieved by using the fabricated composite metamaterial. The measurement and simulation results have good agreement in the transmission part, while variations are observed at frequencies for opaque characteristics due to measurement errors. It is remarkable that the results in Figure 3.57 represent an important demonstrations of double negativity at microwave frequencies.

3.5 Concluding Remarks

In this chapter, we consider design, simulation, and fabrication of inkjet-printed metamaterials involving SRRs and thin wires. When SRRs resonate, they induce negative permeability in their surrounding media, leading to intense attenuation of electromagnetic waves as observed from the near-zone field and power density distributions. In addition to well-known SRR arrays that exhibit single-band characteristics, we consider novel multiband structures involving SRRs of different sizes. For these structures, in order to maintain the compactness of the designs, non-identical SRR arrays cannot be separated too much from each other; however, to avoid disastrous effects of strong couplings between them, they should be carefully positioned that can be achieved in the developed rigorous simulation environment. To further improve the performances of multiband metamaterials, we use careful arrangements of duplicate arrays at the cost of reduced compactness. After numerical results satisfy the design criteria, the low-cost inkjet printing procedure is followed to fabricate the metamaterial structures. It is evident in the simulation and measurement results that single-band and multiband operations for single-negativity characteristics, as well as single-band operation for double-negativity characteristics are achieved with the developed designs. Since the resonance behaviors of SRRs strongly depend on the shape and geometric parameters, it is expected to observe the impact of fabrication errors when using inkjet printing, while the results show that these effects do not significantly change the basic operations of the constructed structures. In the context of simulations, it is also demonstrated that homogenizations of metamaterials can be extremely useful to simplify complex structures and employ simplified models in the analysis of larger systems.

CHAPTER 4

SIMULATIONS OF METALLIC NANOPARTICLES AT TERAHERTZ FREQUENCIES

In this short chapter, we discuss numerical simulations of metallic nanoparticles at lower THz frequencies. Comparisons of PEC and penetrable models, as well as the accuracy and efficiency of penetrable formulations, are presented.

4.1 Nanoscale Metals at Terahertz Frequencies

Among different kinds of metals, Ag, Au, and Cu are mostly used to build nanostructures. At the higher frequencies of the electromagnetic spectrum, the relative permittivities of these metals can be defined as

$$\epsilon_r = -\epsilon_{Rr} + i\epsilon_{Ir}, \tag{4.1}$$

considering them as penetrable materials. Figure 4.1 depicts the relative complex permittivity of silver (Ag) with respect to frequency using Drude model (D model) [81], Lorentz-Drude model (LD model) [82], as well as measurement results from a milestone paper [83]. As one would expect, the sharp decrease in the real part of the relative permittivity at low frequencies is clearly observed. In fact, the relative permittivity of Ag reaches extreme values, such as $\epsilon_r = (-0.3 + i3.4) \times 10^5$ and $\epsilon_r = (-1.7 + i2.0) \times 10^4$ at 1 THz and 10 THz, respectively, according to the LD model. Although metals at such frequencies are treated as PEC objects in general, they should be formulated via penetrable modeling for small-scale structures.

Investigating the exponential part of the homogeneous-space Green's function, which is the kernel function of SIE formulations, provides the key information on the behavior of metals at these frequencies for problems involving extreme permittivity values.

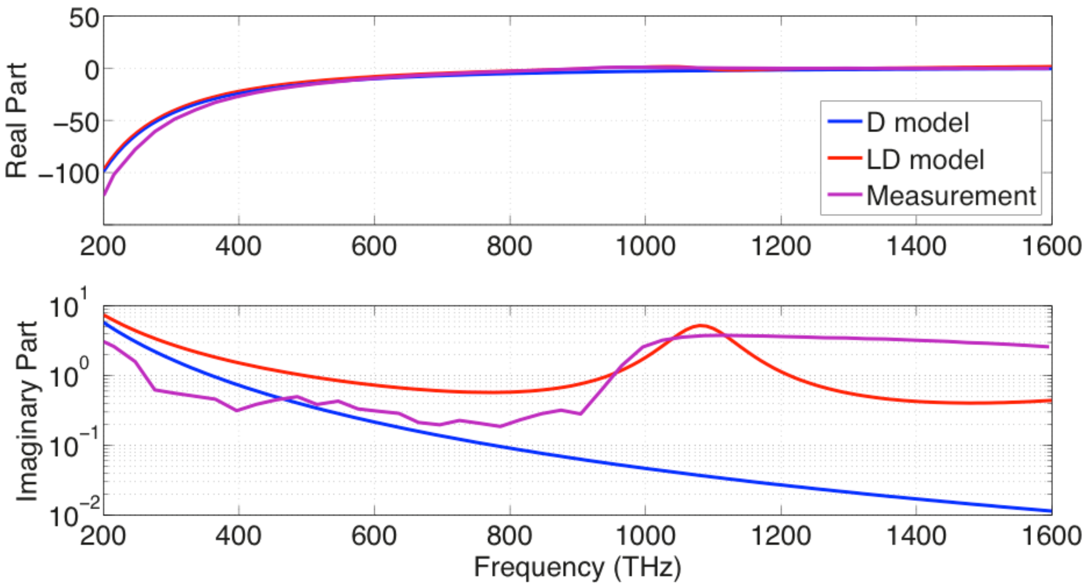

Figure 4.1: Relative complex permittivity of silver (Ag) with respect to frequency.

Specifically, we have

$$\exp(ikR) = \exp(i\omega\sqrt{\epsilon_r\mu_o\epsilon_o}R) = \exp(ik_o\sqrt{-\epsilon_{Rr} + i\epsilon_{Ir}}R), \tag{4.2}$$

where R is the interaction distance. Then, the good balance between the permittivity values and frequency can be written as

$$-k_o \operatorname{Im}\left\{\sqrt{-\epsilon_{Rr} + i\epsilon_{Ir}}\right\} = -\omega\sqrt{\mu_o\epsilon_o}\operatorname{Im}\left\{\sqrt{-\epsilon_{Rr} + i\epsilon_{Ir}}\right\} \approx c. \tag{4.3}$$

For example, at 1 THz for a 100 nm object and at 10 THz for a 10 nm object, the exponential decays $(1 - \exp(cR))$ between two sides of the objects are calculated as approximately 59% and 26.5%, respectively, using the LD model. Hence, despite the quick decay of the Green's function, fields significantly penetrate into metallic objects in this scale. For small-scale objects at few THz frequencies, the unfulfilled localization of the Green's function on surfaces obviously needs penetrable modeling.

4.2 Simulation Method

For accurate and reliable analysis of metallic objects at THz frequencies, the penetrable formulation should be able to operate in a stable manner within a wide range of negative real permittivity values. MCTF, which is given in Chapter 2, is particularly employed for this purpose since it is proven to be suitable for plasmonic structures [10]. MCTF converges into EFIE for increasingly negative real permittivity

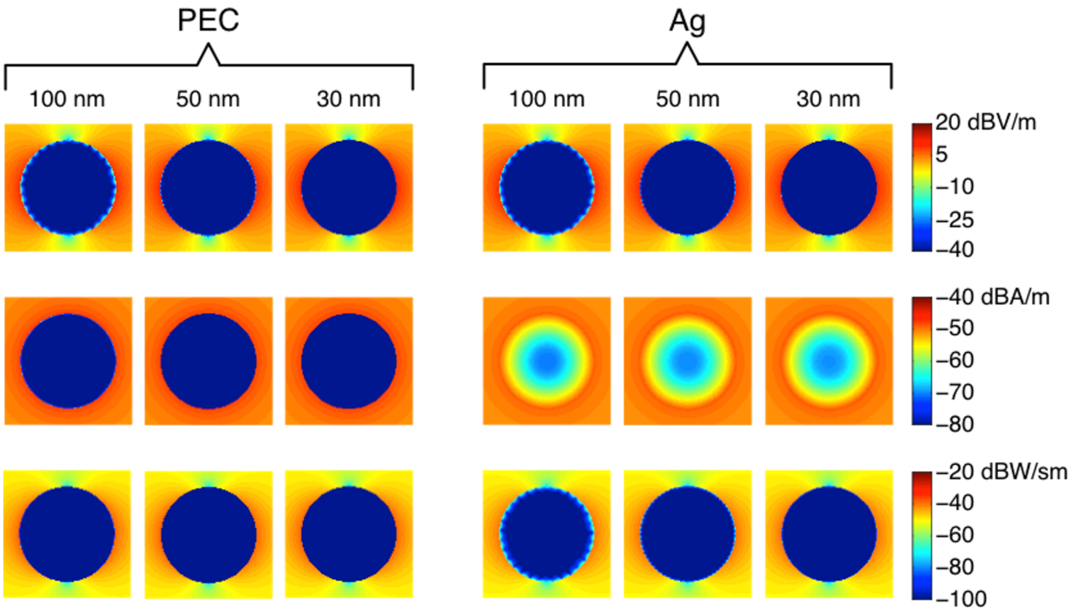

Figure 4.2: Near-zone field intensity and power density distributions for the scattering problems involving PEC and Ag spheres of diameter 1 µm at 1 THz obtained with different mesh sizes.

values; hence, transition from penetrable model to PEC model can smoothly occur. For comparisons of penetrable and impenetrable models, EFIE (derived in Chapter 2) is employed for PEC model solutions, while JMCFIE and PMCHWT formulations (derived in Chapter 2), as well as MCTF are employed on penetrable models.

4.3 Numerical Results

As numerical examples, different-sized spherical particles and different-sized thin slabs that are illuminated via plane waves at different frequencies are investigated [84]. MOM and GMRES iterative solver with a residual error limit of 10^{-4} are used for the solutions of all scattering problems. Figure 4.2 presents near-zone field intensity and power density distributions for PEC and Ag spheres of diameter 1 µm at 1 THz. Mesh sizes of 100 nm, 50 nm, and 30 nm are considered to demonstrate the accuracy of solutions by inspecting similarity and convergence of the results as the discretization is refined. Near-zone electric field intensity (first row), magnetic field intensity (second row), and power density (third row) distributions are shown on E-plane cross sections in Figure 4.2. The electric field intensity and power density

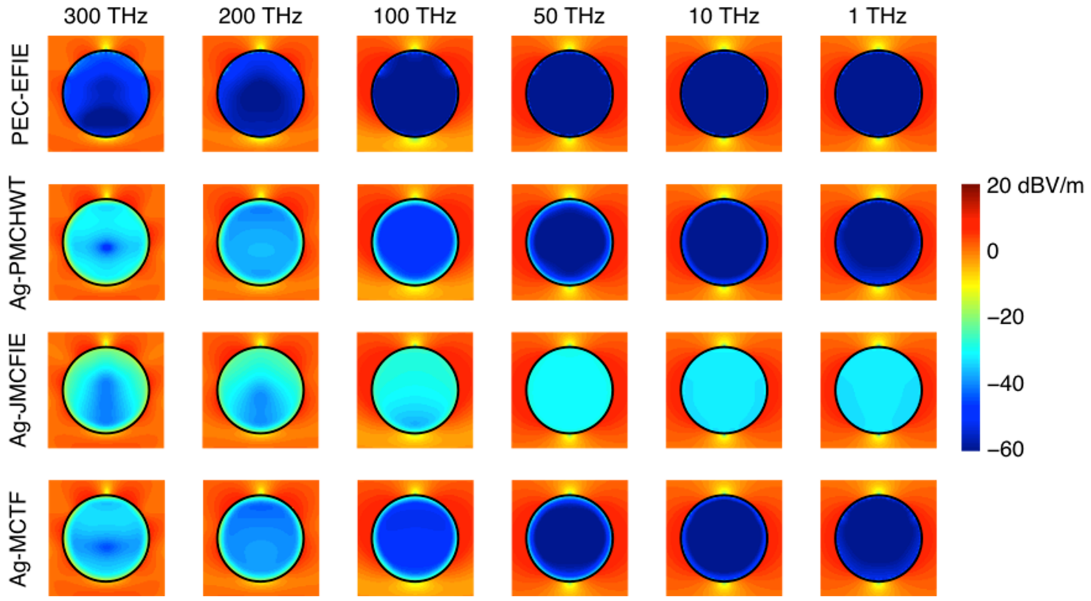

Figure 4.3: Near-zone electric field intensity distributions for scattering problems involving PEC and Ag spheres of diameter 1 μm at different frequencies.

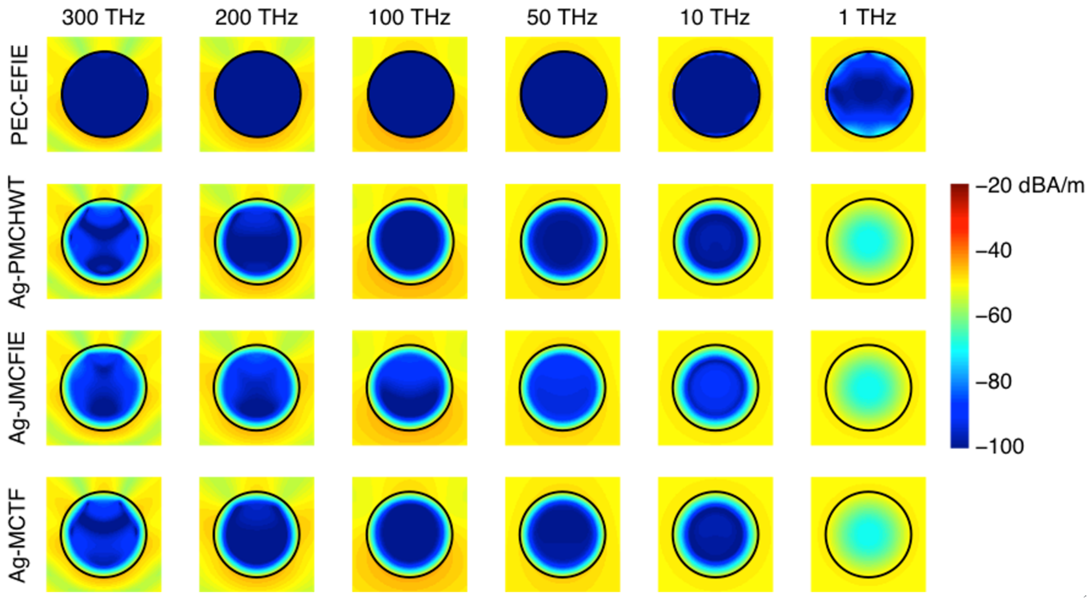

Figure 4.4: Near-zone magnetic field intensity distributions for scattering problems involving PEC and Ag spheres of diameter 1 μm at different frequencies.

distributions for penetrable and PEC models appear to be similar. On the other hand, it is observed that the magnetic field intensity distributions are extremely different for penetrable and PEC models, verifying the necessity of penetrable modeling. We

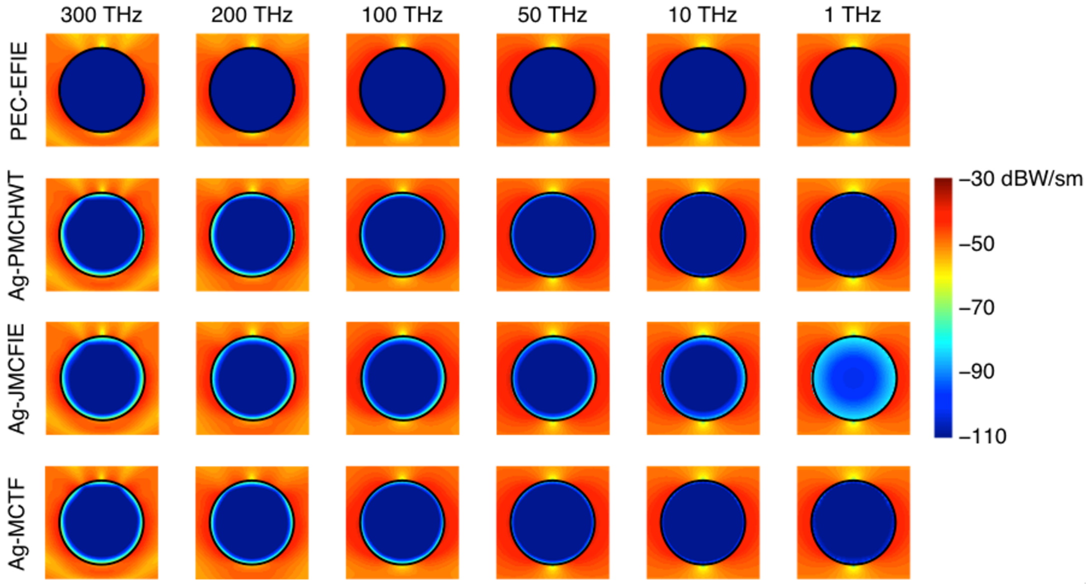

Figure 4.5: Near-zone power density distributions for scattering problems involving PEC and Ag spheres of diameter 1 μm at different frequencies.

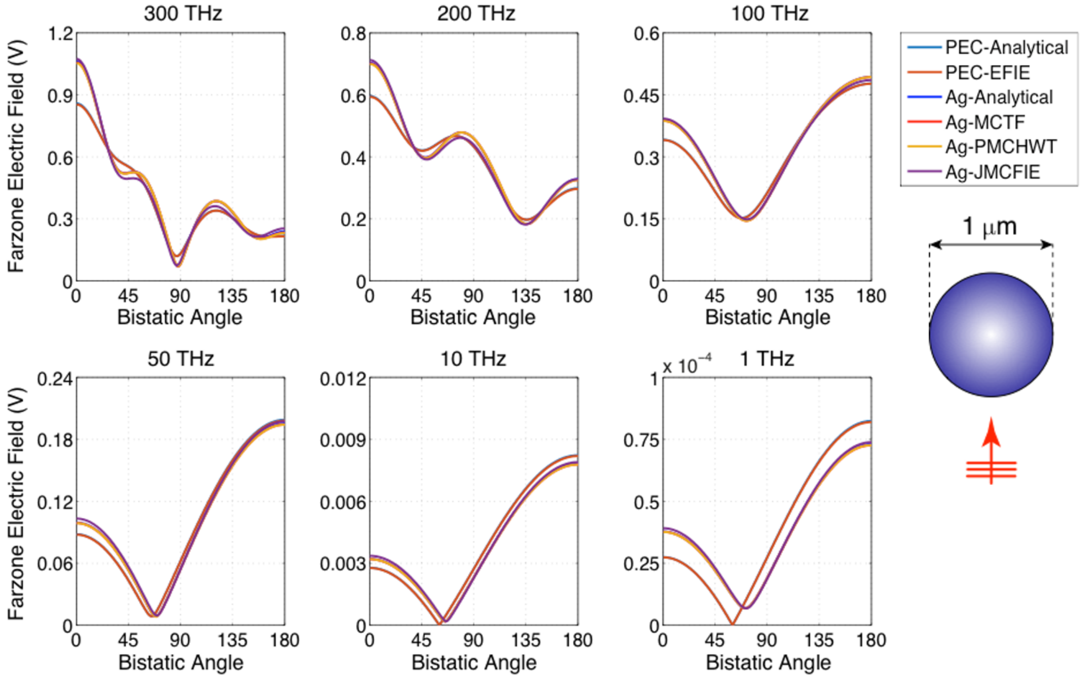

Figure 4.6: Far-zone electric field intensity with respect to bistatic angle for scattering problems involving PEC and Ag spheres of diameter 1 μm at different frequencies.

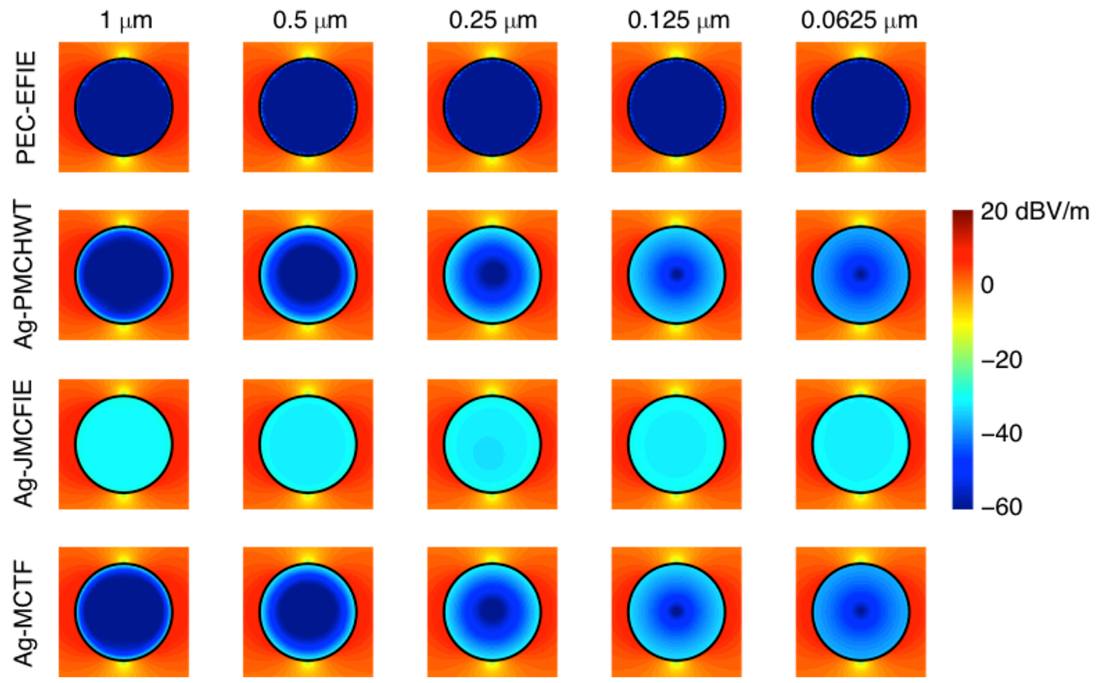

Figure 4.7: Near-zone electric field intensity distributions for scattering problems involving PEC and Ag spheres of different sizes at 50 THz.

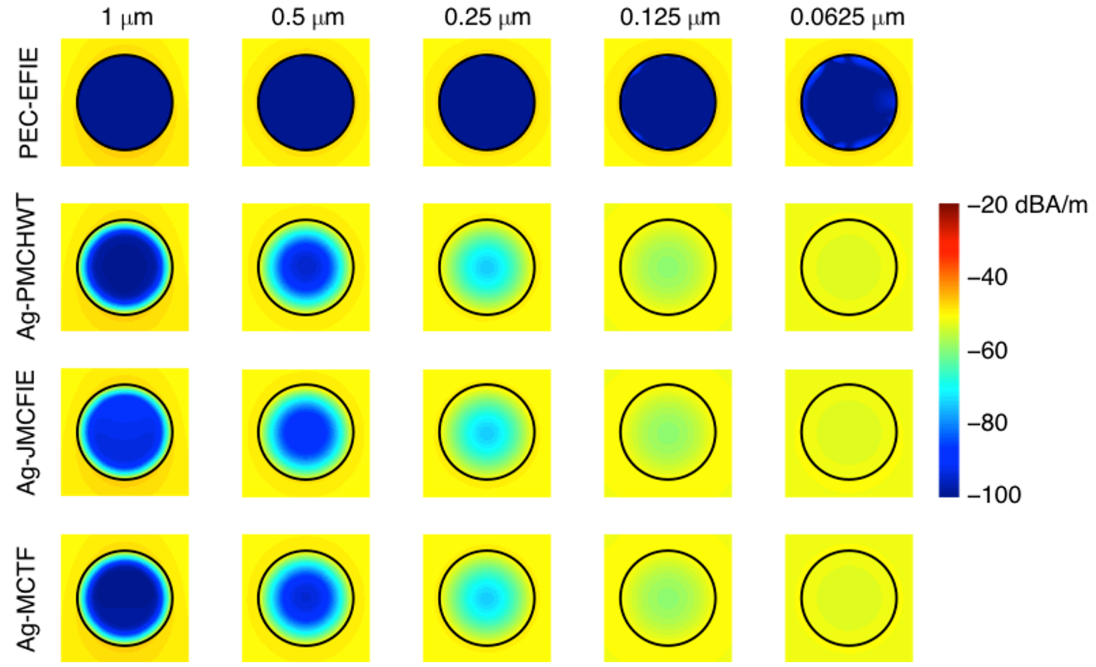

Figure 4.8: Near-zone magnetic field intensity distributions for scattering problems involving PEC and Ag spheres of different sizes at 50 THz.

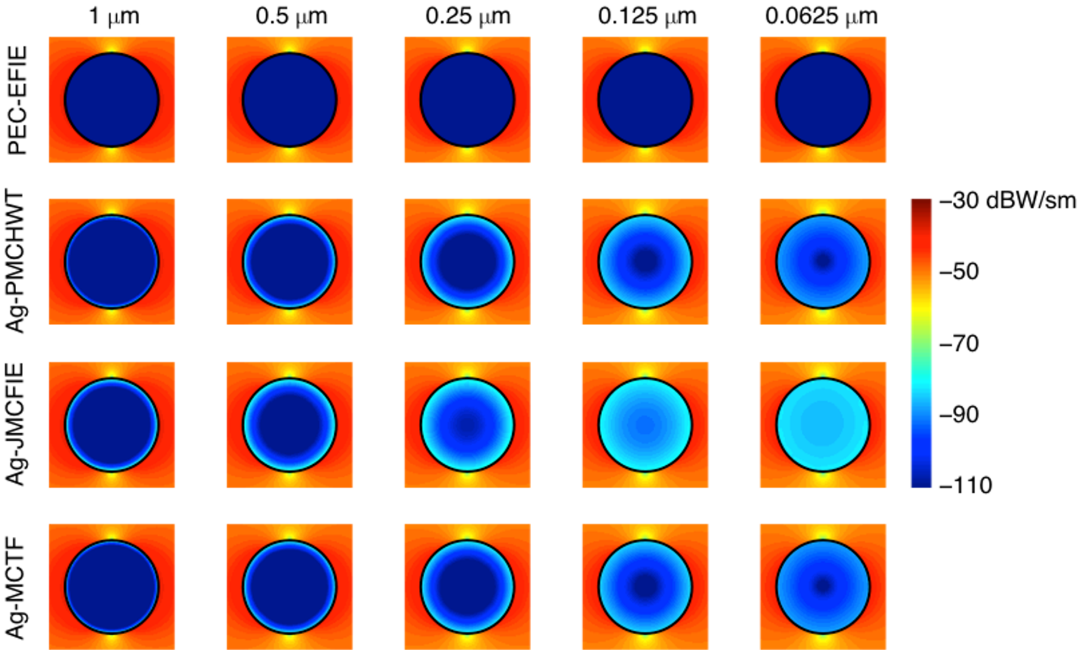

Figure 4.9: Near-zone power density distributions for scattering problems involving PEC and Ag spheres of different sizes at 50 THz.

note that similar power density distributions obtained for PEC and penetrable models are due to vanishingly small electric field intensity values inside the Ag sphere.

Figures 4.3–4.5 show near-zone electric field intensity distributions for PEC and Ag spheres of diameter 1 μm from 300 THz to 1 THz obtained with EFIE for PEC model, as well as with PMCHWT, JMCFIE, and MCTF for penetrable model. The relative permittivity values at 300 THz and 1 THz are $(-41 + 2.8i)$ and $(-0.3 + 3.4i) \times 10^5$, respectively. Using the penetrable model, the electric field intensity inside the sphere approaches zero (becoming consistent with the PEC model) as the frequency decreases, whereas it is clearly nonzero at the higher frequencies. In addition, inaccuracy issues of the JMCFIE formulation should be noted. In Figure 4.4, completely different magnetic field intensity distributions are observed for PEC and Ag spheres at all frequencies. Specifically, at 1 THz, a distinct nonzero magnetic field intensity distribution inside the Ag sphere, as well as the low-frequency breakdown of EFIE are observed. Figure 4.5 reveals again the need for penetrable modeling and the inaccuracy of JMCFIE. The far-zone electric field intensity values with respect to bistatic angle on the E-plane shown in Figure 4.6 clearly indicate the necessity of penetrable

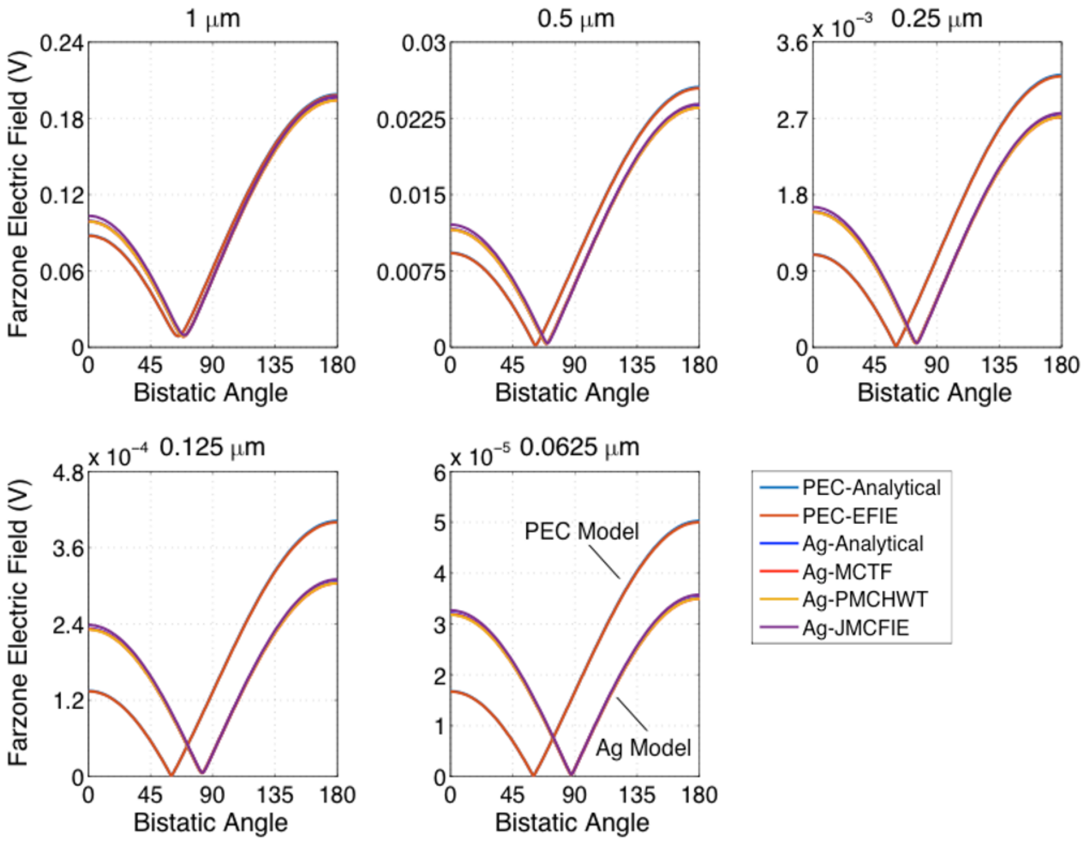

Figure 4.10: Far-zone electric field intensity with respect to bistatic angle on the E-plane for scattering problems involving PEC and Ag spheres of different sizes at 50 THz.

modeling even for far-zone scattering computations. Comparisons with Mie series solutions for both PEC and penetrable models demonstrate the good accuracy of MCTF and inaccuracy of JMCFIE.

Figures 4.7–4.9 present near-zone electric field intensity distributions for PEC and Ag spheres of different sizes from 1 μm to 0.0625 μm at 50 THz obtained with EFIE for PEC and PMCHWT, JMCFIE, and MCTF for penetrable models. The relative permittivity value at 50 THz is $(-1500+360i)$. The mesh size is changed from 50 nm to 3.25 nm, in accordance with the sphere size from 1 μm to 0.0625 μm. The inaccuracy of JMCFIE is immediately observed in the electric field intensity distributions shown in Figure 4.7. In Figure 4.8, a significant penetration of the magnetic field intensity into the spheres is observed especially for small diameter values. Consequently,

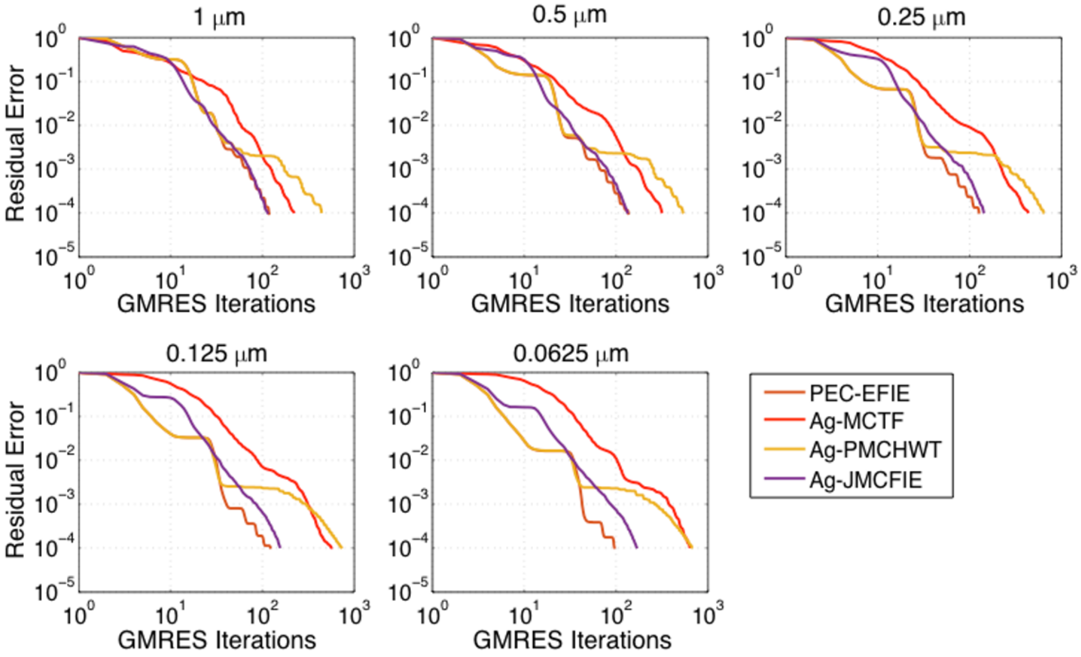

Figure 4.11: Iterative solutions of scattering problems involving PEC and Ag spheres of different sizes at 50 THz.

the power density distributions presented in Figure 4.9 show significant differences between the PEC and penetrable models, strongly proving the necessity of penetrable modeling. Figure 4.10 depicts the bistatic far-zone electric field intensity values for the same scattering problems. The difference between the electromagnetic responses of the PEC and penetrable models is significant when the diameter becomes small. Iterative convergence histories shown in Figure 4.11 reveal that MCTF generally converges faster than PMCHWT, while it also leads to accurate results as shown in Figures 4.7–4.10. We note that the JMCFIE formulation leads to the fastest iterative convergences among penetrable formulations; however, it suffers from severe inaccuracy issues.

Finally, very thin slabs, which are illuminated via plane waves with normal incidences on the large surfaces of the slabs, are investigated as another set of numerical examples. Thin PEC and Ag slabs (with 1 μm × 1 μm base size) of 50 nm and 25 nm thicknesses are considered and the magnetic field intensity is computed on the E-plane (cross-section plane) with EFIE using PEC and PMCHWT, JMCFIE, and MCTF using penetrable models from 300 THz to 1 THz. As shown in Figure 4.12,

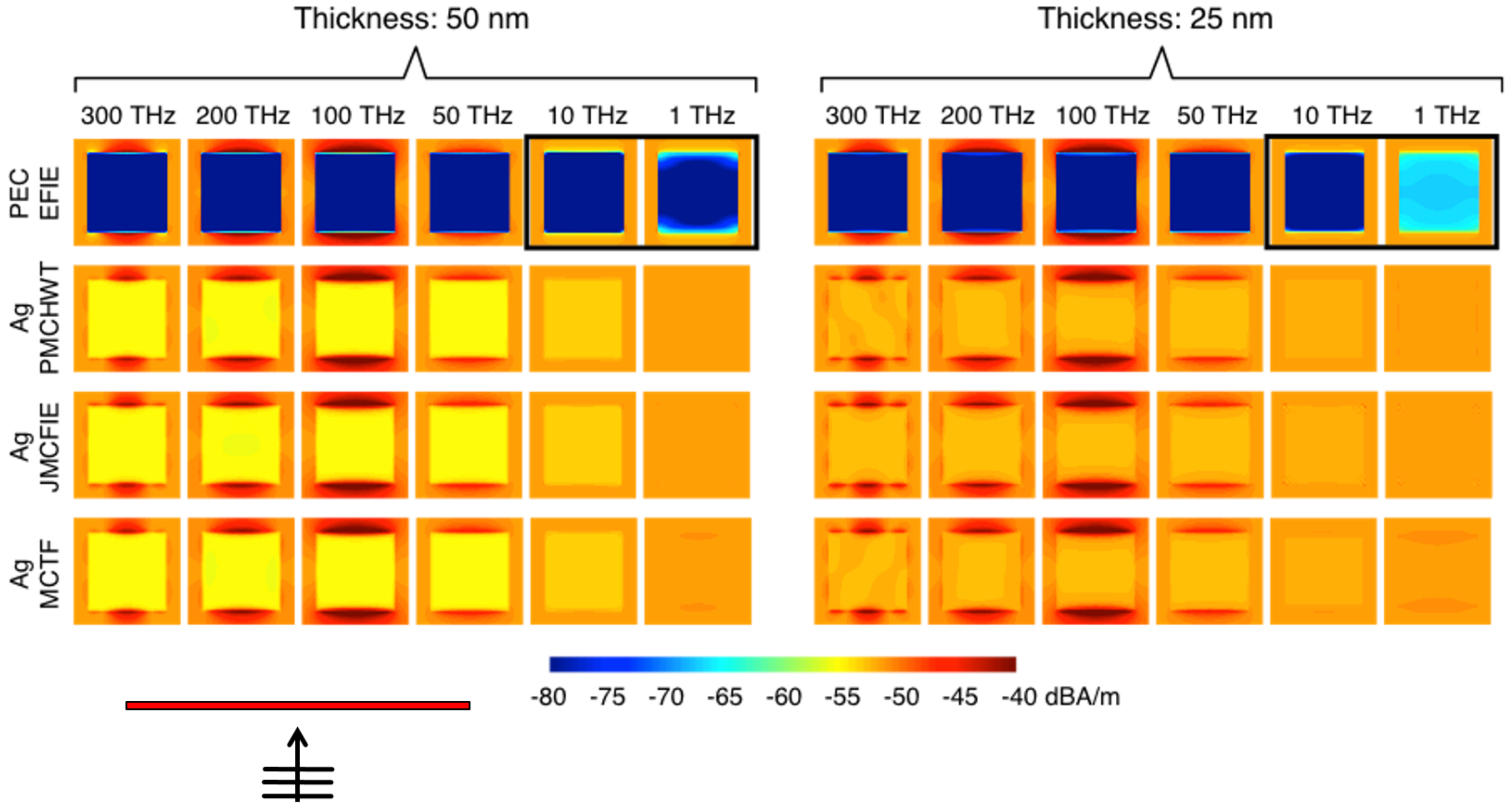

Figure 4.12: Near-zone magnetic field intensity distributions for scattering problems involving PEC and Ag thin slabs (with 1 μm × 1 μm base size) of 50 nm and 25 nm thicknesses at different frequencies.

PEC modeling provides extremely misleading analysis of this kind of thin structures, even at the higher THz frequencies.

4.4 Concluding Remarks

Although metals at lower THz frequencies are treated as PEC objects in general, they should be formulated via penetrable modeling for small-scale structures. For accurate and reliable analysis of metallic objects at THz frequencies, the penetrable formulation should be able to operate in a stable manner within a wide range of negative real permittivity values. Using a penetrable model, the electric field intensity inside a small particle approaches zero (becoming consistent with the PEC model) as the frequency decreases, whereas it is clearly nonzero at the higher frequencies. We observe completely different magnetic field intensity distributions for PEC and Ag particles at all frequencies. The difference between the electromagnetic responses of the PEC and penetrable models of a small particle is also significant in the far-zone electric field intensity plots. Hence, the near-zone field and density distributions, as well as the far-zone plots demonstrate the necessity of penetrable modeling. Considering penetrable modeling, iterative convergence histories reveal that MCTF generally converges faster than PMCHWT, while both formulations lead to accurate result. We note that the JMCFIE formulation leads to the fastest iterative convergences among penetrable formulations; however, it suffers from severe inaccuracy issues. Finally, we show that PEC modeling may provide extremely misleading analysis of thin structures, even at the higher THz frequencies.

CHAPTER 5

CONCLUSION

In this study, design, computational analysis, and realization of metamaterial structures with various exotic properties, i.e., imaginary index, negative index, ZI, and NZI, are presented.

For efficient and accurate iterative solutions of electromagnetic problems involving ZI and NZI materials, new SIE formulations are needed. As permittivity and/or permeability approach zero, conventional formulations suffer from inefficiency (ill-conditioning) and/or inaccuracy. These issues are directly related to the well-known low-frequency breakdowns associated with inner problems, as well as numerical imbalance between inner and outer problems (operators). We show that, by correctly balancing integral-equation and operator combinations, it is possible to obtain robust formulations that provide both efficient and accurate iterative solutions with the conventional discretization schemes.

In addition to robust formulations, AD-MLFMA is used for efficient simulations of large-scale structures involving NZI objects. Without any restriction on the size of interaction boxes, the same tree structure is used for electromagnetic interactions in the host media and inside NZI bodies, as well as in ordinary materials. Depending on its dimensions, a portion of the master tree structure can be used effectively for computing far-zone interactions related to an NZI object. Once the expansion coefficients for electric/magnetic currents are obtained, they are used to generate near-zone electromagnetic fields, as usual.

We present various examples, in which NZI materials are used to improve the performances of electromagnetic devices. We observe excellent stability in iteration counts, particularly considering solutions when both relative permittivity and relative permeability are smaller than unity, using the developed implementation based on the new mixed formulation and AD-MLFMA for NZI materials. On the contrary, using the developed implementation based on JMCFIE and AD-MLFMA for NZI materials, we observe that the iterative convergence deteriorates significantly when the permittivity/permeability decrease. Plots for inner/outer problems for the scattering problems involving spherical particles and various lens structures confirm the accuracy, while consistency of the results obtained with JMCFIE and the new mixed formulation is remarkable. Nevertheless, the number of iterations for JMCFIE can be more than three times of the one for the mixed formulation. Numerical simulations of structures involving NZI materials provide physical information on these interesting objects. For the lens problems, MNZ and ENZ cases are strongly affected by reflections, while no reflection is observed when NZI is achieved by using equal permittivity and permeability values. Computational simulations of three-dimensional composite structures involving NZI materials together with ordinary bodies, such as waveguides are extensively investigated. Using a broadband implementation based on SIEs and MLFMA, accurate and efficient solutions can be obtained, without resorting to volume-based solvers.

Realization of single-band and multiband metamaterials that are fabricated via low-cost inkjet printing is presented. As an alternative to more sophisticated printing methods, by designing and constructing a low-cost setup based on commercial printers loaded with silver-based inks, it is possible to fabricate three-dimensional metamaterial structures, despite the challenges in the fabrication procedures. We show the feasibility of low-cost fabrications by designing and testing single-band metamaterial blocks of SRRs, as well as SRRs and thin wires (demonstrating an interesting phenomenon of negative refractive index) resonating at the C-band and the lower frequencies of the X-band. As a natural drawback of the low-cost printing, the SRRs that are produced are not perfectly identical and the bandwidth of the resonance is slightly narrower than expected for low transmission values. As also presented in this study, it is possible to design high-quality multiband metamaterials with three and more resonances by arranging SRRs in three-dimensional grids. On the other hand, in order to obtain good resonance characteristics, i.e., low transparency at resonance frequencies and high transparency between resonances, geometric parameters must be selected carefully. Accurate simulations demonstrate favorable properties of the designed multiband metamaterials, some of which are also fabricated and tested in a measurement setup. While the measured results are very promising, further improvements in fabrications are needed to demonstrate the excellent transmission properties of the designs, to be presented in future works. The results demonstrate promising properties of the low-cost metamaterials that can be used in massive amounts for alternative applications, such as frequency-selective microwave shielding.

Computational homogenization of finite three-dimensional metamaterials by optimizing the electromagnetic parameters of enclosing boxes is also presented. Electromagnetic problems involving homogeneous objects required for optimization trials are solved accurately via MLFMA. Optimization results for SRR arrays demonstrate promising similarities in the responses of realistic arrays and the corresponding homogeneous models. The proposed approach is also applicable for the homogenization of other metamaterials, as well as those based on measurement results.

Solutions of electromagnetic problems involving metallic nanostructures at THz frequencies are considered. It is shown that the decay of electromagnetic fields inside a metallic nanoparticle at such frequencies may not be sufficient to use a perfectly conducting model. This occurs especially for the conventional metals (e.g., Ag, Au, and Cu) at the lower THz frequencies, where large permittivity values with negative real parts become in balance with the frequency. Based on the observations in this twilight region, penetrable models seem to be reliable options for formulations, not only in contrast to PEC models but also in comparison to quasi-static limits that may not be accurate particularly when nanoparticles are combined as large-scale metastructures. As usual, only correct combinations of integro-differential operators can lead to stable solutions, which can be achieved by using the developed formulations that provide accurate results for wide ranges of permittivity values.

REFERENCES

[1] R. Ziolkowski, “Propagation in and scattering from a matched metamaterial having a zero index of refraction,” *Physical Review E*, vol. 70, Oct. 2004.

[2] M. Silveirinha and N. Engheta, “Tunneling of electromagnetic energy through subwavelength channels and bends using epsilon-near-zero materials,” *Physical Review Letters*, vol. 97, Nov. 2006.

[3] M. Silveirinha and N. Engheta, “Design of matched zero-index metamaterials using nonmagnetic inclusions in epsilon-near-zero media,” *Physical Review B*, vol. 75, Feb. 2007.

[4] A. A. Tavallaee, P. W. C. Hon, K. Mehta, T. Itoh, and B. S. Williams, “Zero-index terahertz quantum-cascade metamaterial lasers,” *IEEE Journal of Quantum Electronics*, vol. 46, pp. 1091–1098, Jul. 2010.

[5] M. Sun, Z. N. Chen, and X. Qing, “Gain enhancement of 60-GHz antipodal tapered slot antenna using zero-index metamaterial,” *IEEE Transactions on Antennas and Propagation*, vol. 61, pp. 1741–1746, Apr. 2013.

[6] J. Luo and Y. Lai, “Anisotropic zero-index waveguide with arbitrary shapes,” *Scientific Reports*, vol. 4, Jul. 2014.

[7] I. Liberal and N. Engheta, “Near-zero refractive index photonics,” *Nature Photonics*, vol. 11, pp. 149–158, Mar. 2017.

[8] I. V. Lindell, J. Markkanen, A. Sihvola, and P. Ylä-Oijala, “Realization of spherical D’B’ boundary by a layer of wave-guiding medium,” *Metamaterials*, vol. 5, pp. 149–154, Dec. 2011.

[9] P. Ylä-Oijala, J. Markkanen, S. Järvenpää, and S. P. Kiminki, “Surface and volume integral equation methods for time-harmonic solutions of Maxwell’s equations,” *Progress in Electromagnetics Research*, vol. 149, pp. 15–44, Jan. 2014.

[10] B. Karaosmanoğlu, A. Yılmaz, and Ö. Ergül, “A comparative study of surface integral equations for accurate and efficient analysis of plasmonic structures,” *IEEE Transactions on Antennas and Propagation*, vol. 65, pp. 3049–3057, Jun. 2017.

[11] Ö. Ergül and B. Karaosmanoğlu, “Broadband multilevel fast multipole algorithm based on an approximate diagonalization of the Green’s function,” *IEEE Transactions on Antennas and Propagation*, vol. 63, pp. 3305–3041, Jul. 2015.

[12] J. B. Pendry, A. J. Holden, D. J. Robbins, and W. J. Stewart, “Magnetism from conductors and enhanced nonlinear phenomena,” *IEEE Transactions on Microwave Theory and Techniques*, vol. 47, pp. 2075–2084, Nov. 1999.

[13] D. R. Smith, W. J. Padilla, D. C. Vier, S. C. Nemat-Nasser, and S. Schultz, “Composite medium with simultaneously negative permeability and permittivity,” *Physical Review Letters*, vol. 84, pp. 4184–4187, May 2000.

[14] J. D. Baena, R. Marqués, F. Medina, and J. Martel, “Artificial magnetic metamaterial design by using spiral resonators,” *Physical Review B*, vol. 69, Jan. 2004.

[15] N. Engheta and R. W. Ziolkowski, “A positive future for double-negative metamaterials,” *IEEE Transactions on Microwave Theory and Techniques*, vol. 53, pp. 1535–1556, Apr. 2005.

[16] M. Gokkavas, K. Guven, I. Bulu, K. Aydin, R. S. Penciu, M. Kafesaki, C. M. Soukoulis, and E. Ozbay, “Experimental demonstration of a left-handed metamaterial operating at 100 GHz,” *Physical Review B*, vol. 73, Jan. 2006.

[17] F. Bilotti, A. Toscano, and L. Vegni, “Design of spiral and multiple split-ring resonators for the realization of miniaturized metamaterial samples,” *IEEE Transactions on Antennas and Propagation*, vol. 55, pp. 2258–2267, Aug. 2007.

[18] E. Rajo-Iglesias, O. Quevedo-Teruel, and M. N. M. Kehn, “Multiband SRR loaded rectangular waveguide,” *IEEE Transactions on Antennas and Propagation*, vol. 57, pp. 1571–1575, May 2009.

[19] E. Ekmekci, K. Topalli, T. Akin, and G. Turhan-Sayan, “A tunable multi-band metamaterial design using micro-split SRR structures,” *Optical Express*, vol. 17, pp. 16046–16058, Aug. 2009.

[20] O. Turkmen, E. Ekmekci, and G. Turhan-Sayan, “Nested U-ring resonators: a novel multi-band metamaterial design in microwave region,” *IET Microwaves, Antennas Propagation*, vol. 6, pp. 1102–1108, Jul. 2012.

[21] M. Kadic, G. W. Milton, M. Van Hecke, and M. Wegener, “3D metamaterials,” *Nature Reviews Physics*, vol. 1, pp. 198–210, Jan. 2019.

[22] L. Gürel, Ö. Ergül, A. Ünal, and T. Malas, “Fast and accurate analysis of large metamaterial structures using the multilevel fast multipole algorithm,” *Progress in Electromagnetics Research*, vol. 95, pp. 179–198, Jan. 2009.

[23] Ö. Ergül and L. Gürel, “Efficient solutions of metamaterial problems using a low-frequency multilevel fast multipole algorithm,” *Progress in Electromagnetics Research*, vol. 108, pp. 81–99, Jan. 2010.

[24] P. V. Nikitin, S. Lam, and K. V. S. Rao, “Low cost silver ink RFID tag antennas,” in *2005 IEEE Antennas and Propagation Society International Symposium*, vol. 2B, (Washington, DC, USA), Jul. 2005.

[25] L. Yang, A. Rida, R. Vyas, and M. M. Tentzeris, “RFID tag and RF structures on a paper substrate using inkjet-printing technology,” *IEEE Transactions on Microwave Theory and Techniques*, vol. 55, pp. 2894–2901, Dec. 2007.

[26] L. Yang, R. Zhang, D. Staiculescu, C. P. Wong, and M. M. Tentzeris, “A novel conformal RFID-enabled module utilizing inkjet-printed antennas and carbon nanotubes for gas-detection applications,” *IEEE Antennas and Wireless Propagation Letters*, vol. 8, pp. 653–656, May 2009.

[27] A. Rida, L. Yang, R. Vyas, and M. M. Tentzeris, “Conductive inkjet-printed antennas on flexible low-cost paper-based substrates for RFID and WSN applications,” *IEEE Antennas and Propagation Magazine*, vol. 51, pp. 13–23, Jun. 2009.

[28] J. R. Cooper, S. Kim, and M. M. Tentzeris, "A novel polarization-independent, free-space, microwave beam splitter utilizing an inkjet-printed, 2-D array frequency selective surface," *IEEE Antennas and Wireless Propagation Letters*, vol. 11, pp. 686–688, Jun. 2012.

[29] B. S. Cook and A. Shamim, "Inkjet printing of novel wideband and high gain antennas on low-cost paper substrate," *IEEE Transactions on Antennas and Propagation*, vol. 60, pp. 4148–4156, Sep. 2012.

[30] A. R. Maza, B. Cook, G. Jabbour, and A. Shamim, "Paper-based inkjet-printed ultra-wideband fractal antennas," *IET Microwaves, Antennas Propagation*, vol. 6, pp. 1366–1373, Sep. 2012.

[31] H. Subbaraman, D. T. Pham, X. Xu, M. Y. Chen, A. Hosseini, X. Lu, and R. T. Chen, "Inkjet-printed two-dimensional phased-array antenna on a flexible substrate," *IEEE Antennas and Wireless Propagation Letters*, vol. 12, pp. 170–173, Feb. 2013.

[32] T. Çiftçi, B. Karaosmanoğlu, and Ö. Ergül, "Low-cost inkjet antennas for RFID applications [extended]," *IOP Conference Series: Materials Science and Engineering*, vol. 120, Apr. 2016.

[33] S. Güler, B. Karaosmanoğlu, and Ö. Ergül, "Design, simulation, and fabrication of a novel type of inkjet-printed pixel antennas," *Progress In Electromagnetics Research Letters*, vol. 64, pp. 51–55, Jan. 2016.

[34] F. Mutlu, C. Önol, B. Karaosmanoğlu, and Ö. Ergül, "Inkjet-printed cage-dipole antennas for radio-frequency applications," *IET Microwaves, Antennas Propagation*, vol. 11, pp. 2016–2020, Dec. 2017.

[35] J. C. Batchelor, E. A. Parker, J. A. Miller, V. Sanchez-Romaguera, and S. G. Yeates, "Inkjet printing of frequency selective surfaces," *Electronics Letters*, vol. 45, pp. 7–8, Jan. 2009.

[36] M. Walther, A. Ortner, H. Meier, U. Löffelmann, P. J. Smith, and J. G. Korvink, "Terahertz metamaterials fabricated by inkjet printing," *Applied Physics Letters*, vol. 95, Jan. 2009.

[37] M. Yoo, H. K. Kim, S. Kim, M. Tentzeris, and S. Lim, "Silver nanoparticle-based inkjet-printed metamaterial absorber on flexible paper," *IEEE Antennas and Wireless Propagation Letters*, vol. 14, pp. 1718–1721, Apr. 2015.

[38] S. N. Zabri, R. Cahill, G. Conway, and A. Schuchinsky, "Inkjet printing of resistively loaded FSS for microwave absorbers," *Electronics Letters*, vol. 51, pp. 999–1001, Jun. 2015.

[39] Ö. Ergül and L. Gürel, *The Multilevel Fast Multipole Algorithm (MLFMA) for Solving Large-Scale Computational Electromagnetics Problems*. Wiley-IEEE, 2014.

[40] A. J. Poggio and E. K. Miller, "Integral equation solutions of three-dimensional scattering problems," in *Computer Techniques for Electromagnetics* (R. Mittra, ed.), ch. 4, pp. 159–264, Oxford: Pergamon Press, 1973.

[41] Y. Chang and R. F. Harrington, "A surface formulation for characteristic modes of material bodies," *IEEE Transactions on Antennas and Propagation*, vol. 25, pp. 789–795, Nov. 1977.

[42] T. K. Wu and L. L. Tsai, "Scattering from arbitrarily-shaped lossy dielectric bodies of revolution," *Radio Science*, vol. 12, pp. 709–718, Sep.-Oct. 1977.

[43] P. Ylä-Oijala, M. Taskinen, and S. Järvenpää, "Surface integral equation formulations for solving electromagnetic scattering problems with iterative methods," *Radio Science*, vol. 40, Nov. 2005.

[44] C. Müller, *Foundations of the Mathematical Theory of Electromagnetic Waves*. New York: Springer, 1969.

[45] P. Ylä-Oijala and M. Taskinen, "Well-conditioned Müller formulation for electromagnetic scattering by dielectric objects," *IEEE Transactions on Antennas and Propagation*, vol. 53, pp. 3316–3323, Oct. 2005.

[46] P. Ylä-Oijala and M. Taskinen, "Application of combined field integral equation for electromagnetic scattering by dielectric and composite objects," *IEEE Transactions on Antennas and Propagation*, vol. 53, pp. 1168–1173, Mar. 2005.

[47] B. G. Galerkin, "Rods and plates. series occurring in various questions concerning the elastic equilibrium of rods and plates," *Engineers Bulletin (Vestnik Inzhenerov)*, vol. 19, pp. 897–908, 1915.

[48] K. Cools, F. P. Andriulli, and E. Michielssen, "A Calderón multiplicative preconditioner for the PMCHWT integral equation," *IEEE Transactions on Antennas and Propagation*, vol. 59, pp. 4579–4587, Dec. 2011.

[49] Ö. Ergül and L. Gürel, "Comparison of integral-equation formulations for the fast and accurate solution of scattering problems involving dielectric objects with the multilevel fast multipole algorithm," *IEEE Transactions on Antennas and Propagation*, vol. 57, pp. 176–187, Jan. 2009.

[50] P. Ylä-Oijala, J. Markkanen, S. Järvenpää, and S. P. Kiminki, "Surface and volume integral equation methods for time-harmonic solutions of Maxwell's equations," *Progress In Electromagnetics Research*, vol. 149, pp. 15–44, 2014.

[51] H. İbili, Y. Koyaz, U. Özmü, B. Karaosmanoğlu, and Ö. Ergül, "Novel SIE implementations for efficient and accurate electromagnetic simulations of zero-index materials," in *Progress in Electromagnetics Research Symposium (PIERS)*, (Rome, Italy), Jun. 2019.

[52] B. Karaosmanoğlu, U. Özmü, and Ö. Ergül, "Novel SIE formulations for accurate and stable analysis of near-zero-index materials," in *IEEE International Symposium on Antennas and Propagation (APS)*, (Atlanta, GA, USA), Jul. 2019.

[53] B. Karaosmanoğlu, Y. Koyaz, H. İbili, and Ö. Ergül, "Fast and accurate analysis of three-dimensional structures involving near-zero-index materials," in *International Conference on Electromagnetics in Advanced Applications (ICEAA)*, (Granada, Spain), Sep. 2019.

[54] R. F. Harrington, *Field Computation by Moment Methods.* New York: Macmillan, 1968.

[55] W. C. Gibson, *The Method of Moments in Electromagnetics.* Boca Raton: Chapman and Hall/CRC, 2007.

[56] S. M. Rao, D. R. Wilton, and A. W. Glisson, "Electromagnetic scattering by surfaces of arbitrary shape," *IEEE Transactions on Antennas and Propagation*, vol. 30, pp. 409–418, May 1982.

[57] R. Coifman, V. Rokhlin, and S. Wandzura, "The fast multipole method for the wave equation: a pedestrian prescription," *IEEE Antennas and Propagation Magazine*, vol. 35, pp. 7–12, Jun. 1993.

[58] J. Song, C.-C. Lu, and W. C. Chew, "Multilevel fast multipole algorithm for electromagnetic scattering by large complex objects," *IEEE Transactions on Antennas and Propagation*, vol. 45, pp. 1488–1493, Oct. 1997.

[59] Z. G. Qian and W. C. Chew, "A quantitative study on the low frequency breakdown of EFIE," *Microwave and Optical Technology Letters*, vol. 50, pp. 1159–1162, 2008.

[60] J.-S. Zhao and W. C. Chew, "Three-dimensional multilevel fast multipole algorithm from static to electrodynamic," *Microwave and Optical Technology Letters*, vol. 26, pp. 43–48, 2000.

[61] L. Jiang and W. C. Chew, "Low-frequency fast inhomogeneous planewave algorithm (LF-FIPWA)," *Microwave and Optical Technology Letters*, vol. 40, pp. 117–122, 2004.

[62] Ö. Ergül and B. Karaosmanoğlu, "Approximate stable diagonalization of the Green's function for low frequencies," *IEEE Antennas and Wireless Propagation Letters*, vol. 13, pp. 1054–1056, 2014.

[63] Y. Saad and M. H. Schultz, "GMRES: A generalized minimal residual algorithm for solving nonsymmetric linear systems," *SIAM Journal on Scientific and Statistical Computing*, vol. 7, pp. 856–859, 1986.

[64] Y. Koyaz, H. İbili, B. Karaosmanoğlu, and Ö. Ergül, "Analysis of composite structures involving near-zero-index materials," in *Int. Conf. on. Microwaves, Communications, Antennas, and Electronic Systems (IEEE COMCAS)*, (Tel Aviv, Israel), Nov. 2019.

[65] M. G. Silveirinha and C. A. Fernandes, “Homogenization of metamaterial surfaces and slabs: the crossed wire mesh canonical problem,” *IEEE Transactions on Antennas and Propagation*, vol. 53, pp. 59–69, Jan 2005.

[66] M. G. Silveirinha and C. A. Fernandes, “Homogenization of 3-D-connected and nonconnected wire metamaterials,” *IEEE Transactions on Microwave Theory and Techniques*, vol. 53, pp. 1418–1430, April 2005.

[67] A. Alù, “First-principles homogenization theory for periodic metamaterials,” *Physical Review B*, vol. 84, Aug. 2011.

[68] I. Bogaert, J. Peeters, and F. Olyslager, “Homogenization of metamaterials using full-wave simulations,” *Metamaterials*, vol. 2, pp. 101–112, 2008.

[69] Ö. Ergül, “Fast and accurate analysis of homogenized metamaterials with the surface integral equations and the multilevel fast multipole algorithm,” *IEEE Antennas and Wireless Propagation Letters*, vol. 10, pp. 1286–1289, 2011.

[70] A. Andryieuski, R. Malureanu, and A. V. Lavrinenko, “Homogenization of metamaterials: Parameters retrieval methods and intrinsic problems,” in *12th International Conference on Transparent Optical Networks*, (Munich, Germany), Jun. 2010.

[71] D. R. Smith and J. B. Pendry, “Homogenization of metamaterials by field averaging,” *Journal of the Optical Society of America B*, vol. 23, pp. 391–403, Mar. 2006.

[72] X.-X. Liu, J. W. Massey, M.-F. Wu, K. T. Kim, R. A. Shore, A. E. Yilmaz, and A. Alù, “Homogenization of three-dimensional metamaterial objects and validation by a fast surface-integral equation solver,” *Optical Express*, vol. 21, pp. 21714–21727, Sep. 2013.

[73] D. R. Luna, C. F. L. Vasconcelos, and R. M. S. Cruz, “Using natural optimization algorithms and artificial neural networks in the design of effective permittivity of metamaterials,” in *2013 SBMO/IEEE MTT-S International Microwave Optoelectronics Conference (IMOC)*, Aug. 2013.

[74] C. Önol and Ö. Ergül, "Optimizations of patch antenna arrays using genetic algorithms supported by the multilevel fast multipole algorithm," *Radioengineering*, vol. 23, pp. 1005–1014, Dec. 2014.

[75] H. İbili and Ö. Ergül, "Very low-cost inkjet-printed metamaterials: Progress and challenges," in *2017 IEEE MTT-S International Microwave Workshop Series on Advanced Materials and Processes for RF and THz Applications (IMWS-AMP)*, Sep. 2017.

[76] H. İbili, B. Karaosmanoğlu, and Ö. Ergül, "Design and fabrication of low-cost inkjet-printed metamaterials," in *2017 IV International Electromagnetic Compatibility Conference (EMC Turkiye)*, Sep. 2017.

[77] H. İbili, S. Keleş, Ö. Eriş, and Ö. Ergül, "Realization of multiband microwave metamaterials fabricated via low-cost inkjet printing," in *European Microwave Conf. in Central Europe (EuMCE)*, May 2019.

[78] H. İbili, S. Keleş, and Ö. Ergül, "Multiband microwave metamaterials based on optimized arrangements of split-ring resonators," in *Progress in Electromagnetics Research Symposium (PIERS)*, Jun. 2019.

[79] H. İbili, B. Karaosmanoğlu, and Ö. Ergül, "Demonstration of negative refractive index with low-cost inkjet-printed microwave metamaterials," *Microwave and Optical Technology Letters*, vol. 60, pp. 187–191, 2018.

[80] H. İbili, B. Karaosmanoğlu, and Ö. Ergül, "Homogenization of microwave metamaterial structures using full-wave solutions and genetic algorithms," in *2018 18th Mediterranean Microwave Symposium (MMS)*, pp. 244–246, Oct. 2018.

[81] P. Drude, "Zur elektronentheorie der metalle," *Annalen der Physik*, vol. 306, pp. 566–613, 1900.

[82] H. A. Lorentz, "The motion of electrons in metallic bodies i," *Koninklijke Nederlandsche Akademie van Wetenschappen Proceedings*, vol. 7, pp. 438–453, 1905.

[83] P. B. Johnson and R. W. Christy, "Optical constants of the noble metals," *Physical Review B*, vol. 6, pp. 4370–4379, Dec. 1972.

[84] H. İbili, S. Güler, B. Karaosmanoğlu, and Ö. Ergül, “Penetrable numerical modeling of metallic nanoparticles at terahertz frequencies,” in *2018 Progress in Electromagnetics Research Symposium (PIERS)*, (Toyama, Japan), Aug. 2018.